Correlated Characterization and Advanced Microscopy of Sulfidic Solid-State Li Batteries

Doctoral Thesis Submitted for the degree of *Doctor of Philosophy*

Robert Scott Young

Supervisors: Dr. Rhodri Jervis and Dr. Alexander Rettie

University College London

Department of Chemical Engineering

2nd June 2025

© Copyright by Robert Scott Young, 2025

To Lucy

Declaration

I, Robert Scott Young confirm that the work presented in this thesis is my own. Where information has been derived from other sources, I confirm that this has been indicated in the thesis.

Abstract

The development of safe, high-energy-density storage devices has driven significant advancements in the field of lithium-ion batteries (LIBs), with solid-state batteries (SSBs) emerging as a promising next-generation energy storage solution. However, the transition to solid-state electrolytes (SEs) introduces novel degradation mechanisms, both mechanical and electro/chemical modalities that need to be better understood before widespread adoption. Here, advanced characterization methods are explored that aim to help further the understanding of the complexity of SSB degradation.

The X-ray computed tomography (XCT) based degradation studies here focus on Li | Li₆PS₅Cl | Li symmetric cells cycled under constant current conditions and track the propagation of cracks/voids. Early results highlighted that degradation has a strong dependence on cell design and manufacturing, demonstrating the necessity of informed structural considerations in producing representative electrochemical cells.

To further investigate the impact of mechanical and chemical degradation, a correlated characterization approach is utilized where XCT is combined with X-ray diffraction computed tomography (XRD-CT). Correlated XCT and XRD-CT datasets shed more light on the novel degradation mechanisms, showcasing the impact of pre-cycling defects on the SE, and exemplify how strain leads to cracks that allow Li to penetrate the SE.

Further advancements in degradation characterization are achieved through the integration of neutron computed tomography (NCT), another technique that is complementary to XCT. Because NCT is sensitive to Li, unlike XCT, a vital question can be answered: where is the Li metal plating during cycling and how does that contribute to degradation?

The correlated imaging approach of studying SE degradation provides tremendous information about the early stages of defect nucleation, informing the design of future SSBs. This work

serves as a foundation for further development in high spatiotemporal resolution studies of SEs, addressing key challenges in understanding degradation pathways and guiding advancements in SSB design and optimization.

Impact statement

With the goal of reaching net zero making the priority list of many countries, the continued development of energy storage devices remains crucial for the effective utilization of renewable energy sources. Secondary batteries are critical for decarbonizing transportation and other portable devices, even finding use in grid-level storage. The introduction of solid-state batteries (SSBs) represents a pivotal step toward safer, higher-energy density storage systems. However, the adoption of SSBs is currently limited by the novel failure mechanisms within solid electrolytes (SEs), which directly impact battery reliability, manufacturability, and lifetime.

This thesis explores the degradation of SSBs and develops methods of performing advanced characterization. The outcomes discussed here form a foundation for future SSB research by enabling earlier detection of degradation pathways, designing experiments to deconvolute degradation mechanisms, and providing more data towards accurate modelling of SSBs under operating conditions. Identifying defects in the earliest stages of degradation can also further inform SSB design, helping avoid failure mechanisms and ultimately work towards reducing the time and cost required to bring SSB technology to the market.

Throughout their PhD, the author was involved in collaborations with UK institutes and international facilities, such as ISIS neutron and muon source, Institut Laue-Langevin (ILL), and the European Synchrotron (ESRF). These collaborations contribute to the output of high-impact research and foster further collaboration in challenges that require significant teamwork

such as innovating energy storage. In addition to supporting collaborations aimed at advancing clean energy storage, the author actively engaged with community outreach to connect with a broad audience. For example, the author runs a scientific communication focused YouTube channel on X-ray physics and organized the STFC Early Career Researchers Conference on Energy Storage. Interaction with the public ensures visibility and accessibility of scientific research, encouraging participation in critical topics such as clean energy and net-zero.

In conclusion, this thesis represents a significant advancement in SSB characterization, offering insights that inform future research and highlight critical challenges hindering the commercialization of innovative technologies like SSBs. Identifying and addressing these challenges are essential for achieving meaningful progress in sustainable energy storage solutions.

UCL Research Paper Declaration Form: referencing the doctoral candidate's

own published work(s)

- 1. For a research manuscript prepared for publication but that has not yet been published:
- (a) What is the current title of the manuscript?

Informed Solid-state Electrochemical Cell Design for *Operando* X-ray Characterisation

(b) Has the manuscript been uploaded to a preprint server e.g.

medRxiv? No

If 'Yes, please give a link or doi:

(c) Where is the work intended to be published?

ChemRxiv

- (d) List the manuscripts authors in the intended authorship order:
- R. S. Young, J. Hu, N. R. H. Popp, F. iacoviello, A. R. T. Morrison, S. Dawes, P. P. Paul, M. D. Michiel, A. J. E. Rettie, R. Jervis
- (e) Stage of publication:

Editing final version

3. For multi-authored work, please give a statement of contribution

covering all authors: RSY writing of original version, conceptualization, experimentation, and data processing, JH cell cycling and experimentation, NRHP FEA analysis and writing, FI early segmentations, ARTM experimentation and editing, SD cell construction and design, PPP experimentation, writing-editing, XRD-CT analysis, MDM beamtime support, AJER funding/supervision and writing-editing, RJ funding/supervision and writing-editing

4. In which chapter(s) of your thesis can this material be found?

Chapter 4 and 5

e-Signatures confirming that the information above is accurate (this

form should be co-signed by the supervisor/ senior author unless this is not appropriate,

e.g. if the paper was a single-author work):

Candidate: R. S. Young

Date: May 1st, 2025

Supervisor/Senior Author signature (where appropriate):

Date:

- 2. For a research manuscript that has already been published:
- (a) What is the title of the manuscript?

Quantifying Heterogeneous Degradation Pathways and Deformation Fields in Solid-State Batteries

(b) Please include a link to or doi for the work:

doi: 10.1002/aenm.202404231

(c) Where was the work published?

Advanced Energy Materials

(d) Who published the work?

Wiley

(e) When was the work published?

04/12/2024

(f) List the manuscript's authors in the order they appear on the publication:

Ji Hu, Robert Scott Young, Bratislav Lukic, Ludovic Broche, Rhodri Jervis, Paul R. Shearing, Marco Di Michiel, Philip J. Withers, Alexander Rettie, Partha P. Paul

(g) Was the work peer reviewed?

Yes

(h) Have you retained the copyright?

Yes (Open access)

- (i) Was an earlier form of the manuscript uploaded to a preprint server (e.g. medRxiv)? Yes, doi: 10.26434/chemrxiv-2024-pwt3p
- ■I acknowledge permission of the publisher named under 1d to include in this thesis portions of the publication named as included in 1c.
- 3. For a research manuscript prepared for publication but that has not yet been published:
- (a) What is the current title of the manuscript?

Towards Correlated *Operando* 4D Neutron and X-ray Imaging for Solid-State Lithium-ion Batteries

(b) Has the manuscript been uploaded to a preprint server e.g.

medRxiv? No

If 'Yes, please give a link or doi:

(c) Where is the work intended to be published?

ChemRxiv

(d) List the manuscripts authors in the intended authorship order:

R. S. Young, M. Jones, P. Naillou, J. Hu, A. Davlantis Lo, L. Helfen, W. Kockelmann, A. Rettie, R. Jervis

(e) Stage of publication:

Editing final version

3. For multi-authored work, please give a statement of contribution

covering all authors: RSY writing of original version, conceptualization, experimentation, and data processing, MJP iterative reconstructions and aided in data processing, PN reconstructed the original raw data, JH aided in cell cycling and experimentation, ADL cell design/manufacturing and experimentation, LH beamtime support, WK beamtime support, AR funding/supervision, RJ funding/supervision and editing

4. In which chapter(s) of your thesis can this material be found?

Chapter 6

e-Signatures confirming that the information above is accurate (this

form should be co-signed by the supervisor/ senior author unless this is not appropriate,

e.g. if the paper was a single-author work):

Candidate: R. S. Young

Date: May 1st, 2025

Supervisor/Senior Author signature (where appropriate):

Date:

Acknowledgements

I would like to take the opportunity to take my UCL supervisors Dr Rhodri Jervis and Dr Alexander Rettie for their continuous support and inspiration throughout the PhD. Additionally, a big thank you to my industrial supervisors from HORIBA, Dr. Michele Braglia and Dr. Richard Stocker for their guiding support and advice. Working within the EIL introduced me to many wonderful characters that made my journey enjoyable and memorable. To list everyone who had a positive impact would require a separate thesis, but I wish to highlight a few.

Firstly, Dr. Ji Hu, who was my partner in crime for much of the solid-state battery work. Of course, there is the other 50 % of the XCT Chaps, Dr. Francesco iacoviello. Francesco introduced me to XCT and ever since has changed how I see the world. Emil, Simon, and the High Precision Design & Fabrication Workshop took my wildest ideas and made them reality; meaning the only limitation on my work was my imagination. Another special thanks to Nick for taking a break from designing satellites to simulate the packing of powder, sometimes there are significant challenges closer to home. To my other research comrades - Shunli, Andrew, Alice, Partha, Shangwei, Matthew, Isabel, Will, Iain, Roby, Isabella, Arthur, and many others - thank you deeply for your friendship; I wish you all the very best in your future endeavours.

My PhD took me to several large-scale research facilities, experiences that were both eyeopening and awe-inspiring. These experiences greatly shaped my future, and I want to give a special thanks to beamline scientists, Dr. Winfried Kockelmann, Dr. Marco Di Michiel, and Dr. Lukas Helfen who made these experiments into epic adventures.

Lastly, I will thank my fiancée Lucy for having the patience to support me throughout. I could not have done it without you.

Table of contents

Declara	tion	3
Abstrac	t	4
Impact s	statement	5
UCL Re	esearch Paper Declaration Form:	7
Acknow	ledgements	10
1 Lis	et of Tables	15
2 Lis	st of Figures	15
3 Lis	st of Abbreviations Used	25
1 Int	roduction	27
1.1	Motivation	27
1.2	Overview	28
2 Lit	erature Review	30
2.1	Lithium-ion Batteries	30
2.1	.1 General Overview	30
2.1	.2 Limitations of Lithium-ion Batteries	31
2.2	Solid-State Lithium Batteries	32
2.2	.1 General Overview	32
2.2	2 Challenges for Solid-State Lithium Batteries	33
2.3	Solid-State Electrolytes	34

2.3.1	Overview and Prospective Properties	34
2.3.2	Ion Mobility in Solid-State Electrolytes	36
2.3.3	Classifications of Solid-State Electrolytes	37
2.3.4	Sulfide-based Solid-State Electrolytes	39
2.4 De	gradation Pathways of Sulfide-based Solid-State Electrolytes	41
2.4.1	Mechanical Degradation Pathways	41
2.4.2	Chemical/Electrochemical Degradation Pathways	42
2.4.3	Strategies and Perspectives to Address the Challenges	43
2.5 Ch	aracterization Strategies of Sulfide-based Solid-State Electrolytes	44
2.6 The	esis Scope	45
3 Methods	s	47
3.1 Pla	netary milling	47
3.1.1	Li ₆ PS ₅ Cl Argyrodite Synthesis	47
3.1.2	Positive Electrode Composite	49
3.2 Ce	ll Assembly	49
3.2.1	Symmetric Cells	50
3.2.2	Full Cells	51
3.3 Ce	lls Architectures	51
3.3.1	The Pressure Cell	51
3.3.2	The Swagelok Cell	53
3.4 Ele	ectrochemical Testing	53

	3.4.	1 Galvanostatic Cycling	53
	3.4.2	2 Electrochemical Impedance Spectroscopy	56
	3.5	Materials Characterization	62
	3.5.	1 X-ray Computed Tomography	62
	3.5.2	2 X-ray Diffraction Computed Tomography	70
	3.5.3	Neutron Computed Tomography	72
	3.5.4	4 Pressure	76
	3.5.	5 Temperature	80
	3.6	Summary	81
4	Tota	al Volume Operando X-ray Computed Tomography	82
	4.1	Aim	82
	4.2	Experimental Setup	82
	4.3	In situ Pressing	87
	4.4	PIP Cell Construction and Operation.	91
	4.5	Electrochemical Degradation of the PIP Cell	96
	4.6	Conclusions.	102
5	Corr	related Diffraction Resolved and X-ray Computed Tomography	104
	5.1	Aim	104
	5.2	Ex situ Cell Shorting	104
	5.3	Stresses Generated in the PIP Cell	115
	5 4	Conclusions	123

6	Tow	wards Operando Correlated X-ray and Neutron Tomography	124
	6.1	Aim	124
	6.2	Cell Development	125
	6.3	Ex situ Experiment	129
	6.4	Operando Experiment	133
	6.5	Conclusions.	140
7	Con	clusions and Future Work	142
8	Refe	erences	146
9	App	pendix	181

1 List of Tables

Table 1 - Instrument breakdown of EIL XCT machines67
2 List of Figures
Figure 2.1 - Schematic of a conventional Li-ion cell consisting of a graphite negative electrode
(left) and a layered transition metal oxide positive electrode (right)
Figure 2.2 - Schematic of an "anode-free" solid-state Li cell consisting of a Cu negative current
collector (left) and a layered transition metal oxide positive electrode (right)33
Figure 2.3 - Examples of the crystallographic defects that facilitate ionic conductivity in solid-state electrolytes
Figure 2.4 - Li ₆ PS ₅ Cl, sulfide-based argyrodite crystal structure40
Figure 3.1 - XRD pattern of the homemade Li ₆ PS ₅ Cl argyrodite powder compared to a standard of Li ₆ PS ₅ Cl argyrodite powder for reference
Figure 3.2 – Li/Li symmetric cell geometry made with Li ₆ PS ₅ Cl SE
Figure 3.3 - Solid state full cell geometry with Li metal paired with a positive electrode and Li ₆ PS ₅ Cl
Figure 3.4 - Pressure cell architecture from Reference 114. Consisting of a PEEK cylinder with
an 8 mm bore encased in brass and surrounded by a stainless-steel brace that allows for the
application of pressure52
Figure 3.5 - Schematic of 3 mm sample diameter Swagelok cell architecture53
Figure 3.6 - Variable current density cycling of homemade (black) and commercial (blue) Li ₆ PS ₅ Cl argyrodite
Figure 3.7 - Nyquist plot and corresponding equivalent circuit model57

Figure 3.8 - Nyquist plot showing electrochemical impedance spectroscopy (EIS) of the
commercial (blue) and homemade (black) Li ₆ PS ₅ Cl argyrodite SEs
Figure 3.9 - Ionic conductivity of Li ₆ PS ₅ Cl represented as a box and whisker plot. The 24
different values used are from 18 unique sources and focus on pure Li ₆ PS ₅ Cl so that variation
in the measured value comes down to material handling and measurement
technique. 72,89,95,98,131–143
Figure 3.10 - A) Nyquist plots of Li ₆ PS ₅ Cl argyrodite SE under pressures between 1000N-
3000N. B) Plot of ionic conductivity vs applied pressure
Figure 3.11 - Schematic of X-ray Computed Tomography setup63
Figure 3.12 - Characteristic X-ray emission of tungsten with diagram explaining the emission
of characteristic X-rays
Figure 3.13 - Bremsstrahlung X-ray emission of tungsten with diagram explaining the emission
of bremsstrahlung energy65
Figure 3.14 - X-ray emission spectra for tungsten at 120 keV
Figure 3.15 - 2D orthogonal slices tracking the cracking of a Li ₃ PS ₄ pellet during cycling at a
synchrotron. Reproduced from Reference 105. ¹⁰⁵
Figure 3.16 - XRD-CT setup and data processing: A) Sample setup and collection of 2D
diffraction patterns, B) Diffraction patterns for each scan as a function of spatial coordinates
after azimuthal integration, C) Sinogram showing scattering intensity as a function of
projection angle, D) Final reconstructed XRD-CT image after filtered back projection (FBP).
Modified from citation 84.84

Figure 3.17 - Schematic of X-ray and neutron interactions with matter. A) shows X-rays
interacting with the electron cloud and B) shows incident neutrons interacting with the nucleus.
73
Figure 3.18 - Comparison of mass attenuation coefficients for 45 keV X-rays and thermal
neutrons (25 meV) as a function of atomic number, assuming natural isotopic abundances for
the neutron cross-section. Reproduced from citation 158. ¹⁵⁸
Figure 3.19 - Geometry of a neutron imaging experiment. Showing a pinhole with size D as
the source, distance to the sample of L, and distance from sample to detector of 175
Figure 3.20 - Ionic conductivity verses applied pressure along with the corresponding XCT
images of the sulfide-based solid electrolyte. Reproduced from Reference 74. ⁷⁴ 77
Figure 3.21 - Cycling stability (discharge capacity and coulombic efficiency verses cycle
number) at C/10 of LiIn Li ₆ PS ₅ Cl NCA solid-state batteries at various fabrication pressures.
Reproduced from Reference 63. ⁶³ 79
Figure 4.1 - XCT images at A) $4 \times$ and corresponding B) $20 \times$ magnifications of loose Li ₆ PS ₅ Cl
argyrodite powder. The tomography shows that agglomerates of Li ₆ PS ₅ Cl powder 100s of
microns in diameter are present in the powder.
Figure 4.2 - Nyquist plots showing the EIS stability results of an (A) LMO/Li and (B)
LNMO/Li full cell over time from manufacturing. Inlaid plots focus on a smaller impedance
range for clarity84
Figure 4.3 - Swagelok solid state full cells made with commercial Li ₆ PS ₅ Cl argyrodite. A) first
attempt at LMO full cell, B) later attempt at LMO full cell with foils, and c) additional attempts
at a LNMO full cell85
Figure 4.4 - Li ₆ PS ₅ Cl argyrodite pellet formed in a 3 mm die, carefully sealed in Kapton, and
imaged to explore pellet formation in a die86

Figure 4.5 - Deben CT5000-TEC load stage (Deben) installed between the source and detector
of the ZEISS Xradia Versa 620
Figure 4.6 - Schematic of 3 mm internal diameter in situ press architecture for producing 3 mm
diameter SE pellets from powders
Figure 4.7 - 3 mm diameter Li ₆ PS ₅ Cl argyrodite SE pellet being formed with in situ press at
4000 N
Figure 4.8 - The various geometries of the in situ press (B-D) compared to a pre-formed pellet
in a Swagelok cell (A). A) 3 mm diameter pre-formed pellet in a Swagelok cell, versus in situ
pressed pellets at B) 1 mm, C) 0.5 mm, and D) 0.35 mm diameters. All pellets were formed
from the same commercial Li ₆ PS ₅ Cl
Figure 4.9 - LMO composite interface with Li ₆ PS ₅ Cl pellet at 500 nm spatial resolution. A) the
greyscale X-ray tomography volume and B) the segmented dataset of electrolyte, positive
electrode material, and voids
Figure 4.10 - Schematic representation of the 1 mm PIP cell and assembly housing. A) the
assembly housing that holds the PIP cell for producing the SE pellet, B) the PIP cell which is
used for operando imaging and electrochemistry, C) constant current cycling of a Li/Li
symmetric cell at 0.1 mA cm ⁻² , and D) X-ray computed tomography (XCT) of the lithium
manganese oxide (LMO)/Li ₆ PS ₅ Cl/Li solid-state full-cell at various resolutions93
Figure 4.11 - In situ pellet formation in PIP cell with XCT, A) Pristine Li ₆ PS ₅ Cl before pellet
formation, B) Li ₆ PS ₅ Cl pellet pressed to 637 MPa at room temperature without deforming
significantly, and C) shows a hot pressed Li ₆ PS ₅ Cl pellet pressed to 637 MPa at 100 °C95
Figure 4.12 - Cycling and progression of mechanical degradation in the PIP cell. A) shows the
Figure 4.12 - Cycling and progression of mechanical degradation in the PIP cell. A) shows the voltage variation during constant current cycling over increasing current densities from 0.3 mA

after cycling at the various rates. The colour coding reflects the various current densities at
which the cell was cycled
Figure 4.13 - Depth profiling of the Li ₆ PS ₅ Cl symmetric cells. A) shows the segmented volume
of voids (including both voids and cracks) in the pristine Li Li ₆ PS ₅ Cl Li cell, C) shows the
segmented volume of voids in the same cell after 88 cycles at various current densities, and B)
shows the void fraction throughout the entire depth and volume of the Li ₆ PS ₅ Cl pellet, with the
inset showing the central region in magnified detail. The colours indicate the various current
densities of each step and are the same colours used in Figure 4.1299
$Figure~4.14-Electrochemical~impedance~spectroscopy~(EIS)~of~the~symmetric~Li ~Li_6PS_5Cl~ Li_6PS_5Cl~ Li_6PS_5Cl$
cell. A) Nyquist plots of the symmetric Li Li ₆ PS ₅ Cl Li cell after the various constant current
cycling procedures, B) shows the real component of impedance (Z_{real}) vs the segmented void
fraction of the cell after the various constant current cycling procedures, and C) shows Z_{real} vs
the current densities used in the electrochemical testing. B) and C) depict the relationship
between the R_{tot} and the defect formation and current density step respectively
Figure 5.1 - Ex situ XCT analysis. Morphology of a 3 mm diameter Li ₆ PS ₅ Cl pellet is shown
in A) the pristine state of a Li $\text{Li}_6\text{PS}_5\text{Cl}$ Li symmetric cell verses B) the post cycling shorted
state. C) displays the constant current cycling at 0.3 mA cm ⁻² and the corresponding voltage
response of the cycled cell shown in B). Further mechanical degradation in the cycled cell is
shown in D). The slices of D) are highlighted in green and purple which show their position
within the pellet within B). A large crack that spans the full thickness is highlighted in magenta.
Figure 5.2 - XCT and XRD-CT correlation flow to display the various datasets available and
how to they can be visualized107

Figure 5.3 - Depth-resolved degradation analysis at the Li/Li ₆ PS ₅ Cl interfaces. A) shows the
fraction of defects in the pristine and shorted cells as a function of depth from the Li metal
interface (0 µm). B) shows the phase segmentation of the shorted cell as a function of depth
showcasing the various compositions found at the interface and their respective volume
fractions. The dashed orange box represents the depth being shown in B) for perspective 108
Figure 5.4 – XCT and XRD-CT comparison within the Li Li ₆ PS ₅ Cl Li symmetric cell. A)
shows an XCT slice through the Li ₆ PS ₅ Cl pellet highlighting some cracks in the green circle.
B) shows the XRD-CT reconstruction at the same slice as A) with intensities focused on the
Li ₆ PS ₅ Cl peak, the colorbar here is in arbitrary units and proportional to the volume of the
material. A noticeable void of Li ₆ PS ₅ Cl is highlighted with a purple circle in B). C) and D) are
the same slice XRD-CT but focused on the peaks of Li ₂ CO ₃ , and LiCl respectively. The
colorbars in C) and D) denote the volume % of that phase within the XRD-CT reconstruction.
Figure 5.5 - XRD-CT reconstructions of pristine Li Li ₆ PS ₅ Cl Li symmetric cell. A) XRD-CT
slice with intensities focused on the Li ₆ PS ₅ Cl peak, B) and C) show the same XRD-CT slice
focused on the peaks of LiCl and Li ₂ CO ₃ respectively. Colorbars denote the volume % of each
phase within the reconstruction
Figure 5.6 - Example of the quantification of strain. A) shows the depth of which the XRD-CT
data was acquired relative to the Li ₆ PS ₅ Cl pellet, B) shows the resultant elastic strain and stress
in Li ₆ PS ₅ Cl due to the degradation of the Li/Li ₆ PS ₅ Cl interface, and C) shows an example of a
produced XRD pattern and the resulting fit from refinement
Figure 5.7 - Segmentation of azimuthal integration for the horizontal and axial reconstructions.
116

Figure 5.8 - XRD-CT analysis and tracking of lattice parameter in 100 μm depth from the Li
interface. A) Visualization of core, middle, and edge of pellet volume used for XRD binning,
B) lattice parameter of Li ₆ PS ₅ Cl and error broken into horizontal and axial components through
a 100 µm depth from the Li interface
Figure 5.9 - Residual strain in a sub-volume of the pristine Li Li $_6$ PS $_5$ Cl Li cell as calculated
via XRD-CT. A) shows the areas the volume was segmented and the strain broken into
horizontal (circles, solid lines) and axial components (squares, dashed lines) and from sampling
the core (purple), middle (red) and edge (pink) zones of the pellet in concentric circles. B)
shows the horizontal and axial components plotted as strain verse binned volume where each
line represents a depth
Figure 5.10 - FEA of the PIP cell during Li ₆ PS ₅ Cl pellet formation, highlighting the stress
contours generated by applying the compressive pressure of 382 MPa as simulated in CalculiX.
A) shows the 1 mm PIP cell modelled after the experimental geometry in Chapter 4, B) and C)
model the same force applied over 3 mm and 5 mm diameter pellets respectively120
Figure 6.1 - Swagelok cell design. A) shows a schematic of the modified Swagelok cell for
neutron imaging, while B) is an internal view of the Swagelok cell showing a Li/Li symmetric
cell. C), D), and E) cross-sectional images from neutron tomography acquired at IMAT, ISIS,
UK. C) is a NatLi/6Li symmetric cell with a stainless-steel outer casing, D) is a 7Li/6Li symmetric
cell with a PTFE casing, E) is a NatLi/7Li symmetric cell with a titanium outer casing126
Figure 6.2 - Schematic of the solid-state operando neutron and X-ray (SONX) cell design. A)
shows a rendering of the SONX cell mounted on the stage of NeXT, ILL, France. B) is a
zoomed in view of the SONX cell with a cross-section showing the internal structure of the
SONX cell. C) shows a sketch of the SONX cell mounted with the NeXT detector, showing

the path of the neutrons and the magnitudes of the cell design. D) an enlarged cutaway view of
the cell
Figure 6.3 - Ex situ analysis of Nat Li Li ₆ PS ₅ Cl 7 Li symmetric cell. A) shows the Nyquist plot
with the initial impedance of the cell, B) shows the result of galvanostatic cycling at 0.3 mA
cm ⁻² and the cell shorting after ~8 hours of plating NatLi onto 7Li, C) 3D rendering of a pristine
neutron tomography, and D) 3D rendering of a shorted cell after the galvanostatic cycling
protocol in B). The voxels that are more green are higher attenuating while the voxels that are
less attenuating are lighter blue
Figure 6.4 - Cross-sectional slice in XY plane comparing post-mortem NCT (A) and XCT (B)
of an observed defect. The red arrows in B) highlight cracks that are not visible in the NCT.
Figure 6.5 – Post-mortem XCT of ex situ NatLi Li ₆ PS ₅ Cl ⁷ Li symmetric cell after galvanostatic
cycling at 0.3 mA cm ⁻² . A) larger field of view XCT through the center of the cell showing
severe degradation of the cell. B) High resolution image of an XCT slice showing a high
porosity area (red circle) along with the main defect of the cell (blue circle) and C) correlated
neutron tomogram of the same region as in B), showing that the main defect and the high
porosity area have a high concentration of NatLi
Figure 6.6 - Galvanostatic cycling profiles obtained during the operando experiment at NeXT.
The colours show the various current densities at which plating of NatLi was plated onto 7Li in
the $^{Nat}Li \mid Li_6PS_5Cl \mid ^7Li$ symmetric cell. A majority of the current density steps show unstable
voltage due to changes in resistance during cell operation. The $^{\rm Nat}Li~ ~Li_6PS_5Cl~ ^7Li$ symmetric
cell was tested from 0.1 mA cm ⁻² to 9.0 mA cm ⁻²
Figure 6.7 - NCT results from operando plating experiment. A) shows a vertical cross-section
to highlight the various components of the NatLi Li ₆ PS ₅ Cl ⁷ Li symmetric cell and horizontal

cross-sections at the ⁷Li interface after various galvanostatic plating steps of increasing current densities from 0.3 mA cm⁻² to 9.0 mA cm⁻². B) shows the difference of the horizontal crosssections compared to the pristine cross-section, highlighting the increase in contrast from the increased presence of NatLi. C) shows the difference of the horizontal cross-sections at each current density minus the step before, highlighting the restructuring behaviour of the contrast Figure 6.8 - Quantification of the amount of high contrast material (NatLi) introduced to the Li electrode volume. A) shows a cross-section of the segmented high contrast material from NCT and the increase presence with increased plating. B) shows how much NatLi that should theoretically be moved to the ⁷Li electrode based on the current densities (black) and the segmented volume of high contrast material introduced to the ⁷Li electrode volume over time Figure 6.9 - Grayscale profiles throughout the depth and volume of the NatLi | Li₆PS₅Cl | ⁷Li symmetric cell, normalized against pristine NCT, showing the depth profile as a distance from the NatLi electrode. The various components are highlighted, and the different current density steps are shown in different colour lines. Positive \(\Delta \)Grayscale levels indicate an increase in NatLi concentration compared to the pristine material, which occurs in both the ⁷Li electrode Figure 6.10 - Correlated NCT and XCT datasets of the operando plating experiment. A) shows a vertical cross-section of the XCT and NCT datasets and highlights the NatLi interface (blue) and ⁷Li interface (red). B) shows the horizontal cross-sections of the ⁷Li interface with XCT and NCT before and after the operando experiment. C) shows the horizontal cross-sections of

3 List of Abbreviations Used

AC alternating current

CB carbon black

CCD critical current density

DVC digital volume correlation

EV electric vehicle

EIS electrochemical impedance spectroscopy

ECM equivalent circuit model

FOV field-of-view

HAXPES hard X-ray photoelectron spectroscopy

ILL Institut Laue-Langevin

ICE internal combustion engine

LMO lithium manganese oxide

LNMO lithium nickel manganese oxide,

LIB lithium-ion battery

NCT neutron computed tomography

OCV open circuit voltage

O-SE oxide-based solid-state electrolyte

PEEK polyether ether ketone

PVDF polyvinylidene fluoride

SE solid electrolyte

SSB solid-state lithium battery

SOC state of charge

S-SE Sulfide-based solid-state electrolyte

ESRF The European Synchrotron Facility

XCT X-ray computed tomography

XRD X-ray diffraction

XRD-CT X-ray diffraction computed tomography

XPS X-ray photoelectron spectroscopy

XRF-CT X-ray fluorescence computed tomography

1 Introduction

1.1 Motivation

The necessity of electrification in the automotive sector is becoming an unavoidable reality. Global sales of electric passenger vehicles accounted for only 9% in 2021, but to stay on track for a global fleet with net-zero carbon emissions by 2050 this must increase drastically. The Electric Vehicle Outlook Report 2022 from BloombergNEF states that zero-emission passenger vehicles will have to account for 61% of the global sales by 2030, 93% by 2035, and 100% by 2038 to reach net-zero carbon emissions by 2050.

Global production of lithium-ion batteries (LIBs) has grown from 242 GWh in 2020 to 411 GWh in 2021.² This is estimated to grow to 1160 GWh by 2026 and 2.7 TWh by 2030.² Methods for facilitating rapid growth in production include streamlining LIB manufacturing and utilizing earth abundant materials for their design.

To substantially increase the sales of electric vehicles (EVs), innovations in the production and performance of EVs must advance as well. Some potential hurdles for the adoption of EVs include range anxiety from consumers, long charging times, and concerns about safety. Tesla currently estimates a range of 652 km on their Model S which is comparable to the range of the petrol fuelled 2022 Toyota Camry at about 662 km.^{3,4}

This may alleviate some of the range anxiety, however, when one compares the nearly instantaneous refuelling of the internal combustion engine (ICE) to the charge time of EVs a further hurdle for adoption is evident. To charge the 100 KWh Model S from 20% state of charge (SOC) to 100% SOC on a conventional public charging station takes upwards of 8 hours, while the public fast charging options pushes this to around 40 mins.⁵

Another factor to consider is perceived safety of EVs. News stations in 2018 highlighted many EV fires even though they are far outweighed by ICE fires.^{6,7} Incidents continue to make

headlines today, bringing the safety of LIBs into question for consumers and thus hindering the movement towards full electrification of the global fleet.

A promising next generation energy storage technology is the solid-state lithium battery (SSB), which has the potential to address concerns in energy density, safety, and fast charge/discharge rates. A SSB replaces the volatile organic solvent-based electrolyte solution with a Li conducting solid. By replacing the solvent-based electrolyte with a solid, it eliminates the possibility of electrolyte leakage and the need for a separator. The solid electrolyte (SE) is more resilient to combustion inherently making them safer than conventional LIBs.⁸ Additionally, with the potentially reduced form factor and possibility to use Li-metal as the negative electrode, SSBs could achieve higher gravimetric and volumetric energy densities compared to conventional LIBs.⁹. Higher gravimetric and volumetric energy densities mean that SSB containing EVs could have increased capacity, and therefore range, with the same weight and size pack when compared to EVs with conventional LIBs.

1.2 Overview

In this work, various methods of gauging the performance and characterizing the degradation of SSB materials are explored. Li₆PS₅Cl argyrodite SE is focused on in this work since it is generally considered industrially relevant given its relatively high ionic conductivity and ease of denification. Here, the various degradation modalities of Li₆PS₅Cl are explored with a combination of advanced characterization methods, X-ray computed tomography (XCT), X-ray diffraction computed tomography (XRD-CT), and neutron computed tomography (NCT). To deconvolute the mechanical and electrochemical defect propagation throughout the SE, these advanced characterization techniques are correlated together and pushed towards operando measurements in order to have the most comprehensive understanding of the dynamic degradation pathways of SSBs. XCT is utilized for tracking/quantifying the mechanical degradation of SSBs, and this work highlights the challenges in producing

replicable X-ray transparent solid-state cells. This work also introduces a solution with the development of the *in situ* PEEK press, utilizing this novel equipment in correlated XCT/XRD-CT studies where the strain and chemical composition are mapped throughout the volume of the interface. Another bespoke cell, the Solid-state *Operando* Neutron and X-ray (SONX) cell, is manufactured to maximize the spatial and temporal resolution of NCT. NCT enables the tracking of Li transport within the SE to see heterogeneities that form during degradation and what conditions lead to cell failure. By optimizing the techniques of XCT, XRD-CT, and NCT for the characterization of SE materials, and further correlating the results, a full story of Li₆PS₅Cl degradation is achieved. This thesis stands as a movement in the direction towards standardized characterization with the aid of advanced correlated techniques.

2 Literature Review

2.1 Lithium-ion Batteries

2.1.1 General Overview

Lithium-ion batteries (LIBs) are a type of energy storage that converts electrochemical potential energy into utilizable electricity. Figure 2.1 shows a schematic of a conventional Liion cell. The conventional LIB cell consists of a positive and negative electrode separated by a permeable porous separator and a solvent-based electrolyte solution. The positive electrode typically consists of a Li transition metal oxide (LiMO₂), the negative electrode is usually graphite, and the electrolyte solution is an organic carbonate-based electrolyte solvent containing a Li salt. The positive and negative electrodes avoid shorting by utilizing a separator, typically a multilayer polypropylene/polyethylene membrane, allowing Li-ion mobility while keeping the electrodes isolated.

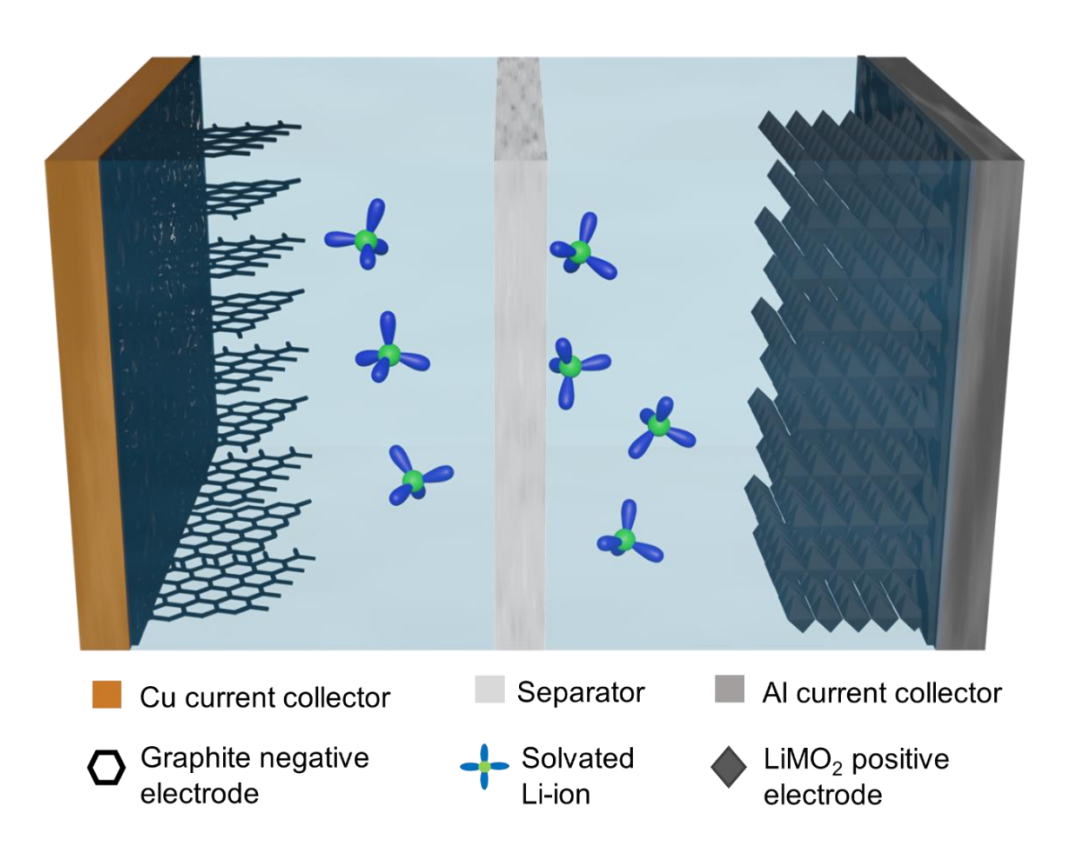


Figure 2.1 - Schematic of a conventional Li-ion cell consisting of a graphite negative electrode (left) and a layered transition metal oxide positive electrode (right)

The cell potential originates from the difference in the electrochemical potentials of Li⁺ in each electrode. During the thermodynamically unfavourable reaction of charging, where the Li travels to the negative electrode, the lithiated negative electrode potential decreases to about $0.08~V~vs.~Li/Li^+$ and the de-lithiated positive electrode potential increases to around $4.5~V~vs.~Li/Li^+$. This sets an upper voltage for the cell at about 4.4~V~since cell potential, V_{cell} , is defined as: $V_{cell} = V_{positive} - V_{negative}$, where $V_{positive}$ is the positive electrode potential and $V_{negative}$ is the negative electrode potential. Discharge of the cell is thermodynamically favourable, Li travels to the positive electrode when the positive and negative electrodes are connected by an external circuit that allows the flow of electrons. This flow of electrons is what is used to power devices, thus producing useful work.

2.1.2 Limitations of Lithium-ion Batteries

Though LIBs are the dominant technology in electrochemical energy storage and have been since there commercialization by Sony in 1991, there still remain challenges that introduce limitations in their performance. ^{12,13} The safety, lifetime, and energy density of LIBs are critical areas of research, especially as the technology is finding more applications in electrifying transportation. ^{14,15} These are often wicked problems as optimizing for one challenge can often negatively impact another. For example, since the 1970s, the use of Li-metal as the negative electrode has demonstrated promise in delivering extremely high energy density batteries; however the technology has been significantly hindered by exacerbating safety issues with the excessive formation of Li dendrites which electrically short the cell, often leading to fires/explosions. ^{16,17}

However, the implementation of a Li-metal negative electrode is still of great interest for applications demanding high energy density because compared to the typical graphite negative

electrode which has a thoretical specific capacity of 372 mAh g⁻¹ a Li-metal negative electrode achieves 3860 mAh g⁻¹.^{16,18} Li-metal batteries were briefy commercialized by Moli Energy Canada in the late 1980s but were recalled due to the safety concerns.¹⁹ The reactivity of solvent based electrolytes with high energy electrodes is being researched continuously, alteratives to highly flammable electrolytes will continue to be explored, and strategically used electrolyte additives show promise in overcoming Li dendrite formation, however overcoming these limitations does inspire exploring alternative battery architectures.^{20,21}

2.2 Solid-State Lithium Batteries

2.2.1 General Overview

Solid-state lithium batteries (SSB) have the same general configuration of the conventional LIB, a positive and negative electrode separated by an electrolyte, with a few exceptional differences. The most obvious difference is that the solvent-based electrolyte of the conventional LIB is replaced with a solid Li⁺ conductor. This inherently increases the safety of SSBs by eliminating electrolyte leakage which is hazardous to living organisms and the environment²². With the solid-state electrolyte (SE), the SSB is more resilient to combustion and there is no need for a separator or individual cell casings to house electrolyte solvent.⁸

Researchers are working towards developing a SE that has high ionic conductivity, high stability, and can utilize either a Li-metal negative electrode or an "anode-free" configuration that simply plates/strips Li onto a bare Cu current collector, further increasing energy density by limiting excess Li. Figure 2.2 shows a schematic of a ceramic solid-state Li cell.

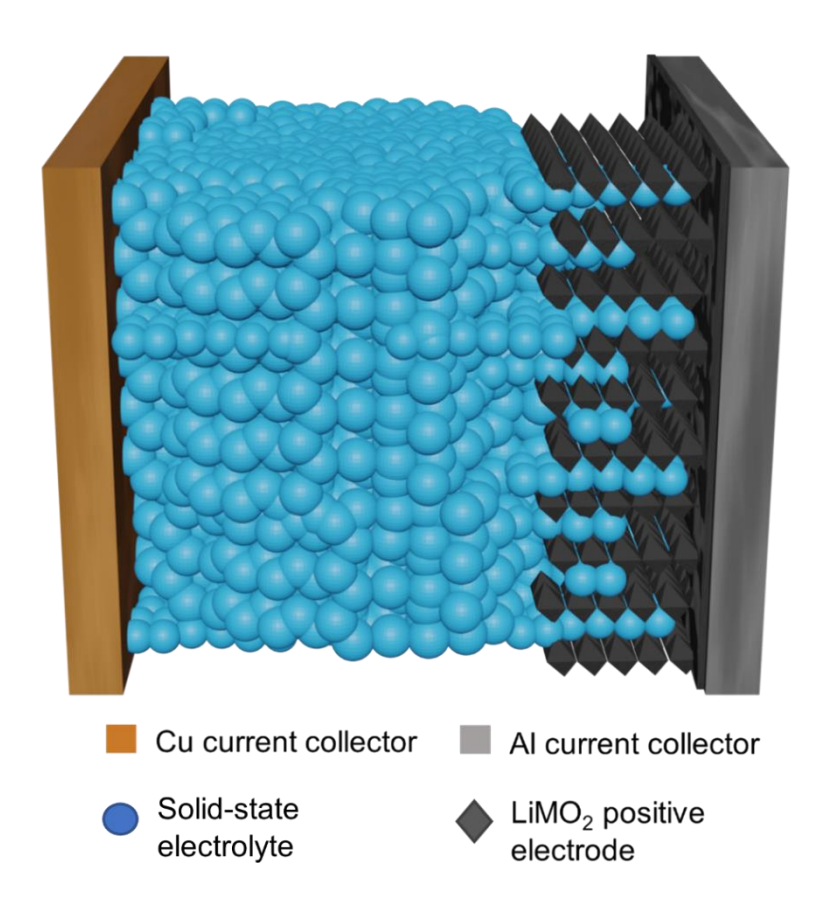


Figure 2.2 - Schematic of an "anode-free" solid-state Li cell consisting of a Cu negative current collector (left) and a layered transition metal oxide positive electrode (right)

With the potentially reduced form factor and the utilization of a Li-metal negative electrode or an "anode-free" configuration, SSBs could achieve higher gravimetric and volumetric energy densities compared to conventional LIBs. ⁹ These projected benefits justify the level of attention SSB research has been receiving in recent years.

2.2.2 Challenges for Solid-State Lithium Batteries

Even though SSBs show great promise, like any new technology, there are many hurdles towards commercialization. Manufacturing SSBs will present major challenges as it includes the need to develop a dense and thin SE with high ionic conductivity. When comparing to conventional liquid electrolytes which can be simply injected into an assembled cell, achieving a stable and low resistance interface between electrodes and electrolyte will be much more

difficult.^{23–25} Many of the challenges in SSBs will arise from the nature of SEs, being susceptible to physical contact loss and defect formation such as voids and cracks. Developing an understanding of the material properties of the various SEs will be key in overcoming these intertwined challenges to therefore realize a practical, scalable, and long life SSB for commercial applications.

2.3 Solid-State Electrolytes

2.3.1 Overview and Prospective Properties

Solid-state electrolytes (SEs) come in many forms; to focus on Li conducting and strictly solid ionic conductors (excluding polymer-based conductors) still leaves many variations in chemistry. A short list would include both crystalline and disordered materials, mainly oxides, sulfides, and halides^{26,27} As of 2021, the number of Li-based SE materials identified by the Materials Project database was 18,578.²⁸

With such an immense catalogue of potential SE materials to choose from, it is important to highlight what the prospective demands for these materials will be:

(i) High ionic conductivity and low electronic conductivity: Electrolytes of any phase must be electrically insulative, to maintain a potential difference between electrodes, and ionically conductive to facilitate the movement of Li⁺ ions. Standard liquid-based electrolytes are typically on the order of ~10 mS cm⁻¹, but due to the low transference numbers (< 0.5), single ion conducting SE materials will have to achieve ~ 1 mS cm⁻¹ conductivity at room temperature to compare.^{29–31} Many variations of SE materials have been reported to reach this goal, but depending on the quality of the interface with the electrodes higher conductivities may be required.^{32–36} Sulfide-based Li SE typically obtain higher ionic conductivities than oxide-based SEs due to the higher

polarizability and larger ionic radius of S^{2-} compared to $O^{2-.37,38}$ Aside from the requirement of high ionic conductivity, having low electronic conductivity is important for cell functionality and reducing degradation such as Li dendrite formation and Li plating within the SE.^{39,40}

- (ii) High current density: SE materials that can operate at high current densities (mA cm⁻²) enable SSBs that are able to charge and discharge faster without degrading. The current density is an important performance metric for SSB cycling and is highly dependent by SE preparation and environment, being affected by factors such as SE porosity and temperature of the cycling. A reported current density to achieve is 3-4 mA cm⁻² for practical use in automotive applications.
- (iii) Ease of manufacturing: Producing thin, dense, SE films into various cell formats will introduce a significant hurdle towards mass manufacturing of SSBs; whether the SE material will enable the typical roll-to-roll techniques or be more suited for novel developments such as 3D printing of electrodes and electrolyes. ^{44–47} A SE that has a lower Young's modulus can be densified easier which can affect not only the porosity and aid in achieving higher current density cycling but can also help form a better interface with electrodes and thus increase the lifetime of the SSB. ^{48–50}
- (iv) Cost: Though cost is a convolution of many variables including the ease of manufacturing, scalability, and cost of raw materials, it is useful to keep cost in mind when exploring the many materials available for SEs. For example, Li₆PS₅Cl argyrodite material cost is two orders of magnitude more than the materials for liquid electrolytes.⁴⁴ Factors such as element abundance should come into consideration when considering a SE for mass market.

2.3.2 Ion Mobility in Solid-State Electrolytes

Due to the nature of the SE, it cannot be displaced to the level a liquid-based electrolyte could be and therefore will not short the cell. By choosing a SE that is highly ionically conductive and electrically insulative, there is no longer a need for a separator in the cell. Li mobility in the SE is quite different from the diffusion in a Li salt containing electrolyte solution. The materials used as SEs rely on solid-state diffusion which takes place via crystallographic defects, mainly Schottky and Frenkel defects.

In Schottky defects, the cation and anion both leave the solid crystal, which can lead to the formation of voids and inherently changes the density of the area. Schottky defects occur more frequently when the size difference between the cation and anion in a crystal are small. Frenkel defects occur in a crystal when the smaller ion moves into a pre-existing void or into an interstitial site in the crystal lattice. With Frenkel defects, the density of the solid is maintained. Frenkel defects are more likely to occur in crystals where the anion is substantially larger than the cation. A graphical representation of Schottky and Frenkel defects is shown in Figure 2.3. When looking at the Li₆PS₅Cl argyrodite material, it is expected that Frenkel defects will contribute a majority of the ionic conductivity due to the size of the Li cation being much smaller than the anionic contributions in the structure.

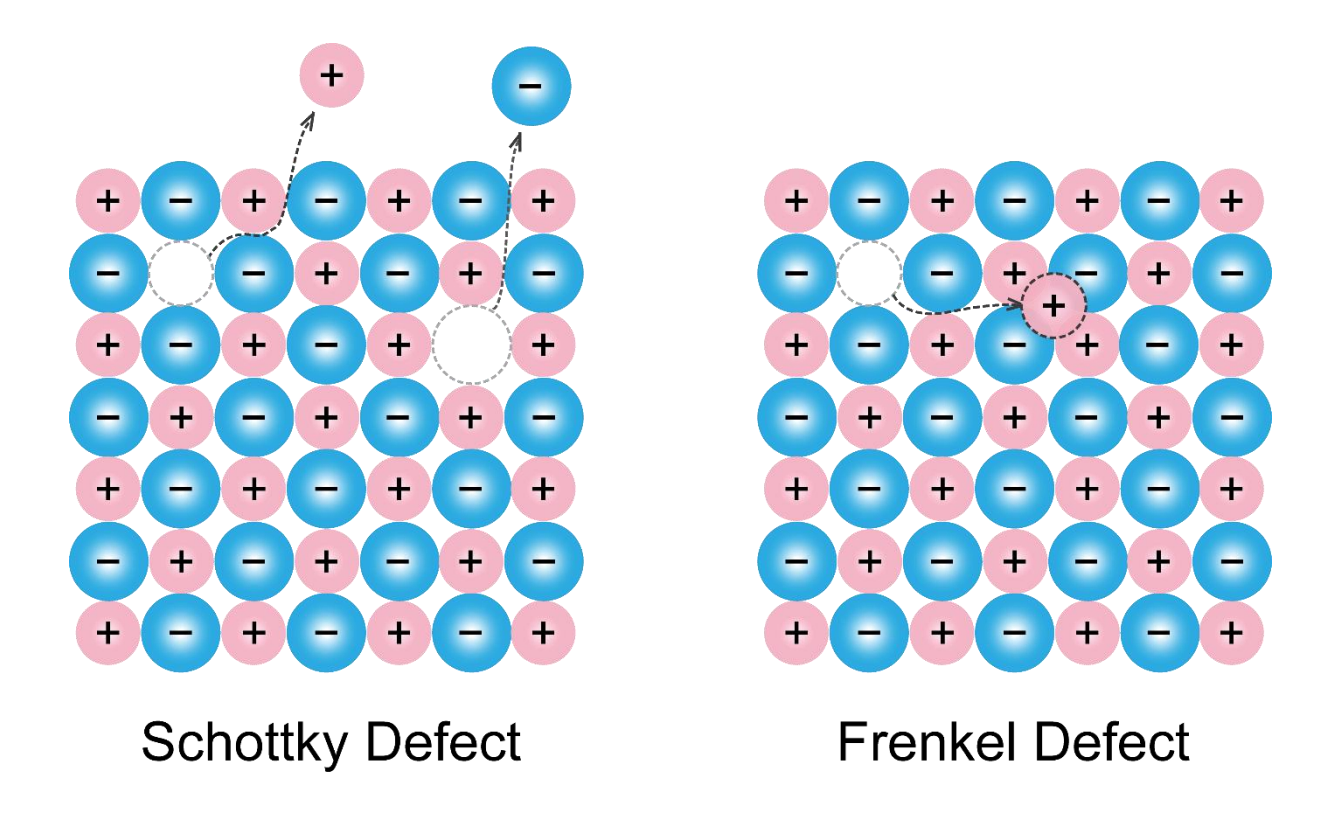


Figure 2.3 - Examples of the crystallographic defects that facilitate ionic conductivity in solid-state electrolytes

2.3.3 Classifications of Solid-State Electrolytes

There exist many variations of SEs with distinct properties, broadly categorized into three main types: solid inorganic electrolytes, solid polymer electrolytes, and solid composite electrolytes. ^{51,52} Excluding the polymer and composite electrolytes, the strict definition of SEs based on defect driven ion diffusion mainly refer to solid inorganic electrolytes. Continuous efforts have been devoted to the advancement of solid inorganic electrolytes, with most work focusing on the three main classes: oxides, halides, and sulfides. ⁵¹

2.3.3.1 Oxides

Oxide-based SEs (O-SEs) have played a pivotal role in the advancement of SSBs, gaining significant attention in the $1970s.^{53,54}$ Goodenough et al. first showcased Na-ion conductivity in $Na_{1+x}Zr_2Si_XP_{3-x}O_{12}$, developing a framework that subsequently inspired the development of numerous Li-based analogues.⁵⁴ Among these, $Li_7La_3Zr_2O_{12}$ (LLZO) has attracted particular

interest due to its moderately high room-temperature ionic conductivity (~1 mS cm⁻¹) and stability against air, moisture, and Li metal.^{53,55} Chemical stability is one of the key advantages of O-SEs, along with their high mechanical strength, and wide electrochemical stability window. However, challenges remain, including their inherent brittleness, the formation of surface layers, and demanding SE pellet processing conditions. O-SE pellets often require formation pressures exceeding 500 MPa and sintering temperatures above 1000 °C. ^{53,56} These challenges, combined with the lower ionic conductivities relative to sulfides continue to constrain the widespread application of O-SEs.

2.3.3.2 Halides

Halide-based SEs have recently gained interest as a promising SE candidate owing to their high ionic conductivity and broad electrochemical stability window. Though there were early discoveries of halide materials such as LiAlCl₄, their low ionic conductivities (<0.1 mS cm⁻¹) limited their appeal.⁵⁷ Interest was reinvigorated in 2018 when Aseno et al. demonstrated that Li₃YCl₆ and Li₃YBr₆ achieved ionic conductivities above 1 mS cm⁻¹.⁵⁸ Advantages of halide materials include high ionic conductivity and the ability to achieve dense pellets under moderate pressures (~500 MPa) and temperatures (~150 °C).⁵⁹ The disadvantages are the extreme sensitivity to air and moisture, poor interfacial stability against Li, complex synthesis requirements, and limited cycling stability.⁶⁰

2.3.3.3 Sulfides

S-SEs have attracted considerable attention due to their exceptionally high ionic conductivity, in some cases surpassing the conventional liquid electrolytes ($\sim 10 \text{ mS cm}^{-2}$). 40,61 The malleable nature of sulfides allow them to be densified under moderate pressures ($\sim 350 \text{MPa}$) at room temperature and often not requiring additional sintering. 62,63 This ease of densification is a clear advantage for SSB manufacturing. While research into sulfides included early discoveries such as Li₂S-P₂S₅ by Mercier et al. in the 1980s, it was the development of S-SEs with unprecedented

ionic conductivity such as Li₁₀GeP₂S₁₂ (12 mS cm⁻²) that sparked widespread interest throughout the last 20 years.^{64,65} Their notably high ionic conductivity gives sulfides an advantage over most halides and oxides. In addition, sulfides form a relatively stable passivating layer with Li, making them promising candidates for commercial SSBs.⁶¹ With its relatively high conductivity of above 1 mS cm⁻² and ease of densification^{27,66}, this work will focus on Li₆PS₅Cl argyrodite material which was first introduced in 2008 by Deiseroth et al. and falls under the category of ceramic based ionic conductors first explored in the 1800's by Michael Faraday and Walther Nerst.^{67,68}

2.3.4 Sulfide-based Solid-State Electrolytes

Sulfide-based solid-state electrolytes (S-SEs) have a few advantages compared to other types of SEs, such as chlorinated argyrodite (Li₆PS₅Cl) which are of particular interest due to their high ionic conductivities and the ability for room temperature densification. ^{10,69,70} S-SEs also have a few disadvantages; for example, they are generally more reactive with both Li-metal and oxide-based positive electrode materials. ⁷¹ S-SEs are also air sensitive and, in most cases, handled in gloveboxes which make them more difficult to work with.

The S-SE that will be focused on in this work is Li₆PS₅Cl argyrodite material, the crystal structure of this material is shown in Figure 2.4. Li₆PS₅Cl, like most S-SEs, is known for having a high ionic conductivity of above 1mS/cm² and a low Young's modulus which makes them easier to densify and better for high-rate applications^{27,72}. The Young's modulus of O-SEs is typically in the range of 100-200 GPa while for S-SEs it is usually in the range of 10-20GPa^{72,73}. SEs with a lower Young's modulus can experience less stress during volume change via strain accommodation⁷³. By better accommodating the stresses of cycling, SEs with a low Young's modulus will have reduced chance of damage and maintain better electrolyte/electrode contact, leading to enhanced cycle life. Further improvement to the ionic conductivity can also be

achieved by reducing voids and grain boundaries in the SE, which is easier to achieve in SEs with a low Young's modulus^{73–75}.

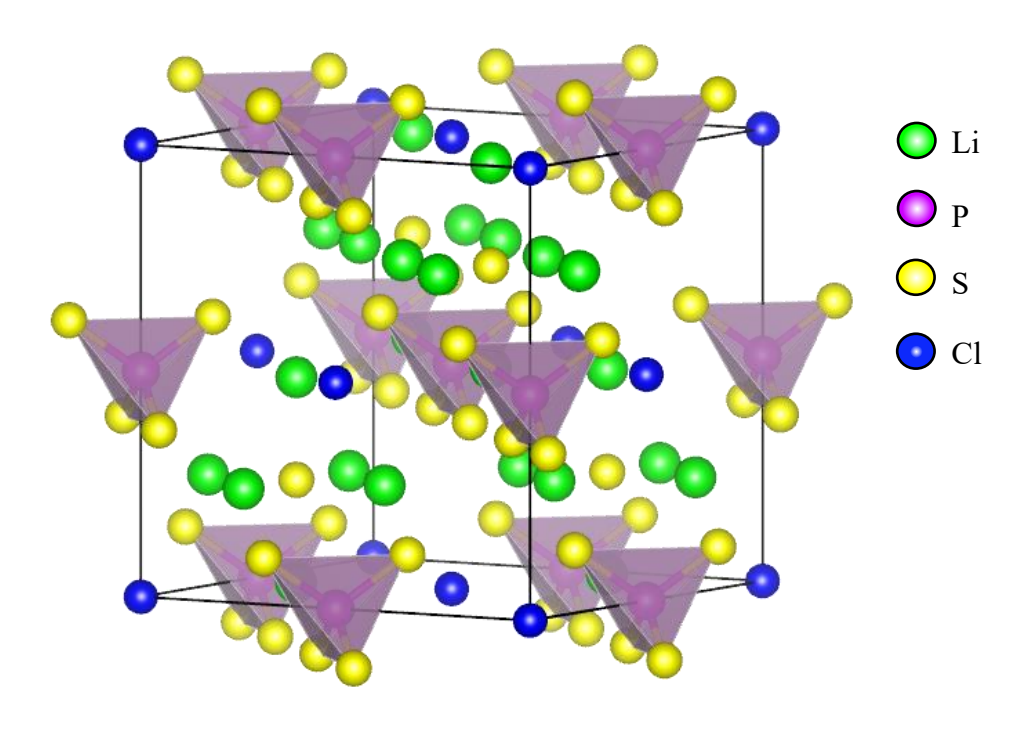


Figure 2.4 - Li₆PS₅Cl, sulfide-based argyrodite crystal structure.

 $\text{Li}_6\text{PS}_5\text{Cl}$ is a crystalline S-SE, with a cubic symmetry F43m and a density of 1.64 g/cm³. $\text{Li}_6\text{PS}_5\text{Cl}$ is air sensitive and hydroscopic, which means that most work is performed in an Arfilled glovebox. If exposed to air, $\text{Li}_6\text{PS}_5\text{Cl}$ can undergo hydrolysis and generate toxic H₂S gas via the following reaction.

$$Li_6PS_5Cl + 4H_2O \rightarrow LiCl + Li_2S + Li_3PO_4 + 4H_2S$$
 (1)

Hydrolysis leads to irreversible sulfur loss which can reduce the ionic conductivity of the S-SE⁷³. Moisture seems to be the main issue with air exposure of Li₆PS₅Cl because work has been done showing its stability in dry room environments⁷². This means that the air sensitivity of Li₆PS₅Cl may not be a critical issue for mass commercialization, since dry rooms are currently implemented in LIB manufacturing.

2.4 Degradation Pathways of Sulfide-based Solid-State Electrolytes

Commercialisation has been impeded by challenges stemming from the fabrication and degradation of the SE. Specifically, the SE is known to degrade through a mix of chemical/electrochemical, and mechanical pathways, lowering lifetime, safety, and permitted current density. These degradation pathways are dynamic in nature, so understanding how they evolve in real time will give better insight into how they nucleate and propagate.

2.4.1 Mechanical Degradation Pathways

Mechanical degradation of the SE arises from materials processing, cell assembly, and cell cycling. Due to the spatial heterogeneity of such mechanisms, a spatially resolved 3D technique that can view the entire cell is desirable. X-ray computed tomography (XCT) has been a popular technique with researchers to characterise systems with similar requirements. XCT enables imaging of the structure/microstructure over large 3D volumes in a relatively short time, allowing for cycling the SSB and imaging them in real time. Ning et al. utilised synchrotronbased XCT to visualize the growth of cracks at the SE and the Li interface, finding that subsurface voids in the SE cause a nucleation of cracks, which can propagate along a path of higher average porosity through the SE¹³. Hao et al. also used synchrotron-based XCT and digital volume correlation (DVC) to track the propagated cracks in SE, along with its associated macroscopic strain²². Kasemchainan et al. found that during subsequent plating and striping, of the Li electrode, voids form at the surface of the Li that cause heterogenous current densities over the surface of the interface, which led to the nucleation of Li filaments. 11 Another study by Ning et al. demonstrated operando XCT with a pixel size of 1.625 µm which informed models to describe the initiation and propagation of Li filaments at the Li₆PS₅Cl/Li interface¹⁵ ; however, this study utilised larger particle sizes than suggested for optimal densification (D50 $\approx 10 \mu m$). Researchers typically use SEs with particle sizes of a few microns or below to have

better compaction/densification and ionic conductivity^{77–79}, meaning that features of interest when studying the nucleation and propagation of voids and cracks are often on the sub- μ m to nm scale.^{80–83} XCT at high resolutions such as that desired in systems utilising ~1 μ m particle size SE often run into the common trade-off between resolution and field-of-view (FOV): if the resolution is too low then features of interest cannot be identified and if the FOV is too small then the probed volume may not be representative of the system as a whole.

2.4.2 Chemical/Electrochemical Degradation Pathways

The reactivity of Li₆PS₅Cl with Li metal also remains a hurdle for the stability of these systems.^{84,85} This reactivity is kinetically limited by the formation of a passivating interphase that forms at the Li₆PS₅Cl/Li interface comprising of reduction products such as Li₂S, LiCl, and Li phosphates^{86,87}. Li metal-induced chemical and electrochemical interfacial degradation has been experimentally observed through techniques such as X-ray photoelectron spectroscopy (XPS) and Raman spectroscopy^{71,79,85}. In recent work by Aktekin et al. utilized hard X-ray photoelectron spectroscopy (HAXPES) to study the reactions at the Li₆PS₅Cl/Li interface in operando conditions, highlighting the importance of operando investigation of the interphase in identifying the composition and kinetics⁸⁵. According to X-ray diffraction computed tomography (XRD-CT) mapping of the interface between Li-metal and SE, there exists undesirable chemical heterogeneity and stress accumulation.⁸⁴ Additionally, the formation of voids and defects at the Li and SE interface during the stripping and plating of the Li anode lead to non-uniform plating currents and strain accumulation. 80,83,88,89 In turn, this results in the nucleation of cracks at the interface that propagate through the SE, leading to mechanical failure of the SE^{88,90,91}. Simultaneously, the strain at the interface leads to the filling of Li metal into cracks and the propagation of Li filaments which eventually cause electrical shorting of the cell which causes cell failure⁸⁴. The use and theory of XRD-CT is discussed in further detail in Chapter 3.5.2. Therefore, there is a pressing need to study these dynamic

chemical, electrochemical, and mechanical processes to develop an understanding of how the degradation nucleates and propagates in SSBs.

2.4.3 Strategies and Perspectives to Address the Challenges

There are several existing methods for overcoming these challenges and degradation modalities, the popular categories include various forms of SE doping, microstructural engineering, and developing composite structures.^{89,92–94} Forming composite structures can take many forms, from mixing Li₆PS₅Cl with polymers to more complicated multi-layered ceramic structures like the SE composites developed by Zhang et al. 92,95 The multi-layered structures studied by Zhang et al. were Li₆PS₅Cl/Li₃ScCl₆/Li₆PS₅Cl and Li₆PS₅Cl/Li₁₀GeP₂S₁₂/Li₆PS₅Cl, enabling Li plating at current densities above 15 mA cm⁻² as the sandwiched structures would suppress crack propagation through the thickness of the SE pellets. 92 Doping of Li₆PS₅Cl has been shown to benefit the stability of Li₆PS₅Cl against a Li-metal electrode while also aiding in achieving higher ionic conductivities. For example, Adeli et al. found that increasing the Cl content in Li₆PS₅Cl to produce a Cl-rich Li_{5.5}PS_{4.5}Cl_{1.5} lead to a nearly fourfold increase in ionic conductivity (9.4±0.1 mS cm⁻¹) compared to Li₆PS₅Cl under identical processing conditions, attributing the benefits to weakening the interactions between Li ions and the surrounding anionic framework.^{66,96,97} Other microstructural engineering approaches to avoid parasitic reactions with Li-metal and the formation of defects include the use of smaller SE particles (~1 µm diameter) and forming SE pellets under high pressures (~450 MPa) and temperatures (~200 °C). 89,98 In general, these strategies still require further understanding to maximize the benefits to stable, high performing Li₆PS₅Cl SEs, which means further characterization to quantify and elucidate the effects of future developments.

2.5 Characterization Strategies of Sulfide-based Solid-State Electrolytes

Early studies on S-SE degradation relied heavily on post-mortem characterization techniques which are *ex situ* in nature. Such techniques include optical microscopy, scanning electron microscopy (SEM), and focused ion beam SEM (FIB-SEM). Post-mortem analysis has informed researchers on the distribution and formation of Li dendrites, and the development of *in situ* SEM set-ups like that of Singh et al. have given enhanced temporal resolution of the dynamic formation of dendrites. These *in situ* studies have highlighted the importance of SE pellet integrity as it showcases pre-existing defects being the nucleation points for Li dendrite growth while flaw-free interfaces show high mechanical endurance. There has been an increased interest in utilizing more non-destructive techniques such as XCT and experiments with more *operando* conditions to give a more representative analysis. One of the earliest examples of the use of synchrotron XCT was by Harry et al. in 2013 in the Advanced Light Source at Lawrence Berkeley National Laboratory where a bespoke polymeric SE cell was imaged in 3D during different states of cycling, revealing complex Li dendrite formation near the Li electrodes. The sum of the sum of the content of the content of the content of the content of the sum of the content of t

In recent time, XCT has become a very popular technique in SSB characterization due to the non-destructive nature, the ability to probe a volume of the sample, and the ease of pairing with other characterization techniques. 88,90,103-106 Multimodal or correlated characterization provides a tremendous amount of data, and when in an *operando* environment, the most detailed representative experiments can be performed. For an example, pairing XCT with the XRD-CT experiment by Villevielle et al. would have provided higher spatial resolution of the mechanical defects within the Li₆PS₅Cl SE that could have been correlated with the spatial distribution of decomposition products observed. The future of characterization is aiming for more data collected in less time with better statistics for the better understanding of

degradation systems and the development of degradation modelling, but the challenge will be setting up these experiments in a representative manor and collecting high quality data.¹⁰⁸

2.6 Thesis Scope

SSBs are going through another wave of interest with the discovery of further SE materials with high ionic conductivity. In order to assess the utility of a particular SE, standardizing the process of characterisation is essential for better understanding the degradation mechanisms of SE materials. The aim of this thesis is to introduce advanced characterisation methods that will aid in further understanding the complexity of SSB degradation. Chapter 3 will first introduce the various methods of manufacturing SSB cells for characterisation, the electrochemical and material testing methods, and provide theory on the numerous techniques utilized.

The subsequent chapters 4, 5, and 6 will dive into the results of the advanced characterisation techniques and highlight the hurdles in optimizing these experiments. Chapter 4 focuses on the fabrication of SSB cells for use in X-ray computed tomography (XCT) experiments and the development of the PEEK *in situ* Press (PIP) cell. The PIP cell design facilitates representative cycling and optimal X-ray imaging, enabling the study of the nucleation and progression of mechanical degradation in a Li| Li₆PS₅Cl |Li symmetric cell throughout the entire volume of the SE. Chapter 5 will employ another X-ray technique to explore the effects of strain accumulation in SE degradation, X-ray diffraction computed tomography (XRD-CT). In the same Li| Li₆PS₅Cl |Li symmetric cell system XRD-CT allows for the mapping of the various materials found and the strain accumulated within the volume of the SE. With the correlated datasets of XCT and XRD-CT, more light is shed on the mechanisms behind phenomena like crack and void formation. Chapter 6 introduces neutron computed tomography (NCT) as another complementary technique to characterize the degradation of a Li| Li₆PS₅Cl |Li

symmetric cell system, answering the vital question: where is the Li metal during degradation? Because NCT is sensitive to Li, unlike XCT, visualisation of where the Li goes during crack formation is possible. Correlated NCT and XCT is explored, and the methods of approaching *operando* conditions are discussed in detail. Chapter 7 will conclude with an analysis of the various correlated techniques and some thoughts towards further development in understanding the degradation of SE materials.

3 Methods

3.1 Planetary milling

Planetary ball milling is a form of mechanical alloying designed to produce fine powdered materials with controlled microstructures. With planetary milling, homogeneous amorphous power mixtures are produced by repeated mixing, plastic deformation, and particle fracturing¹⁰⁹. The type of planetary mill used in this work is a Retsch PM100, where the powders are milled in a steel vial with an inner coating of ZrO₂. The milling media used is 2 mm ZrO₂ balls. The milling vials are placed in the planetary mill and exposed to high centrifugal force that quickly grinds and fractures the powders inside. This leads to particle size reduction, reactions between freshly fractures surfaces, and homogenous mixing of the powders.

3.1.1 Li₆PS₅Cl Argyrodite Synthesis

Using the planetary mill equipped with the ZrO₂ milling jar with thirty 2 mm ZrO₂ balls. For 4 g of Li₆PS₅Cl argyrodite, 1.208 g of Li₂S, 2.344 g of P₂S₅, and 0.448 g of LiCl are added into the milling jar. Corresponding to a weight ratio of (0.302:0.586:0.112) Li₂S:P₂S₅:LiCl or (2.5:1:1) molar ratio which is inspired by previous work¹¹⁰. The powder starts as a minty green and the final product is more beige. This is milled for 6 hours at 350 rpm with 10 min milling intervals and 3 min break times. The resulting powder is sealed under vacuum in a 10 mm quartz tube using a propane torch. The sealed ampoule is heated to 500 °C for 36 hours to obtain the finalized Li₆PS₅Cl argyrodite powder. To confirm the successful synthesis of Li₆PS₅Cl argyrodite, the homemade argyrodite was characterized using X-ray diffraction (XRD), as shown in Figure 3.1.

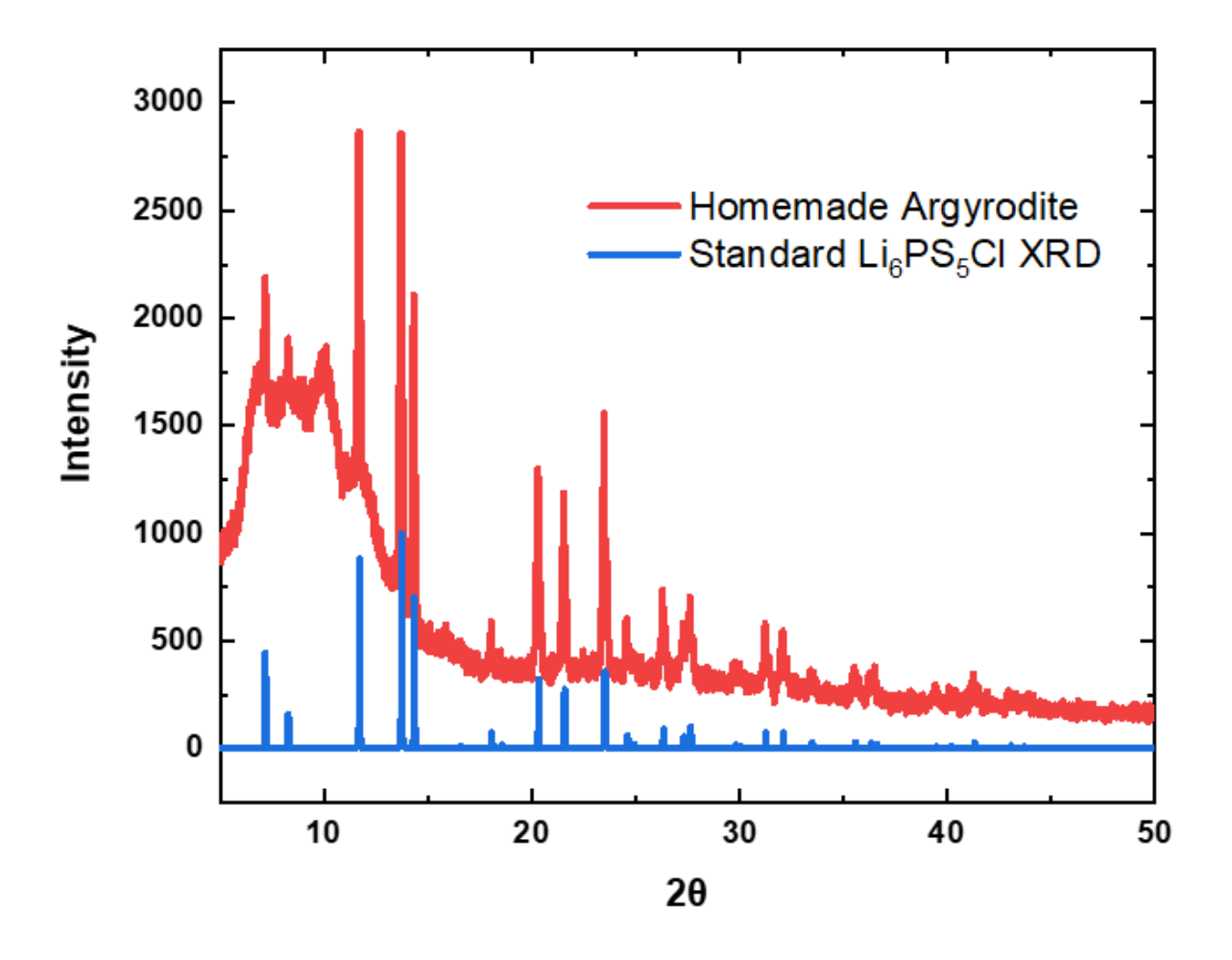


Figure 3.1 - XRD pattern of the homemade Li₆PS₅Cl argyrodite powder compared to a standard of Li₆PS₅Cl argyrodite powder for reference.

The XRD was conducted with a Rigaku Smartlab SE diffractometer with a Mo X-ray source $(\lambda = 0.71 \text{ Å})$ over a 2θ range from 5° to 50° with a step size of 0.01° . As shown in Figure 3.1, the diffraction pattern of the homemade argyrodite (red) contains the characteristic peaks of the standard Li₆PS₅Cl argyrodite pattern (blue). The broad increase in intensity around 7-12° comes from the Kapton tape used in sample preparation. Since Li₆PS₅Cl is air sensitive, powdered samples were prepared in an Ar-filled glovebox by sealing the powder with Kapton tape in the sample holder.

3.1.2 Positive Electrode Composite

Positive electrode composites were produced for use in solid-state full cells. The positive composite was first produced via planetary milling then mixed with solid electrolyte (SE) and sequentially milled. The positive electrode is mixed with SE to facilitate ionic mobility in the electrode since, unlike in a liquid-based system, the electrode is unable to wet with the ionic conductive electrolyte. Lithium manganese oxide, LiMn₂O₄ (LMO) and lithium nickel manganese oxide, Li₂Mn₂Ni₂O₅ (LNMO) positive electrode materials were used to make the positive electrodes. The positive electrode composites in this work utilized binder and an electrically conductive additive found in conventional liquid-based Li-ion batteries (LIB). The binder used was polyvinylidene fluoride (PVDF) and the conductive additive used was high surface area carbon black (CB).

Positive electrode composites were produced with the weight ratio Active:PVDF:CB (94:3:3), similar to other studies, where Active is the lithiated transition metal oxide (either LMO or LNMO). Active:PVDF:CB (94:3:3) composites were made by adding 3.76 g Active, 0.12 g PVDF, and 0.12 g CB into a planetary mill with thirty 2 mm ZrO₂ balls and milling at 500 rpm for 1hr with 20min working intervals and 10min breaks. The resulting Active:PVDF:CB (94:3:3) composites were further mixed via mortar and pestle with the weight ratio Active:Li₆PS₅Cl (50:50) for 10 mins when the colour becomes homogenous. The resulting produced positive electrode composite is then ready for cell assembly.

3.2 Cell Assembly

There are two major cell designs that are used in this work, the Li/Li symmetric cell and a solid-state full cell. These two cell types allow for different types of electrochemical testing. The Li/Li cell can test how efficiently the solid electrolyte allows Li to move back and forth,

testing the plating and stripping of Li on Li to explore dendrite formation in a Li metal cell. The full cell on the other hand exemplifies how a more commercially representative cell would react, allowing for testing of degradation during cycling such as capacity retention.

Along with these two types of cells there are variations of how to prepare cells for testing. Mainly, the solid electrolyte cells can be prepared into pellets which are then subsequently added into a cell, or the pellet can be formed directly in the electrochemical testing cell. The feasibility and effectiveness of each cell preparation is a topic for this work. The cell architectures that will be discussed are the pressure cell, the Swagelok cell, and *in situ* pressed PEEK cells.

3.2.1 Symmetric Cells

Li/Li symmetric cells are formed by placing Li metal on both the positive and negative current collectors with the SE separating them. This cell architecture is helpful when investigating the basic transport properties within the SE since it is a less complex system than implementing a full cell with various Li containing electrodes. The layout of the Li/Li symmetric cell is shown in Figure 3.2.

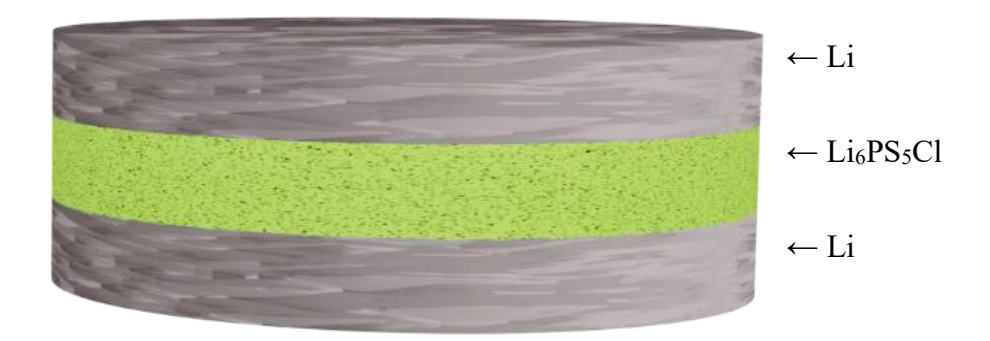


Figure 3.2 – Li/Li symmetric cell geometry made with Li₆PS₅Cl SE.

Symmetric cells have been developed in pressure cells, Swagelok cells, and the *in situ* PEEK cells. In each cell format, the SE pellet is formed before assembling the Li metal electrodes so that the Li metal was not subjected to the massive pressures involved in SE pellet production.

3.2.2 Full Cells

Full cell solid-state LIBs are produced by cycling Li metal verses a positive electrode composite. A schematic of the full cell solid-state LIB is shown in Figure 3.3.



Figure 3.3 - Solid state full cell geometry with Li metal paired with a positive electrode and Li₆PS₅Cl.

The positive electrode composite consists of either LMO or LNMO mixed with binder, conductive additives, and SE. The positive electrode composite and SE are pressed together with the Li being added afterwards to spare the Li metal from the extreme pellet formation pressures.

3.3 Cells Architectures

3.3.1 The Pressure Cell

The design of the colloquially named 'pressure cell' comes from work done by Simon Randau et al in a 2020 publication which sought to establish a baseline for SSB electrochemical

testing¹¹⁴. The design, shown in Figure 3.4, allows the user to produce 8 mm diameter SE pellets and cells.

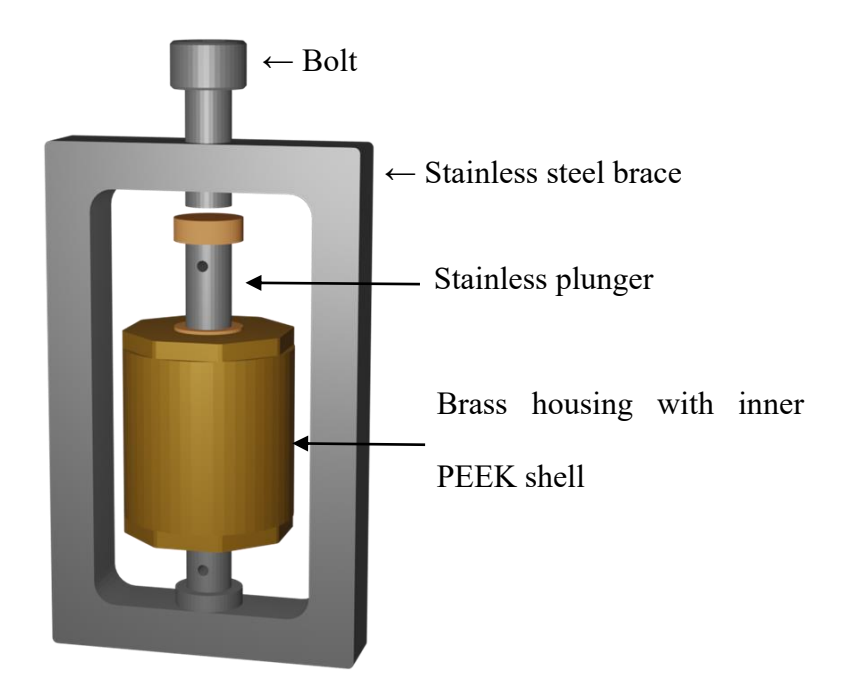


Figure 3.4 - Pressure cell architecture from Reference 114. Consisting of a PEEK cylinder with an 8 mm bore encased in brass and surrounded by a stainless-steel brace that allows for the application of pressure.

Here, the pellet is formed within the housing and pressurized by utilizing the external brace, ideally leading to consistent contact resistance between cells. The design is a great effort by the SSB community to standardize SE electrochemical testing; thus the design is used in initial electrochemical testing of the Li₆PS₅Cl argyrodite SE. The bolt and outer brace allow the user to put around 80 MPa of pressure on the 8 mm diameter SE cell. However, the brace and brass housing makes the pressure cell less appealing for XCT experiments. The brass housing is difficult to image through, and the brace will limit X-ray transmission at some projections, which will make taking high quality images difficult.

3.3.2 The Swagelok Cell

The Swagelok cell, as the name suggests, consists of Swagelok parts that hold the SE pellet in place between two stainless steel plungers. This cell geometry requires manufacturing of a SE pellet prior to cell assembly, where the pre-formed pellet is placed into the Swagelok union to fabricate the cell. Specifically, the 1/8 inch Swagelok union is used with 1/8 inch stainless steel plungers as electrodes. The PFA-220-6 Swagelok union consists of perfluoroalkoxy alkane (PFA)¹¹⁵ and is milled down to reduce the amount of material blocking X-rays from the SE pellet. A depiction of the Swagelok cell is shown in Figure 3.5.

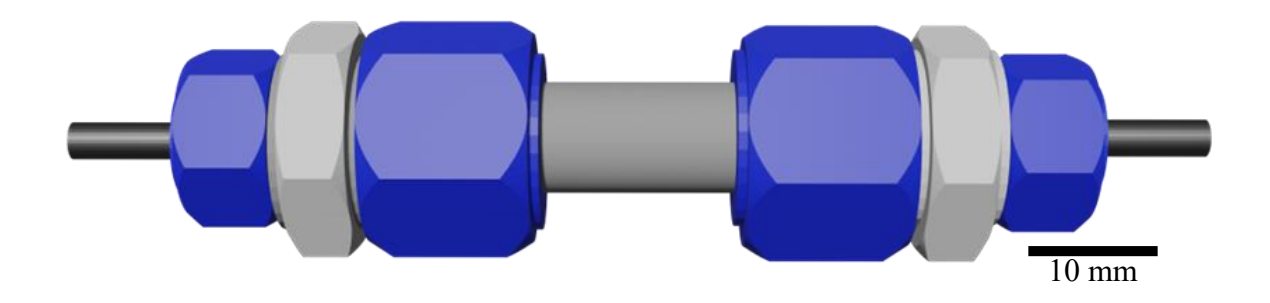


Figure 3.5 - Schematic of 3 mm sample diameter Swagelok cell architecture.

Swagelok parts are used so that the cell will be airtight, and they will enable the use of air sensitive materials such as Li₆PS₅Cl. This cell architecture has been used in previous work successfully³² and enabled the full resolution of the Nikon XTH225 (Nikon) XCT machine over the entire cell volume.

3.4 Electrochemical Testing

3.4.1 Galvanostatic Cycling

During the operation of SSBs, there are many mechanisms of degradation that take place. These degradation mechanisms include shorting, where electrical isolation of the two electrodes is

compromised, and electrons can flow through the electrolyte. Shorting can occur when there is significant damage to the cell, such as penetration of a conductive material or the growth of Li dendrites through the electrolyte.

Li dendrites are a major concern, especially for cells using a Li-metal negative electrode. Li dendrites form when Li begins to plate in stacks, this is affected by the surface diffusivity of Li onto the substrate, the binding energy, and the rate at which the cell is operating. Li dendrites can grow during the plating and striping when cycling a Li-metal negative electrode and have the potential to puncture the SE and short the SSB.

To determine the rate at which the cell failure is inevitable, researchers have compared current densities. If a material being tested has a higher current density than it may be considered a more reliable SE for high-rate applications. Testing for the current density of a SE usually occurs by cycling a cell galvanostatically (with constant current) at increasing current densities until there is a fluctuation of voltage⁸⁰.

Eventually, the cell will not be able to charge or discharge and likely has shorted due to dendrite formation. The current density just before the short are often considered the critical current density (CCD) which is reported as a performance metric of various SE materials¹¹⁶. For context to compare to a Li-metal electrode in liquid electrolyte systems often fail due to dendrite formation at a current density of 1–3 mA cm⁻², while Li₆PS₅Cl CCDs are reported over a wide range of 0.3 – 2.15 mA cm⁻²,^{35,89,117–121} However the concept of CCD and comparing CCDs of various materials has significant limitations due to the results being highly dependent on variables such as particle/grain size, pressure, temperature, cycling protocols, and cell design. Further limitations in this method include not knowing exactly what is leading to a short, not being able to correlate voltage fluctuations to degradation pathways, neglecting the aging of the cell, and test apparatus conditions could alter the results.

The current density of the homemade and commercial Li₆PS₅Cl argyrodite were also compared using the previously mentioned pressure cell. The variable current density cycling is shown in Figure 3.6.

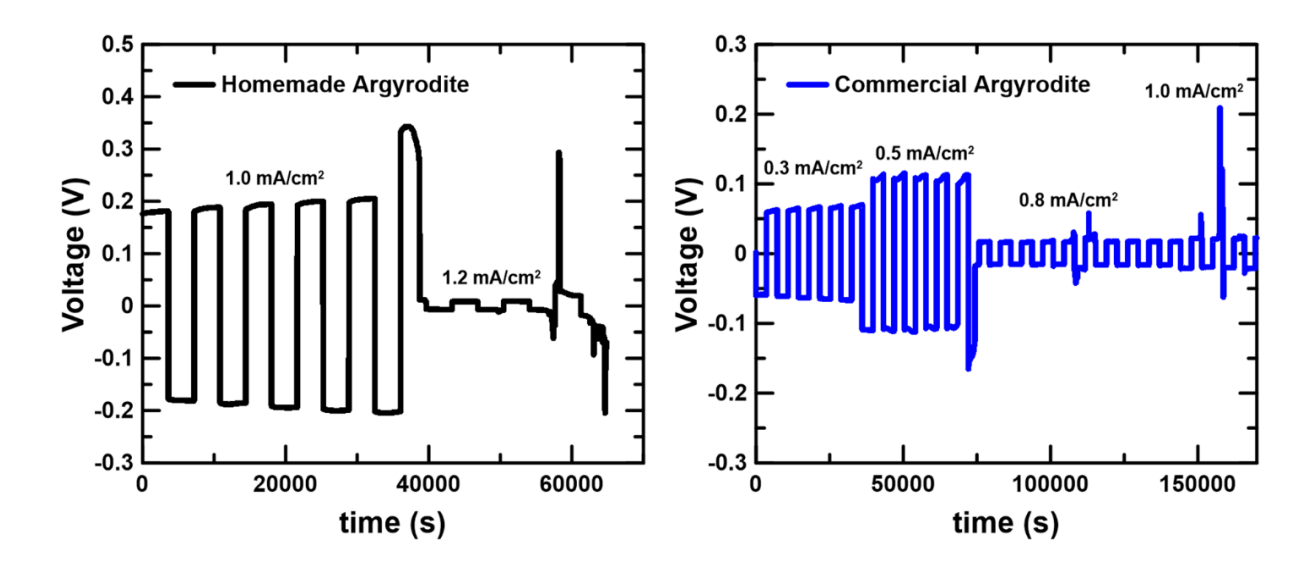


Figure 3.6 - Variable current density cycling of homemade (black) and commercial (blue) Li_6PS_5Cl argyrodite.

At first observation, the homemade argyrodite seems to have a higher current density than the commercial, as it was able to operate at a higher current density than the commercial materials. The homemade SE survives 5 cycles at 1.0 mA cm⁻² while the commercial SE seems to short at 0.8 mA cm⁻². However, these cells were not treated the same and therefore cannot give a clear comparison. This highlights a possible shortcoming in the testing of CCD; if the steps prior to a CCD are changed than the perceived CCD could as well. This inconsistency and the lack of replicates need to be addressed in future work. However, as stated above, commercial Li₆PS₅Cl argyrodite SE was used in further work due to the priority of a consistent baseline over a high performing baseline. All cycling was done with a Gamry Reference 600+ from Gamry Instruments. Cycling on Li/Li symmetric cells is done via chronopotentiometry, where the working current density of the SE is determined by plating and stripping Li at increasing

current densities until cell failure. 1 hour constant current platting and sequential constant current stripping, with a 10 s voltage sampling period, is typically used to test the current density of SEs. If the SE being tested has a higher current density then it could be considered a more favourable, but testing for current density can be sensitive to many variables such as pressure and temperature which is a matter of study for future work.

3.4.2 Electrochemical Impedance Spectroscopy

Electrochemical impedance spectroscopy (EIS) is an effective, non-destructive method of probing the internal impedance of an electrochemical cell. Impedance is highly related to the safety, structural integrity, and rate capability of SSBs. EIS treats the cell as a black box and illustrates the kinetic processes by examining the relationship between an input signal (i.e. an alternating current (AC) potential) and the output (i.e. a current)¹²².

EIS studies a system at equilibrium by applying a small perturbation and observing how the system returns to equilibrium. The amplitude of the perturbation voltage is typically in the mV-range centred around the cell's open circuit voltage (OCV) to maintain a linear relationship between the current response and applied potential^{122,123}. By observing the relationship between a perturbation voltage and the output current, insights into the kinetics involved with Li-ion migration within the SE and the interfacial stability with various materials can be obtained¹²⁴.

The current response from EIS can be analysed as a function of the frequency to distinguish contributions that relate to different kinetic mechanisms. For example, in SSBs, the higher frequency ranges are dominated by the bulk resistance of the SE grains and the grain boundaries, while the lower frequencies are dominated by interfacial resistances and bulk diffusion with the positive electrode¹²⁴.

A good visualization of impedance is the Nyquist plot, which is produced when the negative imaginary impedance is plotted verses the real impedance. The electrochemical behaviour of a cell can be mimicked by an equivalent electrical circuit model to make analysis easier. In an equivalent circuit model (ECM) the kinetics involved in Li-ion transport are replicated with various resistors and capacitors which have different responses to the perturbation voltage. With a resistor, impedance is constant with increasing frequency. With a capacitor, the imaginary impedance approaches zero with increasing frequency adding no real impedance component. An example of a Nyquist plot and is shown in Figure 3.7 along with an inlay of its corresponding equivalent circuit.

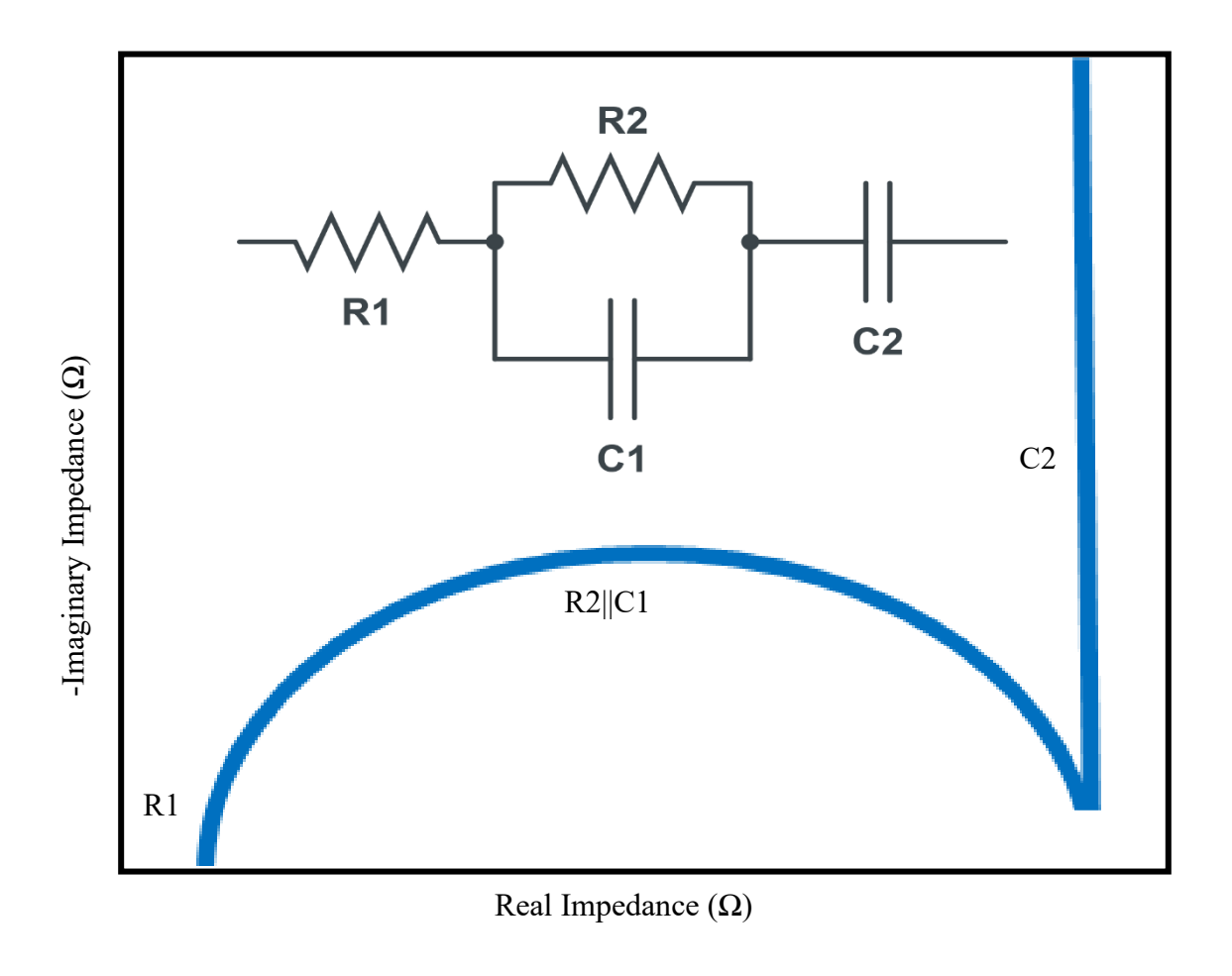


Figure 3.7 - Nyquist plot and corresponding equivalent circuit model

From the Nyquist plot, the total resistance (R_{tot}) or total resistance of charge transfer can be taken as the diameter of the semicircle.

Because EIS can be performed relatively quickly, ~3 mins, it is a good method to implement along with cell cycling. Previously, research has probed impedance at various depths of charge and discharge. These findings show that impedance generally increases during cycling, which will lead to early cell failure¹²⁵. The researchers attributed the increased impedance to damage within the cell and give insight on how to improve the cell design, such as reduced active material grain size^{89,125–127}.

A good addition to this EIS at various depths of charge and discharge would be to pair the technique with a non-intrusive imaging method such as X-ray Computed Tomography (XCT). Another research group probed a similar electrochemical system with XCT and explored the effects of temperature and pressure on the formation of voids within the SSB¹²⁸, which could have been a factor in impedance increase during cycling. Pairing electrochemical techniques with more materials characterization will help deconvolute degradation mechanisms within the SSB and lead to researchers having a clearer understanding of the systems at play.

EIS was executed on the solid-state cell in its pristine state and after cycling to observe changes in internal resistance. Potentiostatic EIS was performed on the solid-state cells utilizing a Gamry Reference 600+ from Gamry Instruments. The frequency range was from 5x10⁶ Hz (5 MHz) to 100 Hz sampling 10 points/decade with an input AC voltage of 10 mV. An EIS scan takes roughly 3 mins to finish, making implementation of EIS during *in situ* experiments easily achievable.

One case where EIS was used in this work was looking into the chemical stability of the positive electrode composite with the SE (see Figure 4.2). In this experiment, EIS over the 5 MHz to 100 Hz frequency range is done on a pristine cell directly after manufacturing. 60 EIS

scans were done sequentially with 500 ms open circuit voltage (OCV) rests between scans. Another usage of EIS is in establishing the relationship between the applied pressure on the cell and internal resistance (see Figure 3.10). In this usage, EIS is performed at controlled pressures and the ionic conductivity is calculated. Ionic conductivity can then be plotted verses applied pressure to expose the relationship of these variables. The EIS of the commercial (blue) and homemade (black) Li₆PS₅Cl argyrodite SEs is compared in Figure 3.8.

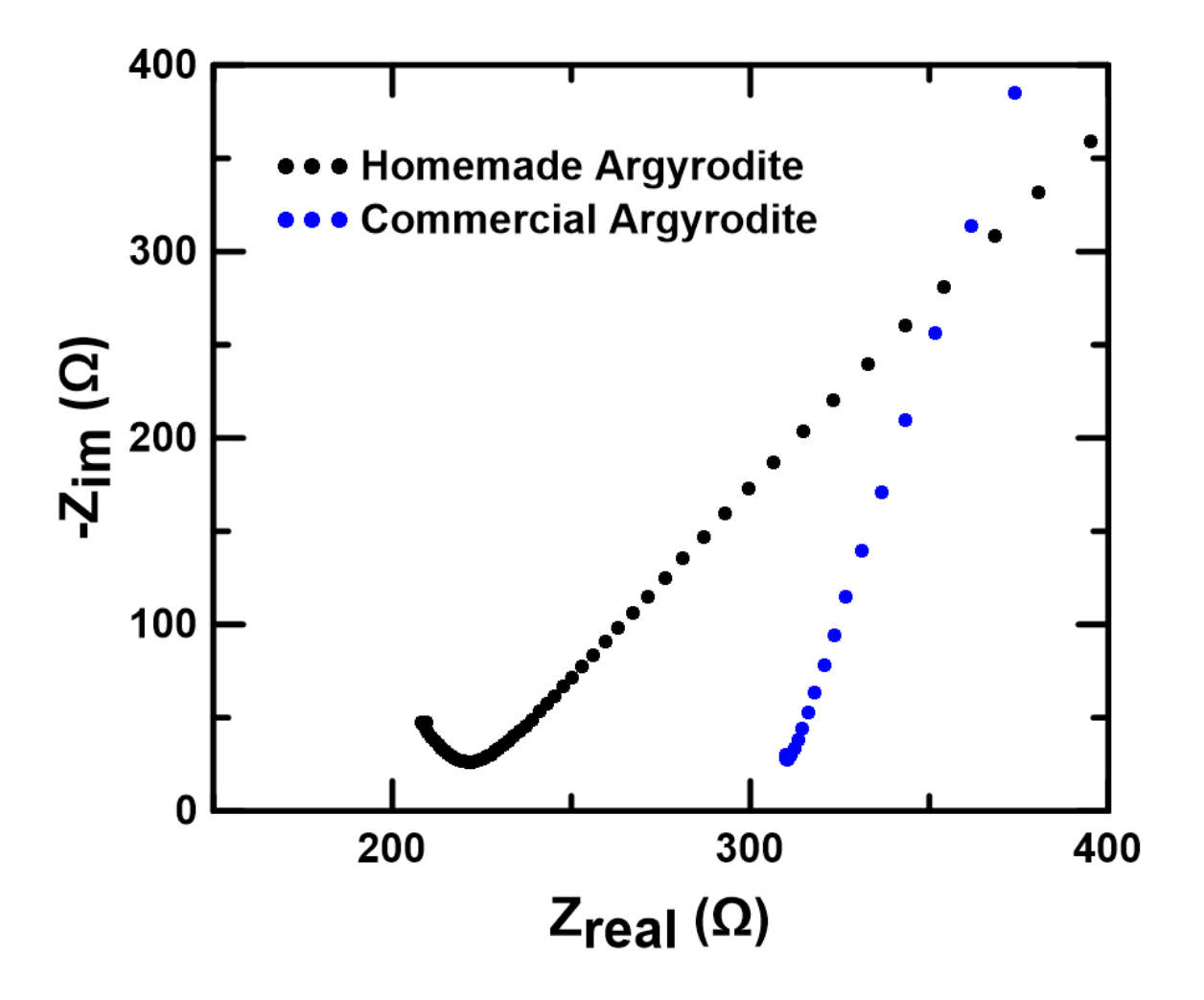


Figure 3.8 - Nyquist plot showing electrochemical impedance spectroscopy (EIS) of the commercial (blue) and homemade (black) Li₆PS₅Cl argyrodite SEs.

The EIS was taken with the use of the pressure cell to help with reproducibility. Based on the comparison of the two cells, the homemade Li₆PS₃Cl argyrodite SE has less resistance than the commercial material, but several replicates should be performed to give the finding statistical significance. The EIS was probed without the introduction of Li metal electrodes to reduce the variables in the test. Based on the diffusion tails at the right-hand side of both functions, the commercial material had variation in contact resistance since it deviated from a 45° angle expected. This variation shows the pressure cell is not perfectly reproducible, which is understandable, and again exemplifies the need for replicates. Regardless of the initial evidence that the homemade SE had lower impedance, without proper understanding of why the impedance is lower, work was carried on using the commercial material.

Once the resistance of a SE is determined, it can be used to calculate the ionic conductivity (σ_{ion}) as shown in the Equation 2 below. Ionic conductivity, or an ability to facilitate ion movement through a material under the influence of an electric field, is an important material property for a SE material. For SSBs to compete with conventional LIBs, they must achieve high ionic conductivity, so understanding what conditions lead to reduced resistances will be important in their development.

$$\sigma_{ion} = \frac{h}{R_{tot} A}$$
 (2)

Where h is the thickness of the SE and A is the cross-sectional area. Researchers have found that ionic conductivity of SSBs depends on many factors such as temperature and pressure^{74,124}. Li₆PS₅Cl is a material of interest due to possessing high ionic conductivities typically on the order of 1-10 mS cm⁻¹, but reported ionic conductivities can vary significantly.^{35,69,70}

In Figure 3.9 the ionic conductivities of pure Li₆PS₅Cl are compared from 18 different sources. The variety in results was limited to variations in material handling, how the pure Li₆PS₅Cl was synthesised, and how the measurement was taken. When doping is introduced the variation

becomes much higher, some doped Li₆PS₅Cl reaching above 10 mS cm⁻¹.^{129,130} From Figure 3.9 the reported ionic conductivities for pure Li₆PS₅Cl vary between 0.014 and 3.56 mS cm⁻¹ with an average value of 1.71 mS cm⁻¹, so the reported values agree with the high conductivity of Li₆PS₅Cl even though synthesis methods and materials handling vary the results.

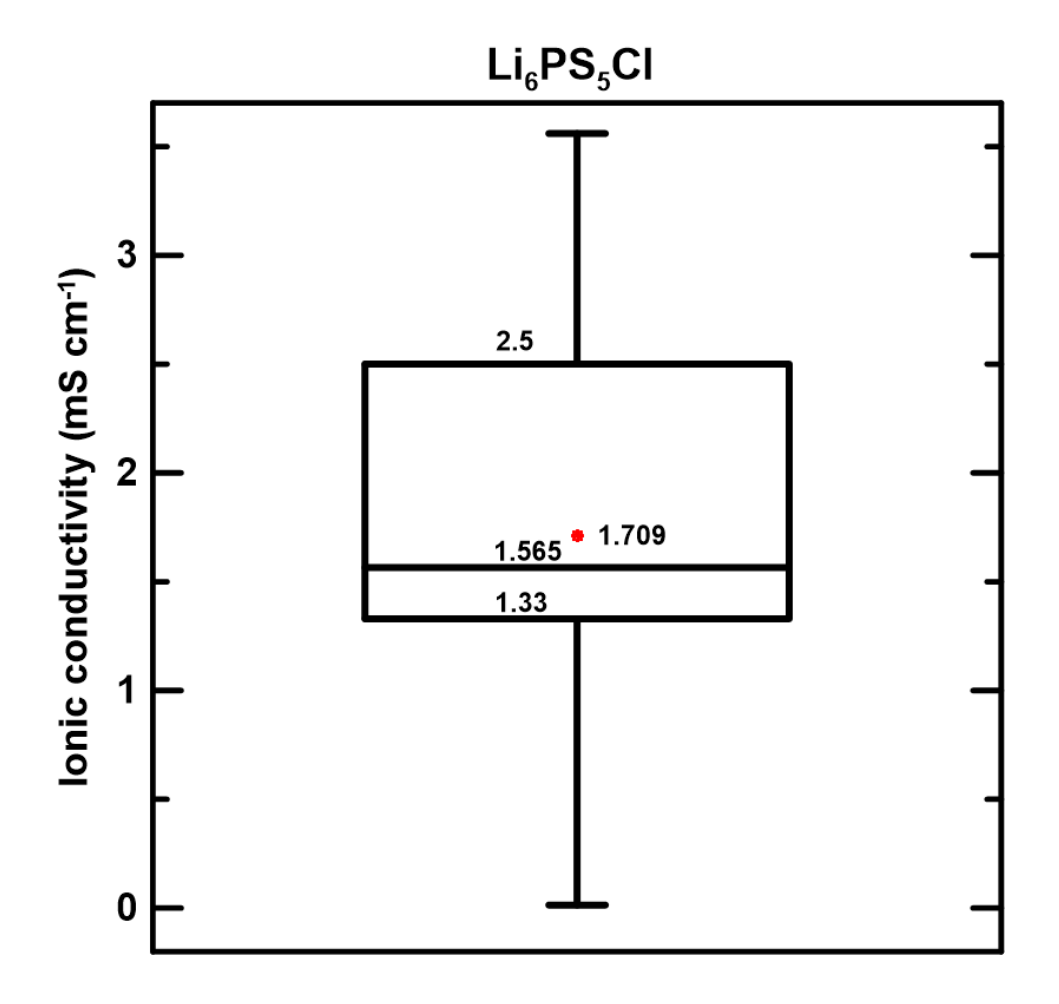


Figure 3.9 - Ionic conductivity of Li_6PS_5Cl represented as a box and whisker plot. The 24 different values used are from 18 unique sources and focus on pure Li_6PS_5Cl so that variation in the measured value comes down to material handling and measurement technique. ^{72,89,95,98,131–143}

A quick experiment that was made possible with the use of an *in situ* pressure rig was probing EIS at the extreme pressures made available by the bespoke setup. Figure 3.10 shows the EIS of the Li₆PS₅Cl argyrodite SE and corresponding ionic conductivity of the pellet.

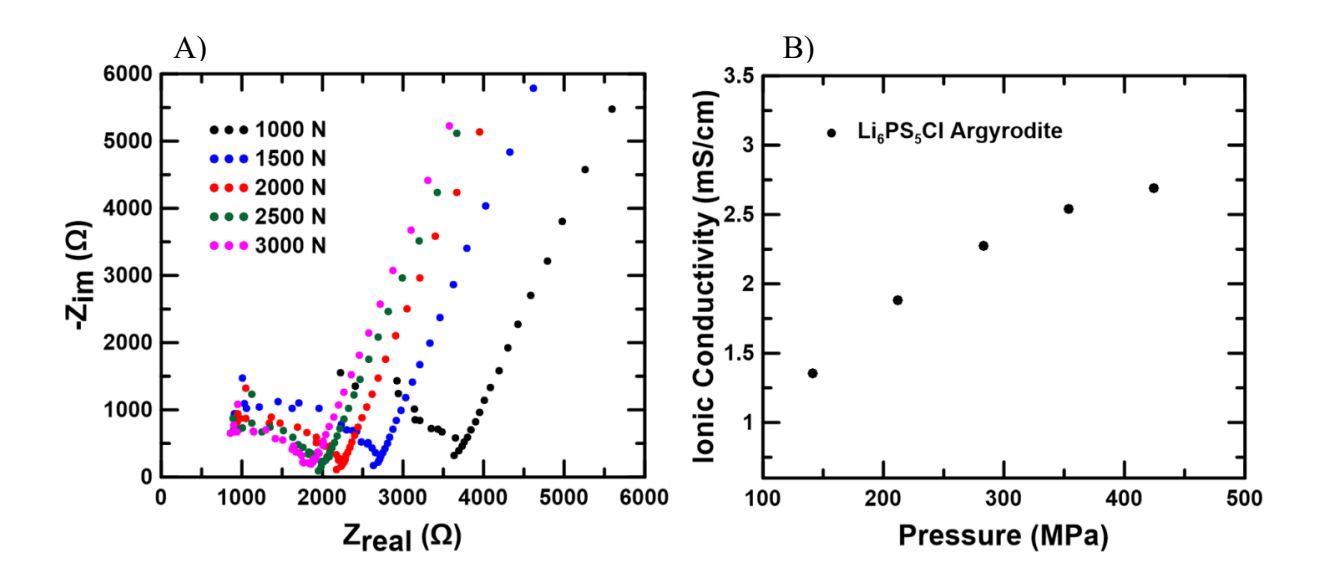


Figure 3.10 - A) Nyquist plots of Li_6PS_5Cl argyrodite SE under pressures between 1000N-3000N. B) Plot of ionic conductivity vs applied pressure.

In Figure 3.10B the trend confirms the thought that higher pressures will produce pellets with lower resistances and therefore higher ionic conductivity. This finding is valuable when developing pellets for future degradation studies.

3.5 Materials Characterization

3.5.1 X-ray Computed Tomography

X-ray computed tomography (XCT) is a form of non-destructive imaging that produces a 3D volume of X-ray attenuation within a sample that can give an internal and topographical view. XCT is commonly used in the medical field to image a patient's internal injuries without having to open them up. There has been an increasing interest in application of XCT in other forms of research as well, with the increasing availability of lab scaled micro-XCT machines and XCT based synchrotron beamlines.^{88,105} For example, since XCT is non-intrusive, electrochemical systems like SSBs can be imaged during cycling and researchers can analyse the propagation of cracks throughout the SE⁸⁸, allowing for continued operation of the cells either during or

after the imaging. The three essential components of the XCT are the X-ray source, a sample on a rotating stage, and a detector as shown in Figure 3.11.

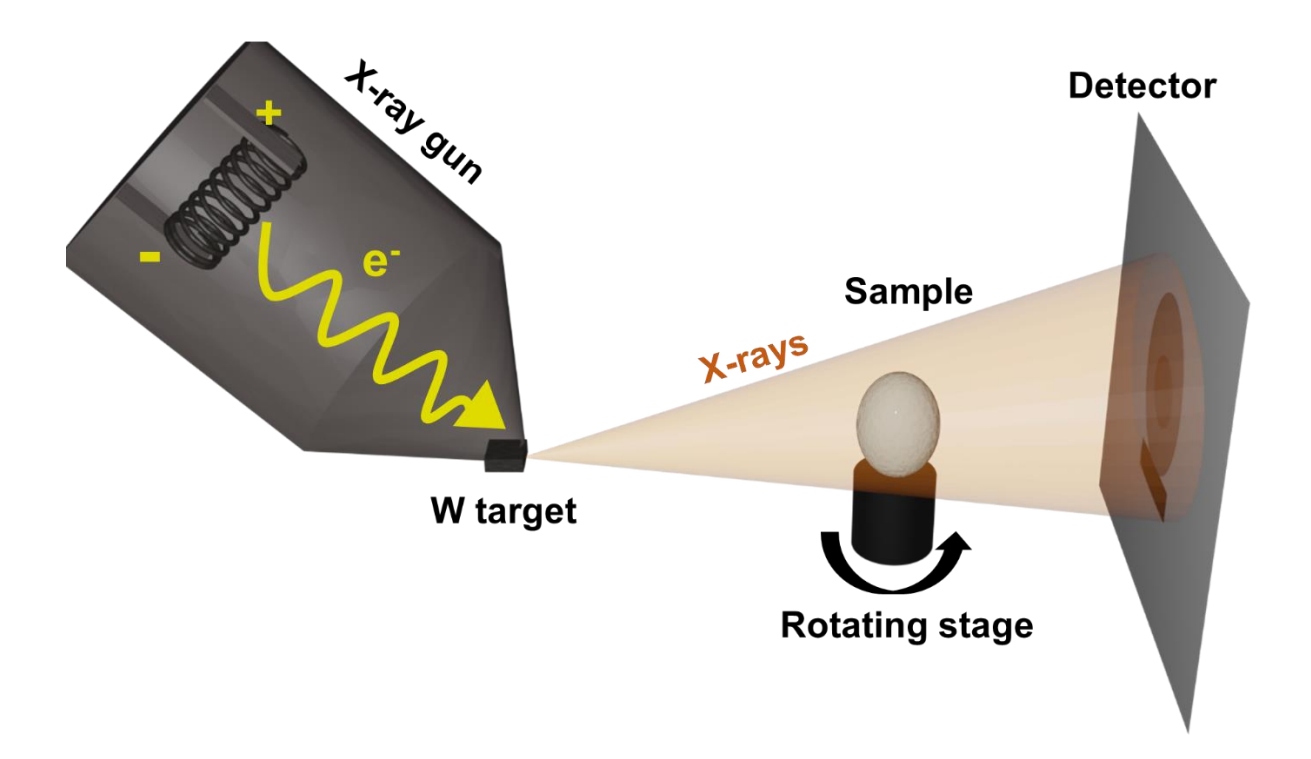


Figure 3.11 - Schematic of X-ray Computed Tomography setup

X-rays are emitted from the X-ray gun and are projected onto the detector through the sample. In the X-ray gun, incident electrons are generated by a tungsten filament in a vacuum tube and irradiated onto a liquid-cooled target electrode. The electrons are accelerated toward the target electrode, typically tungsten, via a potential difference that provides sufficient kinetic energy to knock electrons from the inner orbitals.

When a core electron is ejected, an electron from an outer shell must relax to a lower energy state to occupy the vacancy. This relaxation results in the release of energy in the form of X-rays due to conservation of energy. This form of X-ray emission is classified as characteristic X-ray emission, because each metal has a set of energies corresponding to the energy of relaxation. The characteristic X-ray emission of tungsten is shown in Figure 3.12, showing the

peaks between 58-69 keV, along with a schematic describing characteristic X-ray emission. Tungsten is typically used due its relatively high atomic number and melting point.

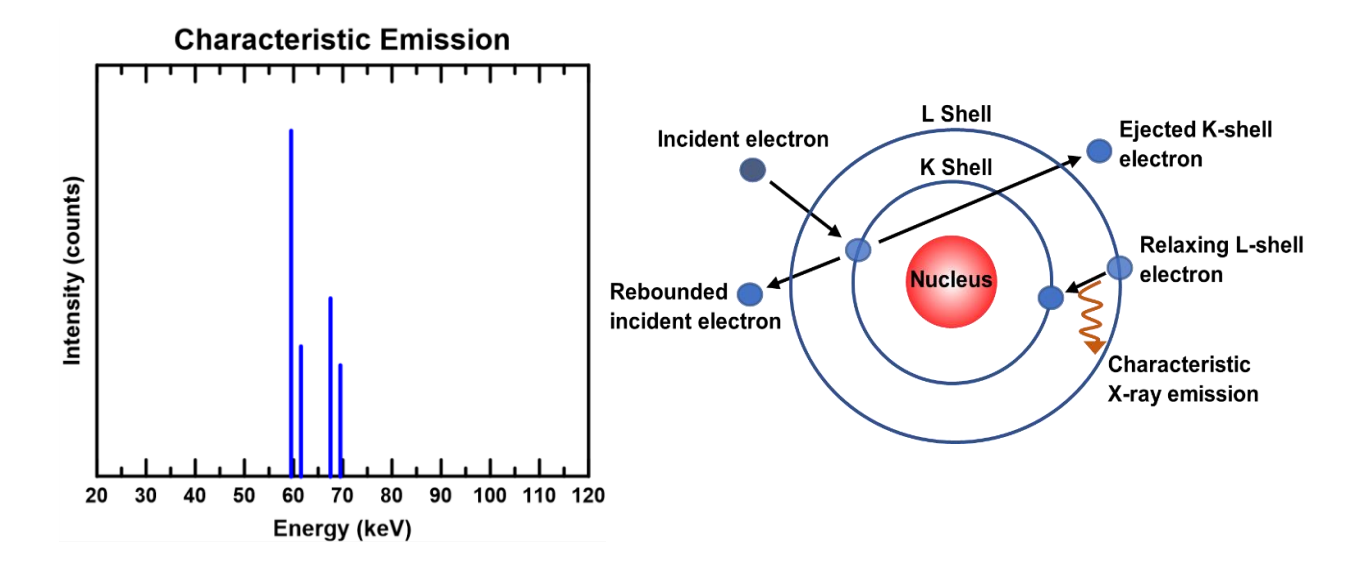


Figure 3.12 - Characteristic X-ray emission of tungsten with diagram explaining the emission of characteristic X-rays

In addition to characteristic X-ray emission, there is another source of X-rays with a board range of energies. This other source is attributed to bremsstrahlung emission. Meaning "breaking radiation" in German, bremsstrahlung emission is a fitting name since it originates from incident electrons being decelerated by various interactions and emitting their kinetic energy as electromagnetic radiation¹⁴⁴. The bremsstrahlung emission spectrum of tungsten is shown in Figure 3.13 along with a schematic describing the emission process.

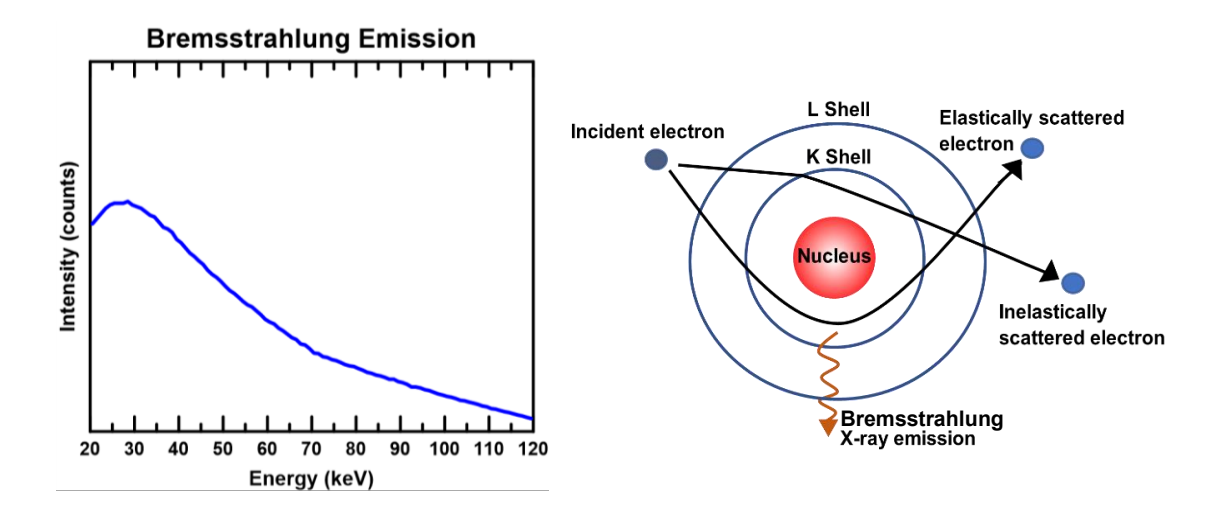


Figure 3.13 - Bremsstrahlung X-ray emission of tungsten with diagram explaining the emission of bremsstrahlung energy

The full X-ray emission spectrum for tungsten is a combination of the characteristic X-ray emission and the bremsstrahlung emission. The setting the X-ray source potential will be influenced by the X-ray emission spectra and the sample. The potential should be set such that the characteristic emission peaks are present to maximize the flux of X-rays. The X-ray emission spectra for tungsten is shown in Figure 3.14.

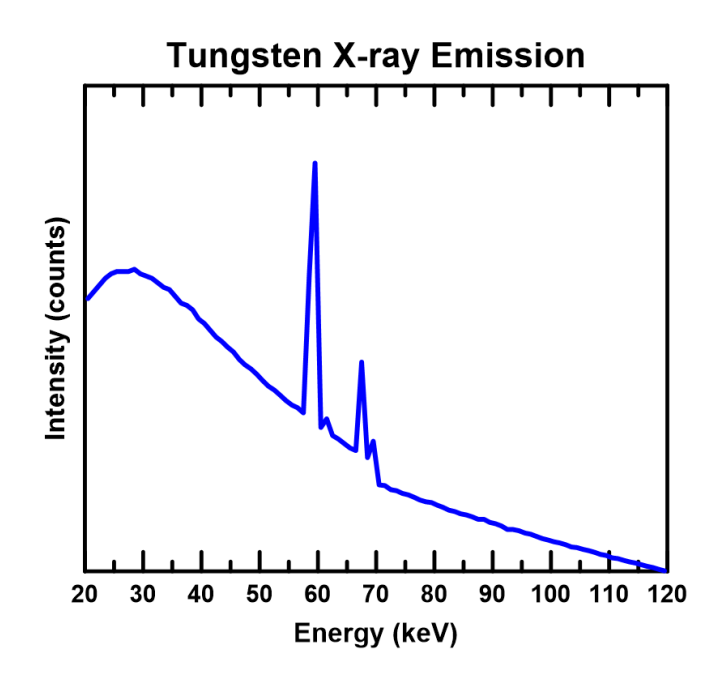


Figure 3.14 - X-ray emission spectra for tungsten at 120 keV

The X-rays interact with the matter of the sample through a combination of absorption and scattering. The absorption and scattering contribute to the attenuation of the X-ray beam as it passes through the sample. The attenuation coefficient can be calculated as a summation of the effects of absorption and scattering multiplied by the number of atoms per unit volume¹⁴⁴, shown in Equation 3.

$$\mu = N_V(\sigma_{abs} + \sigma_s) \quad (3)$$

Where Nv is the number of atoms per unit volume, σ_{abs} is the absorption cross-section, and σ_s is the scattering cross-section. The interactions of X-rays and the sample can be described by the Beer-Lambert law shown in Equation 4, where d is the sample thickness.

$$I = I_0 e^{-\mu d} \quad (4)$$

There will be various levels of attenuation through the sample since it will likely be composed of a combination of elements, as in SSBs. These variations of X-ray flux will be registered by the detector and produce a 2D image of the sample called a radiograph. The detector contains a scintillator that converts the X-ray flux into an electronic signal that can be processed by computer. Areas in a radiograph that appear darker originate from a strongly attenuating portion while lighter areas indicate less X-ray attenuation.

In the XCT scan, radiographs are collected in predetermined steps while the sample rotates. Each radiograph along the rotation is considered a projection, and a typical laboratory scan will contain thousands of projections. The projections are fed to a reconstruction algorithm that combines them into a 3D volume rendering, which is called a tomogram. A tomogram contains the attenuation data in grayscale voxels (volume pixels) so the full volume can be probed.

There are a variety of lab XCT machines commercially available with various levels of resolution. Choosing an XCT instrument to fit your experiment will depend on the size of the region of interest (ROI), the required field of view (FOV), sample density, and the time required to image the sample. There are various XCT machines within the electrochemical innovation lab (EIL), a breakdown of the XCT instruments available at the EIL is given in Table 1.

Table 1 - Instrument breakdown of EIL XCT machines

Instrument	Nikon XTH225	ZEISS	ZEISS
		Xradia 620 Versa	Xradia 810 Ultra
Max Spatial	9 μm	500 nm	50 nm
Resolution			
Corresponding	6.4 mm	350 μm	64 μm
Field of View			
Energy Range	30-225 kV	30-160 kV	5.4 kV
Source	W, Ag, Cu, Mo	W	Cr
Average Time of	1-2 hrs	6-24 hrs	24-48 hrs
Scan			

Aside from lab based XCT, there are also synchrotron X-ray sources with highly advanced XCT equipment. Synchrotron-based XCT is often viewed as the gold standard since it provides high resolution over large FOVs in very short time compared to lab XCT machines. In the field of SSB, many experiments have taken advantage of the power of XCT. Tracking cracks within a solid electrolyte for example is a popular use of XCT.

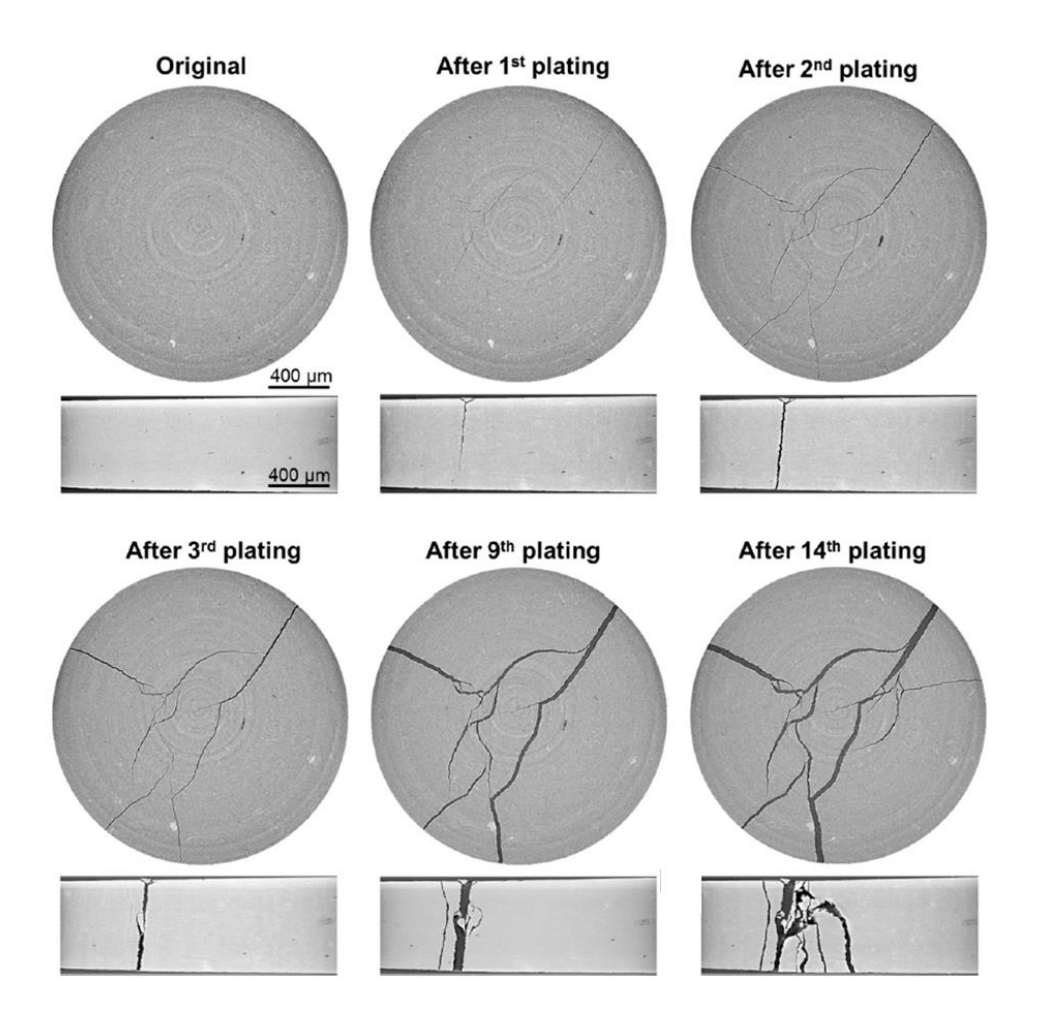


Figure 3.15 - 2D orthogonal slices tracking the cracking of a Li₃PS₄ pellet during cycling at a synchrotron. Reproduced from Reference 105.¹⁰⁵

As shown in Figure 3.15, researchers can track the cracking of the SE during cycling. This is helpful for understanding the degradation of SSBs throughout cycling and inform further research into the cycling conditions that lead to better performance. Other researchers have used XCT to observe different degradation mechanisms such as void formation and loss of interfacial contact⁸⁰.

XCT and subsequent data processing are powerful tools to quantify defects that arise within SSBs. Since XCT is non-invasive, researchers can visualize defects within a SSB during operation, and this technique pairs well with other measurements. For example, some researchers used EIS and the application of pressure with XCT to conduct experiments on the

relationship between pressure and ionic conductivity of SEs⁷⁴. Like most techniques, a more complete understanding is gathered when utilizing multiple measurements *in situ*. More techniques can be partnered with XCT to understand the ideal pressures, temperatures, and cycling conditions to avoid damage to SSBs.

XCT was done on pristine cells to observe the internal structure of the cells and on cycled cells to track degradation. Most of the XCT imaging in this work was done with the Nikon XTH225 (Nikon) and the ZEISS Xradia 620 Versa (Versa) XCT mahcines. Due to the nature of the work, where cell architectures and scanning parameters are constantly being optimized, there are not set parameters that are used for each XCT scan. There are however certain standards used to obtain high quality images from each machine; mainly related to the working voltage and detector saturation.

For both XCT instruments, the goal was to get around 20% X-ray transmission through the sample to get good contrast without oversaturating the detector. The working voltage for both instruments was 80kV since this voltage gave a sufficient intensity through the cell yet is low enough energy to interact with the SE. Scans done on the Nikon XCT machine take under and hour while the Versa XCT machine scans took 4-8 hours. More is done in this work to optimize the scan time by reducing the needed projections and binning the detector data when possible. Synchrotron-based XCT was carried out across two beamlines at ESRF (The European Synchrotron): ID15A and ID19. An X-ray beam from a 17 pole undulator (peak energy at 26.5 keV) was used at the ID19 Beamline. A LuAG screen was used as scintillator on a CMOS detector, (PCO-edge 5.5, 2560 × 2160) was coupled with a ×10 magnification optic to reach an effective pixel size of 0.65 µm. A monochromatic X-ray beam with an energy of 72.5 keV was used at Beamline ID15A. A similar PCO-edge detector (2560 × 2160) with an effective pixel size of 0.70 µm was utilized. Since the field of view was sometimes less than the diameter

of the cell, the tomography scans were conducted with the center of the tomographic rotation at the edge of the recorded frame, to allow for an extended field of view, thus covering the entire cell diameter with a small pixel size.¹⁴⁶ For both beamlines, the Nabu pipeline was used to compute the filtered back projections reconstructions.¹⁴⁷

3.5.2 X-ray Diffraction Computed Tomography

X-ray diffraction computed tomography (XRD-CT) is a technique to obtain spatially resolved 3D powder diffraction patterns using the principles of computed tomography. In XCT, the result of a 3D map of absorption is visualized as grayscale values, XRD-CT on the other hand produces 3D, spatially oriented diffraction information of the materials inside the sample. Each voxel contains a unique diffraction pattern, allowing researchers to study crystallographic heterogeneities and how they change during cell operation. X-ray diffraction (XRD) arises due to the interaction between incident X-rays and the periodic arrangement of atoms within a crystalline material. X-rays can constructively interfere upon scattering from atomic planes if the path difference of the outgoing waves is an integer multiple of the X-ray wavelength, a condition described by Bragg's Law:

$$n\lambda = 2d \sin\theta$$
 (5)

Where λ is the incident X-ray wavelength, d is the spacing between parallel lattice planes, θ is the diffraction angle, and n is an integer number. The resulting XRD pattern is unique to each crystalline material and enables identification as well as characterization. XRD-CT technique requires the use of high energy X-ray sources, so synchrotron X-ray sources are often utilized for faster acquisition times. In the setup of XRD-CT, a microfocused X-ray beam illuminates the sample which is rotated to collect average XRD patterns through the sample depth at each rotation (projection) angle. Subsequently, the sample is moved horizontally/vertically and the rotation repeated. Then, a filtered back projection approach is used to convert the XRD patterns

from the projection space into real space, like XCT. The setup and process of gathering XRD-CT data is shown in Figure 3.16.

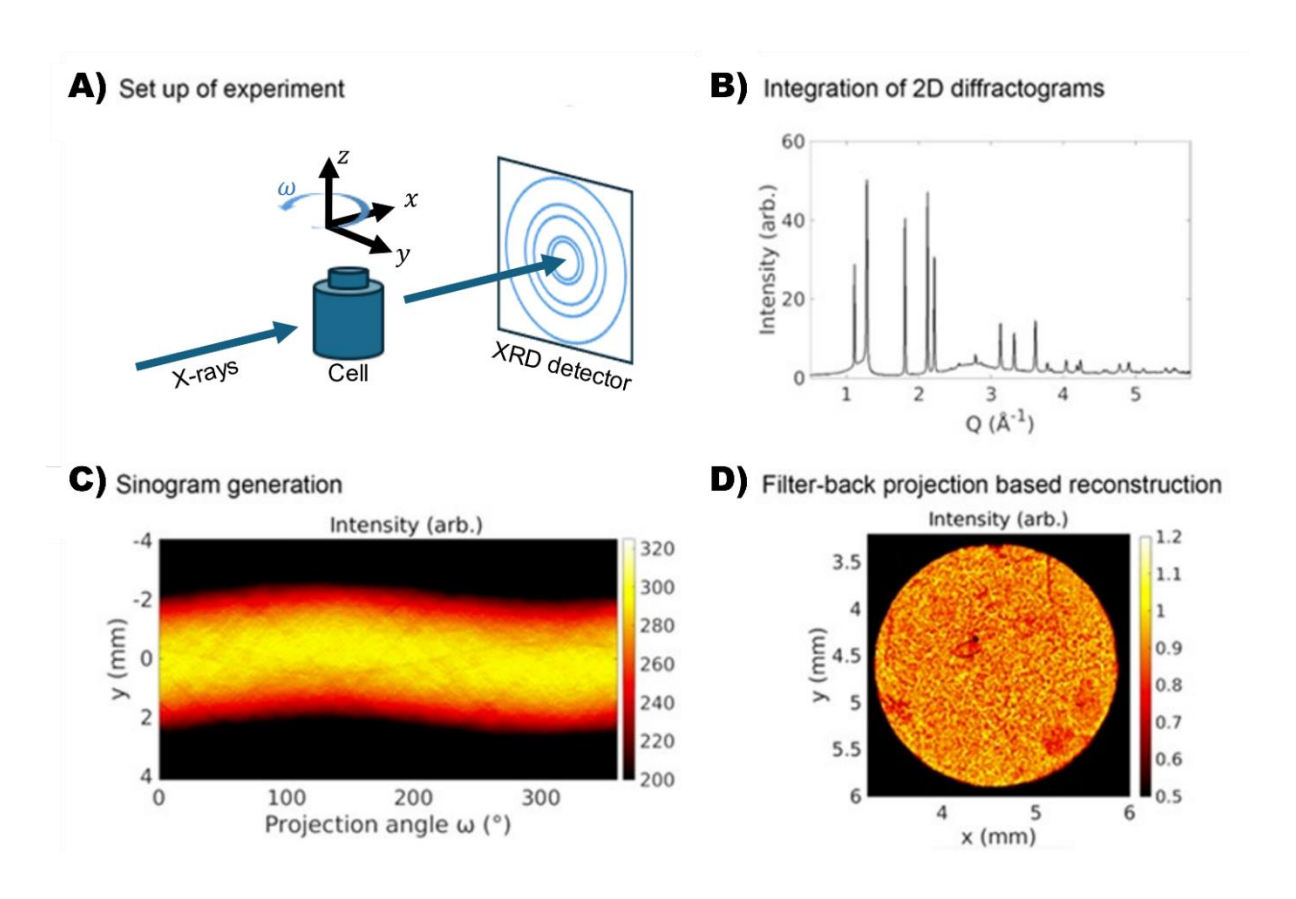


Figure 3.16 - XRD-CT setup and data processing: A) Sample setup and collection of 2D diffraction patterns, B) Diffraction patterns for each scan as a function of spatial coordinates after azimuthal integration, C) Sinogram showing scattering intensity as a function of projection angle, D) Final reconstructed XRD-CT image after filtered back projection (FBP). Modified from citation 84.84

Diffraction rings are captured by a flat panel detector (as shown in Figure 3.16A) as the sample rotates 180° then translated along the y-axis and creates a 2D cross-sectional map. For each spatial and projection angle (y, ω) , the 2D scattering pattern is integrated over the azimuthal angle to produce an XRD pattern like the one shown in Figure 3.16B. The total scattering intensity is then collected as a function of (y, ω) , constructing a sinogram for each 2 θ value as shown in Figure 3.16C. Using a filtered back-projection (FBP) algorithm, the sinograms are

reconstructed to 2D vertical slice, where each pixel is a full diffraction pattern. For 2D measurements, the resulting sinogram contains 2D spatial information and 1D of diffraction. For the 3D measurements, 2D XRD-CT slices are collected through the height of the sample, resulting in a 4D matrix of data. If multiple scans are performed over time, a fifth dimension of time is introduced.

Beyond material identification, the XRD patterns in the XRD-CT volume can also be utilized to study the elastic deformation within the SSE by tracking changes in the lattice parameter. The volumetric strain can be determined and converted into stress using the bulk modulus of the SSE allowing for a non-destructive assessment of internal mechanical stresses in the SSB. ARD-CT has been used extensively in LIB electrodes and other battery material to understand the structural and phase evolution during operation. This technique allows researchers to study the changes in crystallographic structures within electrodes to help understand degradation so that they can improve the performance and longevity of future batteries.

The XRD-CT scan was carried out at beamline ID15A of ESRF, the European Synchrotron. A monochromatic microfocused X-ray beam at 72.5 keV energy and a spot size of 10 µm x 5 µm was used to illuminate the samples. A Pilatus3 X CdTe 2M area detector (Dectris) is used to collect the 2D XRD patterns. Azimuthal integration was conducted using pyFai, followed by tomographic FBP reconstruction, using an in-house Matlab script, to transform the data into Cartesian space through a FBP method. Strain analysis and plotting were performed with TOPAS-7, utilising Rietveld refinement at each voxel. 155,156

3.5.3 Neutron Computed Tomography

Neutron computed tomography (NCT), like XCT, is a non-destructive imaging technique that generates 3D images of the internal structure of an object. The setup is very similar with a

sample setup between a detector and a source (but instead of X-rays) NCT uses neutrons which interact differently with materials, offering unique insights.

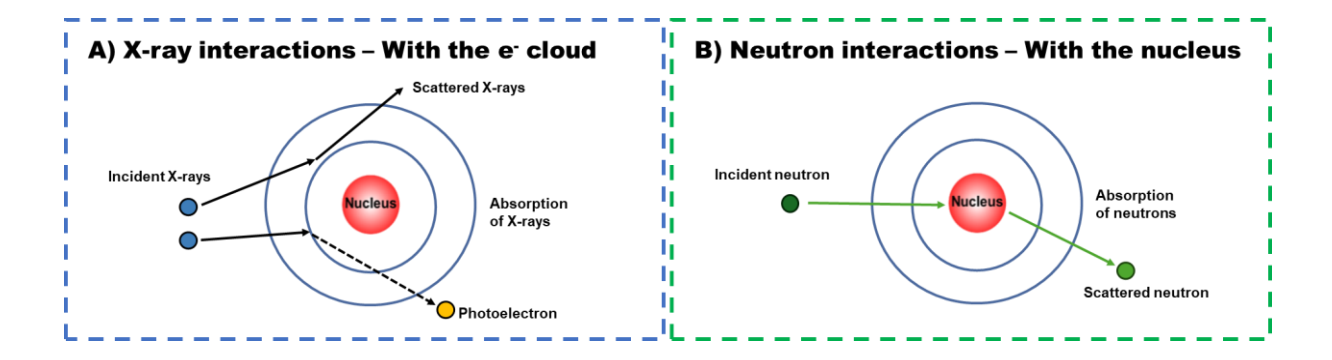


Figure 3.17 - Schematic of X-ray and neutron interactions with matter. A) shows X-rays interacting with the electron cloud and B) shows incident neutrons interacting with the nucleus.

The interaction of neutrons and X-rays with matter differ significantly, and this makes the techniques of XCT and NCT quite complementary. X-rays interact with the electron cloud of atoms, but neutrons primarily interact with atomic nuclei. This distinction, highlighted in the schematic in Figure 3.17, allows NCT to image elements that are difficult to detect with X-rays, such as hydrogen and lithium. This distinction between the interactions between the different sources of radiation with matter has an effect on the mass attenuation coefficient introduced in Equation 3. The variation of mass attenuation coefficient for different elements is shown in Figure 3.18 and this variation will affect the contrast given for different elements.

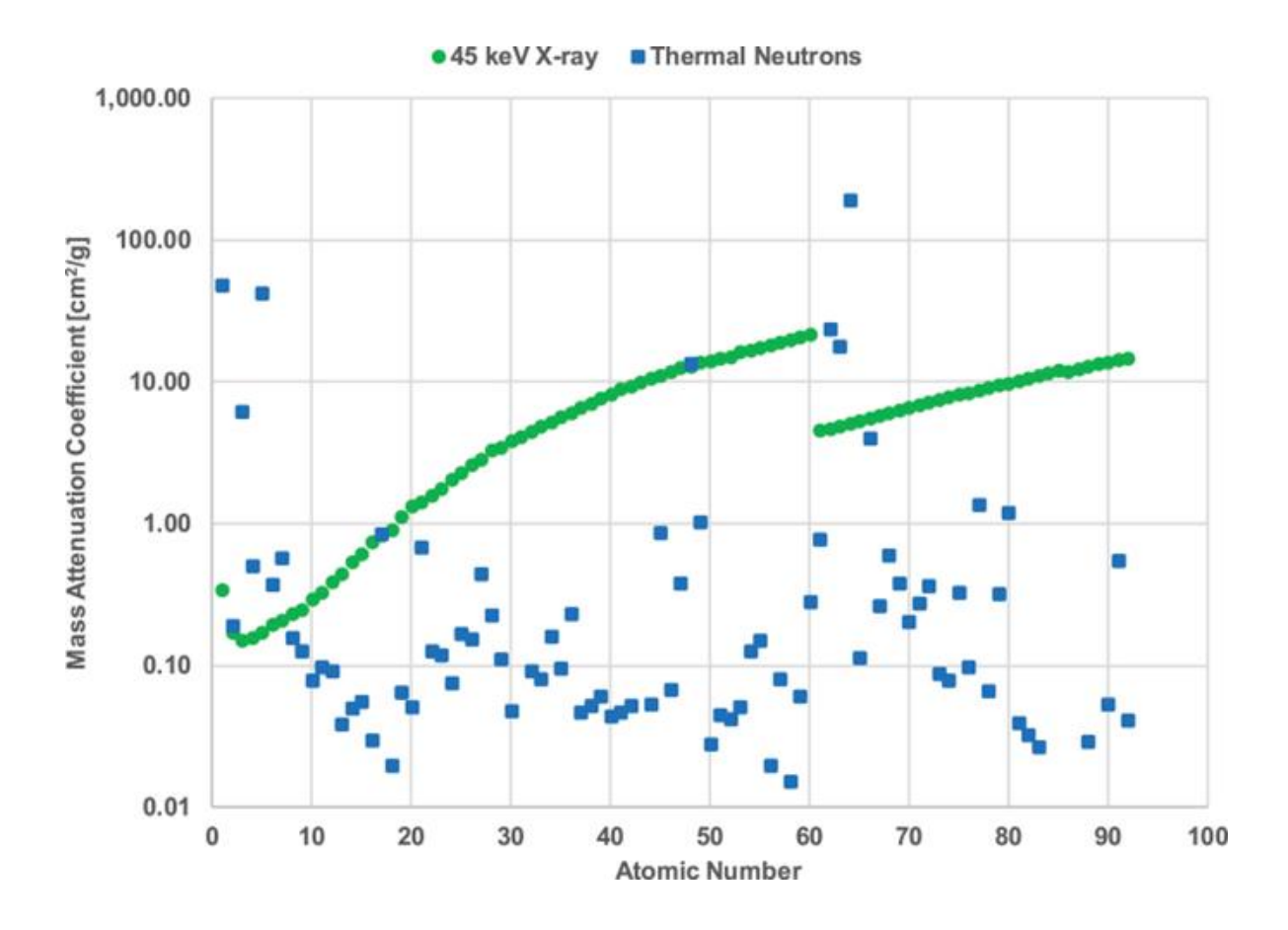


Figure 3.18 - Comparison of mass attenuation coefficients for 45 keV X-rays and thermal neutrons (25 meV) as a function of atomic number, assuming natural isotopic abundances for the neutron cross-section. Reproduced from citation 158. 158

Another important distinction of NCT is the ability to differentiate between isotopes, stemming from the fact that the incoming neutron interacts with the nucleus of the atom. This is very powerful because not only can researchers see Li within their LIBs, but they can choose which Li they wish to see.¹⁵⁹

With these distinctions in the physics between X-rays and neutrons, there are also differences in the setup for NCT, as illustrated in Figure 3.19.

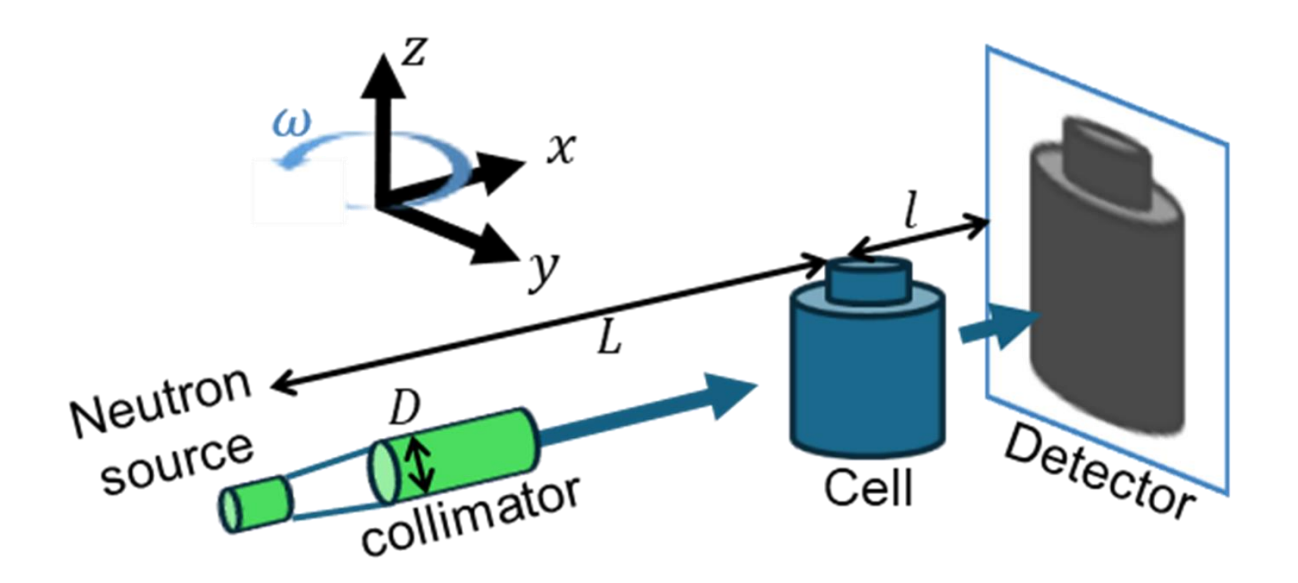


Figure 3.19 - Geometry of a neutron imaging experiment. Showing a pinhole with size D as the source, distance to the sample of L, and distance from sample to detector of l.

In the setup of XCT, the sample would ideally be as close to the conical X-ray source as possible to take advantage of the geometric magnification as the signal travels to the detector. In contrast, the setup of NCT places the sample as close to the detector as possible. Highlighted in Figure 3.19, neutrons are emitted through a pinhole source of diameter D, traveling a distance L to the sample, where it interacts with the sample and then transmits over a path length 1 towards the detector. There is an important equation that will dictate the geometry of the NCT setup when attempting to optimize for high resolution (d) which is given in Equation 6.

$$d = l \cdot \left(\frac{L}{D}\right)^{-1} \tag{6}$$

When optimizing for high resolution NCT, the sample should be positioned as close as possible to the detector to minimize the path length 1 while the L/D ratio should be maximized by restricting the pinhole diameter (D) and increasing the propagation distance to the sample (L).

These optimizations towards high resolution also require longer exposure times which extends the scan times.¹⁵⁷

Neutron imaging, mainly *ex situ* or *in situ* tomography and *operando* radiography, has been applied to LIB research for studying the dynamics of cell gassing and Li mobility in various electrode types. Neutron imaging has also been used previously in various SE systems to visualize the transport of Li into electrodes and throughout the SE. 159,169–175 The goal of tracking Li transport is looking for heterogeneities that would highlight areas of degradation, giving key insight into the mechanics of defect formation to avoid it in future productions.

The neutron sources used in this work include both spallation sources and nuclear reactors, namely the ISIS neutron and muon spallation source in Oxfordshire, UK, and the Institut Laue-Langevin (ILL) reactor source in Grenoble, France. 158,176,177

3.5.4 Pressure

Pressure is a critical variable to consider in the utilization of SEs. High pressures are used to prepare SEs from powders into pellets. For oxide-based materials, formation pressures are around 200 MPa¹⁷⁸ but for sulfide-based materials this pressure can be reduced to around 100 MPa¹²⁸. Formation pressure is highly affected by the material used, the average grain size, and the desired density of the SE. The conditions used to form the SE can have large effects on the pellet's strength and therefore the lifetime of the SSB.

Other than the formation pressures required to produce the SE pellet, it is sometimes reported that SSBs require external pressure during cycling for optimal electrochemical performance. Having the SSB under active pressure increases the contact between SE particles with themselves and the electrode interfaces. This leads to increased ionic conductivity and better cycling performance^{63,74,128}. Researchers found that Li₆PS₅Cl at 80 °C can achieve stable cycling at 0.5 mA cm⁻² with an external pressure of 1 MPa which can increase to stable cycling

at 2.5 mA cm⁻² with an active pressure of 5 MPa¹²⁸. Researchers have also combined the techniques of XCT and EIS together to study the effects of pressure on the ionic conductivity of sulfide-based SEs. This study demonstrated that room-temperature pellet pressing can be visualised under high pressures utilizing *in situ* XCT. As the applied pressure is increased, the ionic conductivity rises⁷⁴

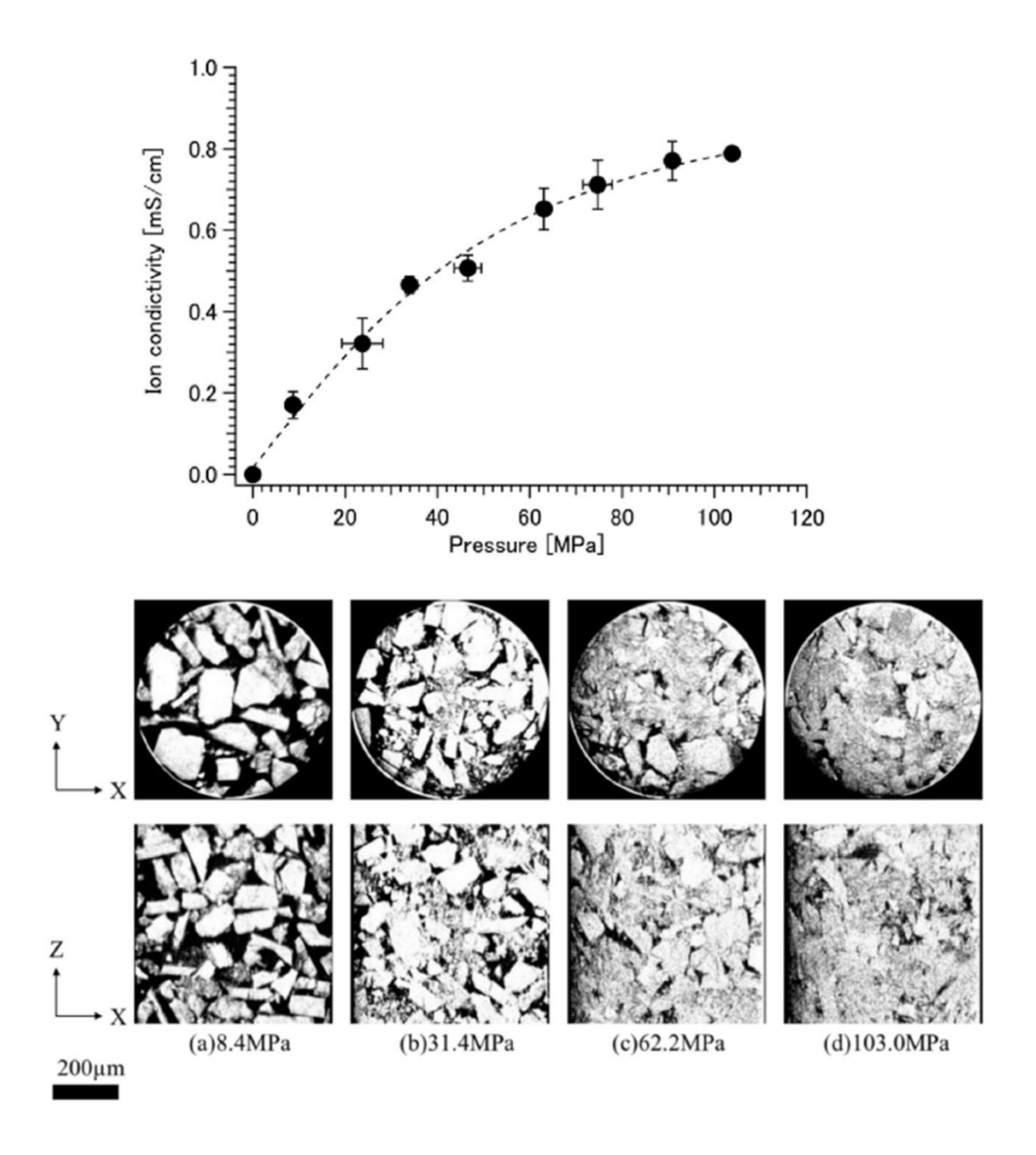


Figure 3.20 - Ionic conductivity verses applied pressure along with the corresponding XCT images of the sulfide-based solid electrolyte. Reproduced from Reference 74.⁷⁴

Figure 3.20 from Kodama et al. shows the relationship between ionic conductivity and applied pressure on a S-SE. The ionic conductivity generally increases with increasing applied pressure. The interesting finding here is that the ionic conductivity appears to plateau around 120 MPa at room temperature, however it has been observed in other work that the ionic conductivity of Li₆PS₅Cl increases continuously up to pressures of 370 MPa.⁶³ Pairing EIS and XCT gave great insight on the densification of S-SE; however, it is desirable to monitor the changing density using XCT where the weight could have been recorded and the exact volume could be extracted from the scan. Mapping the relationship between ionic conductivity and pressure beyond 120 MPa would also be interesting, since other projects have observed benefits up to 370 MPa. Additionally, studying the change in ionic conductivity at various temperature conditions would be beneficial. This would be useful in finding a minimum temperature and pressure combination that produces a maximum ionic conductivity, informing future production of SSBs.

The formation pressure can also influence the capacity retention of the SSB as shown by Doux et al. in Figure 3.21.

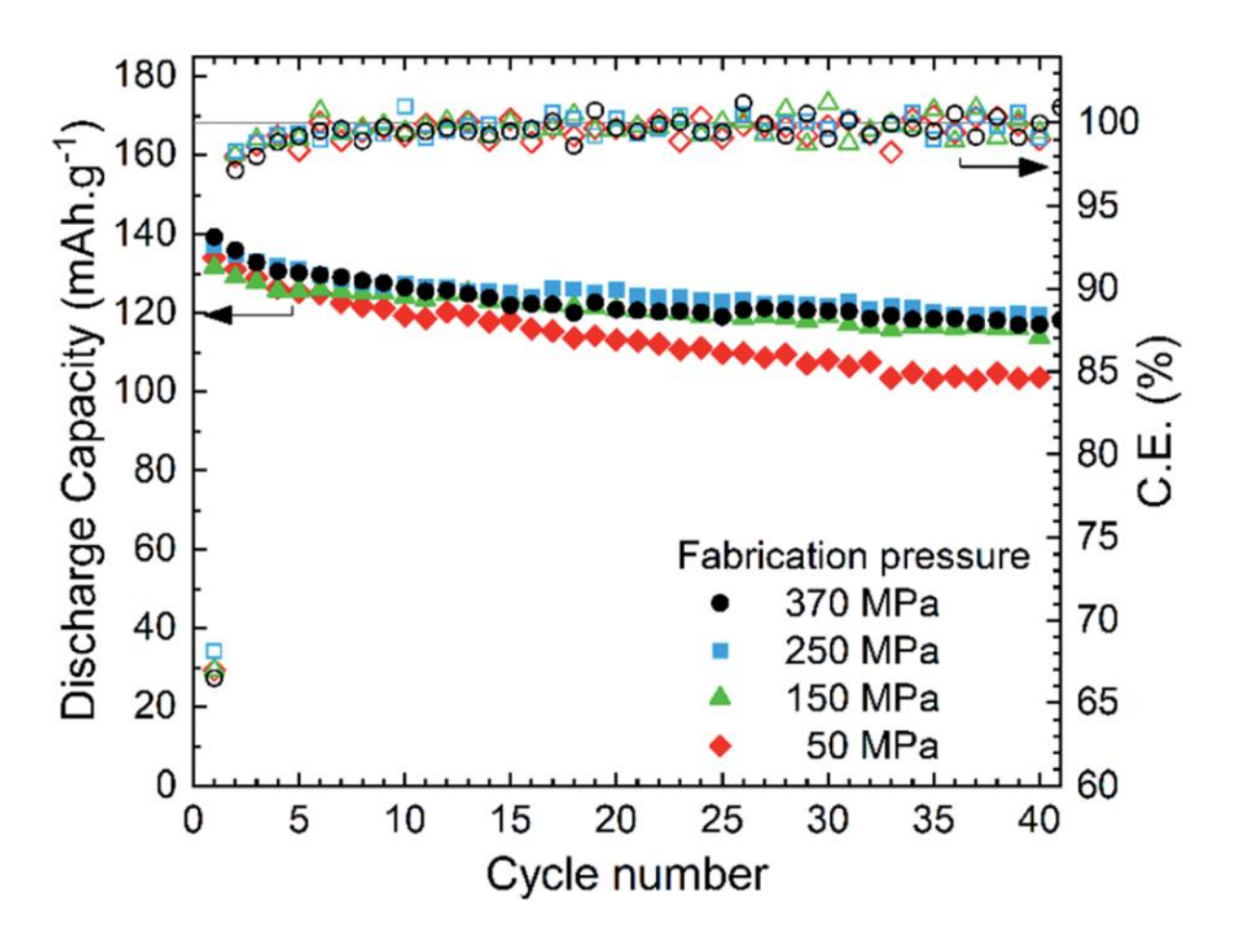


Figure 3.21 - Cycling stability (discharge capacity and coulombic efficiency verses cycle number) at C/10 of $LiIn|Li_6PS_5Cl|NCA$ solid-state batteries at various fabrication pressures. Reproduced from Reference 63.⁶³

SSBs created with high formation pressure (or fabrication pressure), up to 370 MPa, have increased capacity retention than those made at a lower formation pressure of 50 MPa⁶³. Testing the discharge capacity retention is good for understanding the degradation of the SSB in terms of how much capacity is lost over time. Relating this to the mechanical degradation, such as cracking, observed in other studies, would be a valuable addition to the understanding of how influential mechanical degradation is on capacity retention.

3.5.5 Temperature

Temperature is an important parameter to consider for SSBs. It has been shown that the ionic conductivity is temperature dependent, and it is generally accepted this is an Arrhenius-like relationship. This Arrhenius temperature dependence¹²⁴ of ionic conductivity is shown in Equation 7.

$$\sigma_{ion}(T) = \sigma_o(T^{-1}) \exp\left(-\frac{E_a}{RT}\right)$$
 (7)

Here, R is the universal gas constant, E_a is the activation energy, and σ_o(T⁻¹) is a model-dependent coefficient, which contains a T⁻¹ dependency¹⁷⁹. Temperature is also used in preparing SE pellets, where having high density of the pellet is crucial for reaching high current rate cycling. Some oxide-based materials are hot pressed at 1050 °C or sintered after pressing at 1250 °C for hours to reach the desired high densities^{178,180}. Some researchers have explored sintering additives for oxide-based materials, such as B₂O₃ in 7LiLa₃Zr₂O₁₂ which allows for high densification at temperatures as low as 750 °C¹⁸¹. As discussed in Section 2.3.4 about sulfide-based solid electrolyte, S-SE are easier to densify than oxides. Because of this, Li₆PS₅Cl is typically not hot pressed and if sintered at all, they require only 300 °C¹²⁸. Achieving high densities is important for obtaining higher ionic conductivity. As an example of correlated EIS and temperature variation, Feng et al. utilized EIS was test the ionic conductivity of a pellet at various temperatures.¹⁸¹

Temperature not only effects the efficiency of ion transport, but it can also play a role in maintaining interfacial contact during cycling. During the process of plating and stripping there can be a loss of contact at the Li₆PS₅Cl/Li interface and the formation of voids, this leads to rapid impedance increase and the failure of cells¹²⁸. Researchers Spencer et al. demonstrated that at high temperatures, voiding and loss of interfacial contact is decreased, also showing the dependence of the current rate capability on temperature. Li₆PS₅Cl |Li symmetric cells

were charged and discharged at an operating pressure of 1 MPa, the critical current before cell failure increased from <0.25 mA cm⁻² at 25°C to 0.25 mA cm⁻² at 60°C and 0.5 mA cm⁻² at 80° C¹²⁸.

As discussed above, temperature and pressure are key variables that greatly affect the cyclability of SSBs. The ideal pressure and temperature to form and run a SSB will depend on several variables such as the SE and the grainsize used. Having a method to test SEs rapidly and reliably under many combinations of temperature and pressure would help streamline the research into new materials.

3.6 Summary

There are various SEs that may be useful in SSBs of the future, such as the highly ionic conductive sulfides or the chemically stable oxides. There are also many techniques to monitor the health and quality of SSBs, using different techniques in conjunction with each other will tell a fuller story of the existing degradation mechanisms. SSBs have many failure mechanisms and shortcomings that can be probed with methods such as XCT, EIS, XRD-CT, and NCT. These faults are also shown in many cases to be greatly impacted by variables such as pressure and temperature. Exploring the variables and their relationship to the degradation of SSBs will give insight into future production of SSBs.

4 Total Volume *Operando* X-ray Computed Tomography

4.1 Aim

The transition to solid-state electrolytes (SEs) introduces novel degradation modalities, a mixture of chemical/electrochemical and mechanical, that need to be addressed before they will reach mass application. In this chapter, the degradation of solid-state batteries (SSBs) is investigated with a bespoke SSB cell designed for *operando* X-ray imaging and tomography. The PEEK *in situ* Press (PIP) cell enables unprecedented spatial and temporal resolution during *operando* X-ray computed tomography (XCT) experiments. The PIP cell operates with a 1 mm diameter solid electrolyte pellet, providing a spatial resolution of about 2.4 μm on typical labbased XCT experiments over the total volume of the SSB. Li| Li₆PS₅Cl |Li symmetric cells were investigated during various constant current cycling protocols and the cell shows markedly good cyclability compared to other examples in the literature ^{35,80,90}. The degradation of the SE was tracked throughout the entire volume during the experiment and showed spatial variation in crack formation that exemplifies the importance of full volume analysis.

4.2 Experimental Setup

The first step in evaluating the degradation of the commercial Li₆PS₅Cl argyrodite SE (Li₆PS₅Cl; 99.9%, Ampcera Inc.) was to gauge the sizes of the features of interest. To obtain an understanding of the morphology of the commercial powder, X-ray computed tomography (XCT) was performed on the loose powder before pellet formation. Since the Li₆PS₅Cl argyrodite powder is highly air sensitive, the powder was handled in an Ar filled glovebox, prepared into a Kapton tube and fully sealed with epoxy. The Kapton tube was then transferred in the ZEISS Xradia 620 Versa (Versa) XCT machine, which has various magnifications

available for use; $4 \times, 20 \times$, and $40 \times$. In Figure 4.1, the $4 \times$ and corresponding $20 \times$ images are compared for the loose argyrodite powder.

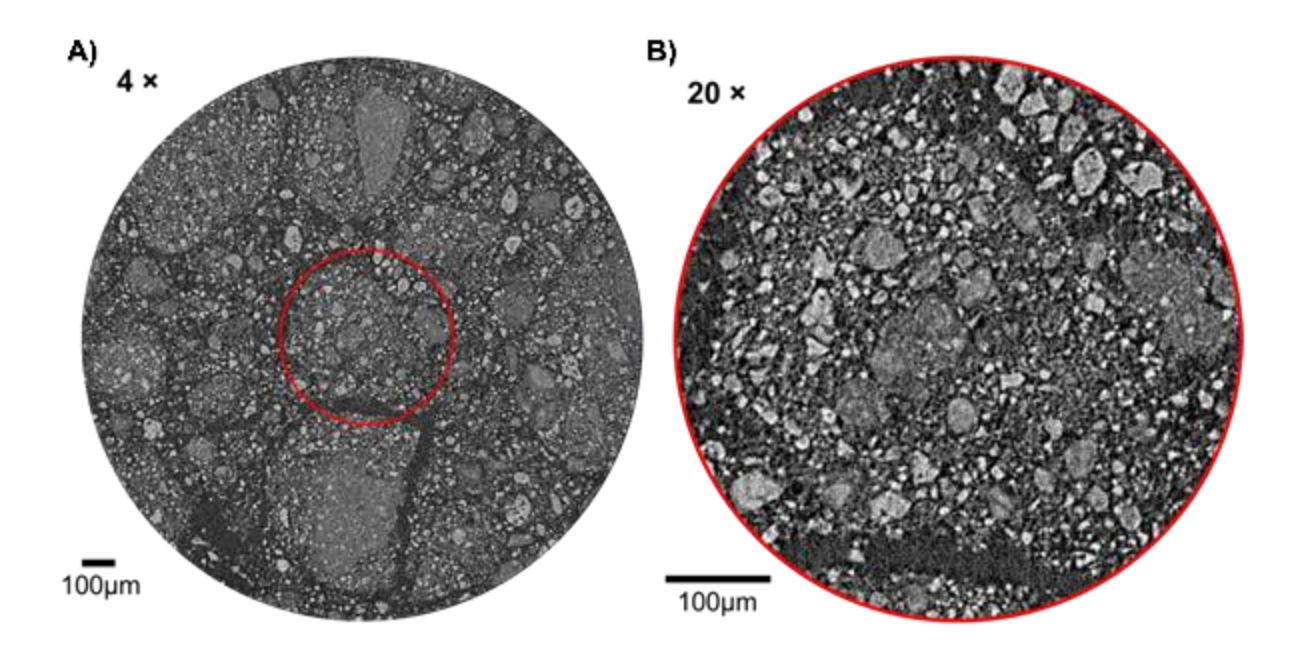


Figure 4.1 - XCT images at A) $4 \times$ and corresponding B) $20 \times$ magnifications of loose Li_6PS_5Cl argyrodite powder. The tomography shows that agglomerates of Li_6PS_5Cl powder 100s of microns in diameter are present in the powder.

This initial tomography was informative as it shows in the 4 × image that the argyrodite grains loosely agglomerate into clumps a few 100 μ m in diameter while the 20 × image shows more clearly that the particles are below ~44 μ m in diameter. The Li₆PS₅Cl powder from AmpceraTM is labelled as ~1 μ m (D50, 325-mesh). This means that 50% of the grains are below ~1 μ m and that it has been run through a 325-mesh sieve, meaning no particles should be above 44 μ m. This seems to be consistent with the XCT findings, but nothing on the label would lead to expecting the few 100 μ m agglomerates. These agglomerates are easy to visualize at lower resolutions, but to resolve the grains within them, of ~1 μ m, a spatial resolution below 1 μ m is ultimately desired. Due to the relationship between spatial resolution and the field of view

(FOV) being inversely proportional in XCT, the volume of the cell was minimized to match the FOV achievable with higher resolutions.

Since various positive electrode materials have been used in the development of solid-state full cells, testing the stability the materials once they are exposed to sulfide-based materials is of interest. Electrochemical impedance spectroscopy (EIS) was used to probe the chemical stability of the solid-state full cell upon manufacturing. Figure 4.2 shows the EIS stability results of a lithium manganese oxide (LMO) and lithium nickel manganese oxide (LNMO) full cell.

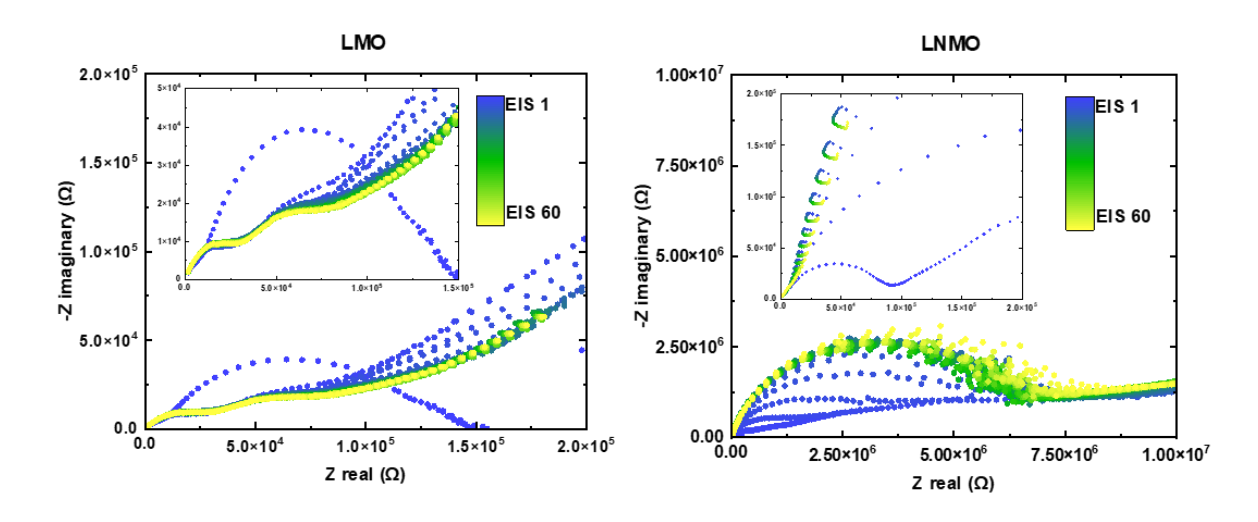


Figure 4.2 - Nyquist plots showing the EIS stability results of an (A) LMO/Li and (B) LNMO/Li full cell over time from manufacturing. Inlaid plots focus on a smaller impedance range for clarity.

EIS was taken at 60 intervals from the point of fabrication, with 500 ms breaks in between. The results shown in Figure 4.2 are quite interesting, as they show LMO and LNMO have drastically different stabilities in the full cell system. The impedance of LMO starts off high and converges onto a lower value, suggesting a reaction that stabilizes with a less resistive interface. LNMO of the other hand starts off in a similar impedance range of the LMO but increases to an order of magnitude higher then LMO. With these initial findings, it appears that

LMO forms a more favourable interphase than a full cell with LNMO. However, as mentioned in previous electrochemical data, more replicates would have to be carried out to give these findings statistical significance. Furthermore, the cells created in these electrochemical tests struggle with mechanical integrity and reproducibility.

The initial attempts at producing full-cell SSBs, Swagelok cells were utilized as discussed in Section 3.3.2 . Swagelok cells enabled the highest resolution XCT imaging in the Nikon XTH225 XCT machine over the total volume; however, good quality Swagelok cells proved difficult to produce. Figure 4.3 shows the first attempts (Figure 4.3A) and later attempts (Figure 4.3B) of producing LMO full cells with commercial Li₆PS₅Cl argyrodite SE. Figure 4.3C shows additional attempts of producing LNMO full cells with commercial Li₆PS₅Cl argyrodite SE. All cells shown in Figure 4.3 are pristine, so the cracking shown is due to manufacturing defects.

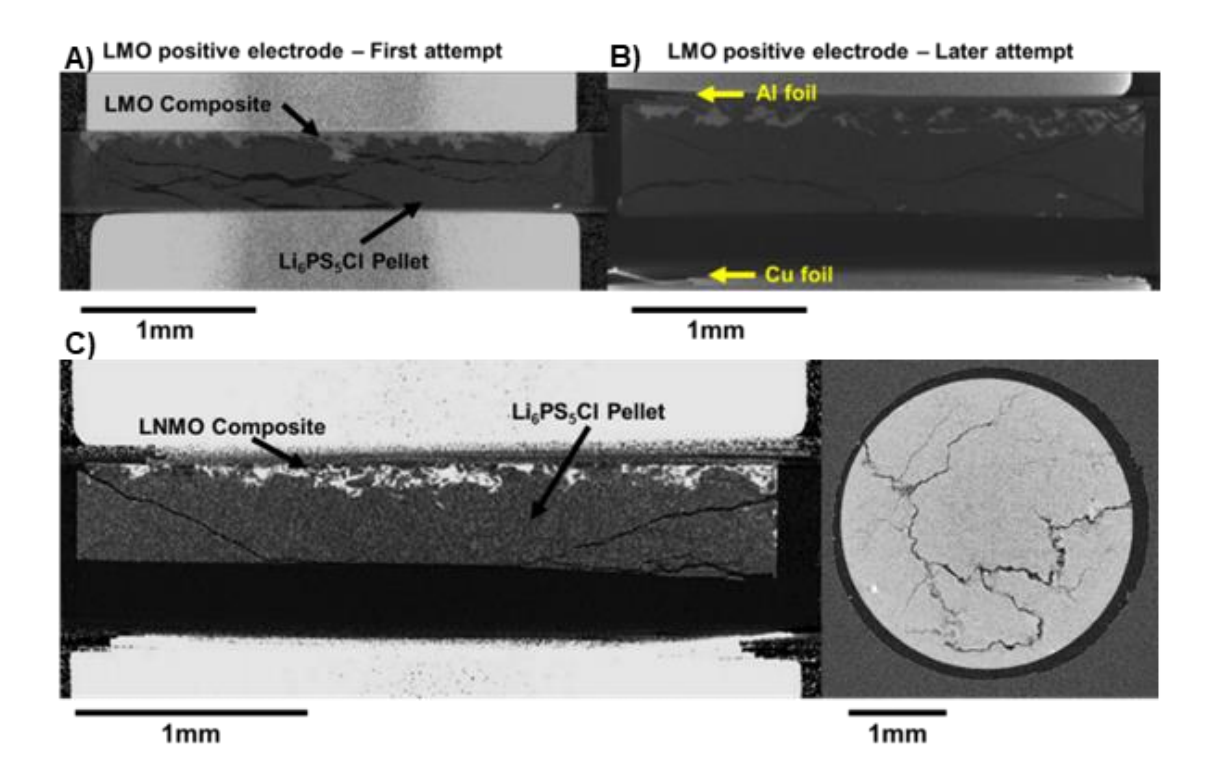


Figure 4.3 - Swagelok solid state full cells made with commercial Li_6PS_5Cl argyrodite. A) first attempt at LMO full cell, B) later attempt at LMO full cell with foils, and c) additional attempts at a LNMO full cell.

Changes were made in later attempts to reduce the cracking in Swagelok cells, such as the addition of current collector foils, as highlighted in Figure 4.3B. Regardless of the changes, it seemed difficult to make a SSB in a Swagelok cell without initial defects, which effects the reproducibility of cell manufacturing.

When handling the pellet and cell with extreme care did not produce defect free pellets, more attention was given to the pellet formation process. To explore this, a pellet was produced, very carefully sealed in Kapton and sequentially imaged with the Nikon XTH225 XCT machine. Figure 4.4 shows the results of the imaged pellet.

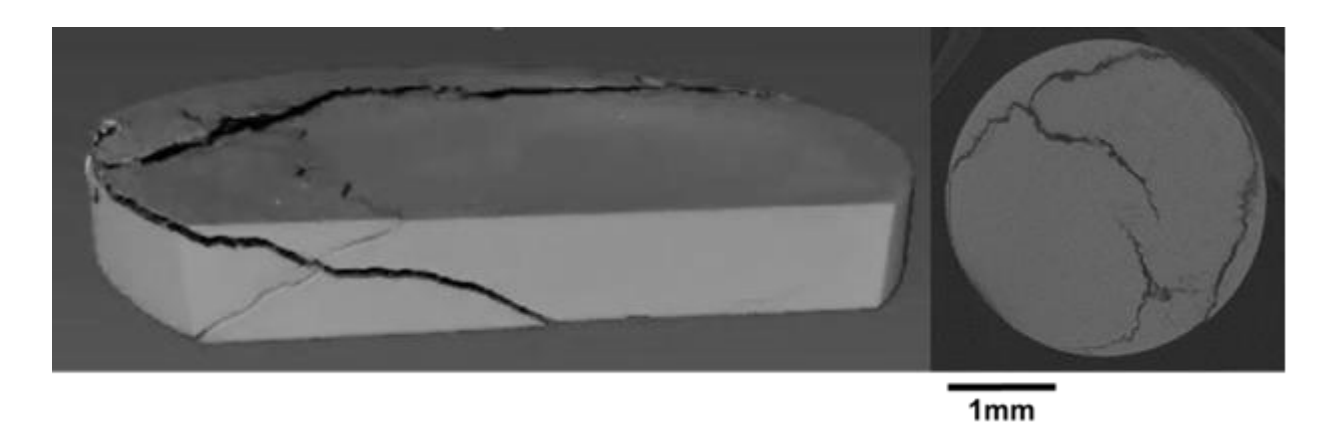


Figure 4.4 - Li_6PS_5Cl argyrodite pellet formed in a 3 mm die, carefully sealed in Kapton, and imaged to explore pellet formation in a die.

Surprisingly, the pellet that was carefully handled after being formed in the die also contained significant cracks. This prompted investigation into the possibility of crack formation during the production of the SE pellet itself in the hope of finding a method of producing defect free SSBs.

4.3 *In situ* Pressing

The colloquially named 'in situ press' is given its name from its function of being able to perform XCT on the cell during pellet formation. The in situ press was developed for use in the DEBEN CT5000TEC (DEBEN, UK) load stage which enables the application of pressure and temperature within the Versa XCT machine. Figure 4.5 shows the Deben load stage installed between the source and detector of the ZEISS Xradia Versa 620.

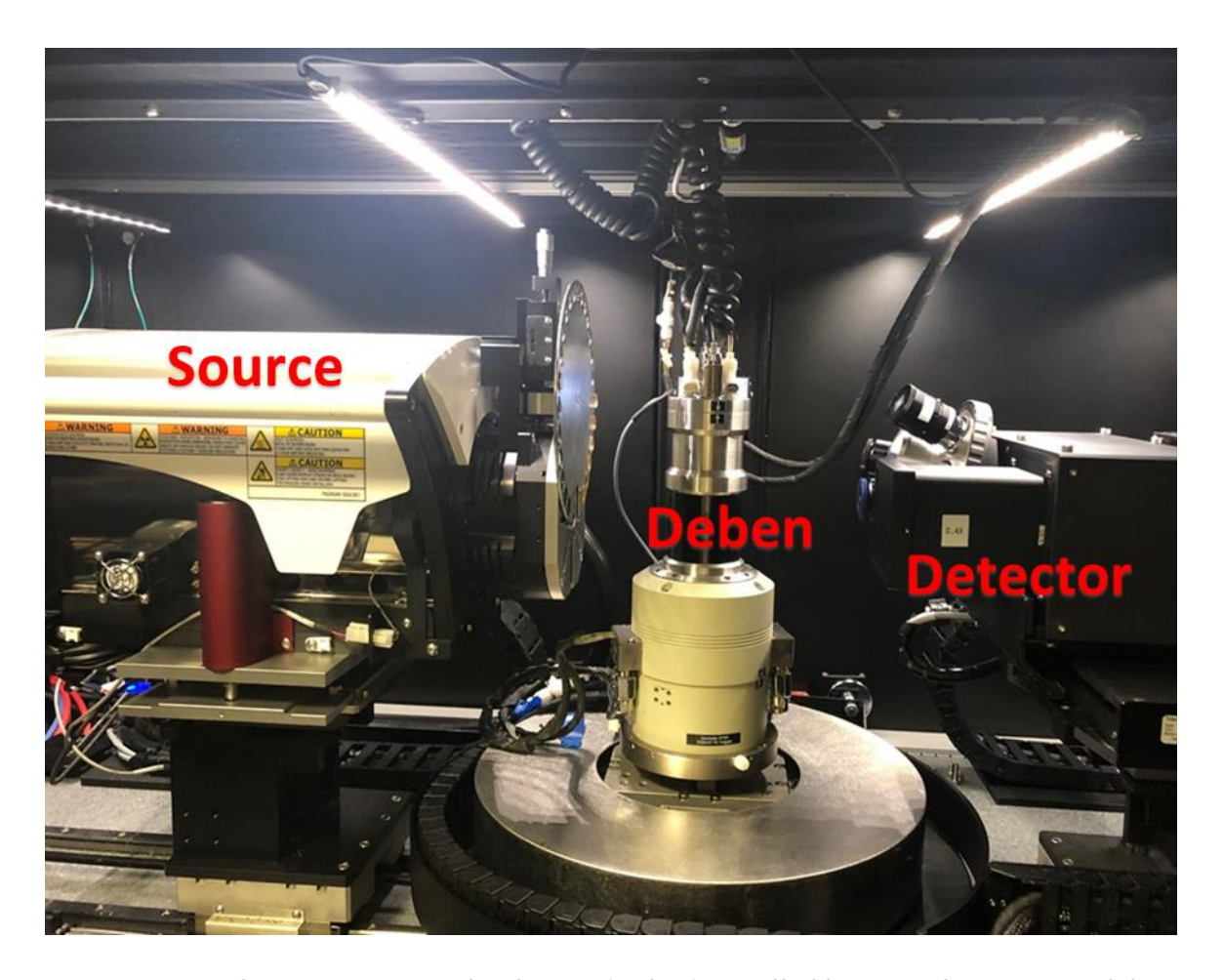


Figure 4.5 - Deben CT5000-TEC load stage (Deben) installed between the source and detector of the ZEISS Xradia Versa 620.

The Deben load stage is a computer controlled linear actuator with a 15 mm travel range and water circulation that adjusts the temperature. The housing also has a 360° carbon window to minimize X-ray attenuation. The Deben load stage is capable of applying loads up to 5000 N

over a temperature range of -20 °C to 160 °C. A blown-up schematic of the first *in situ* press with a 3 mm internal diameter is shown in Figure 4.6 below.

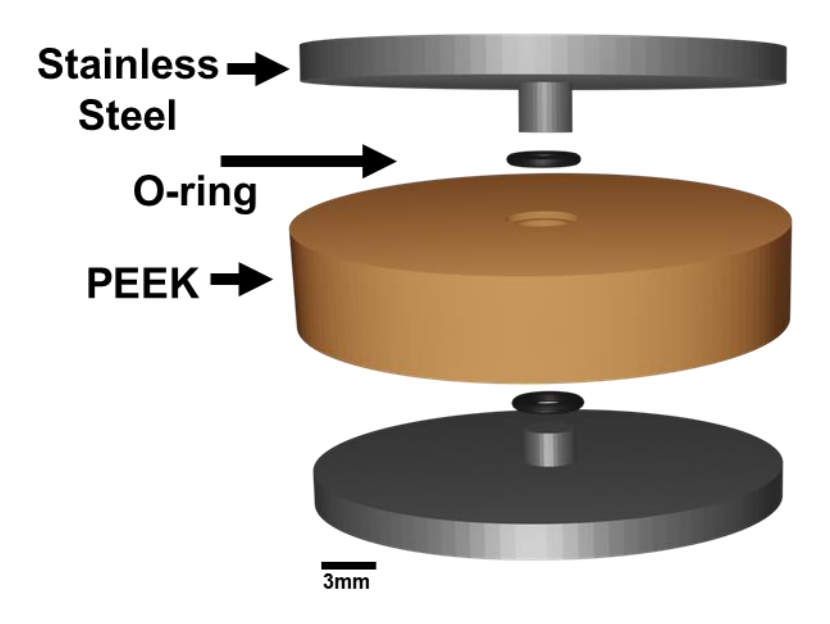


Figure 4.6 - Schematic of 3 mm internal diameter in situ press architecture for producing 3 mm diameter SE pellets from powders.

The design of the *in situ* press is a 27 mm diameter cylinder of Polyether ether ketone (PEEK) with a 3 mm diameter centre bore through. The 27 mm outer diameter allowed the *in situ* press to fit on the Deben load stage and provided a large amount of PEEK to limit pellet deformation during the pressing process. With the special PEEK body, two stainless steel plungers, and Orings the *in situ* press allows the user to produce 3 mm diameter pellets of SE while imaging the process with XCT. PEEK has a high strength to avoid deforming under the immense pressures of pellet formation and a low density for ease of X-ray transmission. The *in situ* press is filled with SE in a glovebox and placed in the centre of the Deben load stage. While forming the pellet, it is possible to take a radiograph, and XCT images are taken before and after pressing.

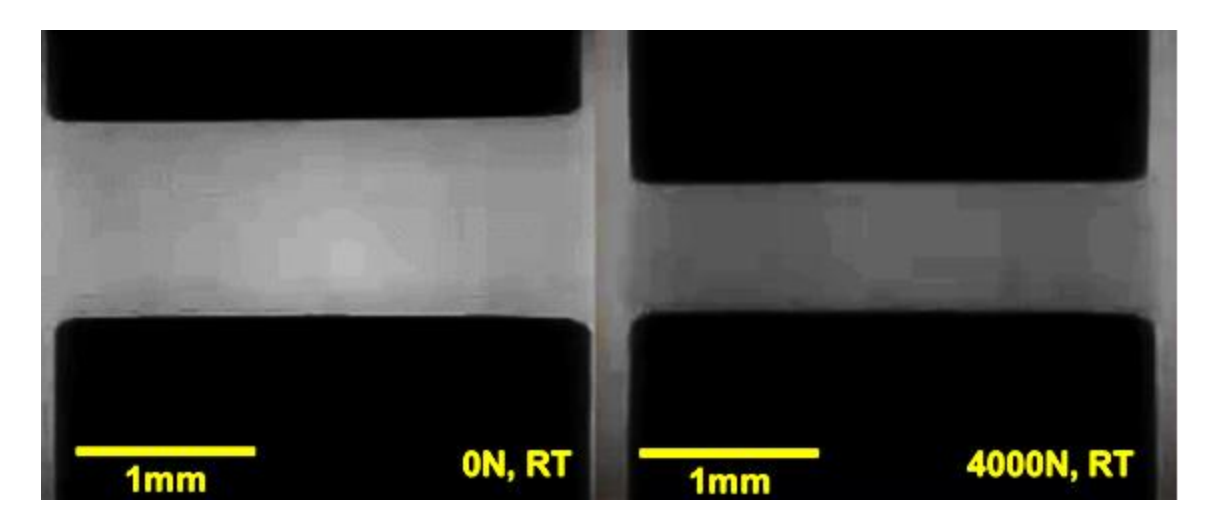


Figure 4.7 - 3 mm diameter Li₆PS₅Cl argyrodite SE pellet being formed with in situ press at 4000 N.

In Figure 4.7, a projection of the 3 mm *in situ* press with commercial Li₆PS₅Cl argyrodite before and after pressing to 4000 N is shown. 4000 N over the 3 mm diameter area results in 565.9 MPa pressure to form the pellet, which is much higher than suggested manufacturing pressures for Li₆PS₅Cl. (typically around 300 to 400 MPa^{63,114,183}). Moreover, the resulting pellet had notability defect free morphology and subsequent pellets showed more promise in terms of reproducibility. The *in situ* press was further modified to include an insert to reduce the diameter further and achieve higher resolutions over the full volume.

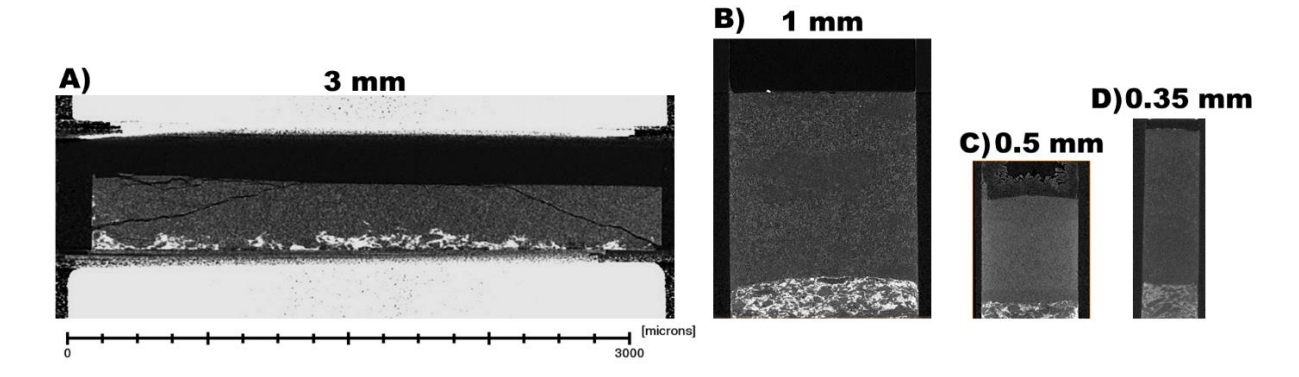


Figure 4.8 - The various geometries of the in situ press (B-D) compared to a pre-formed pellet in a Swagelok cell (A). A) 3 mm diameter pre-formed pellet in a Swagelok cell, versus in situ pressed pellets at B) 1 mm, C) 0.5 mm, and D) 0.35 mm diameters. All pellets were formed from the same commercial Li_6PS_5Cl .

As shown in Figure 4.8, *in situ* pressed cells show SE morphologies without the various cracks seen in the un-cycled pre-formed pellets within Swagelok cells. The ability to produce a cell with minimal pre-cycling defects (defects from manufacturing the SSB) is important when studying degradation and obtaining reproducible results as deconvoluting manufacturing defects with defects caused by electrochemical processes is difficult. The diameter of 0.35 mm was a goal for the use on the Versa XCT machine since this would obtain the maximum spatial resolution of the machine over the entire volume of the cell as shown in Figure 4.9.

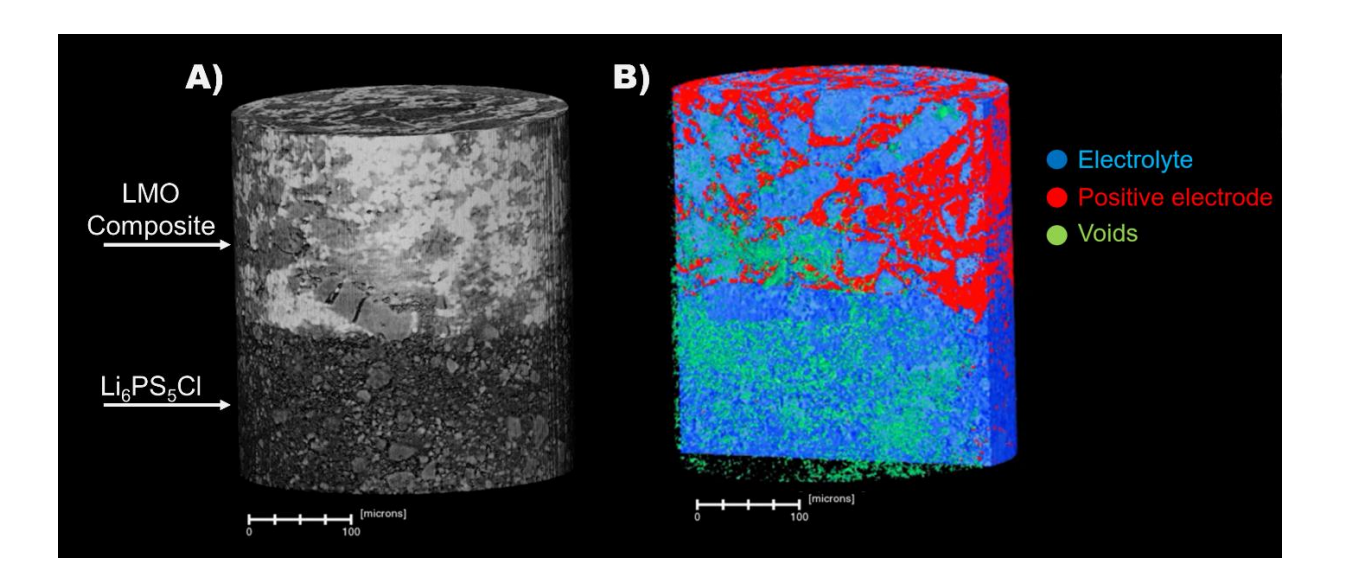


Figure 4.9 - LMO composite interface with Li_6PS_5Cl pellet at 500 nm spatial resolution. A) the greyscale X-ray tomography volume and B) the segmented dataset of electrolyte, positive electrode material, and voids.

The smaller the SSB cell the better for full-volume XCT at high resolutions (such as that desired in systems utilising $\sim 1~\mu m$ particle size SE) due to the trade-off between resolution and FOV: if the resolution is too low then features of interest cannot be identified and if the FOV is too small then the probed volume may not be representative of the system as a whole. Within the

various *in situ* press geometries, the 1 mm diameter press was the easiest to reproduce, providing an electrochemically representative cell that allows for scanning of the entire cell volume at sub-micron resolution to visualize nucleation and growth of cracks and pores within in the SE. The < 1 mm geometries could be further iterated to ease in the manufacturing of reproducible cells, but for now the 1 mm diameter provided a sufficiently small cell that enables investigation into the earliest stages of defect nucleation. This 1 mm diameter cell was explored further as it provides a more holistic view of degradation of the SSB compared to larger cell formats^{88,105}, while increasing the temporal resolution for future *operando* studies.

With all these findings, efforts were focused on producing a reproducible design of a such a cell, capable of full-volume sub-µm resolution XCT. The designed cell has been dubbed the PEEK *in situ* Press cell or PIP cell for short. For validation purposes, focus was kept on the production of Li/Li symmetric cells with sulphide SE optimised for 3D imaging. The design simplifies the materials processing/cell assembly steps and allows for investigation of densification of the SE pellet, reliable cycling, and optimal X-ray imaging. The following work shows the nucleation and progression of mechanical degradation in a Li| Li₆PS₅Cl |Li symmetric cell, from the as-assembled state, through cycling at increasing current densities. Overall, the PIP cell allows for a more thorough and efficient analysis of the dynamic processes involved in SSB degradation and will enable the high-resolution *operando* study of other promising SE materials.

4.4 PIP Cell Construction and Operation

The PEEK *in situ* Press (PIP) cell is a device that was developed for the formation of SE pellets within the operational SSB cell. In order to isolate degradation to the *operando* characterisation of interactions at the Li/SE interface, a symmetric Li| Li₆PS₅Cl |Li cell is chosen. The PIP cell

has in situ in the name because of the ability to observe the formation of the SE pellet under various temperatures and pressures. There are a wealth of cell designs to take inspiration from, some designed to optimize for diffraction/scattering studies 184,185, others to enable high temporal resolution X-ray imaging studies of conventional LIBs^{186–189}. The PIP cell focuses on providing a simplistic and versatile design to enhance the characterisation of SSBs at the various steps of its fabrication and cycling. While designing a cell for operando characterisations, several factors must be considered. First, the cell must be (electro)chemically inert with respect to the electrodes and electrolyte used. Additionally, the cell body needs to be of a lower density compared to the SE, so that it is less attenuating to X-rays, which optimizes X-ray imaging contrast and reduces artefacts. 190 Moreover, the cell diameter must be small to enable full-field (total volume) scans of the cell, while maintaining a sub-µm spatial resolution required to visualize pores/cracks in the SE. Finally, the cell body needs to have mechanical properties to withstand the pressure/temperature for pressing the SE pellet within, as well as strains that develop during cell cycling. This last factor is insignificant if the SE pellets are prepared and sintered prior to assembly into the cell; however, past studies⁸⁴ have shown that when the SE is reactive with air/moisture, the post-sintering assembly of the cell can introduce degradation in the cell prior to cycling; as exemplified in Figure 4.8A with a cracked uncycled pellet in a Swagelok cell. In this study, the Li₆PS₅Cl SE used is considered highly reactive, and therefore the SE powders are densified within the cell body (within an inert environment), avoiding exposure to air during the manufacturing to minimize pre-cycling degradation.

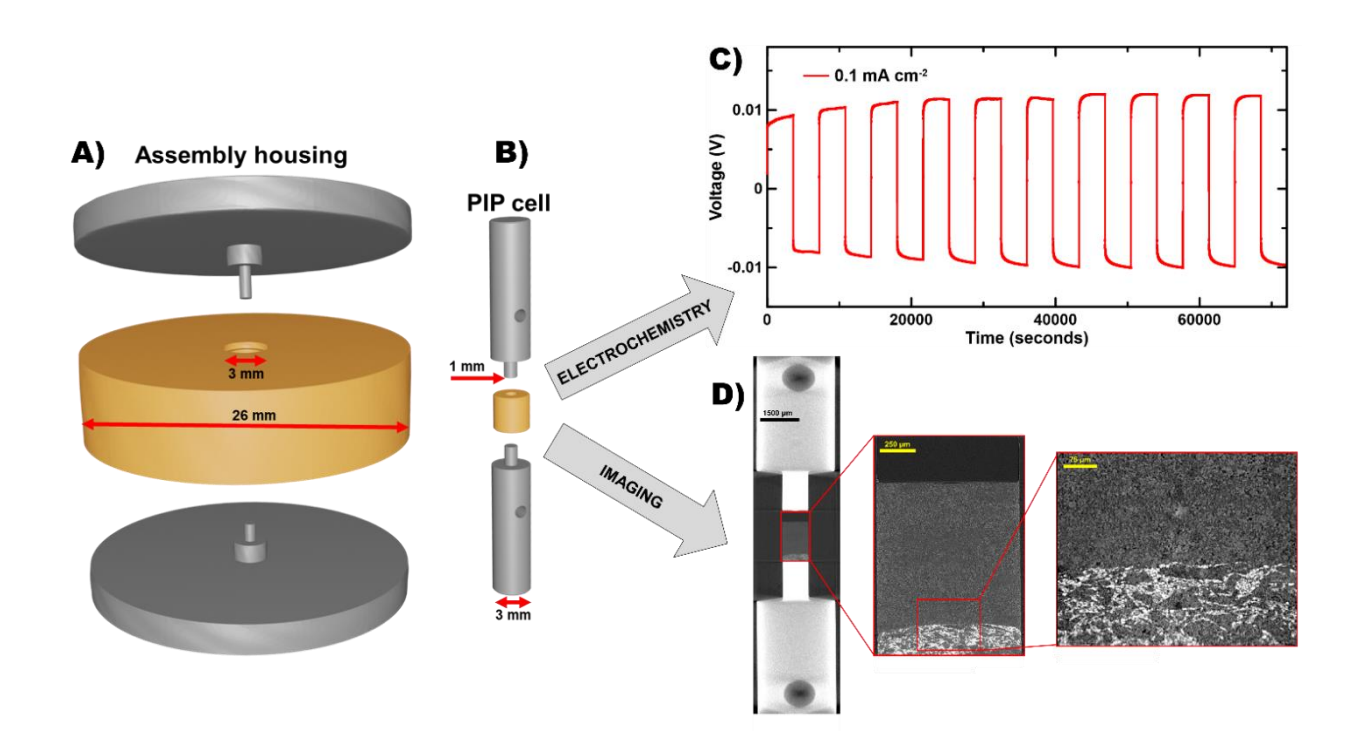


Figure 4.10 - Schematic representation of the 1 mm PIP cell and assembly housing. A) the assembly housing that holds the PIP cell for producing the SE pellet, B) the PIP cell which is used for operando imaging and electrochemistry, C) constant current cycling of a Li/Li symmetric cell at 0.1 mA cm⁻², and D) X-ray computed tomography (XCT) of the lithium manganese oxide (LMO)/Li₆PS₅Cl/Li solid-state full-cell at various resolutions.

Polyether ether ketone (PEEK) has been a popular choice of cell body for previous studies that require relatively low packing pressures and annealing temperatures^{63,74,191,192} as it has a tensile strength of ~95 GPa and a melting point of 343 °C,¹⁸² meaning it can withstand typical formation pressures for Li₆PS₅Cl SEs (around 300 to 400 MPa^{63,114,183}). After pellet formation, the entire PIP insert can be heated to temperatures up to ~250 °C to perform sintering of the pellet if required. The limitation of sintering temperature is introduced by the PEEK, which has a melting point of 343 °C but undergoes a glass transition at 143 °C, while maintaining a continuous service temperature (temperature for which mechanical properties are maintained) of 250 °C ¹⁹³. This thermal limitation indicates that pellets should not be formed at temperatures around 143 °C and thermal sintering should be limited to ~250 °C to avoid permanent deformation. PIP cells were produced with the internal diameters of 1 mm with an objective to

attain a high spatial resolution (\sim 2.4 µm in a lab-based source, \sim 750 nm with synchrotron radiation) while retaining the entire FOV of the SE. Though the design remains flexible and has been tested with internal diameters down to 350 µm, early results showed that fabrication using the 1 mm internal diameter cell was most reproducible.

In situ imaging of the sintering of the SE pellet was enabled by the use of a load frame, the Deben load stage which is designed for *in situ* imaging within the Versa lab XCT machine used. The specifications of the Deben load stage, discussed in Section 4.3, limited the maximum height of the PIP assembly to 15 mm. The SE pellet was filled inside a larger PEEK assembly housing, as shown in Figure 4.10A, which was designed to even the pressure distribution given by the plunger and reduce mechanical deformation of the SE prior to cycling. The fabrication process must occur in an Ar filled glove-box, and the assembly housing maintains this inert environment with the use of O-rings as the PIP cell is transferred into the load frame to be pressed at the required pressure/temperature, as illustrated in Figure 4.10A. Because the Deben load stage allows for imaging to be carried out during the compression process, the integrity of the cell body can be monitored and the user to study variations in fabrication conditions. As shown in Figure 4.11B, the cell can withstand pressures up to 637 MPa at room temperature without deforming significantly.

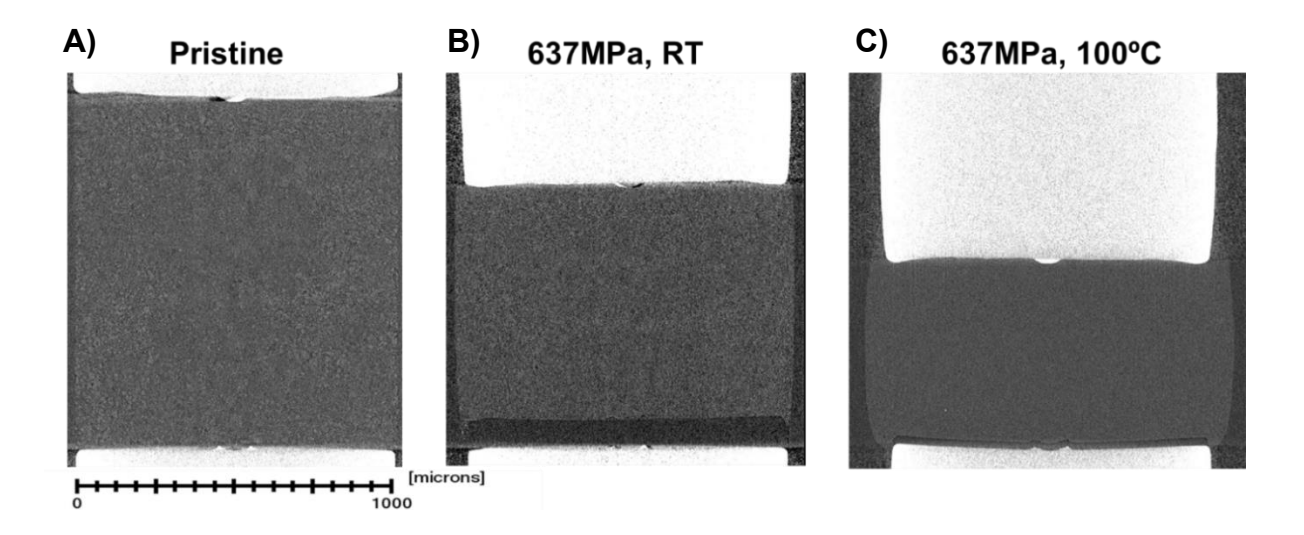


Figure 4.11 - In situ pellet formation in PIP cell with XCT, A) Pristine Li₆PS₅Cl before pellet formation, B) Li₆PS₅Cl pellet pressed to 637 MPa at room temperature without deforming significantly, and C) shows a hot pressed Li₆PS₅Cl pellet pressed to 637 MPa at 100 °C.

Due to PEEK's temperature resistance, hot pressing of pellets is also possible. Figure 4.11C shows an extreme case of 637 MPa at 100 °C, where the pellet appears to be very dense, but the fixture begins to deform. For assembly of the electrodes into the cell, care should be exercised during pressing to avoid cracking of the electrode/electrolyte, especially if the mechanical properties of the electrode and electrolyte are significantly different. For example, lithium is significantly more ductile than the ceramic Li₆PS₅Cl and therefore cannot be copressed with the electrolyte. Thus, after pressing the SE in the assembly housing, the 1 mm PIP cell insert was taken out, and the 1 mm diameter electrodes (Li foil) added. Subsequently, the stainless-steel or titanium current collectors were placed in the 1 mm holes to assemble a symmetric cell. Finally, after adding the electrodes and current collectors, the entire cell was sealed with Kapton tape and epoxy glue as an extra precaution to further limit air exposure. Note that as stated before, this cell design is not limited to symmetric cells but can also be used for full cells with a positive electrode, as shown in Figure 4.10D.

An important advantage of compacting/densifying the SE in the cell within the assembly housing, apart from reducing pre-cycling degradation and the investigation of various fabrication procedures, is the presence of internal pressure between the cell walls and the SE. While several past studies have elucidated the role of axial or "stack" pressure in maintaining conformal interfacial contact between the SE and the electrodes 90,194–197, the horizontal pressure on the SE can also play a role in determining the growth of cracks through the SE. 198 Horizontal pressure can aid in creating cracks that are more tortuous, rather than penetrating straight through the thickness of the SE pellet. Such tortuous cracking, in turn, has an important role in reducing the propensity for the filling of Li metal into the cracks 105, which then delays the eventual shorting of the cell. When the SE is pressed within the cell, such horizontal pressures exist between the cell wall and the SE, as opposed to a pre-pressed SE being assembled into the cell after being formed.

4.5 Electrochemical Degradation of the PIP Cell

After assembly, the PIP cell was cycled through alternate constant current plating and stripping steps, at increasing current densities. The formation pressure of the Li| Li₆PS₅Cl |Li cell was 382 MPa, with no active pressure applied during cycling. Initial cycling was conducted at 0.3 mA cm⁻² and ramped up to 9.0 mA cm⁻² over 88 cycles to expedite degradation. For context, a target of 3-4 mA cm⁻² has been reported to be practical for most automotive applications.⁴³

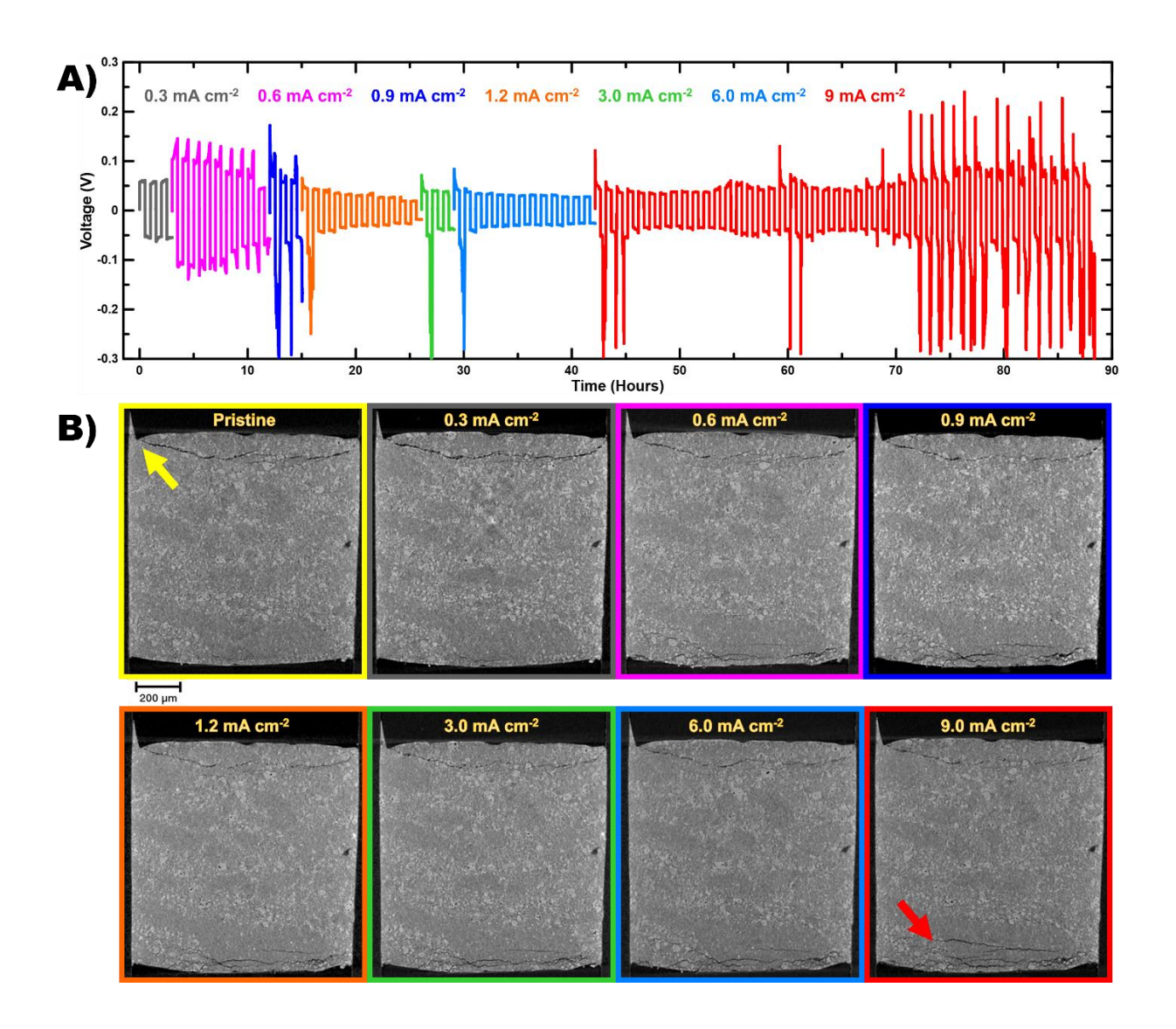


Figure 4.12 - Cycling and progression of mechanical degradation in the PIP cell. A) shows the voltage variation during constant current cycling over increasing current densities from 0.3 mA cm⁻² to 9 mA cm⁻². B) tracks a vertical orthoslice through the XCT volume of the SE pellet after cycling at the various rates. The colour coding reflects the various current densities at which the cell was cycled.

The cycling profile is shown in Figure 4.12A, with each current density colour coded for clarity and to match the corresponding XCT datasets acquired after each current density. The cycling was performed at constant currents from 0.3 mA cm⁻² to 9 mA cm⁻²; the voltage variation originates from the change in current magnitude, current direction, and changes in resistance. Interestingly, the centre of the cell in the pristine state shows some cracks present at the top of the SE, close to the interface with Li (highlighted with a yellow arrow in Figure 4.12B). This

defect appears to have been caused by a chip on the plunger of the PIP cell. The bottom surface, on the other hand, is relatively defect free at the length scale of observation.

Although a pre-deformed cell would not typically be considered a representative sample, the observation of defect formation during operation in this system highlights the importance of probing the full volume of degradation. Additionally, most cells would not have been fully characterised prior to cycling, and these pre-cycling defects are likely a significant contributor in cell-to-cell variation in performance, albeit often unnoticed. As observed in Figure 4.12B, the top, pre-cracked, portion of the cell seems relatively unchanged during the entirety of the experiment, while the bottom surface starts to increasingly develop cracks as cycling progresses. The formation of these cracks is highlighted by the red arrow in Figure 4.12B. This stark asymmetric degradation of a symmetric cell showcases the utility of scanning the entire volume in *operando*, as opposed to limited FOV characterisations. If observation was limited to only the bottom or top of this operational cell, the perceived findings would be completely different.

With the 3D nature of XCT, the entire volume can be considered and produce enhanced statistics as well showing how defects evolve in 3D space. Figure 4.13 shows the 3D rendering of the void structure (including both voids and cracks) by comparing the pristine state of the Li| Li₆PS₅Cl |Li cell (Figure 4.13A, left) against the final state after 88 cycles (Figure 4.13C, right). Note that only voids larger than 10 voxels (> 8 μm pixel size) were considered significant, smaller voids were considered as noise.

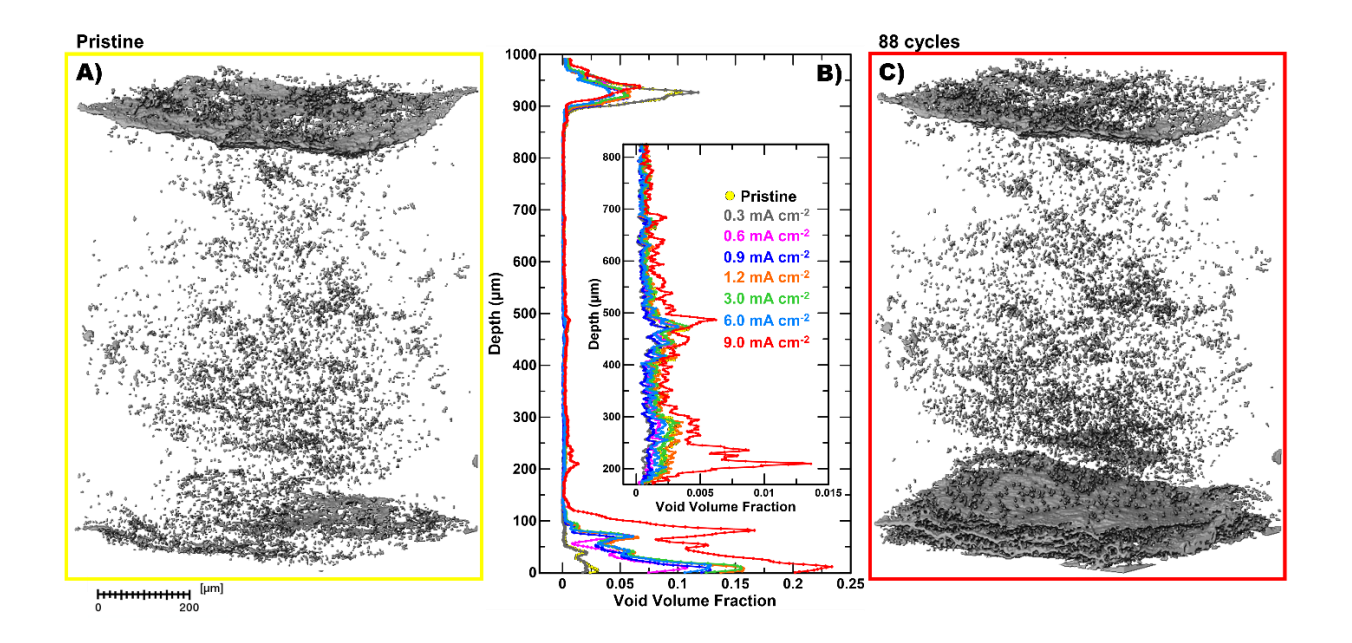


Figure 4.13 - Depth profiling of the Li₆PS₅Cl symmetric cells. A) shows the segmented volume of voids (including both voids and cracks) in the pristine Li| Li₆PS₅Cl |Li cell, C) shows the segmented volume of voids in the same cell after 88 cycles at various current densities, and B) shows the void fraction throughout the entire depth and volume of the Li₆PS₅Cl pellet, with the inset showing the central region in magnified detail. The colours indicate the various current densities of each step and are the same colours used in Figure 4.12.

It is noteworthy that the cracks formed at the bottom of the SE are in the form of planes perpendicular to the axial direction, as opposed to the commonly formed through-electrolyte cracks parallel to this axis. These horizontal cracks, or rifts, are not as detrimental to the cycling of the symmetric cell as the more axially puncturing cracks, which can cause short-circuiting. Comparing the pristine state to the cell after 88 cycles, an increase of misaligned void planes is observed towards the bottom of the SE, with slight increase of the initially observed voids near the centre. This is consistent with previous work, that shows that interfacial degradation is significantly larger than bulk degradation in SSBs^{84,199–201}.

For a more thorough quantification of the defects, the volume was analysed via profiling through the depth (Figure 4.13B and D, centre), where 0 and 1000 μ m represent the boundary of the Li electrodes. In this depth profile, we clearly see an increase in the volume fraction of

voids at the bottom interface through increased cycling, consistent with the formation of the large crack network there. The top crack is shown to slightly increase upon the first cycling period, then slightly reduce until the final 9 mA cm⁻² step. Through the rest of the SE depth, the void fraction shows a steady increase in volume, until the final current density of 9 mA cm⁻², most voids forming at the bottom edge. In Figure 4.13B, the larger spikes in void volume fraction originate in areas that had a higher void fraction to begin with, showing that defects are typically evolving from areas of preexisting heterogeneity. Figure 4.13B inset shows a magnification of the depth profiling to highlight voids that have nucleated at the current density of 9 mA cm⁻², evident from the peak around 200 µm depth that suddenly forms after the 9 mA cm⁻² cycling step.

Along with imaging the cell, the electrochemical impedance of the cell was also tracked throughout cycling. Intuitively, as the cell is cycled more, and at increasingly higher current densities, there appears the formation of more defects such as voids and cracks. However, as shown in Figure 4.14, the impedance of the cell continuously decreased with cycling, as the volume fraction of voids increased, from impedance around 25 k Ω decreasing to values below 2 k Ω over the course of cycling.

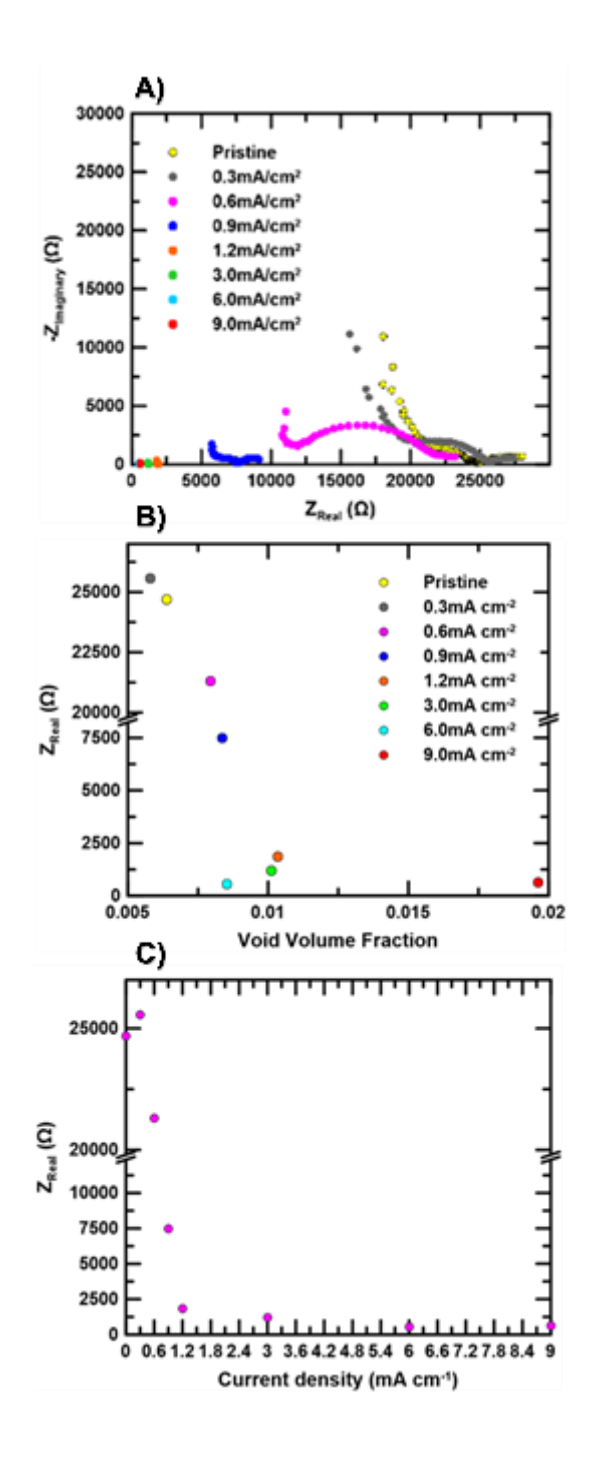


Figure 4.14 - Electrochemical impedance spectroscopy (EIS) of the symmetric Li| Li₆PS₅Cl |Li cell. A) Nyquist plots of the symmetric Li| Li₆PS₅Cl |Li cell after the various constant current cycling procedures, B) shows the real component of impedance (Z_{real}) vs the segmented void fraction of the cell after the various constant current cycling procedures, and C) shows Z_{real} vs the current densities used in the electrochemical testing. B) and C) depict the relationship between the R_{tot} and the defect formation and current density step respectively.

This can be explained by the creation of defects, especially close to the interface, which can be filled with Li metal which could decrease the overall impedance of the cell by increasing the

active surface area of the Li electrode or the lower contact resistance between the Li and SE. In the case of the symmetric cells used here, the cycling is largely unaffected by this Li deposition into defects, since the amount of Li available in the electrodes is significantly higher than the amount of Li being moved through the cell.

These observations also have significant implications for SSB cycling, since the final failure of a cell is caused by Li metal filling a crack through the entire thickness of the SE, which electronically shorts the cell. Here, the defects are more horizontal in nature, producing a more tortuous path for Li to travel through the SE depth. Thus, while pressing the SE into a pellet within the cell body is beneficial for minimizing the parasitic reaction with air/moisture by limiting SE pellet handling, it also seems to play an important role in extending the life cycle and current capability of the SSB by favouring crack formation perpendicular to the direction of Li transport in the SE.

4.6 Conclusions

Here, a bespoke SSB cell designed for *operando* X-ray imaging and tomography was explored. The PEEK *in situ* Press (PIP) cell is a device that enables unprecedented spatial and temporal resolution during *operando* XCT experiments. It was developed for the formation of SE pellets within an operational SSB cell, simplifying the fabrication to reduce the impact of pre-cycling degradation. The PIP cell operates with a SE pellet of 1 mm diameter, providing a spatial resolution of about 2.4 μm on a lab-based XCT experiments or 750 nm utilising synchrotron radiation sources, both over the entire volume of the sample. The PIP cell enables investigation into the earliest stages of defect nucleation while providing a more representative view of degradation throughout the whole SSB. Li| Li₆PS₅Cl |Li symmetric cells were probed during various constant current cycling protocols and the degradation of the SE showed through-

thickness spatial variation that highlights the importance of full volume characterisation. The PIP cell's simple and transferable design allows it to explore various cell chemistries and geometries, even stemming to fields such as geology and pharmacology in the study of powder compaction.

5 Correlated Diffraction Resolved and X-ray Computed

Tomography

5.1 Aim

In the previous chapter, a total-volume approach for monitoring the mechanical degradation modalities in SSBs was explored, here the goal will be to increase the amount of information gathered by introducing another non-destructive characterization technique; X-ray diffraction computed tomography (XRD-CT). As discussed previously, the novel degradation mechanisms in SSBs exist as both mechanical and chemical/electrochemical pathways, both producing heterogeneous deformation fields. Therefore, understanding these deformations requires a multimodal characterization approach sensitive to morphological degradation along with a mapping of the chemical environment present. Correlated XCT and XRD-CT imaging provides a non-destructive method to track propagation of cracks and voids while gathering phase information of the various chemical species within the SSB. Collecting a 3D volume of the structure and a 3D volume of diffraction patterns gives a wealth of information about the SSB during operation. Aside from the chemical information gathered with XRD-CT, there is also the ability to map strain fields by analyzing the deformation of the calculated lattice parameter. Providing this chemical and strain information will aid in deconvoluting the effects of SE manufacturing, cell assembly, and electrochemical deterioration to help better understand the factors that lead to SSB failure so that it can be avoided in future production.

5.2 Ex situ Cell Shorting

A majority of this section has been previously published as J. Hu, R. S. Young, B. Lukic, L. Broche, R. Jervis, P. R. Shearing, M. Di Michiel, P. J. Withers, A. Rettie, P. P. Paul, Quantifying Heterogeneous Degradation Pathways and Deformation Fields in Solid-State

Batteries. Adv. Energy Mater. 2024, 2404231. J. Hu and R. S. Young did a majority of the experimental work and data processing together, with J. Hu conducting a majority of the XRD refinements and reconstructions while R. S. Young conducted a majority of the morphology focused data processing and cell manufacturing.

Two Li| Li₆PS₅Cl |Li cell symmetric cells were used for this correlated XRD-CT study. One cell was scanned in the pristine, as-assembled state (referred to as the pristine cell), while the second cell was cycled to failure (referred to as the shorted cell). The Li₆PS₅Cl pellets were pre-assembled and placed into Swagelok type cells as discussed in Section 3.3.2. The Li₆PS₅Cl pellets were produced using a 3 mm diameter stainless steel die (MSE Supplies) where a uniaxial pressure of 280 MPa was applied via a hydraulic press (MTI, YLJ-15L) to compact about 6 mg of powder. The formed pellets were subsequently wrapped in carbon paper (AvCarb P50, Fuel Cell Store) and placed in an alumina crucible (Almath) before a 15 min annealing step at 300 °C under vacuum in a Buchi oven to densify the electrolyte pellets further. The shorted cell was cycled without additional stack pressure, at room temperature, with a current density of 0.3 mA cm⁻². Alternate plating and stripping of Li was performed before the cell electrically shorted after ~12 h.

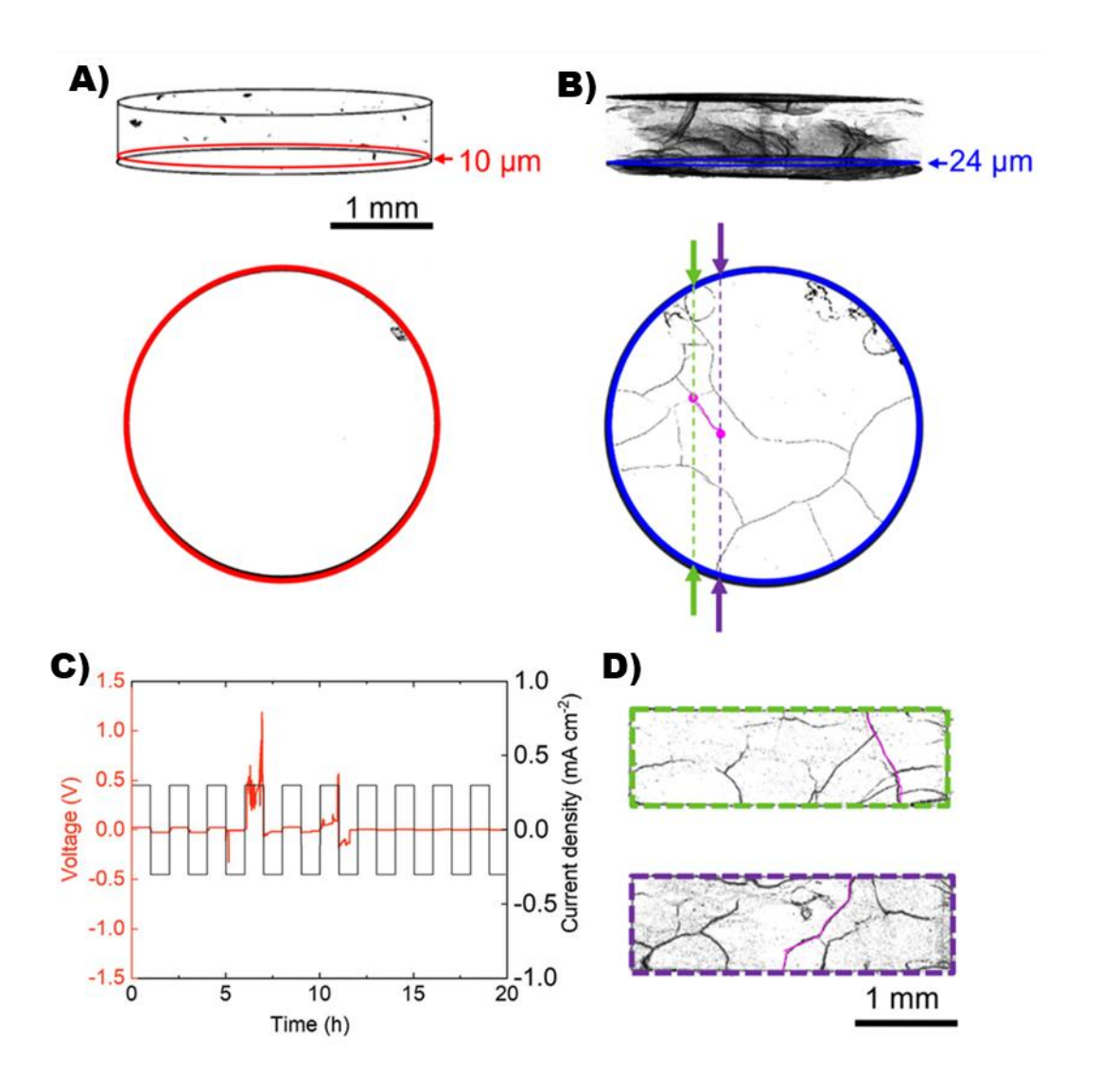


Figure 5.1 - Ex situ XCT analysis. Morphology of a 3 mm diameter Li_6PS_5Cl pellet is shown in A) the pristine state of a Li | Li_6PS_5Cl | Li symmetric cell verses B) the post cycling shorted state. C) displays the constant current cycling at 0.3 mA cm⁻² and the corresponding voltage response of the cycled cell shown in B). Further mechanical degradation in the cycled cell is shown in D). The slices of D) are highlighted in green and purple which show their position within the pellet within B). A large crack that spans the full thickness is highlighted in magenta.

Similar to the previous chapter, Figure 5.1 shows the morphology of the pristine cell compared to a cell that was cycled to failure (the shorted cell). The pristine cell appears largely uniform, with very few voids while the shorted cell displays numerous cracks. Many of these cracks span the diameter of the cell as shown in Figure 5.1B and some cracks penetrate the entire thickness of the SE pellet, such as the magenta highlighted crack in Figure 5.1D. Short

circuiting of the cell likely occurred through one or more of these pathways. The exact physical path for electrical shorting of the cell is unclear because the Li metal is not visible, so all cracks extending the height of the SE pellet are equally likely sites for this failure event. It is important to note that the cracks shown here do not represent all such features across length scales present in the SE; only features above \sim 5 μ m could be reliably segmented due to the voxel size of 0.7 μ m. The difference in morphological degradation between the pristine cell and shorted cell are clearly visible. However, additional data from XRD-CT will hopefully provide further insight into the mechanisms behind this degradation.

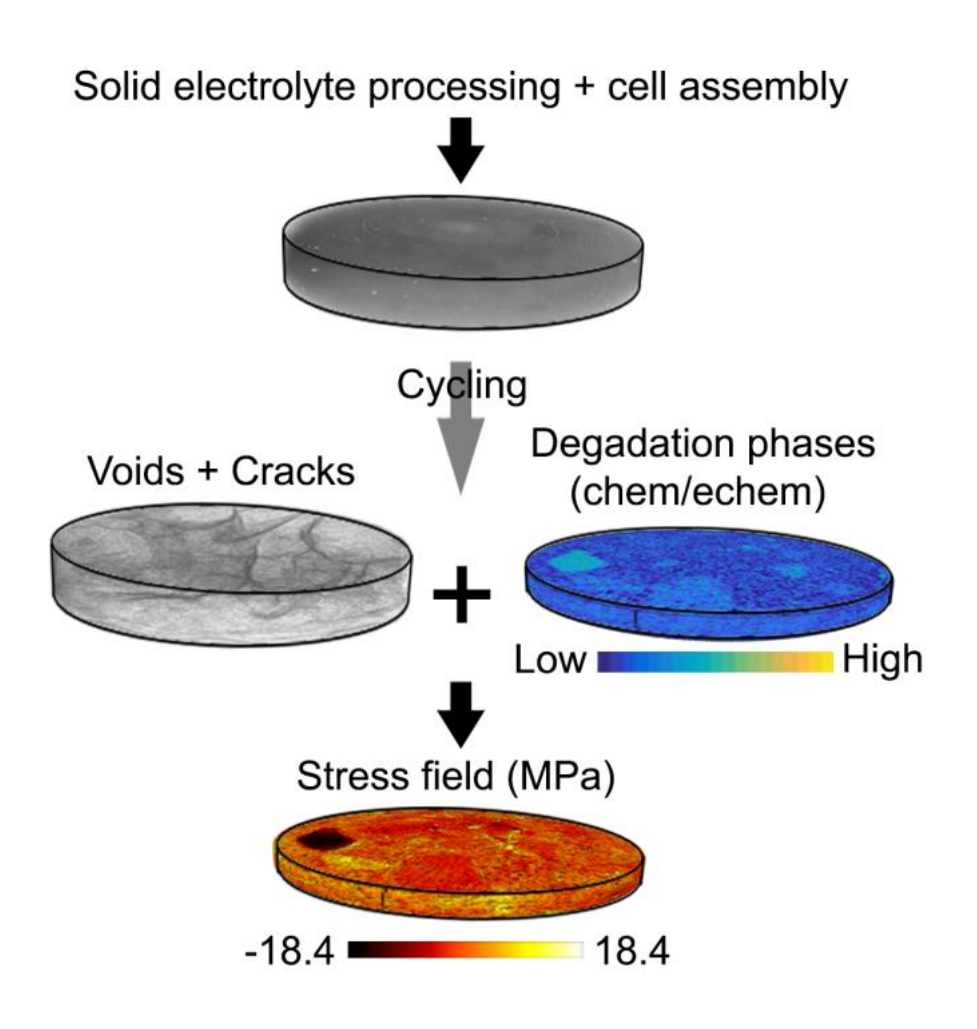


Figure 5.2 - XCT and XRD-CT correlation flow to display the various datasets available and how to they can be visualized.

The workflow of a correlated XRD-CT and XCT study is highlighted in Figure 5.2. In the correlated XCT and XRD-CT study, the pristine volume is first scanned to obtain a baseline. After the electrochemical testing is done, or during if one can achieve high enough temporal resolution, the post-cycled volume can be scanned. XRD-CT will provide volumes of both the chemical composition and of the strain that can be paired together to look for correlations that may better explain the phenomena observed during electrochemical testing.

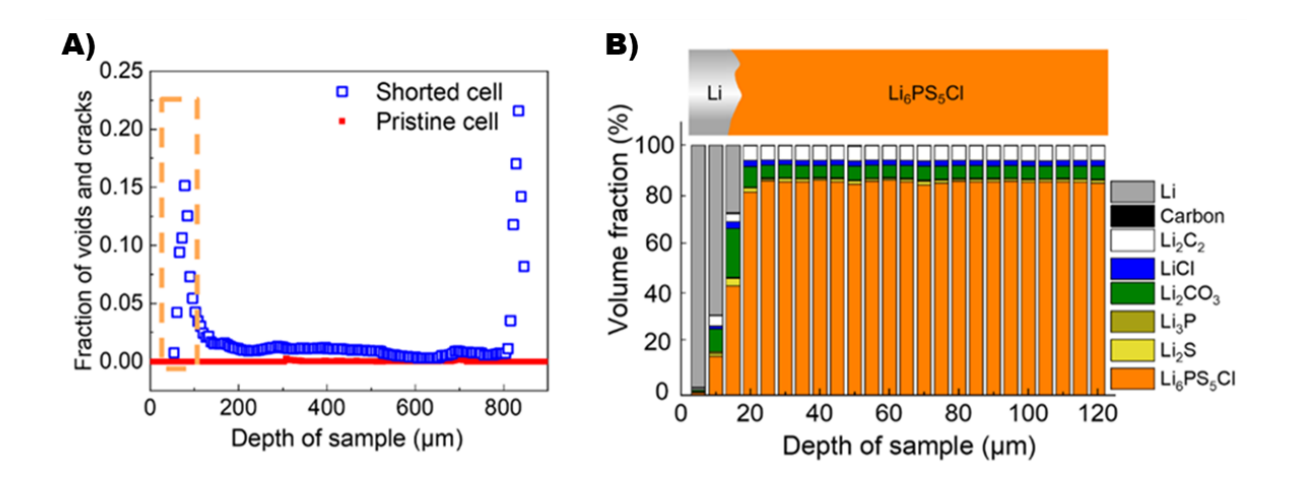


Figure 5.3 - Depth-resolved degradation analysis at the Li/Li₆PS₅Cl interfaces. A) shows the fraction of defects in the pristine and shorted cells as a function of depth from the Li metal interface (0 µm). B) shows the phase segmentation of the shorted cell as a function of depth showcasing the various compositions found at the interface and their respective volume fractions. The dashed orange box represents the depth being shown in B) for perspective.

Since data is gathered throughout the volume of the SE, profiling the depth for voids and defects is possible as shown in Figure 5.3A. Figure 5.3A shows the fraction of cracks and voids as a function of depth from the Li metal interface for both the pristine (in red) and the shorted cell (in blue). The lack of fluctuation in the pristine is representative of a well formed, minimal defect SE pellet. The shorted cell has a significantly larger fraction of cracks and voids near Li/Li₆PS₅Cl interfaces (>20%), compared to the SE bulk (~1-2%). XRD-CT was collected in the volume near the Li/Li₆PS₅Cl interface, in the volume highlighted by the orange dash in

Figure 5.3A. The XRD-CT results, shown in Figure 5.3B, are plotted here as the volume fraction of various phases verses depth in the sample relative to the Li metal interface.

Figure 5.3B shows the phase fractions of the SE, and various degradation products as a function of the distance from the Li/Li₆PS₅Cl interface. These fractions were obtained by averaging the phase fractions for every phase over the entire cross-section at each depth of XRD-CT measurement. Close to the interface, a decrease in the volume fraction of Li₆PS₅Cl is observed, coinciding with an increase in many minor phase fractions. The amount of Li was obtained by segmentation of the XCT slices corresponding to the appropriate XRD-CT slice, because quantification of Li using the XRD signal was challenging. Some phases of interest include Li₂CO₃, LiCl, Li₃C₂, Li₃P and Li₂S, believed to be a combination of air exposure and/or decomposition products. LiCl and Li₂S show a noticeable increase close to the interface, though not as pronounced as Li₂CO₃. There are also phases believed to be from the annealing step during heat treatment (Li₂C₂ and graphite). The Li₃P and Li₂S are considered as the electrochemical degradation products expected from Li₆PS₅Cl in contact with Li.⁸⁶ The reaction of the SE with Li metal appears greatest at the interface, thereby forming various characteristic reaction products. Additionally, air exposure (from cell manufacturing or leakage) occurs over time and areas with a higher concentration of cracks, such as the outer surface of the pellet or the Li/Li₆PS₅Cl interface, giving these areas a higher potential for reaction with air to form Li₂CO₃.

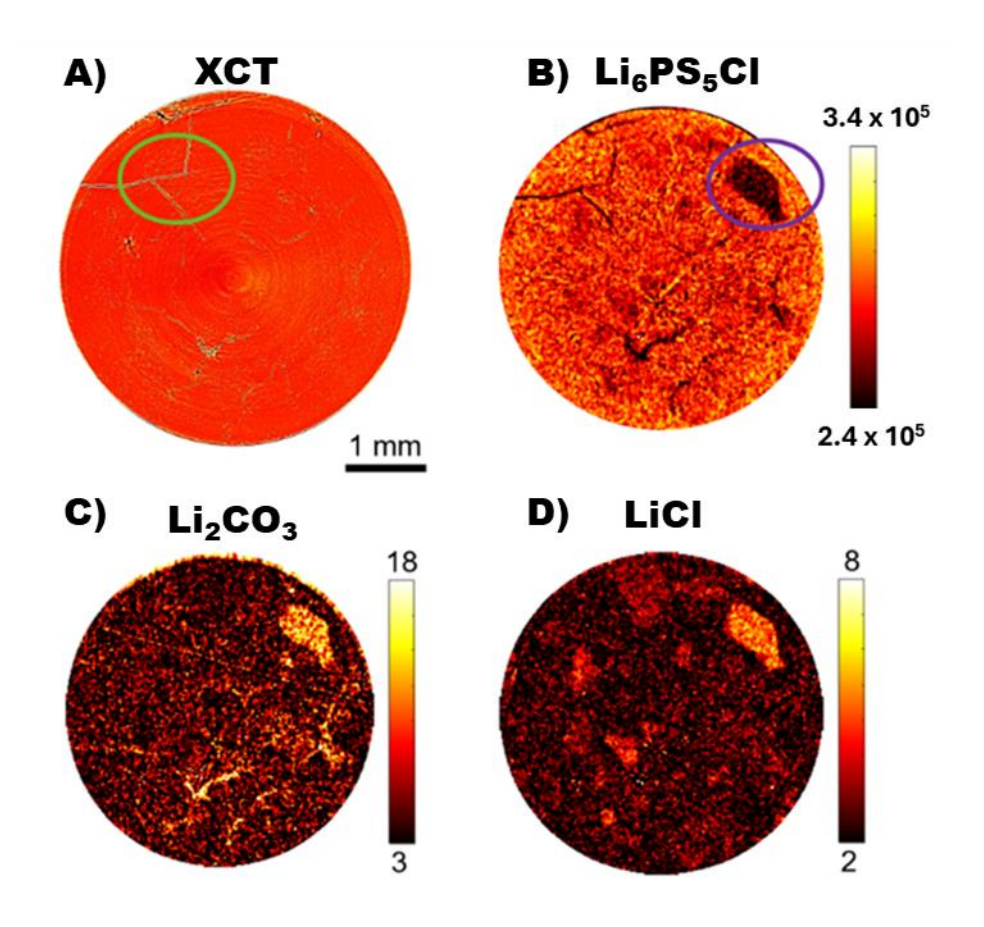


Figure 5.4 – XCT and XRD-CT comparison within the Li| Li₆PS₅Cl |Li symmetric cell. A) shows an XCT slice through the Li₆PS₅Cl pellet highlighting some cracks in the green circle. B) shows the XRD-CT reconstruction at the same slice as A) with intensities focused on the Li₆PS₅Cl peak, the colorbar here is in arbitrary units and proportional to the volume of the material. A noticeable void of Li₆PS₅Cl is highlighted with a purple circle in B). C) and D) are the same slice XRD-CT but focused on the peaks of Li₂CO₃, and LiCl respectively. The colorbars in C) and D) denote the volume % of that phase within the XRD-CT reconstruction.

Figure 5.4 shows a representative XCT slice of the shorted cell and the corresponding XRD-CT phase maps for a cross-section 120 μm from the Li/Li₆PS₅Cl interface. Several cracks are present in the XCT of Figure 5.4A (circled in green) which help correlate to the cracks in the Li₆PS₅Cl phase map of Figure 5.4B. Also, in the Li₆PS₅Cl phase map of Figure 5.4B is a region with a relatively low amount of Li₆PS₅Cl (circled in purple). However, it is evident by comparison with the XCT slice that this region has a density similar to Li₆PS₅Cl and is therefore not a void. Other XRD-CT phase maps (Figure 5.4C and D) show this region to be rich in

Li₂CO₃ and LiCl. LiCl is a commonly used precursor for synthesising Li₆PS₅Cl, with indicates pockets of unreacted precursor material within the SE pellet, unobserved by XCT alone.⁷⁵ Therefore, this low Li₆PS₅Cl volume fraction region is likely from unreacted precursor materials which are also extremely air sensitive and can react with small amounts of CO₂ to form Li₂CO₃. Additionally, LiCl could also be a product resulting from air exposure of the SE pellet.⁸⁶

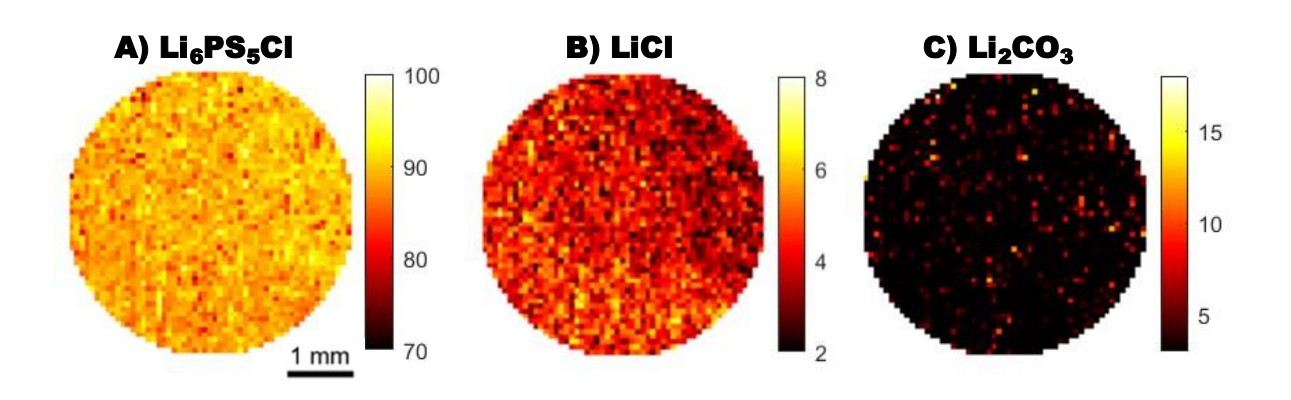


Figure 5.5 - XRD-CT reconstructions of pristine Li| Li₆PS₅Cl |Li symmetric cell. A) XRD-CT slice with intensities focused on the Li₆PS₅Cl peak, B) and C) show the same XRD-CT slice focused on the peaks of LiCl and Li₂CO₃ respectively. Colorbars denote the volume % of each phase within the reconstruction.

When comparing the shorted cell in Figure 5.4 to a pristine cell of the same composition, a better understanding of what phases originate during cycling can be discerned. The XRD-CT reconstructions in Figure 5.5 show a slice through a pristine Li| Li₆PS₅Cl |Li cell symmetric cell, focusing on the Li₆PS₅Cl, LiCl, and Li₂CO₃ phases in Figure 5.5A-C respectively. The key difference in the pristine dataset is that there is a lack of defects/features, similarly to the XCT dataset. The reconstructions in Figure 5.5 appear more homogenous than the shorted cell in Figure 5.4 which had more localized signal of LiCl and Li₂CO₃ phases.

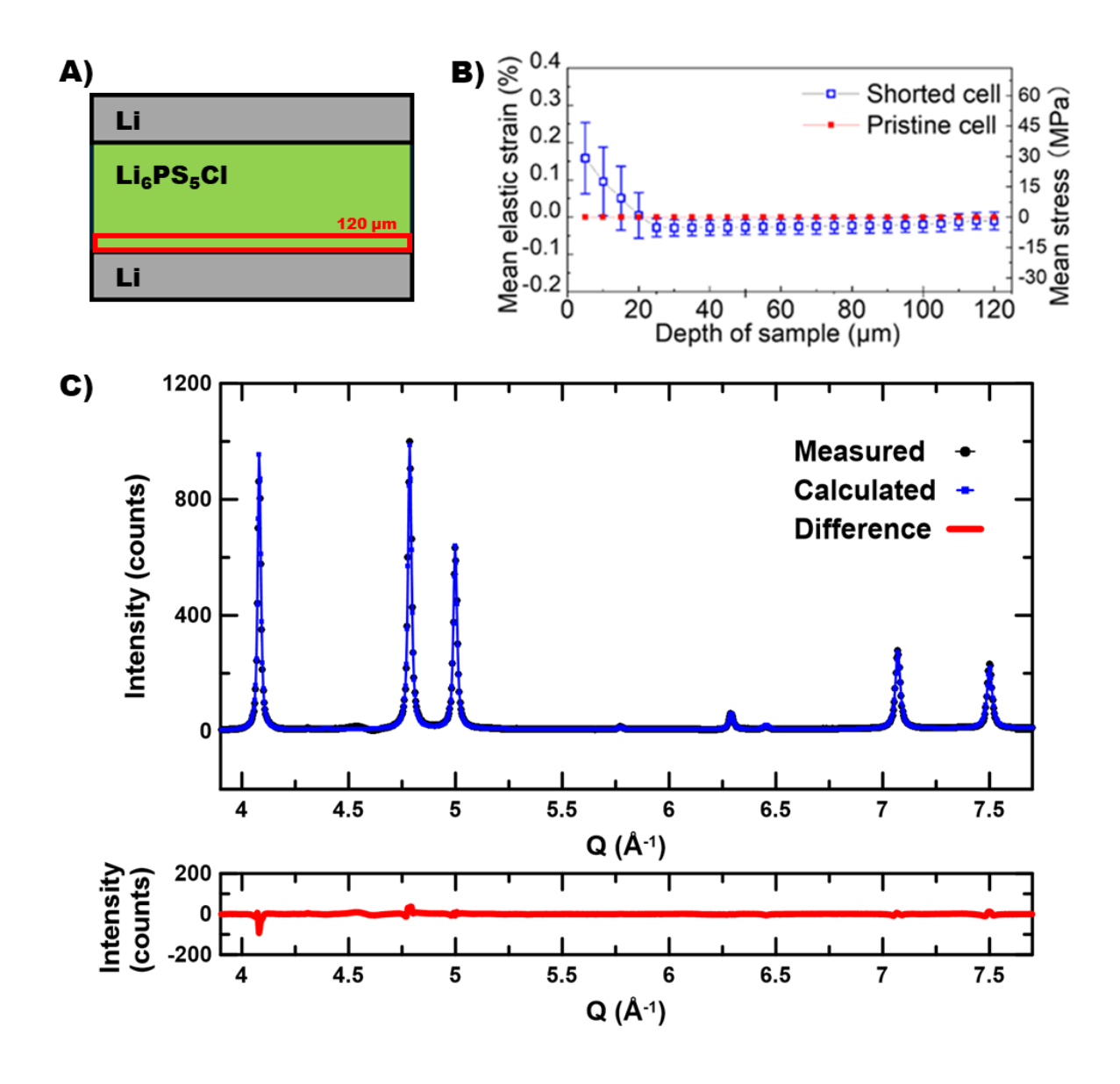


Figure 5.6 - Example of the quantification of strain. A) shows the depth of which the XRD-CT data was acquired relative to the Li_6PS_5Cl pellet, B) shows the resultant elastic strain and stress in Li_6PS_5Cl due to the degradation of the Li/Li_6PS_5Cl interface, and C) shows an example of a produced XRD pattern and the resulting fit from refinement.

XRD-CT also permits the calculation of 3D volumetric strain, by tracking the change in unit cell volume of any phase identified in XRD. Therefore, the strain across the cross-section and through the depth of the SE pellet was also measured as shown in Figure 5.6B. The change in the unit cell volume of Li₆PS₅Cl at each voxel was monitored within the region highlighted in Figure 5.6A and compared to the mean unit cell volume of Li₆PS₅Cl in the bulk of the pellet to calculate the volumetric strain as shown in Equation 8.

$$\varepsilon = \frac{a_{Li_6PS_5Cl}^3 - a_{mean}^3}{a_{mean}^3} \qquad (8)$$

where, *a* represents the lattice parameter of Li₆PS₅Cl at every voxel obtained from XRD refinement (an example given in Figure 5.6C), and *a*_{mean} stands for the reference lattice parameter. This volumetric strain was then converted into the volumetric stress using the bulk modulus (K) of Li₆PS₅Cl. Elastic volumetric strain was measured using the Li₆PS₅Cl phase, chosen for its dominant and intense XRD peaks, though similar calculations can be performed for other phases. The mean unit cell values were determined for each cross-sectional area using a weighted mean to account for variations in Li₆PS₅Cl distribution. In the shorted cell, the bulk SE was assumed to be stress-free. To determine the reference unit cell volume of Li₆PS₅Cl, regions beyond 15 μm from the interface were used, as mean values remained stable (<0.1% variation) at these distances, representing the bulk. This method estimates the equivalent isotropic volumetric strain, providing an isotropic approximation of the 3D stress, though actual stress distribution is not perfectly isotropic.

The Li/Li₆PS₅Cl interface has been shown here to exhibit significantly greater morphological, chemical, and electrochemical degradation than the bulk SE. In Figure 5.6B, the pristine cell (red dotted line) stress remained near zero at all depths; consistent with minimal cracking and limited chemical reactions. In contrast, the shorted cell (blue dotted line) exhibited a small negative mean stress until reaching the interface, where both the mean and variance increased sharply, with the mean stress becoming positive. The greater stress variation near the interface indicates a more heterogeneous stress field, likely due to a higher concentration of defects, stronger heterogeneities around individual degradation sites, or both. For the pristine cell, XRD-CT was not performed for the entire volume because XCT did not reveal significant

degradation at the $\sim \! 10~\mu m$ length scale of XRD-CT. Instead, the phase fraction and strain for the pristine cell were calculated from the average of sub-volumes located at approximately 10 μm and 100 μm from the Li/Li₆PS₅Cl interface.

Converting the volumetric strain into the equivalent stress using the bulk modulus of Li_6PS_5Cl (18.4 GPa)²⁰², the mean value of stress closest to 0 μ m is ~30 MPa which is more than an order of magnitude larger than the yield stress for macroscopic Li (~1 MPa)^{203,204}. The range of strain at a depth of 15 μ m, adjacent to the Li electrode, is between -0.04% to about +0.15%, which is within same range reported by Ning et al.⁹⁰ Thus, at the interface, the degradation results in a mechanical stress field sufficient to push metallic Li into any cracks that have formed at that interface. Around deformation sites, this value is even higher, as evidenced by the large variation in the stress. It is also important to note that the elastic limit of Li is size dependent²⁰⁵ as well as temperature and stress-rate dependent²⁰⁶, with values over a couple of orders of magnitude being reported.

As observed with correlated XCT and XRD-CT measurements, several factors contribute to high deformation (stress). These include cycling, air exposure during cell assembly, and SE processing. Swagelok-style cells are commonly used for studying air-sensitive materials and electrochemical devices. When assembled in an inert-gas glovebox, degradation is often attributed solely to cycling. However, XRD-CT analysis reveals that both SE processing and cell assembly have an influence on how SSBs degrade; highlighting that material processing and assembly conditions can substantially impact cell behaviour.

In the case of Chapter 4, the PIP cell showed much higher resistance to electrochemical shorting and was able to cycle for 88 cycles, up to 9.0 mA cm⁻² without shorting. Both cells were made with the same commercial Li₆PS₅Cl material, just with different pellet formation procedures

and cell designs. In the next section, the influence of the PIP cell design on the performance of Li| Li₆PS₅Cl |Li cell symmetric cells is explored using XRD-CT.

5.3 Stresses Generated in the PIP Cell

The total volume XCT of the PIP cell in the previous chapter demonstrated that horizontal cracks in the cell over repeated cycling and increased current densities do not immediately short the cell but instead decreased the impedance with subsequent cycling. Cell failure via an internal short occurs when an axial crack penetrates entire thickness of the SE pellet, allowing electrical contact of the electrodes via Li filaments. Mechanically, two conditions must be met for cell failure to occur:

- (i) There must be an axial crack that extends through the SE pellet thickness.
- (ii) The stresses generated around such a crack must be high enough to push metallic Li into the crack, forming an electronically conductive pathway for short circuiting the cell.

In the case of the PIP cell, we see that condition (i) has not been met, due to cracks that develop during cycling largely being horizontal. This is in contrast to larger diameter cells preassembled in Section 5.2 (pressed into a 3 mm die) using the same raw materials and cell configuration (Li| Li₆PS₅Cl |Li), where numerous cracks were seen throughout the SE volume, but more importantly, 'critical cracks' through the SE thickness which caused cell failure in 5 cycles at a current density of 0.3 mA cm⁻².⁸⁴

While a smaller cell is best suited for full-volume *operando* characterisation, it needs to be balanced against the challenges of having an electrochemically functioning SSB such as reactivity at the Li/SE interface, the evolution of cracks/voids, and maintaining interfacial contact between the SE and Li metal. Further investigation on the effects of the geometry of

the PIP cell via X-ray diffraction computed tomography (XRD-CT) and finite element analysis (FEA) explore the role of internal stresses generated within the PIP cell in influencing the electrochemical behaviour throughout cycling.

The XRD-CT scan was carried out at beamline ID15A of ESRF, the European Synchrotron. A monochromatic microfocused X-ray beam at 72.5 keV energy and a spot size of 10 μm x 5 μm was used to illuminate the samples. A Pilatus3 X CdTe 2M area detector (Dectris) is used to collect the 2D XRD patterns. Azimuthal integration was broken into two segments (as shown in Figure 5.7), taken here as horizontal (parallel with electrodes) and axial (perpendicular to electrodes) from [15°:345°] plus [165°:195°] and [75°:105°] plus [255°:285°] respectively.

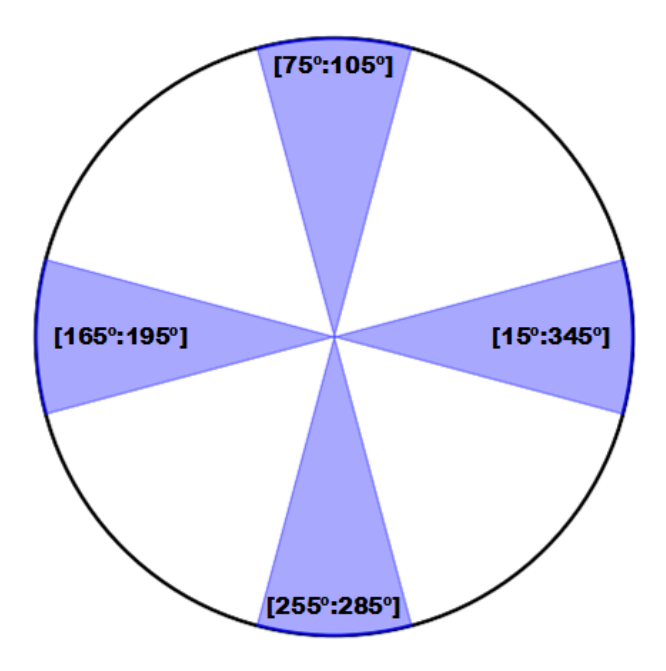


Figure 5.7 - Segmentation of azimuthal integration for the horizontal and axial reconstructions.

The integrations of the horizontal and axial components were conducted using pyFai. Here the horizontal component is taken as the convolution of the radial and angular strains which are non-invariant to the rotations about the tomographic axis while axial is separate and invariant.

Tomographic reconstruction was performed using an in-house Matlab script to transform the data into Cartesian space through a filtered back projection method. Strain analysis and plotting were performed with TOPAS-7, utilising Rietveld refinement at each voxel. Figure 5.8A provides a visual representation of the core, middle, and edge binning of the Li₆PS₅Cl pellet.

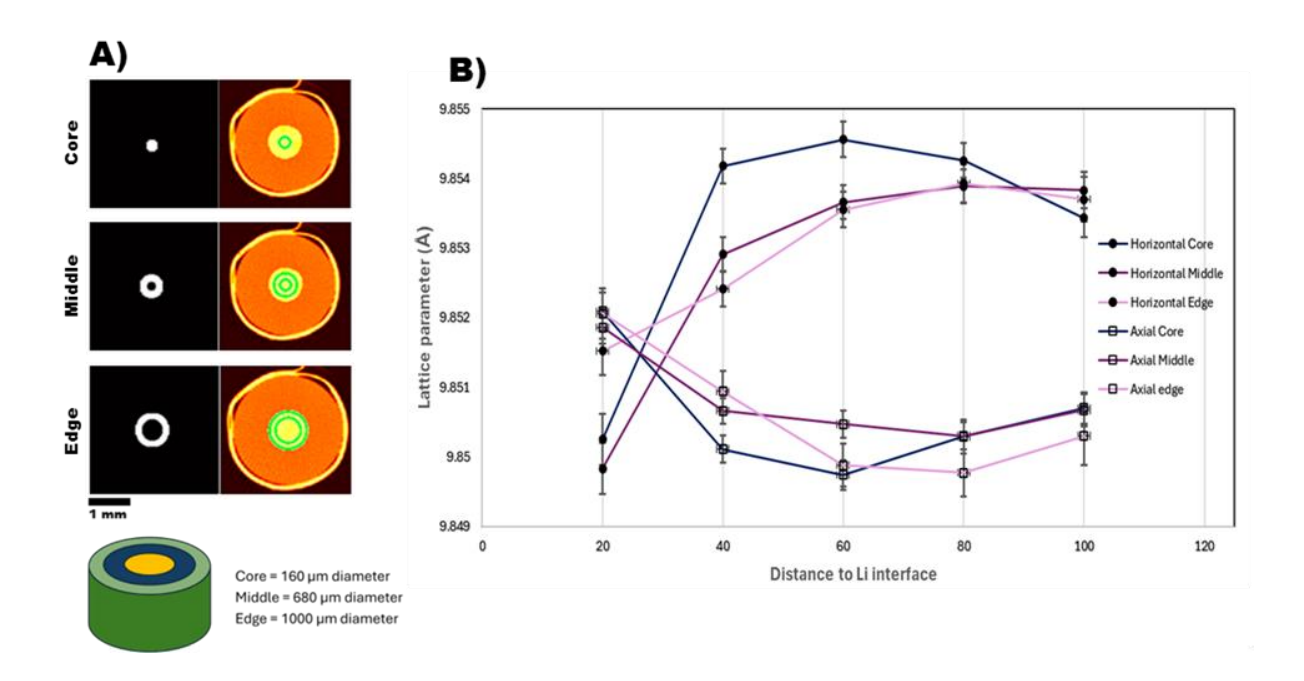


Figure 5.8 - XRD-CT analysis and tracking of lattice parameter in 100 μ m depth from the Li interface. A) Visualization of core, middle, and edge of pellet volume used for XRD binning, B) lattice parameter of Li₆PS₅Cl and error broken into horizontal and axial components through a 100 μ m depth from the Li interface.

Figure 5.8B also provides the tracking of lattice parameter through the $100 \, \mu m$ depth from the Li interface with associated errors and an example of XRD fitting in TOPAS-7 can be found in Figure 5.6C.

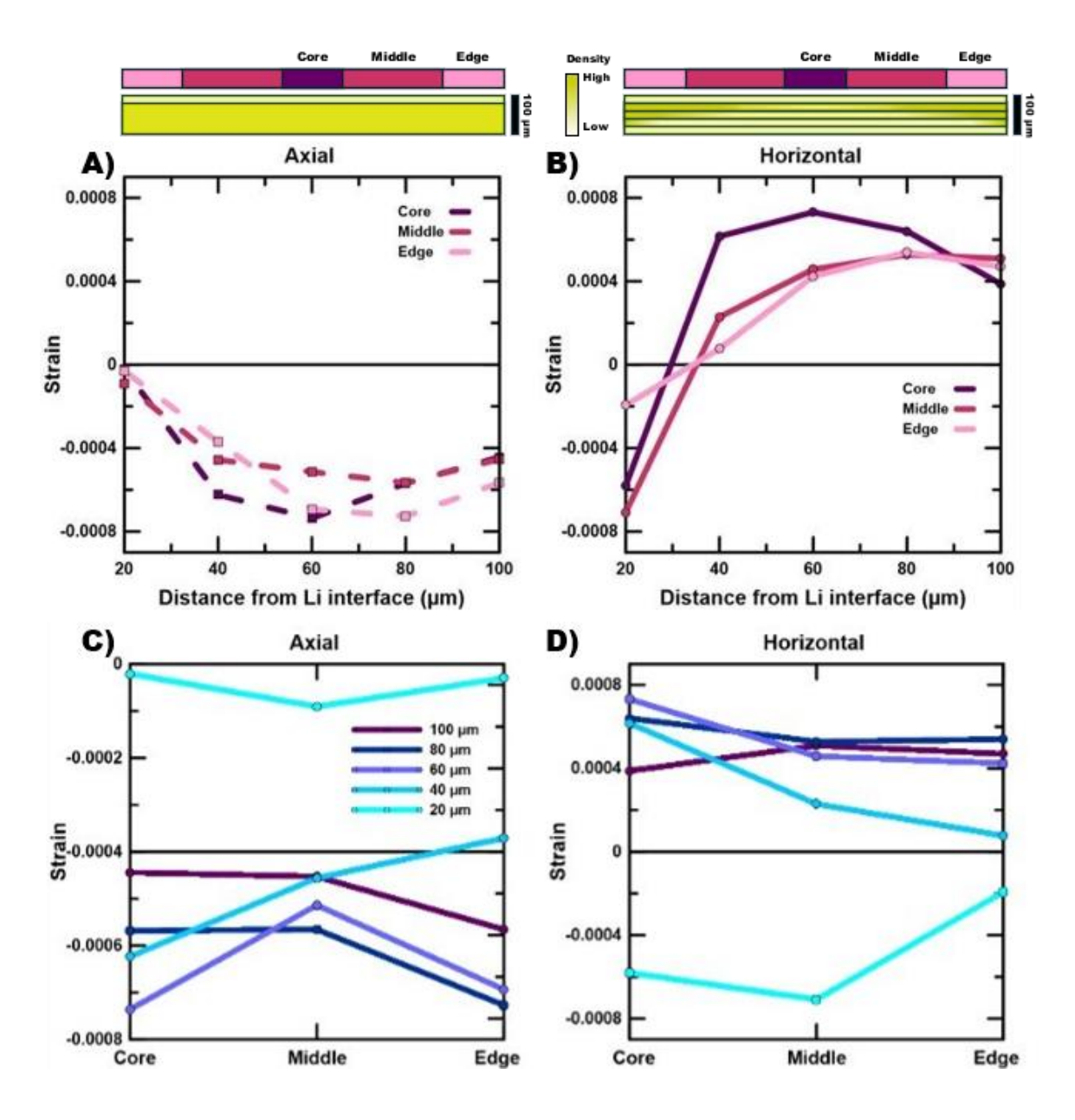


Figure 5.9 - Residual strain in a sub-volume of the pristine Li| Li_6PS_5Cl |Li cell as calculated via XRD-CT. A) shows the areas the volume was segmented and the strain broken into horizontal (circles, solid lines) and axial components (squares, dashed lines) and from sampling the core (purple), middle (red) and edge (pink) zones of the pellet in concentric circles. B) shows the horizontal and axial components plotted as strain verse binned volume where each line represents a depth.

To investigate residual strain that is maintained in the material after cell assembly, XRD-CT data was utilized from the pristine Li| Li₆PS₅Cl |Li cell. Figure 5.9 shows the strain of the pellet in a depth of 100 μ m from an interface with Li, separated in the horizontal and axial directions by segmenting the azimuthal integration into two perpendicular segments as described in

Figure 5.7. The elastic strain was calculated by dividing the measured the unit cell volume in this experiment by that of a strain-free SE pellet ^{148,149}. Hu et al. used the same source of precursor materials of Li₆PS₅Cl, assembled into a standard Swagelok cell, which yielded a mean unit cell volume of 956.3 Å³ in an unstressed state⁸⁴. Interestingly, most of the fluctuation in strain is seen 20 μm from the Li interface, where both axial and horizontal components showed compressive strain. Deeper into the pellet, the unit cell volume is at a compressive strain in the axial direction, while it is primarily in a tensile state in the horizontal direction. However, when looking at the axial data in Figure 5.9A, 20 μm from the Li interface seems to be an outlier in an otherwise similarly strained pellet. During the pellet making process it is reasonable to believe that the area closest to the interface may relax, from processes such as plunger removal. If 20 μm is then considered an outlier, the trend in the horizontal data is much clearer.

In Figure 5.9B horizontal data, the bulk is under tension, however, the areas closest to the interface and closest to the edge are in a more compressed state (still until tension relative to the strain-free). These trends are also shown in Figure 5.9C and Figure 5.9D, suggesting that there is a force in the horizontal direction, effecting more the edge, which is compressing the Li₆PS₅Cl lattice. It seems likely that the stress imposed on the pellet during formation are at least partially retained in the material when assessed with XRD-CT after the pressing process. Note that other studies performed a pellet formation within the SSB cell when characterising SE materials and will experience a similar phenomenon^{63,114}. Figure 5.10A shows the FEA results of Li₆PS₅Cl pellet formation within a 1 mm PIP cell, showing significant stress at the top of the pellet and the stress contours generated from the transmission of the force throughout the volume of the SE.

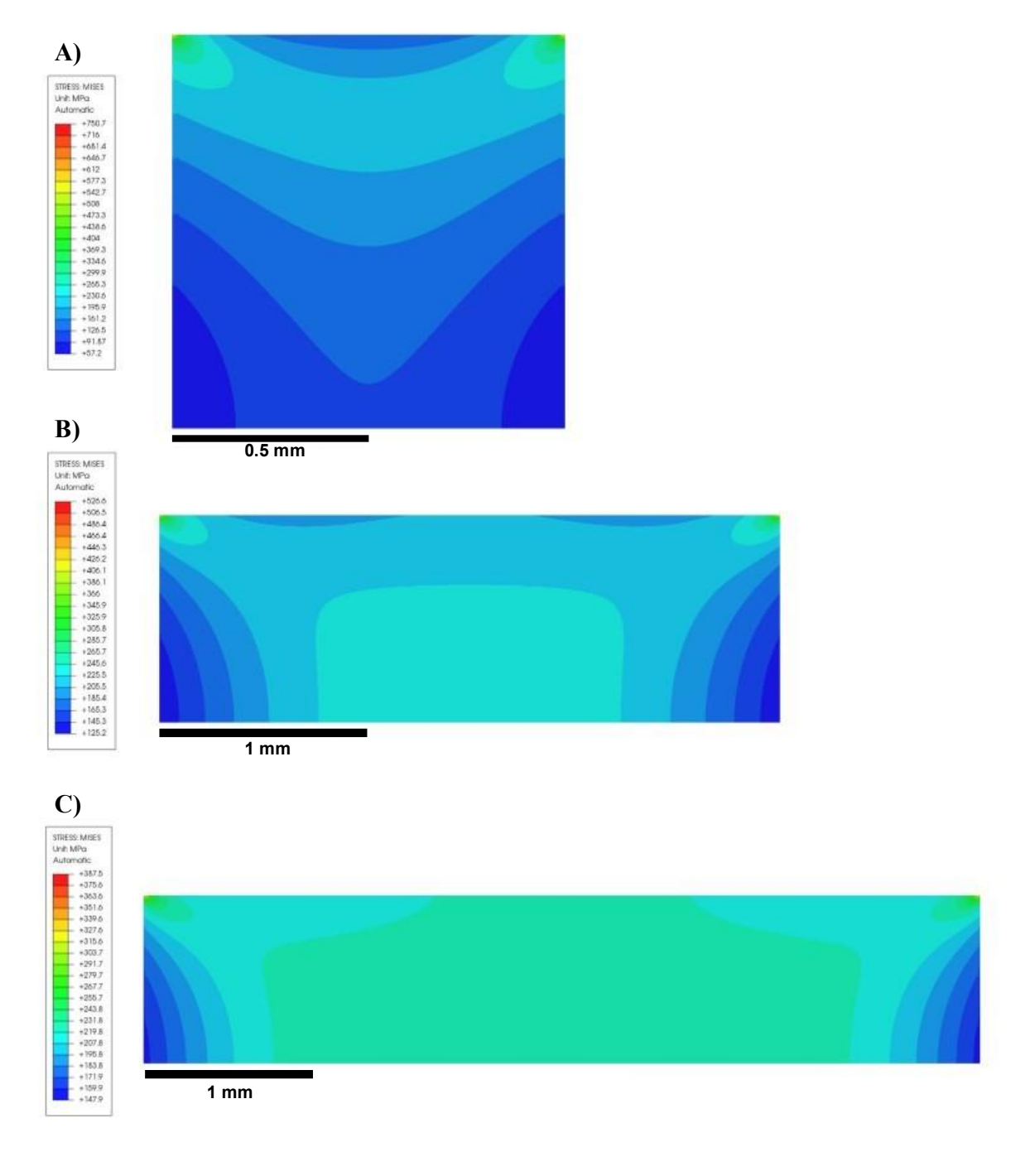


Figure 5.10 - FEA of the PIP cell during Li_6PS_5Cl pellet formation, highlighting the stress contours generated by applying the compressive pressure of 382 MPa as simulated in CalculiX. A) shows the 1 mm PIP cell modelled after the experimental geometry in Chapter 4, B) and C) model the same force applied over 3 mm and 5 mm diameter pellets respectively

FEA was performed using the CalculiX version 2.21 solver, where axisymmetric non-linear conditions were assumed. The PEEK walls of the PIP were modelled as two springs: one in the horizontal direction pushing towards the pellet and one in the axial direction pushing towards

the piston. The spring constant of the force acting in the horizontal direction was directly related to the material properties of PEEK. ¹⁸² The spring constant acting in the axial direction was equated to 1% of the pressure applied by the top piston, which was derived using the calculations of forces within similar systems as described by Thomas et al. ²⁰⁸ These calculations assumed a loss coefficient of 0.01 and a transfer ratio of 0.1 within the SE. The SE material was modelled as solid Li₆PS₅Cl since only 1.3% of the pellet was determined via XCT segmentation to be voids after compression.

The stress contours modelled in Figure 5.10A show heterogeneity throughout the thickness of the pellet during pressing and indicate a horizontal component to the stress as some force is distributed into the PEEK walls. This is particularly evident at the top interface of the pellet / press. A consequence of forming the pellet within the eventual cell casing is that these forces have the potential to be maintained and effect the performance of the SSB.

These different effects of axial and horizontal strains are significant in terms of cell behaviour. Axial strains promote the growth of cracks through the SE thickness, which in turn are candidates for shorting the cell via subsequent filling of metallic Li. On the other hand, horizontal strains result in deflection of cracks horizontally, with fractures following the stress contours developed in pellet formation, delaying the formation of critical cracks through its thickness. Additionally, previous work has shown that the filling of metallic Li is more challenging in the more tortuous cracks. ^{106,198} Horizontal stress heterogeneity generated from the PIP cell seems to have aided in prolonging cycle life of Li₆PS₅Cl in this study, but another variable to account for is the thickness of the SE pellet. A relatively large amount of Li₆PS₅Cl was used in this PIP due to the difficulties in making such a small diameter electrolyte pellet thin. This resulted in a thicker pellet than would be typically used in a SSB (reduced to minimise ionic resistance) and also results in a lower force transmission to the other end of the

pellet. For SSBs to have a high energy density, materials that do not contribute to capacity must be minimized, meaning that SEs will have to be made as thin as possible^{209–211}.

The expected transmission ratio, which is defined as the ratio of stress applied at one end of the pellet to the stress transmitted to the opposite end of the pellet, should range from 0.8-0.9 as determined by Michrafy et al. for a system such as the PIP cell (where there is one fixed end and one moveable plunger applying force during pressing)²¹². The FEA performed for the 1 mm PIP cell determined the transmission ratio to be 0.59, indicating that 41% of the load applied at the top of the pellet was dispersed throughout the system before making it to the other end of the pellet. However, the simulated transmission ratio is highly sensitive to the assumptions of the model, the loss in forces transmitted can largely be attributed to friction between the outer surface of the pellet and the walls of the PEEK body, varying with changes in pellet thickness. Similar to findings by Thomas et al., this stress transmission loss is non-homogenous throughout the volume of the pellet and the thickness of the pellet²⁰⁸.

In addition, the FEA predicts particularly high stress at the pellet interfaces with plungers which indicates a higher probability of defect formation in the top 10% of the pellet thickness, an effect which would be minimized when the width-to-height ratio is increased due to the way the forces are transmitted. Figure 5.10B and Figure 5.10C show the FEA results for 3 mm and 5 mm pellet geometries, respectively, along with the corresponding modelled stress contours. The other geometries show that just as pellet thickness and diameter are important factors in electrochemical performance of the SSB, they will also have a substantial effect on the stress contours developed in pellet formation within a cell, and therefore the degradation during cycling.

5.4 Conclusions

Here, correlated XCT and XRD-CT methods were utilized to investigate degradation in Lil Li₆PS₅Cl |Li cell cells. Degradation near the interface is significantly greater than in the bulk SE, affecting its morphology, chemistry, and electrochemistry. This interfacial degradation induces elevated stresses, reaching an order of magnitude higher than the yield stress of Li. A combined experimental and modelling approach, utilizing XCT, XRD-CT, and FEA, was used to examine how SE pellet formation influenced defect propagation in the SE within an operational cell. Degradation phases were identified, and the resulting deformation was quantified, providing guidance for prioritizing defect mitigation strategies. Pellet thickness and diameter, which are critical to the electrochemical performance of the SSB, also significantly affected stress contours during pellet formation, impacting defect formation during cycling. The integration of XCT imaging, XRD-CT, and FEA modelling highlighted the significant influence of cell geometry and force distributions on SSE performance and degradation during pressing and cycling.

6 Towards *Operando* Correlated X-ray and Neutron Tomography

6.1 Aim

The formation of mechanical defects in SEs, such as the generation of voids and the propagation of Li dendrites, continues to be a major barrier for the application of SSBs. ^{50,198} Imaging techniques such as scanning electron microscopy (SEM), transmission electron microscopy (TEM), and X-ray computed tomography (XCT) have proven useful in understanding the distribution, nucleation, and propagation of voids/dendrites within the SE pellets. ^{213–217} Diaz et al. utilized *ex situ* SEM to show that bulky dendrites appear near the poretype defects while the thinner dendrites follow the shape of grain boundaries. ²¹⁶

While SEM achieves incredibly high spatial resolutions of < 100 nm and can probe small 3D volumes with focused ion beam (FIB) milling, the technique is destructive in nature and often limited to *ex situ* measurements. In contrast, XCT is a non-destructive imaging technique that can probe 3D volumes in *operando* conditions during the SSB cycling. The limitation of XCT in the context of tracking Li dendrite propagation is that attenuation based XCT struggles to identify low-Z materials such as Li; this means that distinguishing between an empty void in the SE and a void filled with Li is difficult. Neutron computed tomography (NCT) is another non-destructive 3D imaging technique which is sensitive to some low-Z elements such as H and Li, which allows researchers to observe the migration of Li throughout the volume of the SE during operation. ^{166,169,172} Neutron imaging has been utilized in various SE systems to visualize the transport of Li into electrodes and throughout the SE. ^{159,169,171–175} Tracking Li transport and highlighting spatial heterogeneities gives key insights into defect formation, but these studies are often limited by the achievable temporal and spatial resolutions of neutron imaging. ²¹⁸

This work focuses on the correlation between XCT and NCT, as well as the optimization of experiments towards *operando* conditions. By utilizing both X-rays and neutrons, the experiment obtains the benefits of high spatial resolution and the ability to image low-Z materials. With the development of a bespoke cell, careful choice of materials, use of limited projections, and iterative reconstruction techniques, the spatiotemporal resolution is maximized to aid in the observation of the dynamic degradation processes of SSB cycling. This allowed for the probing of SSB degradation

6.2 Cell Development

Specific cells were developed for use in both X-ray and neutron imaging. The process of producing a cell optimized for high spatiotemporal resolution starts with careful consideration of the materials, the system, and the imaging geometry. To begin the development, this work started with a previous cell geometry for inspiration, the 3 mm Swagelok cell used in previous electrochemical works. ^{105,116,194,219} The small diameter of the Swagelok cell ensures higher transmission through the cell, limiting exposure times needed for both neutron and X-ray imaging, while also allowing a large representative volume to be examined at high resolutions. A standard Swagelok cell consists of perfluoroalkoxy alkane (PFA) and is ~ 3.6 cm long, machined from a PFA-220-6 Swagelok union with stainless-steel (SS) rods as electrodes. ¹¹⁵ Being a fluoropolymer with a density of 2.12 - 2.17 g cm⁻³, PFA is a very low attenuating material that serves well as a casing for X-ray and neutron imaging. ²²⁰ Here, achievable resolution is ultimately determined by the resolution of the current state of the art detectors such as the sub-4μm spatial resolution single-crystal thin-film scintillation detector at ILL, the Swagelok design was modified to optimize the imaging geometry with this detector. ²²¹ A schematic of the modified Swagelok cell is shown in Figure 6.1.

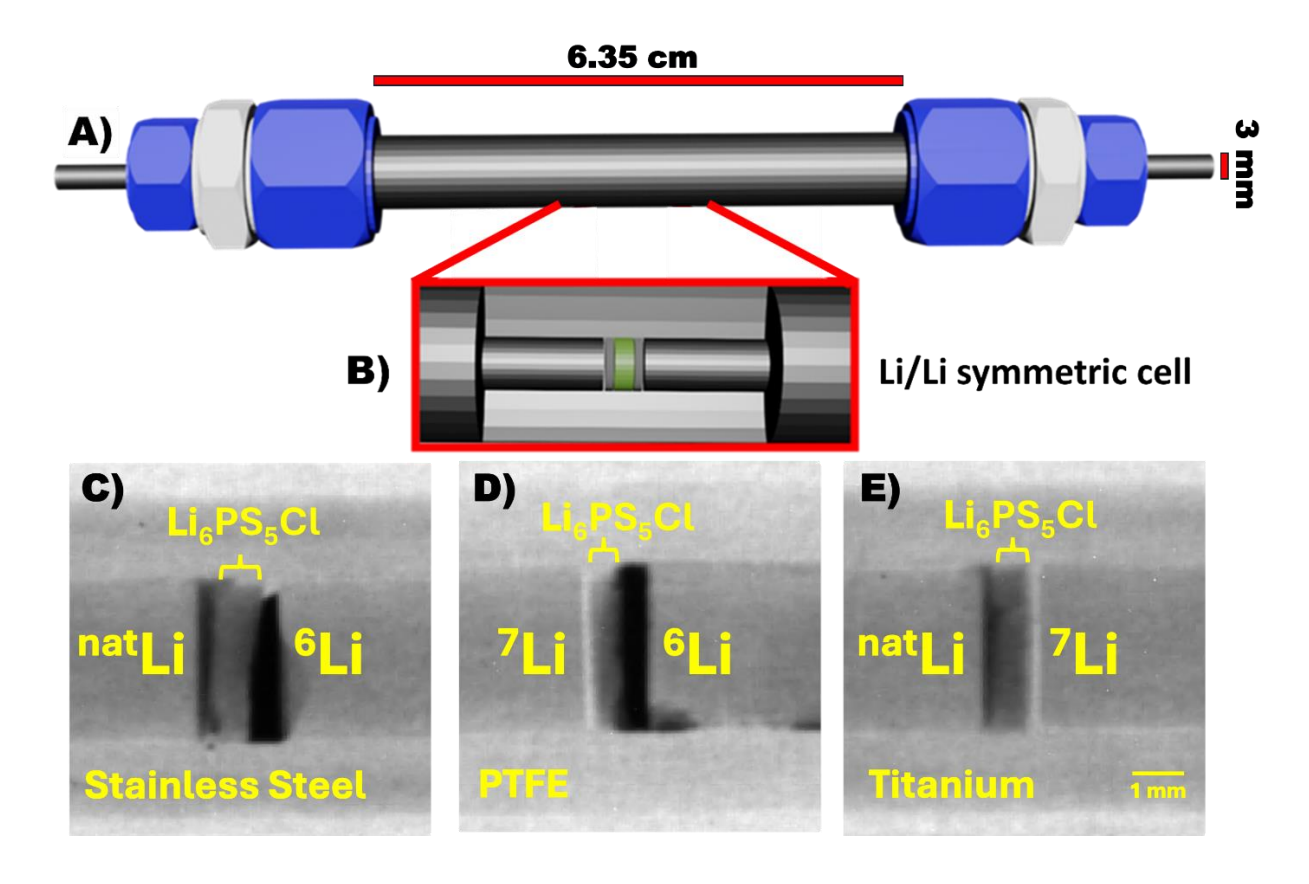


Figure 6.1 - Swagelok cell design. A) shows a schematic of the modified Swagelok cell for neutron imaging, while B) is an internal view of the Swagelok cell showing a Li/Li symmetric cell. C), D), and E) cross-sectional images from neutron tomography acquired at IMAT, ISIS, UK. C) is a Nat Li/ 6 Li symmetric cell with a stainless-steel outer casing, D) is a 7 Li/ 6 Li symmetric cell with a PTFE casing, E) is a Nat Li/ 7 Li symmetric cell with a titanium outer casing.

The body of this modified Swagelok cell was made long enough that the Swagelok components do not impede the sample being placed as close as possible to the detector, maximizing spatial resolution. The material of the body was a total of 6.35 cm long while the original is about 6.7 mm long, reducing the distance from sample-to-detector to ~7 mm which led to high resolution images. The geometric effects on resolution (d) dictated by the NCT setup is given in Equation 6 in Section 3.5.3.

When optimizing for high spatial resolution NCT, the sample should be positioned as close as possible to the detector to minimize the path length l, additionally the L/D ratio (beam

collimation) can be maximized by reducing the pinhole diameter (D) and increasing the propagation distance to the sample (L). These optimizations towards higher resolution lead to higher beam collimation which will give lower flux and require longer exposure times which extends the scan times. 157,222

The NCT of the modified Swagelok cell was carried out on IMAT¹⁷⁷ at ISIS neutron and muon source, achieving a pixel size of 31.42 μm over a field of view 64.6 mm² in ~5 hours depending on the contents on the Swagelok cell. Figure 6.1C, D, and E show orthoslices of NatLi/6Li, ⁷Li/⁶Li, and ^{Nat}Li/⁷Li symmetric cell respectively. Isotope pairing and cell materials experimentation are important as this ensures optimal sample structure for high spatiotemporal resolution. The body of the modified Swagelok cell consisted of metal shells of either Ti of SS coated with Polytetrafluoroethylene (PTFE) on the inside to maintain electrical insulation. PTFE is similar to PFA in terms of polymer structure and remains a very low attenuating material. The results from ISIS in Figure 6.1C, D, and E show that the best material for outer casing was the PTFE for its relatively low contrast, and the best pair of isotopes is NatLi and ⁷Li, as ^{Nat}Li is attenuating to neutrons while ⁷Li is not. ⁶Li is highly attenuating, but so much so that it requires higher exposure times to get sufficient counts for imaging and therefore leads to longer scan times. With the insight from the experimental results shown in Figure 6.1, a further iteration of the optimal cell for high spatiotemporal resolution operando cycling of SSBs was developed. This redesign was titled the Solid-state Operando Neutron and X-ray cell or SONX cell for short.

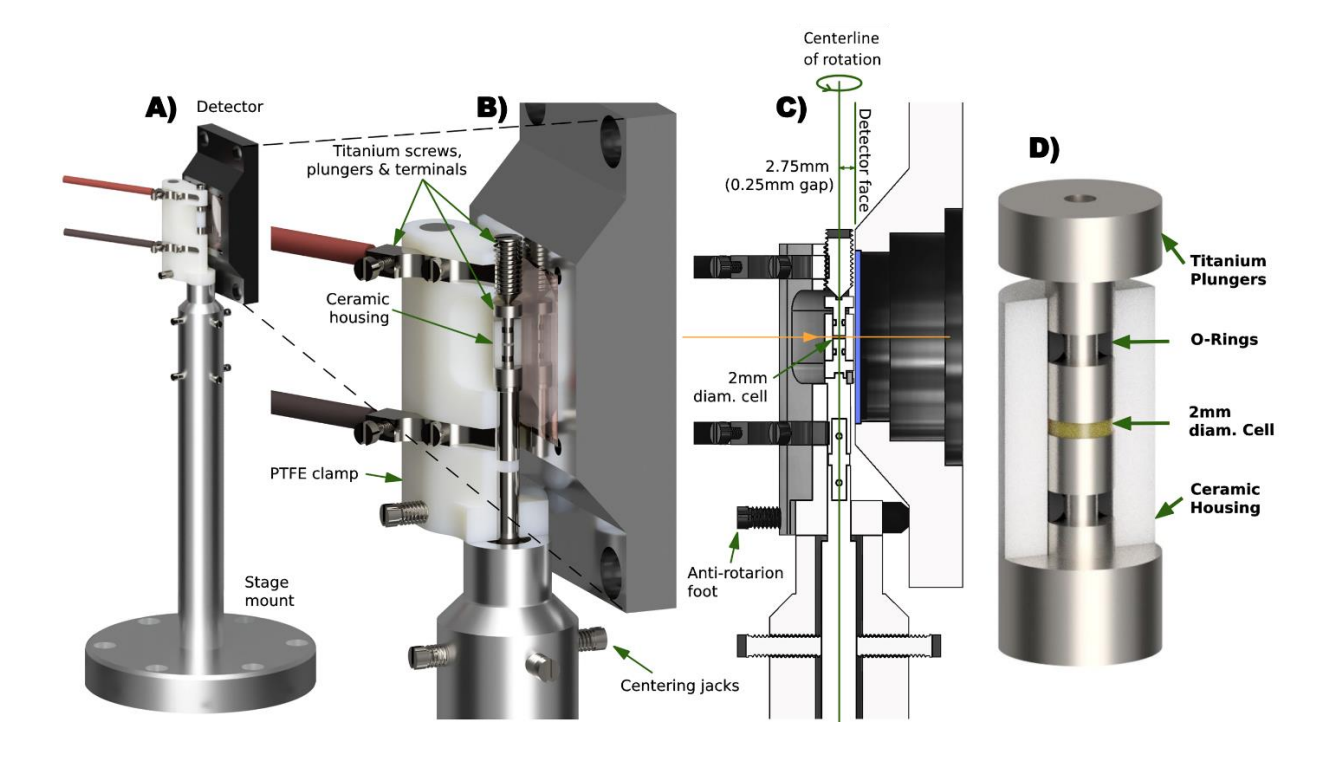


Figure 6.2 - Schematic of the solid-state operando neutron and X-ray (SONX) cell design. A) shows a rendering of the SONX cell mounted on the stage of NeXT, ILL, France. B) is a zoomed in view of the SONX cell with a cross-section showing the internal structure of the SONX cell. C) shows a sketch of the SONX cell mounted with the NeXT detector, showing the path of the neutrons and the magnitudes of the cell design. D) an enlarged cutaway view of the cell.

The design was inspired by the PEEK *In situ* Press cell (PIP) to reduce precycling defects and develop more reliable cells. To achieve the highest resolution, easy installation, and solid-state electrochemical operation; the new cell had to address the following design criteria:

- To reduce the neutron attenuation the design avoids having H in the cell, fluorinated polymers utilized in previous studies was used as material that would be electrically insulative.¹⁰⁵
- In neutron imaging, the distance from the center of the cell to the detector is minimized to reduce the image blurring due to the penumbra effect and achieve clear high-resolution images.²²³

- Due to the low strength of fluorinated polymers, ceramic pellet housings were manufactured to limit the deformation of the cells as they are pressed to 1000 N, 318
 MPa, to form solid electrolyte pellets.
- Ti plungers were fitted with machined O-rings to further limit pre-cycling degradation and exposure to environment during experiment.

With the SONX cell design, both XCT and NCT experiments for SSB can be optimized for low pre-cycling defects and high spatiotemporal resolution to better explore the early stages of degradation in SSBs.

6.3 Ex situ Experiment

The SONX cell was utilized in an *ex situ* experiment utilizing a ^{Nat}Li | Li₆PS₅Cl | ⁷Li symmetric cell architecture and observing the degradation of plating ^{Nat}Li onto ⁷Li until a short circuit occurs.

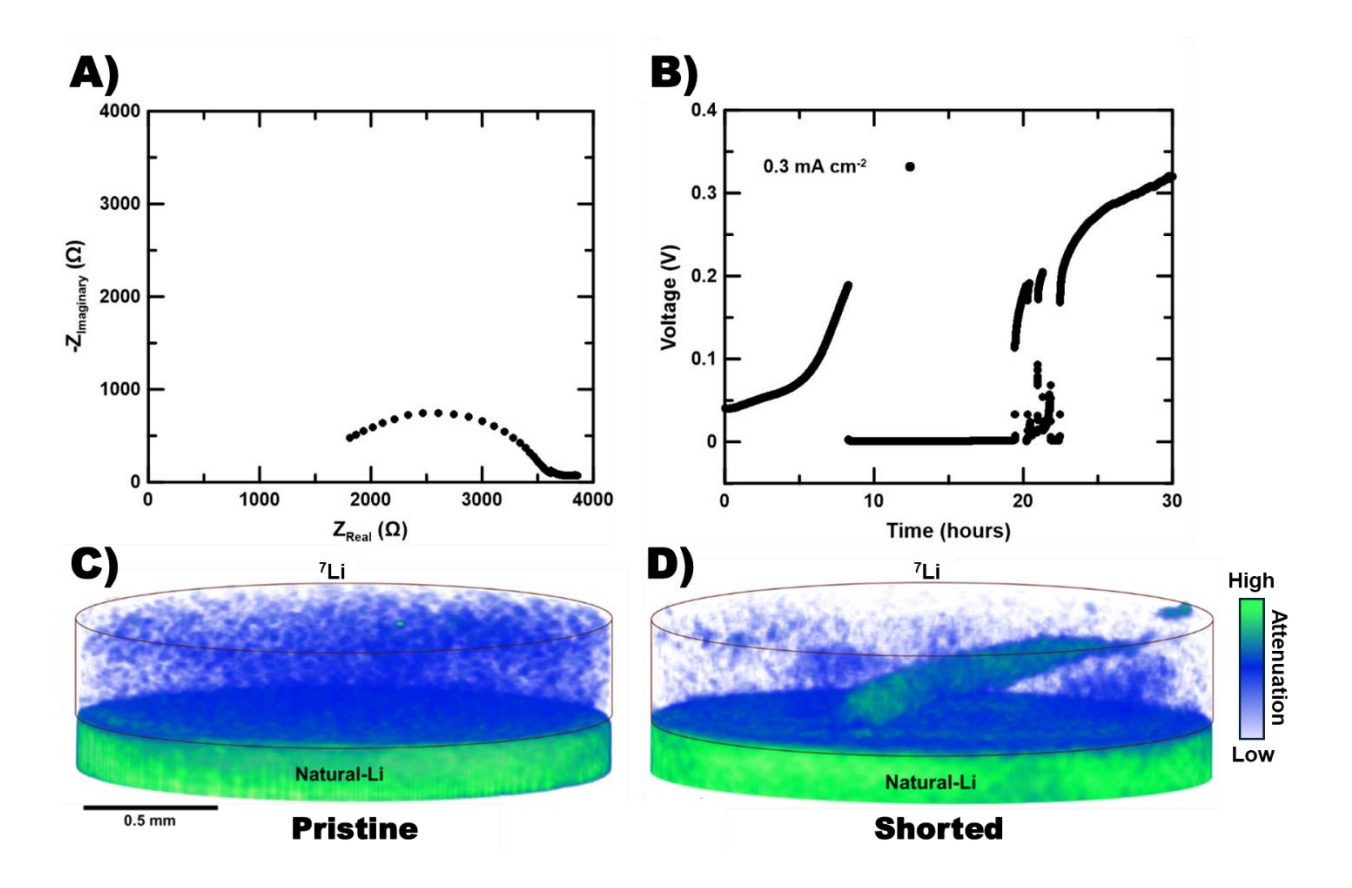


Figure 6.3 - Ex situ analysis of $^{Nat}Li \mid Li_6PS_5Cl \mid ^7Li$ symmetric cell. A) shows the Nyquist plot with the initial impedance of the cell, B) shows the result of galvanostatic cycling at 0.3 mA cm⁻² and the cell shorting after ~8 hours of plating ^{Nat}Li onto 7Li , C) 3D rendering of a pristine neutron tomography, and D) 3D rendering of a shorted cell after the galvanostatic cycling protocol in B). The voxels that are more green are higher attenuating while the voxels that are less attenuating are lighter blue.

Figure 6.3A shows the initial impedance of the cell that was shorted, Figure 6.3B shows the voltage response of the cell after plating for 30 hours at a current density of 0.3 mA cm⁻² with a noticeable reduction of resistance around 8 hours into the test and a noisy recovery later on, indicating a possible internal short circuit. Figure 6.3C and D show neutron tomograms of a pristine cell and the shorted cell, respectively, showing that 7 Li appears completely transparent while $^{\rm Nat}$ Li attenuates strongly, with the highest contrast in the cell (green). These tomograms were gathered on the neutron instrument NeXT¹⁷⁶ at the Institute Laue Langevin, France. Here and in the *operando* study, the tomograms required 5 hrs of acquisition, and the configuration achieves $\sim 4~\mu m$ pixel size over the field of view that covered the entire SONX cell. Figure

6.3D shows that a large structure of ^{Nat}Li penetrated the Li₆PS₅Cl pellet and eventually shorted the cell. There is also a noticeable heterogeneity in the contrast of the Li₆PS₅Cl pellet (patchy blue areas throughout the volume), suggesting a high contrast material such as ^{Nat}Li is unevenly distributed, which could be caused by heterogeneous current density throughout the area of the pellet.

To analyse the mechanical degradation in higher spatial resolution, XCT was performed on the shorted cell. This XCT volume was aligned with the NCT volume to compare a higher resolution image of the NatLi protrusion through the Li₆PS₅Cl pellet.

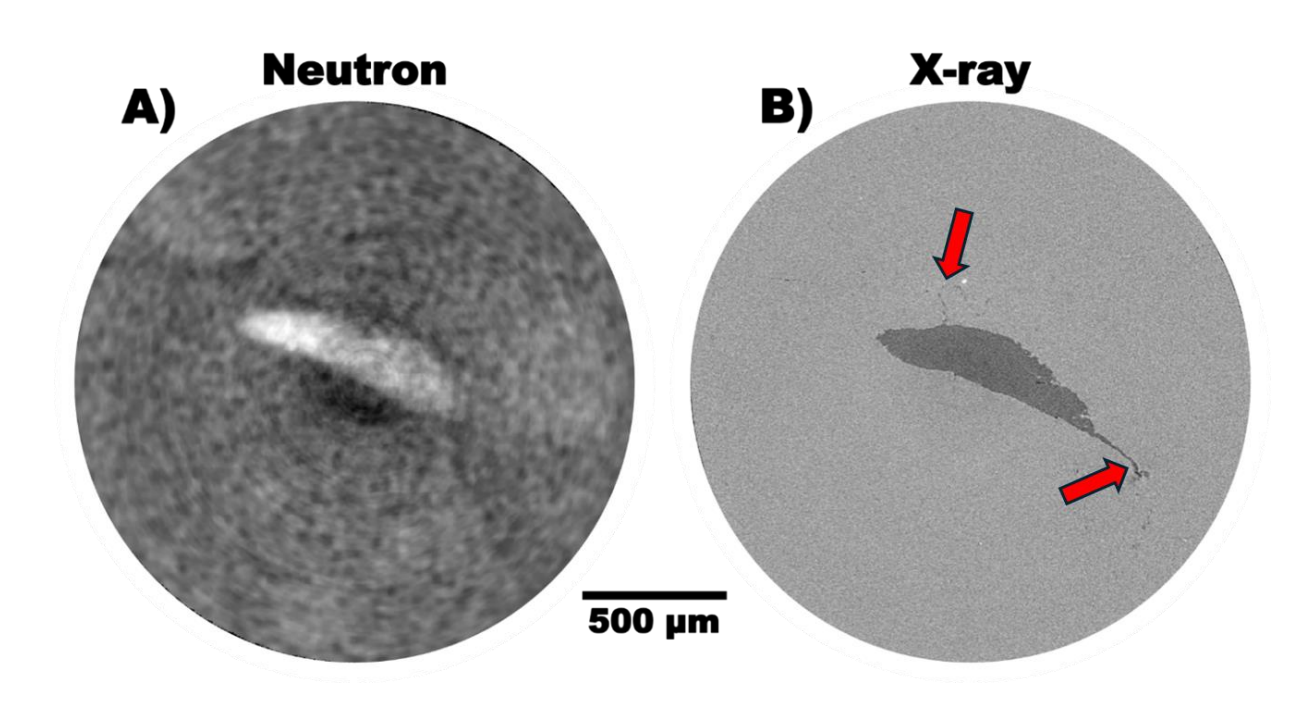


Figure 6.4 - Cross-sectional slice in XY plane comparing post-mortem NCT (A) and XCT (B) of an observed defect. The red arrows in B) highlight cracks that are not visible in the NCT.

Figure 6.4A and B show cross-sectional slices of the NCT and XCT tomograms, respectively. Figure 6.4A shows the ^{Nat}Li as bright pixels, where the same structure appears as a low density (dark grey) region in Figure 6.4B. Figure 6.4A also shows a low attenuating region near the

center of the cell which does not appear in Figure 6.4B, this indicates a variation that X-rays are not sensitive to (such as ^{Nat}Li concentration) or the dark area is a reconstruction artefact in the NCT. The red arrows in Figure 6.4B also show that smaller fractures are formed around the large defect area, a detail not picked up in NCT. The XCT performed on the shorted cell (postmortem XCT) was done 2 weeks after the NCT which gave the Li and Li₆PS₅Cl pellet plenty of time to react with one another, this created challenges in correlating the data sets, while also giving a unique view of Li₆PS₅Cl and Li after being in contact for a prolonged period.

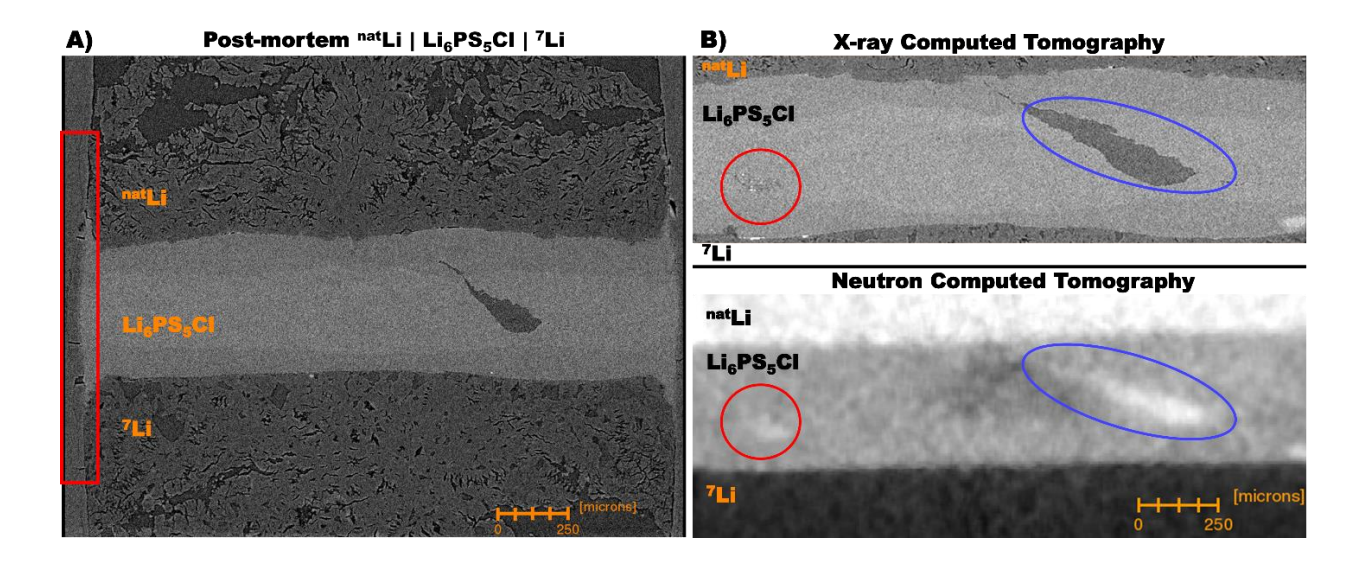


Figure 6.5 – Post-mortem XCT of ex situ $^{Nat}Li \mid Li_6PS_5Cl \mid ^7Li$ symmetric cell after galvanostatic cycling at 0.3 mA cm $^{-2}$. A) larger field of view XCT through the center of the cell showing severe degradation of the cell. B) High resolution image of an XCT slice showing a high porosity area (red circle) along with the main defect of the cell (blue circle) and C) correlated neutron tomogram of the same region as in B), showing that the main defect and the high porosity area have a high concentration of ^{Nat}Li .

Figure 6.5 shows the vertical cross-sectional view of the entire ^{Nat}Li | Li₆PS₅Cl | ⁷Li symmetric cell in both XCT and NCT, highlighting the extent of the degradation during electrochemical shorting and subsequent Li/Li₆PS₅Cl reaction. Figure 6.5A shows the entire cell, post-mortem, highlighting the large ^{Nat}Li protrusion within the Li₆PS₅Cl pellet, as well as noticeable low-density regions at both interfaces of the pellet and significant density variation in the Li metal

electrodes. The red box in Figure 6.5A also highlights some pellet bulging and cell wall defects, an indication that the cell casing of PTFE was too weak to properly form a Li₆PS₅Cl pellet, and this inspired the change to an Al₂O₃ ceramic material being used for the cell casing in further studies. Figure 6.5B compares the XCT and NCT cross-sectional views in the same area. The interfaces between Li and Li₆PS₅Cl have deteriorated significantly (as observed in the XCT) which exemplifies a shortcoming of not carrying out correlated XCT and NCT simultaneously. The blue oval in Figure 6.5B shows the large Nat Li protrusion within the pellet in both X-ray and neutron imaging while the red circle highlights an area within the bulk of the Li₆PS₅Cl pellet that appears to be a porous region in XCT but indicates a high concentration of Nat Li in NCT. The presence of these localized high-neutron-attenuating areas could be an indication of either heterogeneous Li mobility, metallic Li plating within porous areas, or both Nat Li in SONX cell and the correlation of these cutting-edge imaging techniques are highly important for understanding degradation in SSBs but the *ex situ* nature of this experiment was limiting in observing such dynamic systems. The takeaways from this *ex situ* study were utilized to push this experiment towards *operando* conditions.

6.4 *Operando* Experiment

To take advantage of the SONX cell setup, a higher spatiotemporal resolution experiment was conducted to study the earliest stages of the dynamic degradation within the ^{Nat}Li | Li₆PS₅Cl | ⁷Li symmetric cell. XCT was performed at the beginning and end of the electrochemical plating while NCT was performed at various points throughout the experiment.

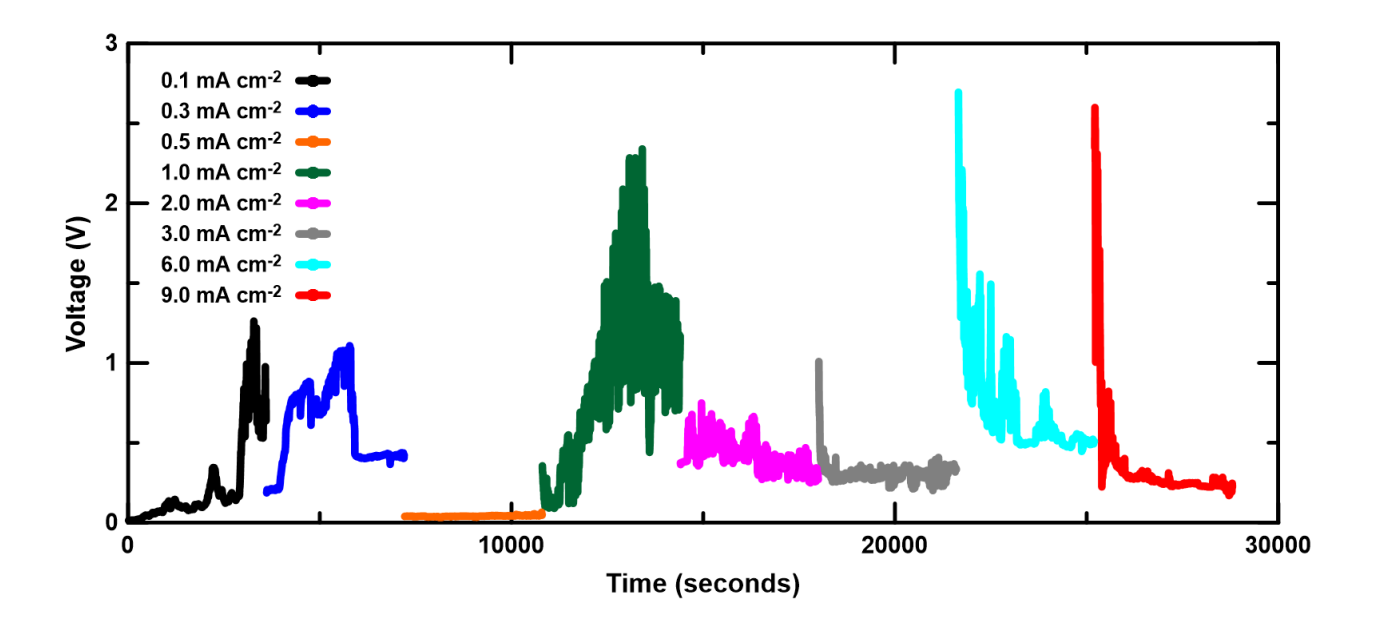


Figure 6.6 - Galvanostatic cycling profiles obtained during the operando experiment at NeXT. The colours show the various current densities at which plating of ^{Nat}Li was plated onto ^{7}Li in the $^{Nat}Li \mid Li_6PS_5Cl \mid ^{7}Li$ symmetric cell. A majority of the current density steps show unstable voltage due to changes in resistance during cell operation. The $^{Nat}Li \mid Li_6PS_5Cl \mid ^{7}Li$ symmetric cell was tested from 0.1 mA cm⁻² to 9.0 mA cm⁻².

Figure 6.6 shows the voltage response of the constant current plating of ^{Nat}Li onto ⁷Li at the various current densities tested. The electrochemical plating was conducted with a Gamry Instruments Reference 600+ at room temperature, without application of constant external pressure applied during cycling. Chronopotentiometry was performed in 60 min intervals at the given current densities, plating ^{Nat}Li onto the ⁷Li electrode. The voltage response shows an unstable resistance during each plating step, with no evidence of a complete electrochemical short circuit during the experiment up to 9.0 mA cm⁻².

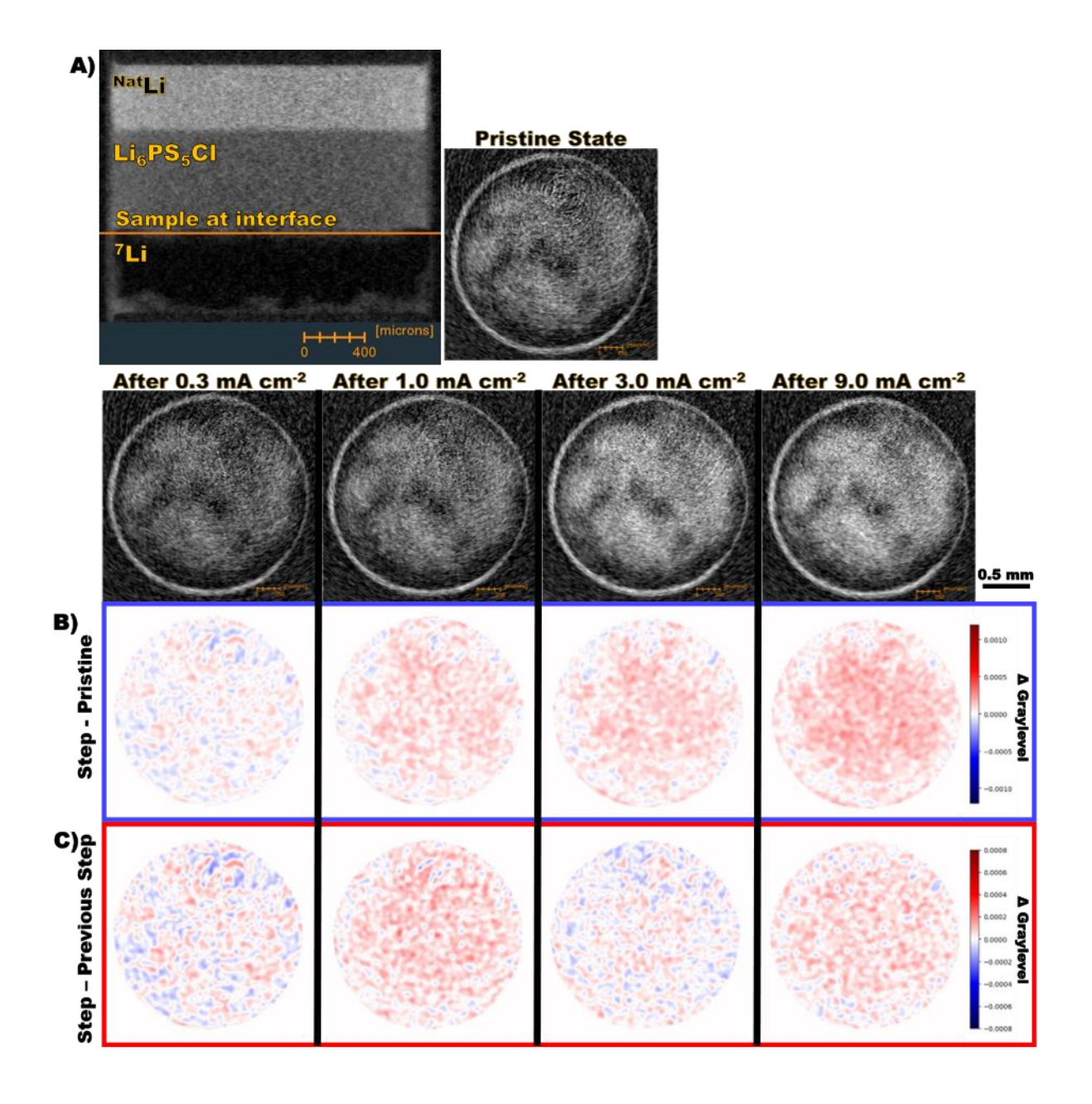


Figure 6.7 - NCT results from operando plating experiment. A) shows a vertical cross-section to highlight the various components of the $^{Nat}Li \mid Li_6PS_5Cl \mid ^7Li$ symmetric cell and horizontal cross-sections at the 7Li interface after various galvanostatic plating steps of increasing current densities from 0.3 mA cm⁻² to 9.0 mA cm⁻². B) shows the difference of the horizontal cross-sections compared to the pristine cross-section, highlighting the increase in contrast from the increased presence of ^{Nat}Li . C) shows the difference of the horizontal cross-sections at each current density minus the step before, highlighting the restructuring behaviour of the contrast which alludes to the way ^{Nat}Li is distributed at the interface.

Figure 6.7 displays multiple slices from the high spatiotemporal resolution NCT experiment and corresponding horizontal cross-sectional contrast difference maps; the high-attenuating

material appears as lighter grey. Figure 6.7A shows a horizontal cross-section of the ⁷Li/Li₆PS₅Cl interface after the various plating steps had completed and a vertical cross-section highlighting the interface placement in the ^{Nat}Li | Li₆PS₅Cl | ⁷Li symmetric cell (orange line in Figure 6.7A). Figure 6.7B shows the ⁷Li/Li₆PS₅Cl interface difference maps, relative to the pristine tomography, showing the general increase in contrast at the interface due to the addition of the high neutron attenuating ^{Nat}Li during the electrochemical plating. Figure 6.7C shows difference maps at the same interface as in Figure 6.7B but change is shown relative to the previous step rather than relative to the pristine state, exemplifying the addition and restructuring of ^{Nat}Li during the various plating steps. This level of spatiotemporal resolution enables the monitoring of the plating process in fine detail, allowing for the further analysis and quantification of ^{Nat}Li movement to the ⁷Li electrode.

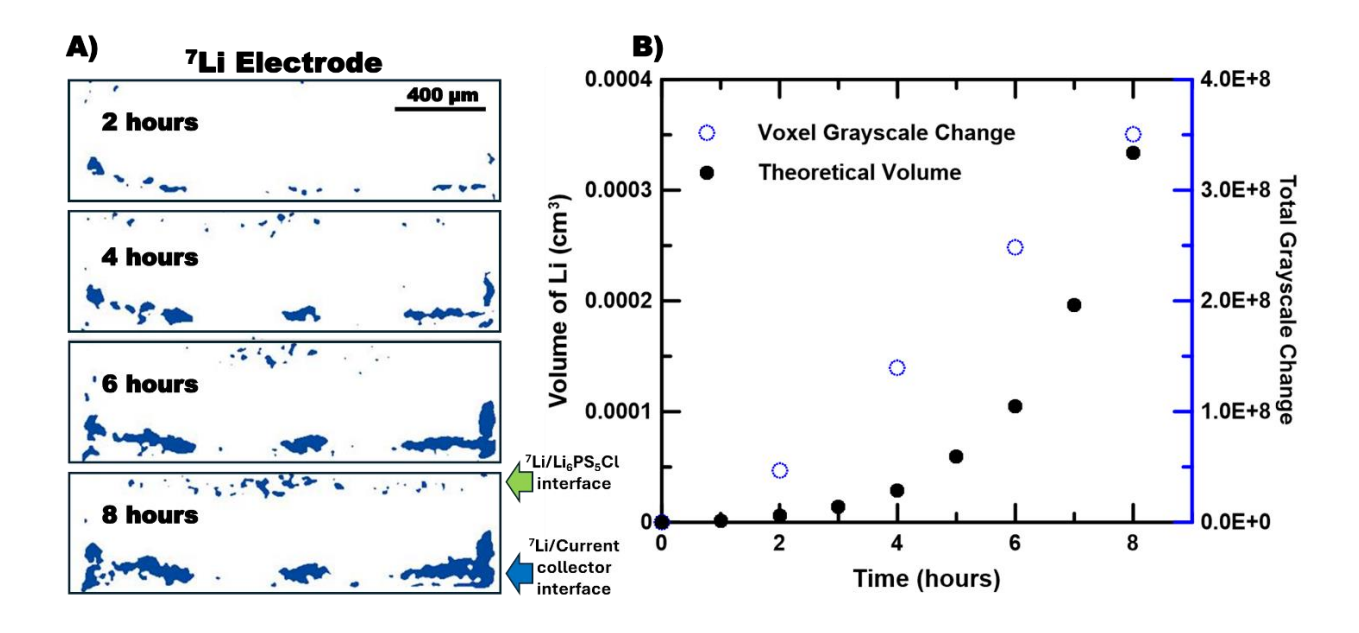


Figure 6.8 - Quantification of the amount of high contrast material (^{Nat}Li) introduced to the ^{7}Li electrode volume. A) shows a cross-section of the segmented high contrast material from NCT and the increase presence with increased plating. B) shows how much ^{Nat}Li that should theoretically be moved to the ^{7}Li electrode based on the current densities (black) and the segmented volume of high contrast material introduced to the ^{7}Li electrode volume over time (blue).

Figure 6.8A displays a vertical cross-section of the ⁷Li electrode volume with the high contrast material segmented in blue. Interestingly, the ^{Nat}Li is built up on the top, which is the ⁷Li/ Li₆PS₅Cl interface (highlighted with green arrow), but also on the edges and bottom of the ⁷Li electrode (highlighted with blue arrow). A possible explanation for the distribution of ^{Nat}Li around the ⁷Li electrode, rather than uniform interfacial plating, is the fixed volume constraint between the Li₆PS₅Cl pellet and the current collector. This spatial limitation may cause the ^{Nat}Li to either plate and induce mechanical displacement through the SE or redistribute around the ⁷Li electrode as additional ^{Nat}Li is deposited. The volume of high contrast material increases as more ^{Nat}Li is plated onto the ⁷Li electrode as expected, but the grayscale volume change is different than anticipated. As shown in Figure 6.8B, the trend of total grayscale change is linear while the theoretical volume of ^{Nat}Li moved should be exponential given the plating protocol. This discrepancy in the trends of theoretical Li volume and grayscale change could mean that the constant current plating is not transporting as much ^{Nat}Li as expected based on calculation or there is additional material contributing to the high neutron attenuating material such as impurities/side reaction.

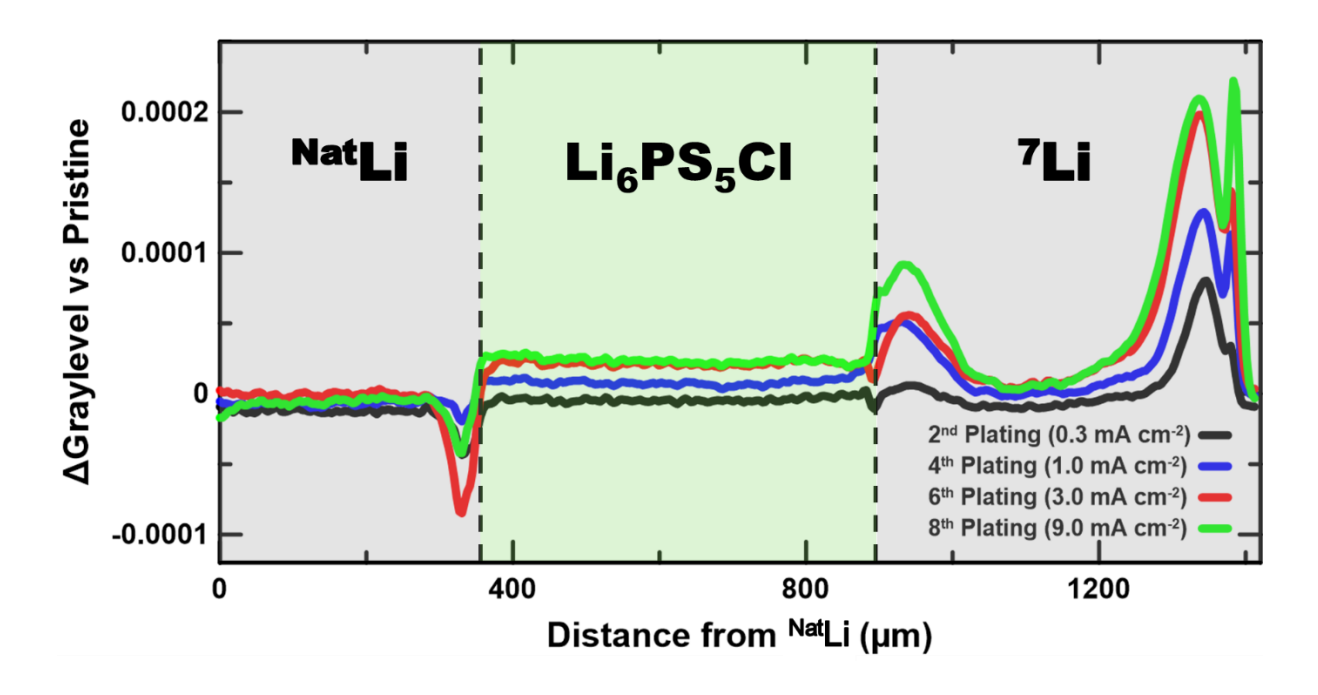


Figure 6.9 - Grayscale profiles throughout the depth and volume of the $^{Nat}Li \mid Li_6PS_5Cl \mid ^7Li$ symmetric cell, normalized against pristine NCT, showing the depth profile as a distance from the ^{Nat}Li electrode. The various components are highlighted, and the different current density steps are shown in different colour lines. Positive Δ Grayscale levels indicate an increase in ^{Nat}Li concentration compared to the pristine material, which occurs in both the 7Li electrode and the SE pellet after progressive plating.

Figure 6.9 shows the grayscale values of each slice of the tomogram through the depth of the NatLi | Li₆PS₅Cl | ⁷Li symmetric cell sample, normalised to the pristine value. the grayscale profiles are the summations of voxels throughout the depth of the cell. The profiles in Figure 6.9 are relative to the grayscale values in the pristine tomogram and labelled as a distance from the beginning of the NatLi electrode. This provides an interesting overview of Li mobility throughout the cell, showcasing the stripping of NatLi from the NatLi/ Li₆PS₅Cl interface and subsequent plating into the ⁷Li electrode. The trends show a clear reduction of contrast near the NatLi interface and an increase in contrast at various depths in the ⁷Li electrode. Another interesting feature is the increase of relative grayscale value of the Li₆PS₅Cl pellet upon

continued plating. The presence of additional ^{Nat}Li within the SE of pellet suggests that ^{Nat}Li is accumulating in the porosity of the SE, rather than incorporating into the Li₆PS₅Cl crystal structure, which already contains ^{Nat}Li. This could be due to ^{Nat}Li plating into nanopores that are unresolved at this imaging resolution.

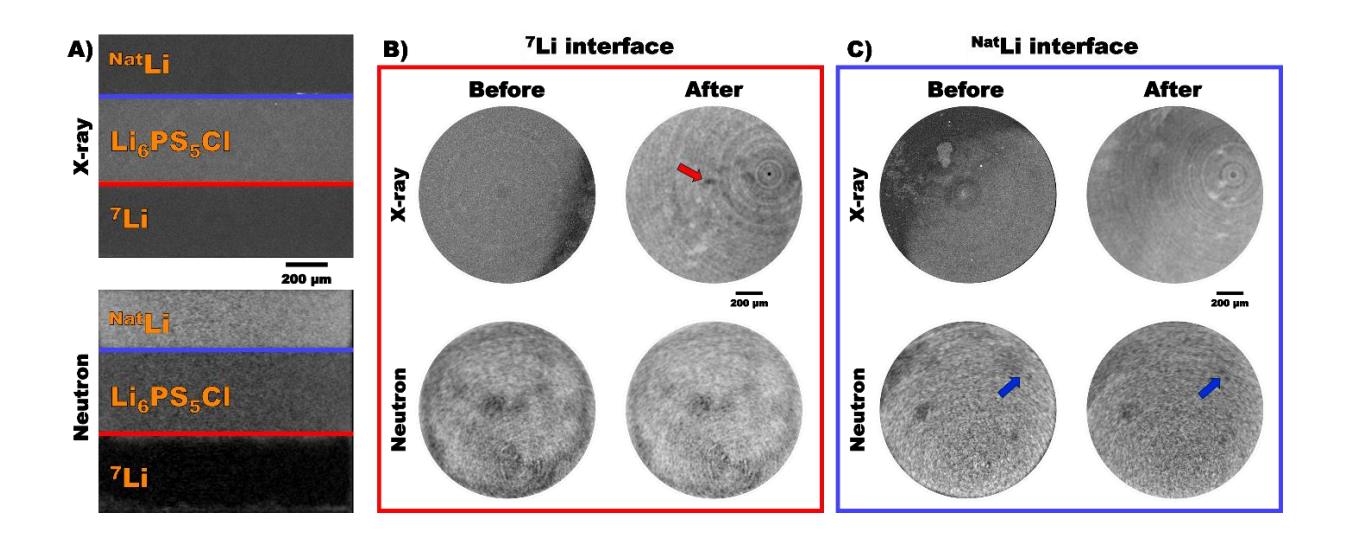


Figure 6.10 - Correlated NCT and XCT datasets of the operando plating experiment. A) shows a vertical cross-section of the XCT and NCT datasets and highlights the ^{Nat}Li interface (blue) and ⁷Li interface (red). B) shows the horizontal cross-sections of the ⁷Li interface with XCT and NCT before and after the operando experiment. C) shows the horizontal cross-sections of the ^{Nat}Li interface with XCT and NCT before and after the operando experiment.

To better understand the degradation at the two interfaces in the symmetric cell, the ⁷Li/Li₆PS₅Cl and ^{Nat}Li/Li₆PS₅Cl interfaces were isolated and examined with correlated XCT and NCT orthoslices, as shown in Figure 6.10. Figure 6.10A shows the vertical cross-section of the ^{Nat}Li | Li₆PS₅Cl | ⁷Li symmetric cell with X-ray and neutron imaging while Figure 6.10B and Figure 6.10C show correlated horizontal cross-sections of the ⁷Li/Li₆PS₅Cl and ^{Nat}Li/Li₆PS₅Cl interfaces, respectively. Figure 6.10B and Figure 6.10C show the interfaces before and after the total electrochemical plating of the experiment, both with X-ray and neutron imaging. At the ⁷Li interphase, more highly-neutron-attenuating ^{Nat}Li is introduced via plating, which is

apparent with the increase in brightness in the "After" NCT compared to the "Before" in Figure 6.10B. The accompanying XCT slices in Figure 6.10B also show the introduction of various low-density defects (voids or pits, example shown by red arrow) forming which are possibly the result of Li pushing into the Li₆PS₅Cl pellet and the earliest sign of dendrite formation.⁹⁰ At the NatLi interphase, NatLi is striped from the NatLi electrode during each of the electrochemical steps in this experiment. Figure 6.10C shows the NatLi interphase before and after the experiment, allowing the observation of changes in the NatLi electrode structure (such as void formation) with variations in the contrast. The XCT slices in Figure 6.10C do not show signs of voids in the Li₆PS₅Cl pellet as in Figure 6.10B. The NCT slices in Figure 6.10C show low contrast spots (voids in the NatLi, example shown with blue arrows) on the interface of the NatLi electrode which change after the plating, this is believed to be NatLi forming and filling voids during the experiment as hypothesized in other literature. 80 Figure 6.9 showcases features that support both the observations in the correlated interface slices of Figure 6.10B and C, mainly the significant decrease in greyscale value at the NatLi electrode supporting the hypothesis that voids are forming in the NatLi upon continued striping as observed in other works^{80,81,83} and the small decreases in greyscale at the ⁷Li electrode which could be the formation of defects in the Li₆PS₅Cl pellet which are later filled with Li, causing the initiation of Li dendrites. 90,91

6.5 Conclusions

This work showcases the advancements in correlated X-ray and neutron computed tomography, utilizing the capabilities of each technique together for studying the degradation of a Li₆PS₅Cl-based solid-state cell. With the bespoke cell holder designed for this project, the Solid-state *Operando* Neutron and X-ray (SONX) cell, this experiment pushed the boundaries of spatiotemporal resolution in a 4D *operando* correlated X-ray computed tomography (XCT) and

neutron computed tomography (NCT) analysis of the earliest stages of degradation in a NatLi | Li₆PS₃Cl | ⁷Li symmetric cell. The strengths of both techniques were utilized to probe the entire volume of the cell during operation, focusing on plating of the high neutron attenuating NatLi onto the low neutron attenuating ⁷Li electrode. XCT was more sensitive to the structural defeats that required higher resolution than what could be achieved with NCT that occurred during the electrochemical plating and NCT was sensitive to presence and isotope of the Li throughout the volume of the solid-state cell. It was observed that the interphase of the stripped electrode loses Li and forms a changing layout of voids, while the interphase of the electrode subject to additional Li plating formed defects in the Li₆PS₃Cl. Thoughtful cell design limited the precycling defects in this solid-state cell, and the high spatiotemporal resolution aids in observing the structural changes within a few microns during various electrochemical processes. This work addresses some key challenges of degradation characterization in operational solid-state batteries (SSBs) and stands as a guide for further development in full-volume high spatiotemporal resolution correlated XCT/NCT *operando* experiments.

7 Conclusions and Future Work

This work demonstrated a comprehensive, multimodal approach for investigating degradation in Li| Li₆PS₅Cl |Li symmetric SSBs, through the development and application of advanced *operando* cell designs and high-resolution X-ray and neutron imaging techniques. This work highlighted the key challenges of manufacturing SSBs for these characterization techniques and provided practical insights to inform the design of more reliable future cell architectures. Producing SSBs that were free of defects from the beginning proved difficult, and having a pristine baseline is important for a representative experiment. *In situ* pellet formation and simultaneous observation with X-ray Computed Tomography (XCT) led to SE pellet production with no pre-cycling defects and inspired the design of an *in situ* pellet press-based cell design.

Chapter 4 introduced the PEEK *in situ* Press (PIP) cell, which enabled *operando* XCT at high spatiotemporal resolution, allowing investigation of early-stage defect formation and full-volume degradation analysis in an electrochemically operating environment. Having the full-volume view provided substantial statistics and allowed for degradation analysis of the full SE environment. Data gathered during the nucleation of defects provided a clearer view of what conditions caused the faults observed. Cracks formed in the Li₆PS₅Cl SE pellet during the plating and stripping of Li within the Li₁ Li₆PS₅Cl |Li symmetric cell at various current densities, a majority forming at the Li/Li₆PS₅Cl interface. These cracks were more horizontally traveling and did not cause electrochemical failure of the symmetric cell which was cycled up to a rate of 9 mA cm⁻².

Through correlated XCT and X-ray Diffraction Computed Tomography (XRD-CT), the influence of pellet geometry and fabrication induced stresses on defect propagation and cell performance was revealed in Chapter 5. In 3 mm Li| Li₆PS₅Cl |Li symmetric Swagelok cells,

degradation was found to be highly localized at the Li/SE interfaces, with accompanying stress fields reaching magnitudes significantly exceeding the yield stress of Li. This concluded that Li would be strained enough at the interface to be pushed into the defects formed in the SE. However, as found in Chapter 4, the cracks formed in the PIP cell were parallel to the electrode surface. Therefore, if Li is pushed into the horizontally travelling tortuous defects, the cell remains operable as electrodes remain isolated. Furthermore, XRD-CT was performed on the Li/Li₆PS₅Cl interface of the PIP cell, showing that there is an additional residual compressive strain on the Li₆PS₅Cl lattice in the horizontal direction, likely originating from the pellet formation within the cell and leading to longer cell life. These correlated characterization methods provided direct quantification of stress fields and identified critical degradation pathways, offering a foundation for targeted defect mitigation strategies.

In Chapter 6, a cell inspired by the PIP cell, the Solid-state *Operando* Neutron and X-ray (SONX) cell extended this analysis beyond X-rays, combining XCT and neutron computed tomography (NCT) to visualize Li movement during electrochemical plating which was correlated with the high-resolution morphological deformation imaging from XCT. This setup enabled unprecedented insights into Li transport, void formation, and interphase instability across the full cell volume, capturing features at high spatiotemporal resolutions for NCT. The movement of the high attenuating NatLi was traceable, and the plating onto the Li electrode was observable. The interface where Li was plated onto showed evidence of SE defects, as seen by XCT, and the interface where Li was stripped from showed void formation and change within the Li electrode, only visible to the NCT.

These experimental advances have paved the way for future work in SSB degradation characterization. Further work should extend this methodology to other SE chemistries, such as other sulfide-based material, halides, or oxides. The combined information from these

correlated techniques will lead to a more thorough characterization of the SE failure mechanisms and therefore aid in solving degradation related issues that are impeding the release of these technologies to the market. More is now understood about the development of representative SSBs for high spatiotemporal resolution experiments, and the findings of combining multiple characterization techniques to study the same system was showcased successfully. More experimentation should be conducted in applying these techniques to additional characterization methods such as X-ray Fluorescence Computed Tomography (XRF-CT), which would provide 3D elemental sensitivity which could be helpful for understanding the effects of dopants, additives, or impurities in the SE on SSB performance.

Aside from opening doors for future advanced experimental studies, there are opportunities in computational advancements to also be made from this work. The correlated techniques can also fortify each other's effectiveness through the implementation of advanced algorithms. For example, the artificial intelligence based approach of up-scaling resolution of XCT tomography, where images are gathered at various field of views (FOVs) and the high resolution of the low FOV tomography is mapped onto the larger FOV.^{225–227} In the future, a similar approach could take these correlated XCT, NCT, and XRD-CT datasets and provide up-scaled resolution of the NCT and XRD-CT datasets, providing unprecedented resolution for these critical techniques that provide visualization of phase/strain mapping and the position of Li metal. When combined with SSB modelling, this multimodal framework provides a robust platform for understanding and predicting mechanical, chemical/electrochemical degradation in SSBs.^{69,91} These large, correlated datasets can serve as valuable inputs for next-generation simulations, improving both their accuracy and generalizability.

In parallel with further utilizing these correlated characterization techniques, more development should be put into the data pipeline for integrating correlated XCT, NCT, and

XRD-CT datasets. Often processing and registering the various data sets is the largest energy barrier to adoption of these advanced techniques, therefore, the more effort put into streamlining this data processing will ultimately lead to more efficient innovation.

8 References

- (1) EVO Report 2022 | BloombergNEF | Bloomberg Finance LP. https://about.bnef.com/electric-vehicle-outlook/ (accessed 2022-07-04).
- (2) Capacity of lithium-ion battery shipments globally 2020-2030 | Statista. https://www.statista.com/statistics/1246914/capacity-of-lithium-ion-batteries-placed-on-the-global-market/ (accessed 2022-07-05).
- (3) 2022 Toyota Camry. https://fueleconomy.gov/feg/Find.do?action=sbs&id=44343 (accessed 2022-07-05).
- (4) Electric Cars, Solar & Clean Energy | Tesla United Kingdom. https://www.tesla.com/en GB/ (accessed 2022-07-05).
- (5) Tesla Model S Charging Time | homechargingstations.com. https://www.homechargingstations.com/tesla-model-s-charging-time/ (accessed 2022-07-05).
- (6) Government data show gasoline vehicles are up to 100x more prone to fires than EVs. https://electrek.co/2022/01/12/government-data-shows-gasoline-vehicles-are-significantly-more-prone-to-fires-than-evs/ (accessed 2022-07-05).
- (7) Tesla Model S Catches Fire in Los Gatos, Reignites Hours Later at Tow Yard NBC Bay Area. https://www.nbcbayarea.com/news/local/tesla-vehicle-catches-fire-in-losgatos/200148/ (accessed 2022-07-05).
- (8) Inoue, T.; Mukai, K. Are All-Solid-State Lithium-Ion Batteries Really Safe?—verification by Differential Scanning Calorimetry with an All-Inclusive Microcell. *ACS Appl. Mater. Interfaces* **2017**, *9* (2), 1507–1515. https://doi.org/10.1021/acsami.6b13224.

- (9) Yang, X.; Adair, K. R.; Gao, X.; Sun, X. Recent Advances and Perspectives on Thin Electrolytes for High-Energy-Density Solid-State Lithium Batteries. *Energy Environ*. *Sci.* Royal Society of Chemistry 2021, pp 643–671. https://doi.org/10.1039/d0ee02714f.
- (10) Chen, T.; Zhang, L.; Zhang, Z.; Li, P.; Wang, H.; Yu, C.; Yan, X.; Wang, L.; Xu, B. Argyrodite Solid Electrolyte with a Stable Interface and Superior Dendrite Suppression Capability Realized by ZnO Co-Doping. ACS Appl. Mater. Interfaces 2019, 11 (43), 40808–40816. https://doi.org/10.1021/acsami.9b13313.
- (11) Nitta, N.; Wu, F.; Lee, J. T.; Yushin, G. Li-Ion Battery Materials: Present and Future.

 Mater. Today.* Elsevier B.V. 2015, 252–264.

 https://doi.org/10.1016/j.mattod.2014.10.040.
- (12) Grey, C. P.; Hall, D. S. Prospects for Lithium-Ion Batteries and beyond—a 2030 Vision.

 Nat. Commun. 2020. https://doi.org/10.1038/s41467-020-19991-4.
- (13) Nishi, Y. Lithium Ion Secondary Batteries; Past 10 Years and the Future. *J. Power Sources.* **2001**, *100* (1–2), 101–106. https://doi.org/10.1016/S0378-7753(01)00887-4.
- (14) Xu, X.; Han, X.; Lu, L.; Wang, F.; Yang, M.; Liu, X.; Wu, Y.; Tang, S.; Hou, Y.; Hou, J.; Yu, C.; Ouyang, M. Challenges and Opportunities toward Long-Life Lithium-Ion Batteries. J. Power Sources. 2024, 603, 234445. https://doi.org/10.1016/j.jpowsour.2024.234445.
- (15) Masias, A.; Marcicki, J.; Paxton, W. A. Opportunities and Challenges of Lithium Ion Batteries in Automotive Applications. *ACS Energy Lett.* **2021**, *6* (2), 621–630. https://doi.org/10.1021/acsenergylett.0c02584.

- (16) Cheng, X.-B.; Zhang, R.; Zhao, C.-Z.; Zhang, Q. Toward Safe Lithium Metal Anode in Rechargeable Batteries: A Review. *Chem. Rev.* **2017**, *117* (15), 10403–10473. https://doi.org/10.1021/acs.chemrev.7b00115.
- (17) Xu, W.; Wang, J.; Ding, F.; Chen, X.; Nasybulin, E.; Zhang, Y.; Zhang, J.-G. Lithium Metal Anodes for Rechargeable Batteries. *Energy Environ. Sci.* **2014**, *7* (2), 513–537. https://doi.org/10.1039/C3EE40795K.
- (18) Xu, J.; Cai, X.; Cai, S.; Shao, Y.; Hu, C.; Lu, S.; Ding, S. High-Energy Lithium-Ion Batteries: Recent Progress and a Promising Future in Applications. *ENERGY Environ*. *Mater.* **2023**, *6* (5). https://doi.org/10.1002/eem2.12450.
- (19) Shaibani, M.; Majumder, M. Lithium–Sulfur Battery. In *Storing Energy*; Elsevier, **2022**; pp 309–328. https://doi.org/10.1016/B978-0-12-824510-1.00024-6.
- (20) Eftekhari, A. High-Energy Aqueous Lithium Batteries. *Adv. Energy Mater.* **2018**, *8* (24). https://doi.org/10.1002/aenm.201801156.
- (21) Li, W.; Yao, H.; Yan, K.; Zheng, G.; Liang, Z.; Chiang, Y.-M.; Cui, Y. The Synergetic Effect of Lithium Polysulfide and Lithium Nitrate to Prevent Lithium Dendrite Growth.

 Nat. Commun. 2015, 6 (1), 7436. https://doi.org/10.1038/ncomms8436.
- (22) Vimmerstedt, L. J.; Ring, S.; Hammel, C. J. Current Status of Environmental, Health, and Safety Issues of Lithium Ion Electric Vehicle Batteries; 1995.
- (23) Xia, S.; Wu, X.; Zhang, Z.; Cui, Y.; Liu, W. Practical Challenges and Future Perspectives of All-Solid-State Lithium-Metal Batteries. *Chem.* **2019**, *5* (4), 753–785. https://doi.org/10.1016/j.chempr.2018.11.013.
- (24) Schnell, J.; Tietz, F.; Singer, C.; Hofer, A.; Billot, N.; Reinhart, G. Prospects of Production Technologies and Manufacturing Costs of Oxide-Based All-Solid-State

- Lithium Batteries. *Energy Environ. Sci.* **2019**, *12* (6), 1818–1833. https://doi.org/10.1039/C8EE02692K.
- (25) Sung, J.; Heo, J.; Kim, D.-H.; Jo, S.; Ha, Y.-C.; Kim, D.; Ahn, S.; Park, J.-W. Recent Advances in All-Solid-State Batteries for Commercialization. *Mater. Chem. Front.* **2024**, 8 (8), 1861–1887. https://doi.org/10.1039/D3QM01171B.
- (26) Morales, D. J.; Greenbaum, S. NMR Investigations of Crystalline and Glassy Solid Electrolytes for Lithium Batteries: A Brief Review. *Int. J. Mol. Sci.* 2020, 21 (9). https://doi.org/10.3390/ijms21093402.
- Wang, S.; Xu, X.; Zhang, X.; Xin, C.; Xu, B.; Li, L.; Lin, Y. H.; Shen, Y.; Li, B.; Nan,
 C. W. High-Performance Li6PS5Cl-Based All-Solid-State Lithium-Ion Batteries. *J. Mater. Chem. A* 2019, 7 (31), 18612–18618. https://doi.org/10.1039/c9ta04289j.
- (28) Choi, E.; Jo, J.; Kim, W.; Min, K. Searching for Mechanically Superior Solid-State Electrolytes in Li-Ion Batteries via Data-Driven Approaches. *ACS Appl. Mater. Interfaces.* **2021**. https://doi.org/10.1021/acsami.1c07999.
- (29) Ohno, S.; Banik, A.; Dewald, G. F.; Kraft, M. A.; Krauskopf, T.; Minafra, N.; Till, P.; Weiss, M.; Zeier, W. G. Materials Design of Ionic Conductors for Solid State Batteries.

 Prog. Energy. 2020, 2 (2), 022001. https://doi.org/10.1088/2516-1083/ab73dd.
- (30) Lin, L.-Y.; Chen, C.-C. Accurate Characterization of Transference Numbers in Electrolyte Systems. *J. Power Sources.* **2024**, *603*, 234236. https://doi.org/10.1016/j.jpowsour.2024.234236.
- (31) Kato, Y.; Hori, S.; Saito, T.; Suzuki, K.; Hirayama, M.; Mitsui, A.; Yonemura, M.; Iba,
 H.; Kanno, R. High-Power All-Solid-State Batteries Using Sulfide Superionic
 Conductors. *Nat. Energy.* 2016, *1* (4), 16030. https://doi.org/10.1038/nenergy.2016.30.

- (32) Krauskopf, T.; Mogwitz, B.; Rosenbach, C.; Zeier, W. G.; Janek, J. Diffusion Limitation of Lithium Metal and Li–Mg Alloy Anodes on LLZO Type Solid Electrolytes as a Function of Temperature and Pressure. *Adv. Energy Mater.* **2019**, *9* (44). https://doi.org/10.1002/aenm.201902568.
- (33) Bielefeld, A.; Weber, D. A.; Janek, J. Modeling Effective Ionic Conductivity and Binder Influence in Composite Cathodes for All-Solid-State Batteries. *ACS Appl. Mater. Interfaces.* **2020**, *12* (11), 12821–12833. https://doi.org/10.1021/acsami.9b22788.
- (34) Minnmann, P.; Quillman, L.; Burkhardt, S.; Richter, F. H.; Janek, J. Editors' Choice—
 Quantifying the Impact of Charge Transport Bottlenecks in Composite Cathodes of AllSolid-State Batteries. *J. Electrochem. Soc.* **2021**, *168* (4), 040537.
 https://doi.org/10.1149/1945-7111/abf8d7.
- (35) Liu, G.; Weng, W.; Zhang, Z.; Wu, L.; Yang, J.; Yao, X. Densified Li 6 PS 5 Cl Nanorods with High Ionic Conductivity and Improved Critical Current Density for All-Solid-State Lithium Batteries. *Nano. Lett.* 2020, 20 (9), 6660–6665. https://doi.org/10.1021/acs.nanolett.0c02489.
- (36) Zhu, L.; Wang, Y.; Chen, J.; Li, W.; Wang, T.; Wu, J.; Han, S.; Xia, Y.; Wu, Y.; Wu, M.; Wang, F.; Zheng, Y.; Peng, L.; Liu, J.; Chen, L.; Tang, W. Enhancing Ionic Conductivity in Solid Electrolyte by Relocating Diffusion Ions to Under-Coordination Sites. Sci. Adv. 2022, 8 (11). https://doi.org/10.1126/sciadv.abj7698.
- (37) Yao, X.; Huang, B.; Yin, J.; Peng, G.; Huang, Z.; Gao, C.; Liu, D.; Xu, X. All-Solid-State Lithium Batteries with Inorganic Solid Electrolytes: Review of Fundamental Science. *Chinese Phys. B.* **2016**, *25* (1), 018802. https://doi.org/10.1088/1674-1056/25/1/018802.

- (38) Yu, C.; Zhao, F.; Luo, J.; Zhang, L.; Sun, X. Recent Development of Lithium Argyrodite Solid-State Electrolytes for Solid-State Batteries: Synthesis, Structure, Stability and Dynamics. *Nano Energy*. **2021**, 83, 105858. https://doi.org/10.1016/j.nanoen.2021.105858.
- (39) Han, F.; Westover, A. S.; Yue, J.; Fan, X.; Wang, F.; Chi, M.; Leonard, D. N.; Dudney, N. J.; Wang, H.; Wang, C. High Electronic Conductivity as the Origin of Lithium Dendrite Formation within Solid Electrolytes. *Nat. Energy.* 2019, 4 (3), 187–196. https://doi.org/10.1038/s41560-018-0312-z.
- (40) Liu, J.; Yuan, H.; Liu, H.; Zhao, C.; Lu, Y.; Cheng, X.; Huang, J.; Zhang, Q. Unlocking the Failure Mechanism of Solid State Lithium Metal Batteries. *Adv. Energy Mater.* **2022**, *12* (4). https://doi.org/10.1002/aenm.202100748.
- (41) Janek, J.; Zeier, W. G. A Solid Future for Battery Development. *Nat. Energy.* 2016, 1(9), 16141. https://doi.org/10.1038/nenergy.2016.141.
- (42) Diallo, M. S.; Shi, T.; Zhang, Y.; Peng, X.; Shozib, I.; Wang, Y.; Miara, L. J.; Scott, M. C.; Tu, Q. H.; Ceder, G. Effect of Solid-Electrolyte Pellet Density on Failure of Solid-State Batteries. *Nat. Commun.* 2024, *15* (1), 858. https://doi.org/10.1038/s41467-024-45030-7.
- (43) Albertus, P.; Babinec, S.; Litzelman, S.; Newman, A. Status and Challenges in Enabling the Lithium Metal Electrode for High-Energy and Low-Cost Rechargeable Batteries.

 Nat. Energy. 2017, 3 (1), 16–21. https://doi.org/10.1038/s41560-017-0047-2.
- (44) Tan, D. H. S.; Meng, Y. S.; Jang, J. Scaling up High-Energy-Density Sulfidic Solid-State Batteries: A Lab-to-Pilot Perspective. *Joule.* **2022**, *6* (8), 1755–1769. https://doi.org/10.1016/j.joule.2022.07.002.

- (45) Zhao, B.; Lu, Y.; Yuan, B.; Wang, Z.; Han, X. Preparation of Free-Standing Li3InCl6 Solid Electrolytes Film with Infiltration-Method Enable Roll-to-Roll Manufacture.

 Mater. Lett. 2022, 310, 131463. https://doi.org/10.1016/j.matlet.2021.131463.
- (46) Chen, A.; Qu, C.; Shi, Y.; Shi, F. Manufacturing Strategies for Solid Electrolyte in Batteries. *Front. Energy Res.* **2020**, *8*. https://doi.org/10.3389/fenrg.2020.571440.
- (47) Hatzell, K. B.; Zheng, Y. Prospects on Large-Scale Manufacturing of Solid State Batteries. *MRS Energy Sustain*. **2021**, *8* (1), 33–39. https://doi.org/10.1557/s43581-021-00004-w.
- (48) Cheng, L.; Chen, W.; Kunz, M.; Persson, K.; Tamura, N.; Chen, G.; Doeff, M. Effect of Surface Microstructure on Electrochemical Performance of Garnet Solid Electrolytes.
 ACS Appl. Mater. Interfaces. 2015, 7 (3), 2073–2081.
 https://doi.org/10.1021/am508111r.
- (49) Tsai, C.-L.; Roddatis, V.; Chandran, C. V.; Ma, Q.; Uhlenbruck, S.; Bram, M.; Heitjans,
 P.; Guillon, O. Li 7 La 3 Zr 2 O 12 Interface Modification for Li Dendrite Prevention.
 ACS Appl. Mater. Interfaces. 2016, 8 (16), 10617–10626.
 https://doi.org/10.1021/acsami.6b00831.
- (50) Zhang, W.; Weber, D. A.; Weigand, H.; Arlt, T.; Manke, I.; Schröder, D.; Koerver, R.; Leichtweiss, T.; Hartmann, P.; Zeier, W. G.; Janek, J. Interfacial Processes and Influence of Composite Cathode Microstructure Controlling the Performance of All-Solid-State Lithium Batteries. ACS Appl. Mater. Interfaces. 2017, 9 (21), 17835–17845. https://doi.org/10.1021/acsami.7b01137.
- (51) Famprikis, T.; Canepa, P.; Dawson, J. A.; Islam, M. S.; Masquelier, C. Fundamentals of Inorganic Solid-State Electrolytes for Batteries. *Nat. Mater.* 2019, 18 (12), 1278–1291. https://doi.org/10.1038/s41563-019-0431-3.

- (52) Li, S.; Zhang, S.; Shen, L.; Liu, Q.; Ma, J.; Lv, W.; He, Y.; Yang, Q. Progress and Perspective of Ceramic/Polymer Composite Solid Electrolytes for Lithium Batteries. *Adv. Sci.* **2020**, *7* (5). https://doi.org/10.1002/advs.201903088.
- (53) Umair, M.; Zhou, S.; Li, W.; Rana, H. T. H.; Yang, J.; Cheng, L.; Li, M.; Yu, S.; Wei, J. Oxide Solid Electrolytes in Solid-State Batteries. *Batter. Supercaps.* 2024. https://doi.org/10.1002/batt.202400667.
- (54) Goodenough, J. B.; Hong, H. Y.-P.; Kafalas, J. A. Fast Na+-Ion Transport in Skeleton Structures. *Mater. Res. Bull.* **1976**, *11* (2), 203–220. https://doi.org/10.1016/0025-5408(76)90077-5.
- (55) Murugan, R.; Thangadurai, V.; Weppner, W. Fast Lithium Ion Conduction in Garnet-Type Li 7 La 3 Zr 2 O 12. *Angew. Chemie Int. Ed.* **2007**, *46* (41), 7778–7781. https://doi.org/10.1002/anie.200701144.
- (56) Zhu, J.; Wu, Y.; Zhang, H.; Xie, X.; Yang, Y.; Peng, H.; Liang, X.; Qi, Q.; Lin, W.; Peng, D.-L.; Wang, L.; Lin, J. Impact of Compaction Pressure on Formation and Performance of Garnet-Based Solid-State Lithium Batteries. *Energy Mater.* 2025, 5 (4). https://doi.org/10.20517/energymater.2024.201.
- (57) Weppner, W.; Huggins, R. A. Ionic Conductivity of Solid and Liquid LiAlCl4. *J. Electrochem. Soc.* **1977**, *124* (1), 35–38. https://doi.org/10.1149/1.2133238.
- (58) Asano, T.; Sakai, A.; Ouchi, S.; Sakaida, M.; Miyazaki, A.; Hasegawa, S. Solid Halide Electrolytes with High Lithium-Ion Conductivity for Application in 4 V Class Bulk-Type All-Solid-State Batteries. *Adv. Mater.* **2018**, *30* (44). https://doi.org/10.1002/adma.201803075.

- (59) Nie, B.; Wang, T.-W.; Sun, H. Cold Sintering of Halide-in-Oxide Composite Solid-State Electrolytes. July 23, **2024**. https://doi.org/10.26434/chemrxiv-2024-nqsh2.
- (60) Xu, R.; Wu, Y.; Dong, Z.; Zheng, R.; Song, Z.; Wang, Z.; Sun, H.; Liu, Y.; Zhang, L. Halide Solid Electrolytes in All-Solid-State Batteries: Ion Transport Kinetics, Failure Mechanisms and Improvement Strategies. *Nano Energy.* 2024, 132, 110435. https://doi.org/10.1016/j.nanoen.2024.110435.
- (61) Zhang, Q.; Cao, D.; Ma, Y.; Natan, A.; Aurora, P.; Zhu, H. Sulfide-Based Solid-State Electrolytes: Synthesis, Stability, and Potential for All-Solid-State Batteries. *Adv. Mater.* 2019, 31 (44). https://doi.org/10.1002/adma.201901131.
- (62) Liu, Y.; Sun, Q.; Wang, D.; Adair, K.; Liang, J.; Sun, X. Development of the Cold Sintering Process and Its Application in Solid-State Lithium Batteries. *J. Power Sources*.
 2018, 393, 193–203. https://doi.org/10.1016/j.jpowsour.2018.05.015.
- (63) Doux, J. M.; Yang, Y.; Tan, D. H. S.; Nguyen, H.; Wu, E. A.; Wang, X.; Banerjee, A.; Meng, Y. S. Pressure Effects on Sulfide Electrolytes for All Solid-State Batteries. J. Mater. Chem. A Mater. 2020, 8 (10), 5049–5055. https://doi.org/10.1039/c9ta12889a.
- (64) Kamaya, N.; Homma, K.; Yamakawa, Y.; Hirayama, M.; Kanno, R.; Yonemura, M.; Kamiyama, T.; Kato, Y.; Hama, S.; Kawamoto, K.; Mitsui, A. A Lithium Superionic Conductor. *Nat. Mater.* 2011, 10 (9), 682–686. https://doi.org/10.1038/nmat3066.
- (65) Mercier, R.; Malugani, J.-P.; Fahys, B.; Robert, G. Superionic Conduction in Li 2 S P 2 S 5 - LiI - Glasses. *Solid State Ionics* 1981, 5, 663–666. https://doi.org/10.1016/0167-2738(81)90341-6.
- (66) Feng, X.; Chien, P.-H. H.; Wang, Y.; Patel, S.; Wang, P.; Liu, H.; Immediato-Scuotto, M.; Hu, Y.-Y. Y. Enhanced Ion Conduction by Enforcing Structural Disorder in Li-

- Deficient Argyrodites Li6-xPS5-xC11+x. *Energy Storage Mater.* **2020**, *30*, 67–73. https://doi.org/10.1016/j.ensm.2020.04.042.
- (67) Funke, K. Solid State Ionics: From Michael Faraday to Green Energy—the European Dimension. *Sci. Technol. Adv. Mater.* **2013**, *14* (4), 043502. https://doi.org/10.1088/1468-6996/14/4/043502.
- (68) Deiseroth, H.; Kong, S.; Eckert, H.; Vannahme, J.; Reiner, C.; Zaiß, T.; Schlosser, M. Li 6 PS 5 X: A Class of Crystalline Li-Rich Solids With an Unusually High Li + Mobility.

 Angew. Chemie Int. Ed. 2008, 47 (4), 755–758. https://doi.org/10.1002/anie.200703900.
- (69) Xiao, Y.; Wang, Y.; Bo, S.-H.; Kim, J. C.; Miara, L. J.; Ceder, G. Understanding Interface Stability in Solid-State Batteries. *Nat. Rev. Mater.* 2019, 5 (2), 105–126. https://doi.org/10.1038/s41578-019-0157-5.
- (70) Mangani, L. R.; Villevieille, C. Mechanical vs. Chemical Stability of Sulphide-Based Solid-State Batteries. Which One Is the Biggest Challenge to Tackle? Overview of Solid-State Batteries and Hybrid Solid State Batteries. *J. Mater. Chem. A Mater.* **2020**, 8 (20), 10150–10167. https://doi.org/10.1039/D0TA02984J.
- (71) Zhou, Y.; Doerrer, C.; Kasemchainan, J.; Bruce, P. G.; Pasta, M.; Hardwick, L. J. Observation of Interfacial Degradation of Li6PS5Cl against Lithium Metal and LiCoO2 via In Situ Electrochemical Raman Microscopy. *Batter. Supercaps.* 2020, 3 (7), 647–652. https://doi.org/10.1002/batt.201900218.
- (72) Chen, Y. T.; Marple, M. A. T.; Tan, D. H. S.; Ham, S. Y.; Sayahpour, B.; Li, W. K.; Yang, H.; Lee, J. B.; Hah, H. J.; Wu, E. A.; Doux, J. M.; Jang, J.; Ridley, P.; Cronk, A.; Deysher, G.; Chen, Z.; Meng, Y. S. Investigating Dry Room Compatibility of Sulfide Solid-State Electrolytes for Scalable Manufacturing. *J. Mater. Chem. A Mater.* 2022, 10 (13), 7155–7164. https://doi.org/10.1039/d1ta09846b.

- (73) Kim, K. J.; Balaish, M.; Wadaguchi, M.; Kong, L.; Rupp, J. L. M. Solid-State Li-Metal Batteries: Challenges and Horizons of Oxide and Sulfide Solid Electrolytes and Their Interfaces. *Adv. Energy Mater*. Wiley-VCH Verlag January 1, **2021**. https://doi.org/10.1002/aenm.202002689.
- (74) Kodama, M.; Komiyama, S.; Ohashi, A.; Horikawa, N.; Kawamura, K.; Hirai, S. High-Pressure in Situ X-Ray Computed Tomography and Numerical Simulation of Sulfide Solid Electrolyte. *J. Power Sources.* 2020, 462. https://doi.org/10.1016/j.jpowsour.2020.228160.
- (75) Randrema, X.; Barcha, C.; Chakir, M.; Viallet, V.; Morcrette, M. A Detailed Characterisation Study of Li6PS5Cl Ionic Conductors from Several Synthetic Routes. *Solid State Sci.* **2021**, *118*. https://doi.org/10.1016/j.solidstatesciences.2021.106681.
- (76) *mp-985592: Li6PS5Cl (cubic, F-43m, 216)*. https://materialsproject.org/materials/mp-985592/ (accessed 2022-07-13).
- (77) Li, J.; Kim, S.; Mezzomo, L.; Chart, Y.; Aspinall, J.; Ruffo, R.; Pasta, M. Processing-Structure-Property Relationships in Practical Thin Solid-Electrolyte Separators for All-Solid-State Batteries. *J. Phys. Energy.* **2024**, *6* (2), 025023. https://doi.org/10.1088/2515-7655/ad3d0b.
- (78) Schlautmann, E.; Weiß, A.; Maus, O.; Ketter, L.; Rana, M.; Puls, S.; Nickel, V.; Gabbey, C.; Hartnig, C.; Bielefeld, A.; Zeier, W. G. Impact of the Solid Electrolyte Particle Size Distribution in Sulfide-Based Solid-State Battery Composites. *Adv. Energy Mater.* **2023**, *13* (41). https://doi.org/10.1002/aenm.202302309.
- (79) Narayanan, S.; Ulissi, U.; Gibson, J. S.; Chart, Y. A.; Weatherup, R. S.; Pasta, M. Effect of Current Density on the Solid Electrolyte Interphase Formation at the

- Lithium|Li6PS5Cl Interface. *Nat. Commun.* **2022**, *13* (1), 7237. https://doi.org/10.1038/s41467-022-34855-9.
- (80) Kasemchainan, J.; Zekoll, S.; Spencer Jolly, D.; Ning, Z.; Hartley, G. O.; Marrow, J.; Bruce, P. G. Critical Stripping Current Leads to Dendrite Formation on Plating in Lithium Anode Solid Electrolyte Cells. *Nat. Mater.* 2019, *18* (10), 1105–1111. https://doi.org/10.1038/s41563-019-0438-9.
- (81) Lu, Y.; Zhao, C.-Z.; Hu, J.-K.; Sun, S.; Yuan, H.; Fu, Z.-H.; Chen, X.; Huang, J.-Q.; Ouyang, M.; Zhang, Q. The Void Formation Behaviors in Working Solid-State Li Metal Batteries. *Sci. Adv.* **2022**, *8* (45). https://doi.org/10.1126/sciadv.add0510.
- (82) Porz, L.; Swamy, T.; Sheldon, B. W.; Rettenwander, D.; Frömling, T.; Thaman, H. L.; Berendts, S.; Uecker, R.; Carter, W. C.; Chiang, Y. Mechanism of Lithium Metal Penetration through Inorganic Solid Electrolytes. *Adv. Energy Mater.* 2017, 7 (20). https://doi.org/10.1002/aenm.201701003.
- (83) Raj, V.; Venturi, V.; Kankanallu, V. R.; Kuiri, B.; Viswanathan, V.; Aetukuri, N. P. B. Direct Correlation between Void Formation and Lithium Dendrite Growth in Solid-State Electrolytes with Interlayers. *Nat. Mater.* **2022**, *21* (9), 1050–1056. https://doi.org/10.1038/s41563-022-01264-8.
- (84) Hu, J.; Young, R. S.; Lukic, B.; Broche, L.; Jervis, R.; Shearing, P. R.; Michiel, M. Di; Withers, P. J.; Rettie, A.; Paul, P. P. Quantifying Heterogeneous Degradation Pathways and Deformation Fields in Solid State Batteries. https://doi.org/10.26434/chemrxiv-2024-pwt3p.
- (85) Aktekin, B.; Kataev, E.; Riegger, L. M.; Garcia-Diez, R.; Chalkley, Z.; Becker, J.; Wilks, R. G.; Henss, A.; Bär, M.; Janek, J. Operando Photoelectron Spectroscopy Analysis of

- Li 6 PS 5 Cl Electrochemical Decomposition Reactions in Solid-State Batteries. *ACS Energy Lett.* **2024**, *9* (7), 3492–3500. https://doi.org/10.1021/acsenergylett.4c01072.
- (86) Tan, D. H. S.; Wu, E. A.; Nguyen, H.; Chen, Z.; Marple, M. A. T.; Doux, J.-M.; Wang, X.; Yang, H.; Banerjee, A.; Meng, Y. S. Elucidating Reversible Electrochemical Redox of Li 6 PS 5 Cl Solid Electrolyte. ACS Energy Lett. 2019, 4 (10), 2418–2427. https://doi.org/10.1021/acsenergylett.9b01693.
- (87) Wenzel, S.; Sedlmaier, S. J.; Dietrich, C.; Zeier, W. G.; Janek, J. Interfacial Reactivity and Interphase Growth of Argyrodite Solid Electrolytes at Lithium Metal Electrodes. *Solid State Ionics.* **2018**, *318*, 102–112. https://doi.org/10.1016/j.ssi.2017.07.005.
- (88) Ning, Z.; Jolly, D. S.; Li, G.; De Meyere, R.; Pu, S. D.; Chen, Y.; Kasemchainan, J.; Ihli, J.; Gong, C.; Liu, B.; Melvin, D. L. R.; Bonnin, A.; Magdysyuk, O.; Adamson, P.; Hartley, G. O.; Monroe, C. W.; Marrow, T. J.; Bruce, P. G. Visualizing Plating-Induced Cracking in Lithium-Anode Solid-Electrolyte Cells. *Nat. Mater.* **2021**, *20* (8), 1121–1129. https://doi.org/10.1038/s41563-021-00967-8.
- (89) Singh, D. K.; Henss, A.; Mogwitz, B.; Gautam, A.; Horn, J.; Krauskopf, T.; Burkhardt, S.; Sann, J.; Richter, F. H.; Janek, J. Li6PS5Cl Microstructure and Influence on Dendrite Growth in Solid-State Batteries with Lithium Metal Anode. *Cell Rep. Phys. Sci.* **2022**, *3* (9), 101043. https://doi.org/10.1016/j.xcrp.2022.101043.
- (90) Ning, Z.; Li, G.; Melvin, D. L. R.; Chen, Y.; Bu, J.; Spencer-Jolly, D.; Liu, J.; Hu, B.;
 Gao, X.; Perera, J.; Gong, C.; Pu, S. D.; Zhang, S.; Liu, B.; Hartley, G. O.; Bodey, A. J.;
 Todd, R. I.; Grant, P. S.; Armstrong, D. E. J.; Marrow, T. J.; Monroe, C. W.; Bruce, P.
 G. Dendrite Initiation and Propagation in Lithium Metal Solid-State Batteries. *Nature*2023, 618 (7964), 287–293. https://doi.org/10.1038/s41586-023-05970-4.

- (91) Shishvan, S. S.; Fleck, N. A.; McMeeking, R. M.; Deshpande, V. S. Void Growth in Metal Anodes in Solid-State Batteries: Recent Progress and Gaps in Understanding. *Eur. J. Mech. A/Solids* 2023, 100. https://doi.org/10.1016/j.euromechsol.2023.104998.
- (92) Hu, B.; Zhang, S.; Ning, Z.; Spencer-Jolly, D.; Melvin, D. L. R.; Gao, X.; Perera, J.; Pu, S. D.; Rees, G. J.; Wang, L.; Yang, L.; Gao, H.; Marathe, S.; Burca, G.; Marrow, T. J.; Bruce, P. G. Deflecting Lithium Dendritic Cracks in Multi-Layered Solid Electrolytes. *Joule.* 2024. https://doi.org/10.1016/j.joule.2024.06.024.
- (93) Arnold, W.; Shreyas, V.; Li, Y.; Koralalage, M. K.; Jasinski, J. B.; Thapa, A.; Sumanasekera, G.; Ngo, A. T.; Narayanan, B.; Wang, H. Synthesis of Fluorine-Doped Lithium Argyrodite Solid Electrolytes for Solid-State Lithium Metal Batteries. ACS Appl. Mater. Interfaces. 2022, 14 (9), 11483–11492. https://doi.org/10.1021/acsami.1c24468.
- (94) Serbessa, G. G.; Taklu, B. W.; Nikodimos, Y.; Temesgen, N. T.; Muche, Z. B.; Merso, S. K.; Yeh, T.-I.; Liu, Y.-J.; Liao, W.-S.; Wang, C.-H.; Wu, S.-H.; Su, W.-N.; Yang, C.-C.; Hwang, B. J. Boosting the Interfacial Stability of the Li 6 PS 5 Cl Electrolyte with a Li Anode via In Situ Formation of a LiF-Rich SEI Layer and a Ductile Sulfide Composite Solid Electrolyte. ACS Appl. Mater. Interfaces. 2024, 16 (8), 10832–10844. https://doi.org/10.1021/acsami.3c14763.
- (95) Ahmed, F.; Chen, A.; Altoé, M. V. P.; Liu, G. Argyrodite-Li 6 PS 5 Cl/Polymer-Based Highly Conductive Composite Electrolyte for All-Solid-State Batteries. *ACS Appl. Energy Mater.* **2024**, *7* (5), 1842–1853. https://doi.org/10.1021/acsaem.3c02858.
- (96) Lei, T.; Peng, L.; Liao, C.; Chen, S.; Cheng, S.; Xie, J. Optimizing Milling and Sintering Parameters for Mild Synthesis of Highly Conductive Li 5.5 PS 4.5 Cl 1.5 Solid

- Electrolyte. *Chem. Commun.* **2023**, *59* (96), 14285–14288. https://doi.org/10.1039/D3CC05099H.
- (97) Adeli, P.; Bazak, J. D.; Park, K. H.; Kochetkov, I.; Huq, A.; Goward, G. R.; Nazar, L. F. Boosting Solid-State Diffusivity and Conductivity in Lithium Superionic Argyrodites by Halide Substitution. *Angew. Chemie.* 2019, 131 (26), 8773–8778. https://doi.org/10.1002/ange.201814222.
- (98) Wang, Y.; Lim, R.; Larson, K.; Knab, A.; Fontecha, D.; Caverly, S.; Song, J.; Park, C.; Albertus, P.; Rubloff, G. W.; Lee, S. B.; Kozen, A. C. Chemical and Electrochemical Characterization of Hot-Pressed Li 6 PS 5 Cl Solid State Electrolyte: Operating Pressure-Invariant High Ionic Conductivity. *ChemSusChem* 2024, 17 (21). https://doi.org/10.1002/cssc.202400718.
- (99) Brissot, C.; Rosso, M.; Chazalviel, J.-N.; Lascaud, S. In Situ Concentration Cartography in the Neighborhood of Dendrites Growing in Lithium/Polymer-Electrolyte/Lithium Cells. *J. Electrochem. Soc.* **1999**, *146* (12), 4393–4400. https://doi.org/10.1149/1.1392649.
- (100) Singh, D. K.; Fuchs, T.; Krempaszky, C.; Mogwitz, B.; Janek, J. Non-Linear Kinetics of The Lithium Metal Anode on Li 6 PS 5 Cl at High Current Density: Dendrite Growth and the Role of Lithium Microstructure on Creep. *Adv. Sci.* **2023**, *10* (22). https://doi.org/10.1002/advs.202302521.
- (101) Rosso, M.; Brissot, C.; Teyssot, A.; Dollé, M.; Sannier, L.; Tarascon, J.-M.; Bouchet, R.; Lascaud, S. Dendrite Short-Circuit and Fuse Effect on Li/Polymer/Li Cells. *Electrochim. Acta.* 2006, 51 (25), 5334–5340. https://doi.org/10.1016/j.electacta.2006.02.004.

- (102) Harry, K. J.; Hallinan, D. T.; Parkinson, D. Y.; MacDowell, A. A.; Balsara, N. P. Detection of Subsurface Structures underneath Dendrites Formed on Cycled Lithium Metal Electrodes. *Nat. Mater.* 2014, *13* (1), 69–73. https://doi.org/10.1038/nmat3793.
- (103) Yamamoto, K.; Liu, X.; Park, J.; Watanabe, T.; Takami, T.; Sakuda, A.; Hayashi, A.; Tastumisago, M.; Uchimoto, Y. Lithium Dendrite Formation inside Li 3 PS 4 Solid Electrolyte Observed Via Multimodal/Multiscale Operando X-Ray Computed Tomography. ECS Meeting Abstracts 2023, MA2023-02 (4), 739–739. https://doi.org/10.1149/MA2023-024739mtgabs.
- (104) Park, Y.; Park, J.; Yamamoto, K.; Matsunaga, T.; Watanabe, T.; Uchimoto, Y. Investigating the Mechanisms of Li Dendrite Formation in Sulfide Solid Electrolytes for All-Solid-State Batteries. *ECS Meeting Abstracts* **2023**, *MA2023-02* (4), 725–725. https://doi.org/10.1149/MA2023-024725mtgabs.
- (105) Hao, S.; Daemi, S. R.; Heenan, T. M. M.; Du, W.; Tan, C.; Storm, M.; Rau, C.; Brett, D. J. L.; Shearing, P. R. Tracking Lithium Penetration in Solid Electrolytes in 3D by In-Situ Synchrotron X-Ray Computed Tomography. *Nano Energy* 2021, 82, 105744. https://doi.org/10.1016/j.nanoen.2021.105744.
- (106) Hao, S.; Bailey, J. J.; Iacoviello, F.; Bu, J.; Grant, P. S.; Brett, D. J. L.; Shearing, P. R.
 3D Imaging of Lithium Protrusions in Solid-State Lithium Batteries Using X-Ray
 Computed Tomography. *Adv. Funct. Mater.* 2021, 31 (10).
 https://doi.org/10.1002/adfm.202007564.
- (107) Villevieille, C.; Thompson, O.; Vaughan, G. Revealing the Spatial Distribution of Decomposition Products upon Ageing on Li6PS5Cl Solid Electrolyte via X-Ray Diffraction Computed Tomography. October 28, 2024. https://doi.org/10.21203/rs.3.rs-5191594/v1.

- (108) De Gol, A.; Dermenci, K. B.; Farkas, L.; Berecibar, M. Electro-Chemo-Mechanical Degradation in Solid-State Batteries: A Review of Microscale and Multiphysics Modeling. *Adv. Energy Mater.* **2024**, *14* (47). https://doi.org/10.1002/aenm.202403255.
- (109) Zhang, D. L. Processing of Advanced Materials Using High-Energy Mechanical Milling. *Prog. Mater. Sci.* **2004**, Vol. 49, pp 537–560. https://doi.org/10.1016/S0079-6425(03)00034-3.
- (110) Park, Y. S.; Lee, J. M.; Yi, E. J.; Moon, J. W.; Hwang, H. All-Solid-State Lithium-Ion Batteries with Oxide/Sulfide Composite Electrolytes. *Materials*. **2021**, *14* (8). https://doi.org/10.3390/ma14081998.
- (111) Yu, C.; van Eijck, L.; Ganapathy, S.; Wagemaker, M. Synthesis, Structure and Electrochemical Performance of the Argyrodite Li 6 PS 5 Cl Solid Electrolyte for Li-Ion Solid State Batteries. *Electrochim. Acta.* **2016**, *215*, 93–99. https://doi.org/10.1016/j.electacta.2016.08.081.
- (112) Kang, H.; Lim, C.; Li, T.; Fu, Y.; Yan, B.; Houston, N.; De Andrade, V.; De Carlo, F.; Zhu, L. Geometric and Electrochemical Characteristics of LiNi1/3Mn1/3Co1/3O2 Electrode with Different Calendering Conditions. *Electrochim. Acta.* **2017**, *232*, 431–438. https://doi.org/10.1016/j.electacta.2017.02.151.
- (113) Wan, Z.; Pannala, S.; Solbrig, C.; Garrick, T. R.; Stefanopoulou, A. G.; Siegel, J. B. Degradation and Expansion of Lithium-Ion Batteries with Silicon/Graphite Anodes: Impact of Pretension, Temperature, C-Rate and State-of-Charge Window. eTransportation. 2025, 24, 100416. https://doi.org/10.1016/j.etran.2025.100416.
- (114) Randau, S.; Weber, D. A.; Kötz, O.; Koerver, R.; Braun, P.; Weber, A.; Ivers-Tiffée, E.; Adermann, T.; Kulisch, J.; Zeier, W. G.; Richter, F. H.; Janek, J. Benchmarking the

- Performance of All-Solid-State Lithium Batteries. *Nat. Energy.* **2020**, *5* (3), 259–270. https://doi.org/10.1038/s41560-020-0565-1.
- (115) PFA Swagelok Tube Fitting, Union, 1/8 in. Tube Fitting. https://products.swagelok.com/en/c/straights/p/PFA-220-6.
- (116) Flatscher, F.; Philipp, M.; Ganschow, S.; Wilkening, H. M. R.; Rettenwander, D. The Natural Critical Current Density Limit for Li7La3Zr2O12garnets. *J. Mater. Chem. A Mater.* **2020**, *8* (31), 15782–15788. https://doi.org/10.1039/c9ta14177d.
- (117) Ham, S. Y.; Yang, H.; Nunez-cuacuas, O.; Tan, D. H. S.; Chen, Y. T.; Deysher, G.; Cronk, A.; Ridley, P.; Doux, J. M.; Wu, E. A.; Jang, J.; Meng, Y. S. Assessing the Critical Current Density of All-Solid-State Li Metal Symmetric and Full Cells. *Energy Storage Mater.* **2023**, *55*, 455–462. https://doi.org/10.1016/j.ensm.2022.12.013.
- (118) Aurbach, D. A Short Review of Failure Mechanisms of Lithium Metal and Lithiated Graphite Anodes in Liquid Electrolyte Solutions. *Solid State Ionics*. **2002**, *148* (3–4), 405–416. https://doi.org/10.1016/S0167-2738(02)00080-2.
- (119) Liu, Z.; Qi, Y.; Lin, Y. X.; Chen, L.; Lu, P.; Chen, L. Q. Interfacial Study on Solid Electrolyte Interphase at Li Metal Anode: Implication for Li Dendrite Growth. *J. Electrochem. Soc.* **2016**, *163* (3), A592–A598. https://doi.org/10.1149/2.0151605jes.
- (120) Tron, A.; Orue, A.; López-Aranguren, P.; Beutl, A. Critical Current Density Measurements of Argyrodite Li 6 PS 5 Cl Solid Electrolyte at Ambient Pressure. *J. Electrochem. Soc.* **2023**, *170* (10), 100525. https://doi.org/10.1149/1945-7111/ad01e3.
- (121) Wang, Y.; Hao, H.; Naik, K. G.; Vishnugopi, B. S.; Fincher, C. D.; Yan, Q.; Raj, V.;
 Celio, H.; Yang, G.; Fang, H.; Chiang, Y.; Perras, F. A.; Jena, P.; Watt, J.; Mukherjee,
 P. P.; Mitlin, D. Mechanical Milling Induced Microstructure Changes in Argyrodite

- LPSCl Solid-State Electrolyte Critically Affect Electrochemical Stability. *Adv. Energy Mater.* **2024**, *14* (23). https://doi.org/10.1002/aenm.202304530.
- (122) M. E. Orazem; B. Tribollet. Electrochemical Impedance Spectroscopy; 2017.
- (123) A. Lasia. Electrochemical Impedance Spectroscopy and Its Applications; 2014.
- (124) Vadhva, P.; Hu, J.; Johnson, M. J.; Stocker, R.; Braglia, M.; Brett, D. J. L.; Rettie, A. J. E. Electrochemical Impedance Spectroscopy for All-Solid-State Batteries: Theory, Methods and Future Outlook. *ChemElectroChem*. John Wiley and Sons Inc June 1, 2021, pp 1930–1947. https://doi.org/10.1002/celc.202100108.
- (125) Fan, B.; Guan, Z.; Wang, H.; Wu, L.; Li, W.; Zhang, S.; Xue, B. Electrochemical Processes in All-Solid-State Li-S Batteries Studied by Electrochemical Impedance Spectroscopy. *Solid State Ionics*. **2021**, *368*. https://doi.org/10.1016/j.ssi.2021.115680.
- (126) Kim, J.; Kim, M. J.; Kim, J.; Lee, J. W.; Park, J.; Wang, S. E.; Lee, S.; Kang, Y. C.; Paik, U.; Jung, D. S.; Song, T. High-Performance All-Solid-State Batteries Enabled by Intimate Interfacial Contact Between the Cathode and Sulfide-Based Solid Electrolytes. Adv. Funct. Mater. 2023, 33 (12). https://doi.org/10.1002/adfm.202211355.
- (127) Cañas, N. A.; Hirose, K.; Pascucci, B.; Wagner, N.; Friedrich, K. A.; Hiesgen, R. Investigations of Lithium–Sulfur Batteries Using Electrochemical Impedance Spectroscopy. *Electrochim. Acta.* 2013, 97, 42–51. https://doi.org/10.1016/j.electacta.2013.02.101.
- (128) Spencer Jolly, D.; Ning, Z.; Hartley, G. O.; Liu, B.; Melvin, D. L. R.; Adamson, P.; Marrow, J.; Bruce, P. G. Temperature Dependence of Lithium Anode Voiding in Argyrodite Solid-State Batteries. ACS Appl. Mater. Interfaces. 2021, 13 (19), 22708–22716. https://doi.org/10.1021/acsami.1c06706.

- (129) Hikima, K.; Huy Phuc, N. H.; Tsukasaki, H.; Mori, S.; Muto, H.; Matsuda, A. High Ionic Conductivity of Multivalent Cation Doped Li 6 PS 5 Cl Solid Electrolytes Synthesized by Mechanical Milling. *RSC Adv.* **2020**, *10* (38), 22304–22310. https://doi.org/10.1039/D0RA02545C.
- (130) Choi, Y. J.; Kim, S.-I.; Son, M.; Lee, J. W.; Lee, D. H. Cl- and Al-Doped Argyrodite Solid Electrolyte Li6PS5Cl for All-Solid-State Lithium Batteries with Improved Ionic Conductivity. *Nanomaterials* **2022**, *12* (24), 4355. https://doi.org/10.3390/nano12244355.
- (131) Yubuchi, S.; Uematsu, M.; Deguchi, M.; Hayashi, A.; Tatsumisago, M. Lithium-Ion-Conducting Argyrodite-Type Li 6 PS 5 X (X = Cl, Br, I) Solid Electrolytes Prepared by a Liquid-Phase Technique Using Ethanol as a Solvent. *ACS Appl. Energy Mater.* **2018**, *1* (8), 3622–3629. https://doi.org/10.1021/acsaem.8b00280.
- (132) Zhou, L.; Park, K.-H.; Sun, X.; Lalère, F.; Adermann, T.; Hartmann, P.; Nazar, L. F. Solvent-Engineered Design of Argyrodite Li 6 PS 5 X (X = Cl, Br, I) Solid Electrolytes with High Ionic Conductivity. *ACS Energy Lett.* **2019**, *4* (1), 265–270. https://doi.org/10.1021/acsenergylett.8b01997.
- (133) Rajagopal, R.; Subramanian, Y.; Jung, Y. J.; Kang, S.; Ryu, K.-S. Rapid Synthesis of Highly Conductive Li 6 PS 5 Cl Argyrodite-Type Solid Electrolytes Using Pyridine Solvent. *ACS Appl. Energy Mater.* **2022**, 5 (8), 9266–9272. https://doi.org/10.1021/acsaem.2c01157.
- (134) Adeli, P.; Bazak, J. D.; Park, K. H.; Kochetkov, I.; Huq, A.; Goward, G. R.; Nazar, L. F. Boosting Solid-State Diffusivity and Conductivity in Lithium Superionic Argyrodites by Halide Substitution. *Angew. Chemie Int. Ed.* 2019, 58 (26), 8681–8686. https://doi.org/10.1002/anie.201814222.

- (135) Rao, R. P.; Adams, S. Studies of Lithium Argyrodite Solid Electrolytes for All-solid-state Batteries. *Phys. status solidi.* **2011**, *208* (8), 1804–1807. https://doi.org/10.1002/pssa.201001117.
- (136) Yubuchi, S.; Teragawa, S.; Aso, K.; Tadanaga, K.; Hayashi, A.; Tatsumisago, M. Preparation of High Lithium-Ion Conducting Li6PS5Cl Solid Electrolyte from Ethanol Solution for All-Solid-State Lithium Batteries. *J. Power Sources.* 2015, 293, 941–945. https://doi.org/10.1016/j.jpowsour.2015.05.093.
- (137) Yu, C.; Li, Y.; Willans, M.; Zhao, Y.; Adair, K. R.; Zhao, F.; Li, W.; Deng, S.; Liang, J.; Banis, M. N.; Li, R.; Huang, H.; Zhang, L.; Yang, R.; Lu, S.; Huang, Y.; Sun, X. Superionic Conductivity in Lithium Argyrodite Solid-State Electrolyte by Controlled Cl-Doping. *Nano Energy* **2020**, *69*, 104396. https://doi.org/10.1016/j.nanoen.2019.104396.
- (138) Kang, S. H.; Kim, J. Y.; Shin, D. O.; Lee, M. J.; Lee, Y.-G. 2D Argyrodite LPSCl Solid Electrolyte for All-Solid-State Li-Ion Battery Using Reduced Graphene Oxide Template.

 Mater. Today Energy. 2022, 23, 100913. https://doi.org/10.1016/j.mtener.2021.100913.
- (139) Rosero-Navarro, N. C.; Niwa, H.; Miura, A.; Tadanaga, K. Two-Step Liquid-Phase Synthesis of Argyrodite Li6PS5Cl Solid Electrolyte Using Nonionic Surfactant. *Boletín la Soc. Española Cerámica y Vidr.* **2023**, *62* (2), 187–193. https://doi.org/10.1016/j.bsecv.2021.12.001.
- (140) Boulineau, S.; Courty, M.; Tarascon, J.-M.; Viallet, V. Mechanochemical Synthesis of Li-Argyrodite Li6PS5X (X=Cl, Br, I) as Sulfur-Based Solid Electrolytes for All Solid State Batteries Application. *Solid State Ionics*. **2012**, 221, 1–5. https://doi.org/10.1016/j.ssi.2012.06.008.

- (141) Bachman, J. C.; Muy, S.; Grimaud, A.; Chang, H.-H.; Pour, N.; Lux, S. F.; Paschos, O.; Maglia, F.; Lupart, S.; Lamp, P.; Giordano, L.; Shao-Horn, Y. Inorganic Solid-State Electrolytes for Lithium Batteries: Mechanisms and Properties Governing Ion Conduction. *Chem. Rev.* 2016, 116 (1), 140–162. https://doi.org/10.1021/acs.chemrev.5b00563.
- (142) Indrawan, R. F.; Gamo, H.; Nagai, A.; Matsuda, A. Chemically Understanding the Liquid-Phase Synthesis of Argyrodite Solid Electrolyte Li 6 PS 5 Cl with the Highest Ionic Conductivity for All-Solid-State Batteries. *Chem. Mater.* 2023, 35 (6), 2549–2558. https://doi.org/10.1021/acs.chemmater.2c03818.
- (143) Wang, S.; Zhang, Y.; Zhang, X.; Liu, T.; Lin, Y.-H.; Shen, Y.; Li, L.; Nan, C.-W. High-Conductivity Argyrodite Li 6 PS 5 Cl Solid Electrolytes Prepared via Optimized Sintering Processes for All-Solid-State Lithium–Sulfur Batteries. ACS Appl. Mater. Interfaces. 2018, 10 (49), 42279–42285. https://doi.org/10.1021/acsami.8b15121.
- (144) John Banhart. Advanced Tomographic Methods in Materials Research and Engineering; 2008.
- (145) Vaughan, G. B. M.; Baker, R.; Barret, R.; Bonnefoy, J.; Buslaps, T.; Checchia, S.; Duran, D.; Fihman, F.; Got, P.; Kieffer, J.; Kimber, S. A. J.; Martel, K.; Morawe, C.; Mottin, D.; Papillon, E.; Petitdemange, S.; Vamvakeros, A.; Vieux, J.-P.; Di Michiel, M. ID15A at the ESRF a Beamline for High Speed Operando X-Ray Diffraction, Diffraction Tomography and Total Scattering. *J. Synchrotron Radiat.* 2020, 27 (2), 515–528. https://doi.org/10.1107/S1600577519016813.
- (146) Kyrieleis, A.; Ibison, M.; Titarenko, V.; Withers, P. J. Image Stitching Strategies for Tomographic Imaging of Large Objects at High Resolution at Synchrotron Sources.

- Nucl. Instrum. Methods Phys. Res. A. **2009**, 607 (3), 677–684. https://doi.org/10.1016/j.nima.2009.06.030.
- (147) P. Paleo, H. Payno, N. Vigano, C. N. Nabu 2021.2.0. https://zenodo.org/records/5916579.
- (148) Mote, V.; Purushotham, Y.; Dole, B. Williamson-Hall Analysis in Estimation of Lattice Strain in Nanometer-Sized ZnO Particles. *J. Theor. Appl. Phys.* **2012**, *6* (1), 6. https://doi.org/10.1186/2251-7235-6-6.
- (149) Singh, A. K. The Lattice Strains in a Specimen (Cubic System) Compressed Nonhydrostatically in an Opposed Anvil Device. *J. Appl. Phys.* **1993**, *73* (9), 4278–4286. https://doi.org/10.1063/1.352809.
- (150) Pietsch, P.; Hess, M.; Ludwig, W.; Eller, J.; Wood, V. Combining Operando Synchrotron X-Ray Tomographic Microscopy and Scanning X-Ray Diffraction to Study Lithium Ion Batteries. *Sci. Rep.* **2016**, *6* (1), 27994. https://doi.org/10.1038/srep27994.
- (151) Sottmann, J.; Di Michiel, M.; Fjellvåg, H.; Malavasi, L.; Margadonna, S.; Vajeeston, P.; Vaughan, G. B. M.; Wragg, D. S. Chemical Structures of Specific Sodium Ion Battery Components Determined by Operando Pair Distribution Function and X-ray Diffraction Computed Tomography. *Angew. Chemie Int. Ed.* 2017, 56 (38), 11385–11389. https://doi.org/10.1002/anie.201704271.
- (152) Tonin, G.; Vaughan, G. B. M.; Bouchet, R.; Alloin, F.; Di Michiel, M.; Barchasz, C. Operando Investigation of the Lithium/Sulfur Battery System by Coupled X-Ray Absorption Tomography and X-Ray Diffraction Computed Tomography. *J. Power Sources.* 2020, 468, 228287. https://doi.org/10.1016/j.jpowsour.2020.228287.

- (153) Jensen, K. M. Ø.; Yang, X.; Laveda, J. V.; Zeier, W. G.; See, K. A.; Michiel, M. Di; Melot, B. C.; Corr, S. A.; Billinge, S. J. L. X-Ray Diffraction Computed Tomography for Structural Analysis of Electrode Materials in Batteries. *J. Electrochem. Soc.* 2015, 162 (7), A1310–A1314. https://doi.org/10.1149/2.0771507jes.
- (154) Liu, H.; Kazemiabnavi, S.; Grenier, A.; Vaughan, G.; Di Michiel, M.; Polzin, B. J.; Thornton, K.; Chapman, K. W.; Chupas, P. J. Quantifying Reaction and Rate Heterogeneity in Battery Electrodes in 3D through Operando X-Ray Diffraction Computed Tomography. ACS Appl. Mater. Interfaces. 2019, 11 (20), 18386–18394. https://doi.org/10.1021/acsami.9b02173.
- (155) Warren, B. E. X-Ray Diffraction; 1969. https://doi.org/10.1107/S0567739471000445.
- (156) McCusker, L. B.; Von Dreele, R. B.; Cox, D. E.; Louër, D.; Scardi, P. Rietveld Refinement Guidelines. J. Appl. Crystallogr. 1999, 32 (1), 36–50. https://doi.org/10.1107/S0021889898009856.
- (157) Squires, G. L. *Introduction to the Theory of Thermal Neutron Scattering*; Cambridge University Press, 2012. https://doi.org/10.1017/CBO9781139107808.
- (158) LaManna, J. M.; Hussey, D. S.; Baltic, E.; Jacobson, D. L. Neutron and X-Ray Tomography (NeXT) System for Simultaneous, Dual Modality Tomography. Rev. Sci. Instrum. 2017, 88 (11). https://doi.org/10.1063/1.4989642.
- (159) Kobayashi, T.; Ohnishi, T.; Osawa, T.; Pratt, A.; Tear, S.; Shimoda, S.; Baba, H.; Laitinen, M.; Sajavaara, T. In-Operando Lithium-Ion Transport Tracking in an All-Solid-State Battery. *Small.* **2022**, *18* (46), 1–9. https://doi.org/10.1002/smll.202204455.

- (160) Nie, Z.; Ong, S.; Hussey, D. S.; Lamanna, J. M.; Jacobson, D. L.; Koenig, G. M. Probing Transport Limitations in Thick Sintered Battery Electrodes with Neutron Imaging. *Mol. Syst. Des. Eng.* **2020**, *5* (1), 245–256. https://doi.org/10.1039/c9me00084d.
- (161) Nie, Z.; McCormack, P.; Bilheux, H. Z.; Bilheux, J. C.; Robinson, J. P.; Nanda, J.; Koenig, G. M. Probing Lithiation and Delithiation of Thick Sintered Lithium-Ion Battery Electrodes with Neutron Imaging. *J. Power Sources.* 2019, 419 (January), 127–136. https://doi.org/10.1016/j.jpowsour.2019.02.075.
- (162) Nazer, N. S.; Strobl, M.; Kaestner, A.; Vie, P. J. S.; Yartys, V. A. Operando Neutron Imaging Study of a Commercial Li-Ion Battery at Variable Charge-Discharge Current Densities. *Electrochim. Acta.* 2022, 427 (2027), 140793. https://doi.org/10.1016/j.electacta.2022.140793.
- (163) Siegel, J. B.; Lin, X.; Stefanopoulou, A. G.; Hussey, D. S.; Jacobson, D. L.; Gorsich, D. Neutron Imaging of Lithium Concentration in LFP Pouch Cell Battery. *J. Electrochem. Soc.* 2011, 158 (5), A523. https://doi.org/10.1149/1.3566341.
- (164) Atkins, D.; Capria, E.; Edström, K.; Famprikis, T.; Grimaud, A.; Jacquet, Q.; Johnson, M.; Matic, A.; Norby, P.; Reichert, H.; Rueff, J. P.; Villevieille, C.; Wagemaker, M.; Lyonnard, S. Accelerating Battery Characterization Using Neutron and Synchrotron Techniques: Toward a Multi-Modal and Multi-Scale Standardized Experimental Workflow. Adv. Energy Mater. 2022, 12 (17). https://doi.org/10.1002/aenm.202102694.
- (165) Michalak, B.; Sommer, H.; Mannes, D.; Kaestner, A.; Brezesinski, T.; Janek, J. Gas Evolution in Operating Lithium-Ion Batteries Studied in Situ by Neutron Imaging. *Sci. Rep.* **2015**, *5*, 1–9. https://doi.org/10.1038/srep15627.

- (166) Ziesche, R. F.; Kardjilov, N.; Kockelmann, W.; Brett, D. J. L.; Shearing, P. R. Neutron Imaging of Lithium Batteries. *Joule.* **2022**, *6* (1), 35–52. https://doi.org/10.1016/j.joule.2021.12.007.
- (167) Butler, L. G.; Schillinger, B.; Ham, K.; Dobbins, T. A.; Liu, P.; Vajo, J. J. Neutron Imaging of a Commercial Li-Ion Battery during Discharge: Application of Monochromatic Imaging and Polychromatic Dynamic Tomography. *Nucl. Instrum. Methods Phys. Res. A.* 2011, 651 (1), 320–328. https://doi.org/10.1016/j.nima.2011.03.023.
- (168) Deng, Z.; Lin, X.; Huang, Z.; Meng, J.; Zhong, Y.; Ma, G.; Zhou, Y.; Shen, Y.; Ding, H.; Huang, Y. Recent Progress on Advanced Imaging Techniques for Lithium-Ion Batteries. *Adv. Energy Mater.* **2021**, *11* (2), 1–24. https://doi.org/10.1002/aenm.202000806.
- (169) Bradbury, R.; Kardjilov, N.; Dewald, G. F.; Tengattini, A.; Helfen, L.; Zeier, W. G.; Manke, I. Visualizing Lithium Ion Transport in Solid-State Li–S Batteries Using 6Li Contrast Enhanced Neutron Imaging. *Adv. Funct. Mater.* 2023, 33 (38), 1–10. https://doi.org/10.1002/adfm.202302619.
- (170) Wang, C.; Gong, Y.; Dai, J.; Zhang, L.; Xie, H.; Pastel, G.; Liu, B.; Wachsman, E.; Wang, H.; Hu, L. In Situ Neutron Depth Profiling of Lithium Metal-Garnet Interfaces for Solid State Batteries. *J. Am. Chem. Soc.* **2017**, *139* (40), 14257–14264. https://doi.org/10.1021/jacs.7b07904.
- (171) Yang, G.; Zhang, Y.; Bilheux, J.; Self, E.; Westover, A.; Chen, J.; Bilheux, H.; Nanda, J. Tracking the Initial Capacity Loss in Solid-State Batteries Using in-Situ Neutron Tomography and Raman Imaging. *Nat. Portfolio.* 2023. https://doi.org/10.21203/rs.3.rs-3761624/v1

- (172) Bradbury, R.; Dewald, G. F.; Kraft, M. A.; Arlt, T.; Kardjilov, N.; Janek, J.; Manke, I.; Zeier, W. G.; Ohno, S. Visualizing Reaction Fronts and Transport Limitations in Solid-State Li–S Batteries via Operando Neutron Imaging. *Adv. Energy Mater.* **2023**, *13* (17). https://doi.org/10.1002/aenm.202203426.
- (173) Cao, D.; Zhang, Y.; Ji, T.; Zhu, H. In Operando Neutron Imaging Characterizations of All-Solid-State Batteries. *MRS Bull.* **2023**, *48* (12), 1257–1268. https://doi.org/10.1557/s43577-023-00611-7.
- (174) Cressa, L.; Boillat, P.; Gerard, M.; Sun, Y.; Sharma, S.; De Castro, O.; Nojabaee, M.; Schmitz, G.; Wirtz, T.; Eswara, S. Investigation of Li Accumulations in LLZO Based Solid State Batteries via Operando Neutron Imaging and Ex-Situ Correlative Structural and Chemical Analysis. *Electrochim. Acta.* 2024, 494 (May), 144397. https://doi.org/10.1016/j.electacta.2024.144397.
- (175) Liu, M.; Ganapathy, S.; Wagemaker, M. A Direct View on Li-Ion Transport and Li-Metal Plating in Inorganic and Hybrid Solid-State Electrolytes. *Acc. Chem. Res.* **2022**, 55 (3), 333–344. https://doi.org/10.1021/acs.accounts.1c00618.
- (176) Tengattini, A.; Lenoir, N.; Andò, E.; Giroud, B.; Atkins, D.; Beaucour, J.; Viggiani, G. NeXT-Grenoble, the Neutron and X-Ray Tomograph in Grenoble. *Nucl. Instrum. Methods Phys. Res. A.* **2020**, *968*, 163939. https://doi.org/10.1016/j.nima.2020.163939.
- (177) Minniti, T.; Watanabe, K.; Burca, G.; Pooley, D. E.; Kockelmann, W. Characterization of the New Neutron Imaging and Materials Science Facility IMAT. *Nucl. Instrum. Methods Phys. Res. A.* **2018**, 888, 184–195. https://doi.org/10.1016/j.nima.2018.01.037.
- (178) Huang, X.; Lu, Y.; Song, Z.; Xiu, T.; Badding, M. E.; Wen, Z. Preparation of Dense Ta-LLZO/MgO Composite Li-Ion Solid Electrolyte: Sintering, Microstructure,

- Performance and the Role of MgO. *J. Energy Chem.* **2019**, *39*, 8–16. https://doi.org/10.1016/j.jechem.2019.01.013.
- (179) Gao, Y.; Nolan, A. M.; Du, P.; Wu, Y.; Yang, C.; Chen, Q.; Mo, Y.; Bo, S. H. Classical and Emerging Characterization Techniques for Investigation of Ion Transport Mechanisms in Crystalline Fast Ionic Conductors. *Chem. Rev.* American Chemical Society July 8, 2020, pp 5954–6008. https://doi.org/10.1021/acs.chemrev.9b00747.
- (180) Wolfenstine, J.; Rangasamy, E.; Allen, J. L.; Sakamoto, J. High Conductivity of Dense Tetragonal Li 7La 3Zr 2O 12. *J. Power Sources.* **2012**, 208, 193–196. https://doi.org/10.1016/j.jpowsour.2012.02.031.
- (181) Feng, L.; Li, L.; Zhang, Y.; Peng, H.; Zou, Y. Low Temperature Synthesis and Ion Conductivity of Li7La3Zr2O12 Garnets for Solid State Li Ion Batteries. *Solid State Ionics*. **2017**, *310*, 129–133. https://doi.org/10.1016/j.ssi.2017.08.016.
- (182) Fatigue and Tribological Properties of Plastics and Elastomers; Elsevier, 2010. https://doi.org/10.1016/C2009-0-20351-5.
- (183) Puls, S.; Nazmutdinova, E.; Kalyk, F.; Woolley, H. M.; Thomsen, J. F.; Cheng, Z.; Fauchier-Magnan, A.; Gautam, A.; Gockeln, M.; Ham, S.-Y.; Hasan, M. T.; Jeong, M.-G.; Hiraoka, D.; Kim, J. S.; Kutsch, T.; Lelotte, B.; Minnmann, P.; Miß, V.; Motohashi, K.; Nelson, D. L.; Ooms, F.; Piccolo, F.; Plank, C.; Rosner, M.; Sandoval, S. E.; Schlautmann, E.; Schuster, R.; Spencer-Jolly, D.; Sun, Y.; Vishnugopi, B. S.; Zhang, R.; Zheng, H.; Adelhelm, P.; Brezesinski, T.; Bruce, P. G.; Danzer, M.; El Kazzi, M.; Gasteiger, H.; Hatzell, K. B.; Hayashi, A.; Hippauf, F.; Janek, J.; Jung, Y. S.; McDowell, M. T.; Meng, Y. S.; Mukherjee, P. P.; Ohno, S.; Roling, B.; Sakuda, A.; Schwenzel, J.; Sun, X.; Villevieille, C.; Wagemaker, M.; Zeier, W. G.; Vargas-Barbosa, N. M.

- Benchmarking the Reproducibility of All-Solid-State Battery Cell Performance. *Nat. Energy.* **2024**. https://doi.org/10.1038/s41560-024-01634-3.
- (184) Magnussen, O. M.; Drnec, J.; Qiu, C.; Martens, I.; Huang, J. J.; Chattot, R.; Singer, A. In Situ and Operando X-Ray Scattering Methods in Electrochemistry and Electrocatalysis. *Chem. Rev.* **2024**. https://doi.org/10.1021/acs.chemrev.3c00331.
- (185) Borkiewicz, O. J.; Shyam, B.; Wiaderek, K. M.; Kurtz, C.; Chupas, P. J.; Chapman, K. W. The AMPIX Electrochemical Cell: A Versatile Apparatus for in Situ X-Ray Scattering and Spectroscopic Measurements. J. Appl. Crystallogr. 2012, 45 (6), 1261–1269. https://doi.org/10.1107/S0021889812042720.
- (186) Diaz-Lopez, M.; Cutts, G. L.; Allan, P. K.; Keeble, D. S.; Ross, A.; Pralong, V.; Spiekermann, G.; Chater, P. A. Fast Operando X-Ray Pair Distribution Function Using the DRIX Electrochemical Cell. *J. Synchrotron Radiat.* 2020, 27 (5), 1190–1199. https://doi.org/10.1107/S160057752000747X.
- (187) Finegan, D. P.; Vamvakeros, A.; Tan, C.; Heenan, T. M. M.; Daemi, S. R.; Seitzman, N.; Di Michiel, M.; Jacques, S.; Beale, A. M.; Brett, D. J. L.; Shearing, P. R.; Smith, K. Spatial Quantification of Dynamic Inter and Intra Particle Crystallographic Heterogeneities within Lithium Ion Electrodes. *Nat. Commun.* 2020, 11 (1), 631. https://doi.org/10.1038/s41467-020-14467-x.
- (188) Tan, C.; Daemi, S. R.; Taiwo, O. O.; Heenan, T. M. M.; Brett, D. J. L.; Shearing, P. R. Evolution of Electrochemical Cell Designs for In-Situ and Operando 3D Characterization. *Materials.* **2018**, *11* (11), 2157. https://doi.org/10.3390/ma11112157.
- (189) Dugas, R.; Forero-Saboya, J. D.; Ponrouch, A. Methods and Protocols for Reliable Electrochemical Testing in Post-Li Batteries (Na, K, Mg, and Ca). *Chem. Mater.* **2019**, *31* (21), 8613–8628. https://doi.org/10.1021/acs.chemmater.9b02776.

- (190) Lommen, J.; Schorn, L.; Sproll, C.; Haussmann, J.; Kübler, N. R.; Budach, W.; Rana, M.; Tamaskovics, B. Reduction of CT Artifacts Using Polyetheretherketone (PEEK), Polyetherketoneketone (PEKK), Polyphenylsulfone (PPSU), and Polyethylene (PE) Reconstruction Plates in Oral Oncology. *J. Oral Maxillofac. Surg.* 2022, 80 (7), 1272–1283. https://doi.org/10.1016/j.joms.2022.03.004.
- (191) Han, S. Y.; Lee, C.; Lewis, J. A.; Yeh, D.; Liu, Y.; Lee, H. W.; McDowell, M. T. Stress Evolution during Cycling of Alloy-Anode Solid-State Batteries. *Joule.* **2021**, *5* (9), 2450–2465. https://doi.org/10.1016/j.joule.2021.07.002.
- (192) Miao, N.; Hai, B.; Wang, S.; Ni, J.; Li, X.; Wei, H.; Zhang, K.; Wang, X.; Huang, W. An In-Situ X-Ray Computed Tomography Imaging Apparatus with Stack Pressures for Rechargeable Batteries. *Scr. Mater.* **2023**, *229*. https://doi.org/10.1016/j.scriptamat.2023.115381.
- (193) Parker, D.; Bussink, J.; van de Grampel, H. T.; Wheatley, G. W.; Dorf, E.-U.; Ostlinning, E.; Reinking, K.; Schubert, F.; Jünger, O. Polymers, High-Temperature. *Ullmann's Encycl. Ind. Chem.* Wiley-VCH Verlag GmbH & Co. KGaA: Weinheim, Germany, 2012. https://doi.org/10.1002/14356007.a21_449.pub3.
- (194) Ye, L.; Li, X. A Dynamic Stability Design Strategy for Lithium Metal Solid State Batteries. *Nature*. **2021**, *593* (7858), 218–222. https://doi.org/10.1038/s41586-021-03486-3.
- (195) Gao, X.; Liu, B.; Hu, B.; Ning, Z.; Jolly, D. S.; Zhang, S.; Perera, J.; Bu, J.; Liu, J.; Doerrer, C.; Darnbrough, E.; Armstrong, D.; Grant, P. S.; Bruce, P. G. Solid-State Lithium Battery Cathodes Operating at Low Pressures. *Joule.* **2022**, *6* (3), 636–646. https://doi.org/10.1016/j.joule.2022.02.008.

- (196) Doux, J.; Nguyen, H.; Tan, D. H. S.; Banerjee, A.; Wang, X.; Wu, E. A.; Jo, C.; Yang, H.; Meng, Y. S. Stack Pressure Considerations for Room-Temperature All-Solid-State Lithium Metal Batteries. *Adv. Energy Mater.* 2020, 10 (1). https://doi.org/10.1002/aenm.201903253.
- (197) Wood, K. N.; Noked, M.; Dasgupta, N. P. Lithium Metal Anodes: Toward an Improved Understanding of Coupled Morphological, Electrochemical, and Mechanical Behavior. *ACS Energy Lett.* **2017**, *2* (3), 664–672. https://doi.org/10.1021/acsenergylett.6b00650.
- (198) Fincher, C. D.; Athanasiou, C. E.; Gilgenbach, C.; Wang, M.; Sheldon, B. W.; Carter, W. C.; Chiang, Y. M. Controlling Dendrite Propagation in Solid-State Batteries with Engineered Stress. *Joule.* 2022, 6 (12), 2794–2809. https://doi.org/10.1016/j.joule.2022.10.011.
- (199) Krauskopf, T.; Richter, F. H.; Zeier, W. G.; Janek, J. Physicochemical Concepts of the Lithium Metal Anode in Solid-State Batteries. *Chem. Rev.* **2020**, *120* (15), 7745–7794. https://doi.org/10.1021/acs.chemrev.0c00431.
- (200) Hatzell, K. B.; Chen, X. C.; Cobb, C. L.; Dasgupta, N. P.; Dixit, M. B.; Marbella, L. E.;
 McDowell, M. T.; Mukherjee, P. P.; Verma, A.; Viswanathan, V.; Westover, A. S.; Zeier,
 W. G. Challenges in Lithium Metal Anodes for Solid-State Batteries. *ACS Energy Lett.*2020, 5 (3), 922–934. https://doi.org/10.1021/acsenergylett.9b02668.
- (201) Jia, L.; Zhu, J.; Zhang, X.; Guo, B.; Du, Y.; Zhuang, X. Li–Solid Electrolyte Interfaces/Interphases in All-Solid-State Li Batteries. *Electrochem. Energy Rev.* **2024**, 7 (1), 12. https://doi.org/10.1007/s41918-024-00212-1.
- (202) Deng, Z.; Wang, Z.; Chu, I.-H.; Luo, J.; Ong, S. P. Elastic Properties of Alkali Superionic Conductor Electrolytes from First Principles Calculations. *J. Electrochem. Soc.* **2016**, *163* (2), A67–A74. https://doi.org/10.1149/2.0061602jes.

- (203) Aspinall, J.; Armstrong, D. E. J.; Pasta, M. EBSD-Coupled Indentation: Nanoscale Mechanics of Lithium Metal. *Mater. Today Energy.* **2022**, *30*. https://doi.org/10.1016/j.mtener.2022.101183.
- (204) Fincher, C. D.; Ojeda, D.; Zhang, Y.; Pharr, G. M.; Pharr, M. Mechanical Properties of Metallic Lithium: From Nano to Bulk Scales. *Acta. Mater.* **2020**, *186*, 215–222. https://doi.org/10.1016/j.actamat.2019.12.036.
- (205) Xu, C.; Ahmad, Z.; Aryanfar, A.; Viswanathan, V.; Greer, J. R. Enhanced Strength and Temperature Dependence of Mechanical Properties of Li at Small Scales and Its Implications for Li Metal Anodes. *Proc. Natl. Acad. Sci.* 2017, 114 (1), 57–61. https://doi.org/10.1073/pnas.1615733114.
- (206) LePage, W. S.; Chen, Y.; Kazyak, E.; Chen, K.-H.; Sanchez, A. J.; Poli, A.; Arruda, E. M.; Thouless, M. D.; Dasgupta, N. P. Lithium Mechanics: Roles of Strain Rate and Temperature and Implications for Lithium Metal Batteries. *J. Electrochem. Soc.* 2019, 166 (2), A89–A97. https://doi.org/10.1149/2.0221902jes.
- (207) Design of Highly Conductive Iongel Soft Solid Electrolytes for Li-O2 Batteries. *Energy Mater.* **2022**, *3* (1), 300003. https://doi.org/10.20517/energymater.2022.59.
- (208) Thomas, A.; Clayton, J. Stress Distribution in a Powder Column under Uniaxial Compression. *Powder Technol.* **2022**, 408, 117768. https://doi.org/10.1016/j.powtec.2022.117768.
- (209) Whiteley, J. M.; Taynton, P.; Zhang, W.; Lee, S. Ultra-thin Solid-State Li-Ion Electrolyte Membrane Facilitated by a Self-Healing Polymer Matrix. *Adv. Mater.* **2015**, 27 (43), 6922–6927. https://doi.org/10.1002/adma.201502636.

- (210) Luo, S.; Wang, Z.; Fan, A.; Liu, X.; Wang, H.; Ma, W.; Zhu, L.; Zhang, X. A High Energy and Power All-Solid-State Lithium Battery Enabled by Modified Sulfide Electrolyte Film. *J. Power Sources.* **2021**, 485, 229325. https://doi.org/10.1016/j.jpowsour.2020.229325.
- (211) Khan, A. J.; Gao, L.; Zhang, Y.; Su, Q.; Li, Z.; Lu, Y.; Liu, H.; Zhao, G. Advancements and Challenges in Si-Based Solid-State Batteries: From Anode Design to Manufacturing Processes. *Next Mater.* **2024**, *7*, 100371. https://doi.org/10.1016/j.nxmate.2024.100371.
- (212) Michrafy, A.; Kadiri, M. S.; Dodds, J. A. Wall Friction and Its Effects on the Density Distribution in the Compaction of Pharmaceutical Excipients. *Chem. Eng. Res. Des.* **2003**, *81* (8), 946–952. https://doi.org/10.1205/026387603322482185.
- (213) Lim, H.; Jun, S.; Song, Y. B.; Bae, H.; Kim, J. H.; Jung, Y. S. Operando Electrochemical Pressiometry Probing Interfacial Evolution of Electrodeposited Thin Lithium Metal Anodes for All-Solid-State Batteries. *Energy Storage Mater.* **2022**, *50*, 543–553. https://doi.org/10.1016/j.ensm.2022.05.050.
- (214) Garcia-Mendez, R.; Smith, J. G.; Neuefeind, J. C.; Siegel, D. J.; Sakamoto, J. Correlating Macro and Atomic Structure with Elastic Properties and Ionic Transport of Glassy Li 2 S-P 2 S 5 (LPS) Solid Electrolyte for Solid-State Li Metal Batteries. *Adv. Energy Mater.* **2020**, *10* (19). https://doi.org/10.1002/aenm.202000335.
- (215) Lewis, J. A.; Cortes, F. J. Q.; Liu, Y.; Miers, J. C.; Verma, A.; Vishnugopi, B. S.; Tippens, J.; Prakash, D.; Marchese, T. S.; Han, S. Y.; Lee, C.; Shetty, P. P.; Lee, H.-W.; Shevchenko, P.; De Carlo, F.; Saldana, C.; Mukherjee, P. P.; McDowell, M. T. Linking Void and Interphase Evolution to Electrochemistry in Solid-State Batteries Using Operando X-Ray Tomography. *Nat. Mater.* **2021**, *20* (4), 503–510. https://doi.org/10.1038/s41563-020-00903-2.

- (216) Diaz, M.; Mohayman, Z.; Shozib, I.; Tu, H. Q.; Kushima, A. Accelerated Li Penetration and Crack Propagation Due to Mechanical Degradation of Sulfide-Based Solid Electrolyte. *Small Methods.* **2024**. https://doi.org/10.1002/smtd.202301582.
- (217) Cheng, E. J.; Sharafi, A.; Sakamoto, J. Intergranular Li Metal Propagation through Polycrystalline Li6.25Al0.25La3Zr2O12 Ceramic Electrolyte. *Electrochim. Acta.* **2017**, 223, 85–91. https://doi.org/10.1016/j.electacta.2016.12.018.
- (218) Lehmann, E. H.; Frei, G.; Kühne, G.; Boillat, P. The Micro-Setup for Neutron Imaging: A Major Step Forward to Improve the Spatial Resolution. *Nucl. Instrum. Methods Phys. Res. A.* **2007**, *576* (2–3), 389–396. https://doi.org/10.1016/j.nima.2007.03.017.
- (219) Vanpeene, V.; Villanova, J.; King, A.; Lestriez, B.; Maire, E.; Roué, L. Dynamics of the Morphological Degradation of Si-Based Anodes for Li-Ion Batteries Characterized by In Situ Synchrotron X-Ray Tomography. *Adv. Energy Mater.* 2019, 9 (18). https://doi.org/10.1002/aenm.201803947.
- (220) Holscot. PFA. https://holscot.com/glossary/pfa/.
- (221) Tengattini, A.; Kardjilov, N.; Helfen, L.; Douissard, P.-A.; Lenoir, N.; Markötter, H.; Hilger, A.; Arlt, T.; Paulisch, M.; Turek, T.; Manke, I. Compact and Versatile Neutron Imaging Detector with Sub-4μm Spatial Resolution Based on a Single-Crystal Thin-Film Scintillator. Opt. Express. 2022, 30 (9), 14461. https://doi.org/10.1364/OE.448932.
- (222) Tengattini, A.; Lenoir, N.; Andò, E.; Viggiani, G. Neutron Imaging for Geomechanics:

 A Review. *Geomech. Energy Environ.* **2021**, *27*, 100206.

 https://doi.org/10.1016/j.gete.2020.100206.
- (223) Shafabakhsh, P.; Cordonnier, B.; Pluymakers, A.; Le Borgne, T.; Mathiesen, J.; Linga, G.; Hu, Y.; Kaestner, A.; Renard, F. 4D Neutron Imaging of Solute Transport and Fluid

- Flow in Sandstone Before and After Mineral Precipitation. *Water Resour. Res.* **2024**, *60* (3). https://doi.org/10.1029/2023WR036293.
- (224) Zhan, Y.-X.; Shi, P.; Zhang, X.-Q.; Ding, F.; Huang, J.-Q.; Jin, Z.; Xiang, R.; Liu, X.; Zhang, Q. The Insights of Lithium Metal Plating/Stripping in Porous Hosts: Progress and Perspectives. *Energy Technol.* **2021**, *9* (2). https://doi.org/10.1002/ente.202000700.
- (225) Johnson, N. S.; Trenikhina, Y.; Bale, H.; Kelly, S. Deep-Learning Models Enable High-Resolution Reconstruction of Large-Volume x-Ray Microscopy Datasets. *Dev. X-Ray Tomogr. XV*; Müller, B., Wang, G., Eds.; SPIE, 2024; p 28. https://doi.org/10.1117/12.3027501.
- (226) Villarraga-Gómez, H.; Crosby, K.; Terada, M.; Rad, M. N. Assessing Electronics with Advanced 3D X-Ray Imaging Techniques, Nanoscale Tomography, and Deep Learning. *J. Fail. Anal. Prev.* **2024**, *24* (5), 2113–2128. https://doi.org/10.1007/s11668-024-01989-5.
- (227) Green, C.; Ahmed, S.; Marathe, S.; Perera, L.; Leonardi, A.; Gmyrek, K.; Dini, D.; Le Houx, J. Three-Dimensional, Multimodal Synchrotron Data for Machine Learning Applications. *Sci. Data* **2025**, *12* (1), 329. https://doi.org/10.1038/s41597-025-04605-9.

9 Appendix

License Number	6021570099074		Printable Details
License date	May 03, 2025		
Licensed Content		Order Details	
Licensed Content Publisher Licensed Content Publication Licensed Content Title	Elsevier Nano Energy Tracking lithium penetration in solid electrolytes in 3D by in- situ synchrotron X-ray computed tomography Shual Hao,Sohrab R. Daemi,Thomas M.M. Heenan,Wenjia	Type of Use Portion Number of figures/tables/illustrations Format Are you the author of this Elsevier article?	reuse in a thesis/dissertation figures/tables/illustrations 1 electronic No
Licensed Content Author	Du,Chun Tan,Malte Storm,Christoph Rau,Dan J.L. Brett,Paul R. Shearing	Will you be translating?	No
Licensed Content Date	Apr 1, 2021		
Licensed Content Volume Licensed Content Issue	82 n/a		
Licensed Content Pages	1		
Erecised content rages			
About Your Work		Additional Data	
Title of new work	Correlated Characterization and Advanced Microscopy of Sulfidic Solid-State Li Batteries	Portions	Fig. 2. 2D orthogonal slices extracted from 3D tomogram, comparing them at original state (b, e) and after 1st (c, f), 2nd (d, g), 3rd (h, k), 9th (i, l) and 14th (j, m) plating.
Institution name Expected presentation date	University College London Jul 2025	The Requesting Person / Organization to	
Expected presentation date	jui 2023	Appear on the License	Robert Young, Univeristy College London
Requestor Location		Tax Details	
Requestor Location	Mr. Robert Young TORRINGTON PLACE London, WC1E 7JE United Kingdom	Publisher Tax ID	GB 494 6272 12
License Number	6021570929644		🖨 Printable Details
License Number	6021570929644 May 03, 2025		Printable Details
		Order Details	Printable Details
License date Licensed Content Licensed Content Publisher	May 03, 2025 Elsevier	Type of Use	reuse in a thesis/dissertation
License date Licensed Content	May 03, 2025 Elsevier Journal of Power Sources	Type of Use Portion	reuse in a thesis/dissertation figures/tables/illustrations
License date Licensed Content Licensed Content Publisher	May 03, 2025 Elsevier	Type of Use Portion Number of figures/tables/illustrations	reuse in a thesis/dissertation figures/tables/illustrations 1
License date Licensed Content Licensed Content Publisher Licensed Content Publication	May 03, 2025 Elsevier Journal of Power Sources High-pressure in situ X-ray computed tomography and numerical simulation of sulfide solid electrolyte M. Kodama, S. Komiyama, A. Ohashi, N. Horikawa, K.	Type of Use Portion	reuse in a thesis/dissertation figures/tables/illustrations
Licensed date Licensed Content Licensed Content Publisher Licensed Content Publication Licensed Content Title Licensed Content Author	May 03, 2025 Elsevier Journal of Power Sources High-pressure in situ X-ray computed tomography and numerical simulation of sulfide solid electrolyte M. Kodama,S. Komiyama,A. Ohashi,N. Horikawa,K. Kawamura,S. Hiral	Type of Use Portion Number of figures/tables/illustrations Format	reuse in a thesis/dissertation figures/tables/illustrations 1 both print and electronic
License date Licensed Content Licensed Content Publisher Licensed Content Publication Licensed Content Title	May 03, 2025 Elsevier Journal of Power Sources High-pressure in situ X-ray computed tomography and numerical simulation of sulfide solid electrolyte M. Kodama, S. Komiyama, A. Ohashi, N. Horikawa, K.	Type of Use Portion Number of figures/tables/illustrations Format Are you the author of this Elsevier article?	reuse in a thesis/dissertation figures/tables/illustrations 1 both print and electronic No
License date Licensed Content Licensed Content Publisher Licensed Content Publication Licensed Content Title Licensed Content Author Licensed Content Date	Elsevier Journal of Power Sources High-pressure in situ X-ray computed tomography and numerical simulation of sulfide solid electrolyte M. Kodama, S. Komiyama, A. Ohashi, N. Horikawa, K. Kawamura, S. Hirai Jun 30, 2020	Type of Use Portion Number of figures/tables/illustrations Format Are you the author of this Elsevier article?	reuse in a thesis/dissertation figures/tables/illustrations 1 both print and electronic No
License date Licensed Content Licensed Content Publisher Licensed Content Publication Licensed Content Title Licensed Content Author Licensed Content Date Licensed Content Date Licensed Content Date	Elsevier Journal of Power Sources High-pressure in situ X-ray computed tomography and numerical simulation of sulfide solid electrolyte M. Kodama,S. Komlyama,A. Ohashi,N. Horikawa,K. Kawamura,S. Hirai Jun 30, 2020 462	Type of Use Portion Number of figures/tables/illustrations Format Are you the author of this Elsevier article?	reuse in a thesis/dissertation figures/tables/illustrations 1 both print and electronic No
Licensed Content Licensed Content Publisher Licensed Content Publication Licensed Content Title Licensed Content Author Licensed Content Date Licensed Content Volume Licensed Content Issue	Elsevier Journal of Power Sources High-pressure in situ X-ray computed tomography and numerical simulation of sulfide solid electrolyte M. Kodama. S. Komlyama, A. Ohashi, N. Horikawa, K. Kawamura, S. Hirai Jun 30, 2020 462 n/a	Type of Use Portion Number of figures/tables/illustrations Format Are you the author of this Elsevier article?	reuse in a thesis/dissertation figures/tables/illustrations 1 both print and electronic No
Licensed Content Licensed Content Publisher Licensed Content Publication Licensed Content Title Licensed Content Author Licensed Content Date Licensed Content Volume Licensed Content Issue Licensed Content Pages About Your Work Title of new work	Elsevier Journal of Power Sources High-pressure in situ X-ray computed tomography and numerical simulation of sulfide solid electrolyte M. Kodama,S. Komlyama,A. Ohashi,N. Horikawa,K. Kawamura,S. Hiral Jun 30, 2020 462 n/a 1 Correlated Characterization and Advanced Microscopy of Sulfidic Solid-State Li Batteries	Type of Use Portion Number of figures/tables/illustrations Format Are you the author of this Elsevier article? Will you be translating?	reuse in a thesis/dissertation figures/tables/illustrations 1 both print and electronic No No Fig. 3. (a)lonic conductivity, (b) X-ray computed tomography images of solid electrolyte (white: solid electrolyte; black:
Licensed date Licensed Content Publisher Licensed Content Publication Licensed Content Title Licensed Content Author Licensed Content Date Licensed Content Volume Licensed Content Issue Licensed Content Pages About Your Work Title of new work Institution name	Elsevier Journal of Power Sources High-pressure in situ X-ray computed tomography and numerical simulation of sulfide solid electrolyte M. Kodama,S. Komiyama,A. Ohashi,N. Horikawa,K. Kawamura,S. Hirai Jun 30, 2020 462 n/a 1 Correlated Characterization and Advanced Microscopy of Sulfidic Solid-State U Batteries University College London	Type of Use Portion Number of figures/tables/illustrations Format Are you the author of this Elsevier article? Will you be translating? Additional Data Portions	reuse in a thesis/dissertation figures/tables/illustrations 1 both print and electronic No No
Licensed Content Licensed Content Publisher Licensed Content Publication Licensed Content Title Licensed Content Author Licensed Content Date Licensed Content Volume Licensed Content Issue Licensed Content Pages About Your Work Title of new work	Elsevier Journal of Power Sources High-pressure in situ X-ray computed tomography and numerical simulation of sulfide solid electrolyte M. Kodama,S. Komlyama,A. Ohashi,N. Horikawa,K. Kawamura,S. Hiral Jun 30, 2020 462 n/a 1 Correlated Characterization and Advanced Microscopy of Sulfidic Solid-State Li Batteries	Type of Use Portion Number of figures/tables/illustrations Format Are you the author of this Elsevier article? Will you be translating?	reuse in a thesis/dissertation figures/tables/illustrations 1 both print and electronic No No Fig. 3. (a)lonic conductivity, (b) X-ray computed tomography images of solid electrolyte (white: solid electrolyte; black:
Licensed Content Licensed Content Publisher Licensed Content Publication Licensed Content Title Licensed Content Author Licensed Content Date Licensed Content Volume Licensed Content Issue Licensed Content Pages About Your Work Title of new work Institution name	Elsevier Journal of Power Sources High-pressure in situ X-ray computed tomography and numerical simulation of sulfide solid electrolyte M. Kodama,S. Komiyama,A. Ohashi,N. Horikawa,K. Kawamura,S. Hirai Jun 30, 2020 462 n/a 1 Correlated Characterization and Advanced Microscopy of Sulfidic Solid-State U Batteries University College London	Type of Use Portion Number of figures/tables/illustrations Format Are you the author of this Elsevier article? Will you be translating? Additional Data Portions The Requesting Person / Organization to	reuse in a thesis/dissertation figures/tables/illustrations 1 both print and electronic No No Fig. 3. (a)lonic conductivity, (b) X-ray computed tomography images of solid electrolyte (white: solid electrolyte; black: pore).
License date Licensed Content Licensed Content Publisher Licensed Content Publication Licensed Content Title Licensed Content Author Licensed Content Date Licensed Content Volume Licensed Content Issue Licensed Content Pages About Your Work Title of new work Institution name Expected presentation date	Elsevier Journal of Power Sources High-pressure in situ X-ray computed tomography and numerical simulation of sulfide solid electrolyte M. Kodama,S. Komiyama,A. Ohashi,N. Horikawa,K. Kawamura,S. Hirai Jun 30, 2020 462 n/a 1 Correlated Characterization and Advanced Microscopy of Sulfidic Solid-State U Batteries University College London	Type of Use Portion Number of figures/tables/illustrations Format Are you the author of this Elsevier article? Will you be translating? Additional Data Portions The Requesting Person / Organization to Appear on the License	reuse in a thesis/dissertation figures/tables/illustrations 1 both print and electronic No No Fig. 3. (a)lonic conductivity, (b) X-ray computed tomography images of solid electrolyte (white: solid electrolyte; black: pore).
Licensed date Licensed Content Licensed Content Publisher Licensed Content Publication Licensed Content Title Licensed Content Author Licensed Content Date Licensed Content Volume Licensed Content Issue Licensed Content Pages About Your Work Title of new work Institution name Expected presentation date	Elsevier Journal of Power Sources High-pressure in situ X-ray computed tomography and numerical simulation of sulfide solid electrolyte M. Kodama, S. Komiyama, A. Ohashi, N. Horikawa, K. Kawamura, S. Hirai Jun 30, 2020 462 n/a 1 Correlated Characterization and Advanced Microscopy of Sulfidic Solid-State Li Batteries University College London Jul 2025 Mr. Robert Young	Type of Use Portion Number of figures/tables/illustrations Format Are you the author of this Elsevier article? Will you be translating? Additional Data Portions The Requesting Person / Organization to Appear on the License Tax Details	reuse in a thesis/dissertation figures/tables/illustrations 1 both print and electronic No No Fig. 3. (a)lonic conductivity, (b) X-ray computed tomography images of solid electrolyte (white: solid electrolyte; black: pore), Robert Young, University College London

03-May-2025 1606070-1 Type of Use Publisher Republish in a thesis/dissertation Royal Society of Chemistry Chart/graph/table/figure Order Date Order License ID 2050-7496 ISSN Portion Journal of materials chemistry. A, Materials for energy and sustainability Publication Title Publication Type Start Page 5049 Pressure Effects on Sulfide Electrolytes for Article Title End Page 5055 All Solid-State Batteries Issue 10 Royal Society of Chemistry (Great Britain) Author / Editor Volume 01/01/2013 Date URL http://pubs.rsc.org/en/journals/journaliss... Language English Country United Kingdom of Great Britain and Northern Ireland Rightsholder Royal Society of Chemistry Portion Type Chart/graph/table/figure Distribution Worldwide Number of Charts / Graphs / Tables / Translation Original language of publication Figures Requested Copies for the Disabled? No Format (select all that apply) Print, Electronic Minor Editing Privileges? Ves Who Will Republish the Content? Academic institution Incidental Promotional Use? No Duration of Use Life of current edition Currency Up to 499 Lifetime Unit Quantity Rights Requested Main product Correlated Characterization and Advanced Institution Name
Microscopy of Sulfidic Solid-State Li Expected Presenta Title University College London 2025-07-15 Expected Presentation Date Batteries Instructor Name Rhodri Jervis ADDITIONAL DETAILS The Requesting Person / Organization to Appear on the License Order Reference Number N/A Robert Young, University College London Title, Description or Numeric Reference Fig. 5 (a) Cycling stability at C/10 as a Title of the Article / Chapter the Portion Is Pressure Effects on Sulfide Electrolytes for function of the fabrication pressure of LiIn | LPSCI | NCA solid-state batteries. All these cells were cycled at room temperature at a of the Portion(s) All Solid-State Batteries Doux, Jean-Marie; Yang, Yangyuchen; Tan, Darren H. S.; Nguyen, Han; Wu, Erik A.; Wang, Xuefeng; Banerjee, Abhik; Meng, Ying Shirley Author of Portion(s) stack pressure of 25 MPa. Doux, Jean-Marie; Yang, Yangyuchen; Tan, Darren H. S.; Nguyen, Han; Wu, Erik A.; Wang, Xuefeng; Banerjee, Abhik; Meng, Ying Shirley Editor of Portion(s) 10 Issue, if Republishing an Article From a Publication Date of Portion 2020-01-01 Volume / Edition

Page or Page Range of Portion

5049-5055

License Number	6021581496438		Printable Details
License date	May 03, 2025		
Licensed Content		Order Details	
Licensed Content Publisher	AIP Publishing	Type of Use	Thesis/Dissertation
Licensed Content Publication	Review of Scientific Instruments	Requestor type	Student
Licensed Content Title	Neutron and X-ray Tomography (NeXT) system for simultaneous, dual modality tomography	Format Portion	Print and electronic Figure/Table
Licensed Content Author	LaManna, J. M.; Hussey, D. S.	Number of figures/tables	1
Licensed Content Date	Nov 27, 2017	Will you be translating?	No
Licensed Content Volume	88	, ,	
Licensed Content Issue	11		
About Your Work		Additional Data	
Title of new work	Correlated Characterization and Advanced Microscopy of Sulfidic Solid-State LI Batteries	Portions	Comparison of mass attenuation coefficients for 45 keV X-rays and thermal neutrons (25 meV) as a function of atomic
Institution name	University College London	Portions	number, assuming natural isotopic abundances for the
Expected presentation date	Jul 2025		neutron cross-section
		The Requesting Person / Organization to Appear on the License	Robert Young, University College London
Requestor Location		■ Tax Details	
	Mr. Robert Young TORRINGTON PLACE		
Requestor Location			
	London, WC1E 7JE United Kingdom		
Billing Information			
Billing Type	Invoice		
8 -7F-	University College London		
	TORRINGTON PLACE		
Billing address			
	London, United Kingdom WC1E 7JE		